Tools for Noninvasive Imaging and Control of Engineered Bacteria In Vivo

Thesis by

Marjorie Theresa Buss

In Partial Fulfillment of the Requirements for
the Degree of Doctor of Philosophy in
Chemical Engineering

CALIFORNIA INSTITUTE OF TECHNOLOGY
Pasadena, California

2024
(Defended May 10, 2024)

Marjorie Theresa Buss
ORCID: 0000-0002-4266-9197

ACKNOWLEDGEMENTS

I am extremely grateful to everyone who has helped me on my academic journey so far. First, I would like to thank my PhD advisor Prof. Mikhail G. Shapiro. Everyone who has been in his lab would agree that Mikhail is the best PI in the world. His creativity, optimism, patience, passion for science, and ability to clearly communicate science are infectious, fostering an incredible lab environment. I feel very fortunate to have been able to work and learn a lot in his lab the past 6 years.

I would also like to thank my thesis committee members. I'd like to thank Prof. Rustem Ismagilov for letting me be a TA for his undergraduate thermodynamics class. I learned a lot from his fun teaching style and incredible organization of the class. I'd like to thank Prof. Sarkis Mazmanian for always being willing to meet to help troubleshoot my animal experiments and sharing his lab's expertise as well as equipment. I'd like to thank Prof. Dianne Newman for teaching incredible microbiology classes which changed the way I think about experiments.

Next, I would like to thank my collaborators in the Shapiro Lab who are all awesome. Pradeep was an amazing rotation mentor when I first started in the lab and created such a fun environment despite the difficult animal experiments. Audrey and Margaret were also essential in helping me get through the animal experiments, whether it be with the red tape or with difficult injections. I also appreciate the opportunity to have worked closely with Rob and Tom on our ARG2.0 paper to make it the best that it could be. I learned so much from them and from Danny and Zhiyang, who seem to know everything about ultrasound. I also really enjoyed working with Avinoam, Paulene, and Lealia on their interesting projects. I am in debt to Ann and Jamie who are amazing undergraduate students that really helped push several projects forward. And thank you Dina for keeping me company talking about random things in the middle of the night in lab, and Di and Rohit for always planning fun lab events.

I would also like to thank all of my mentors from before Caltech. When I was at MIT, I learned so much from Jason King, Ben Woolston, Prof. Greg Stephanopoulos, Prof. Kris Prather, Brian Teague, and Wenda Tian. I really appreciate all of their time in teaching and advising me. Thank you to my high school teachers who first got me interested in science and engineering, including Mr. Mosier for computer science, Mrs. Doherty for chemistry, Mr. Hensley for math, and Mrs. Ueckermann for guidance counseling.

I would like to thank all of my friends and family who have supported me. Thanks to everyone in the Caltech tennis community for always being down to hit and help me take a break from lab, especially JK, Yuxing, Przemek, Meera, Cedric, Vignesh, and Keon Ha.

Thanks to everyone in the LA tennis community which has felt like a second family, especially Tina, Demi, Vicky, Serena, and Jen – it has been a blast going to sectionals and on other fun trips and adventures together. And most of all, thank you to my mother Mary and my twin brother Kieran for their constant support and encouragement.

Lastly, I would like to thank the countless mice who gave their lives for the experiments over the past 6 years. Without them, my work and countless other scientific discoveries would not have been possible.

ABSTRACT

Genetically engineered bacteria are promising new cell-based diagnostic and therapeutic agents due to their ability to sense and respond to unique signals, access and interface with hard-to-reach areas of the body, and deliver therapeutics directly to these areas. However, currently tools to noninvasively monitor and control their activity in vivo are limited. Optical imaging methods, which are based on fluorescent and luminescent reporter genes, and optogenetics, which are based on light-activated proteins, are widely used in cell culture and rodent studies. However, these optical methods suffer from the poor penetration depth of light in tissue which limits their use in larger animals like humans. On the other hand, nuclear imaging methods such as PET and SPECT have good imaging depth but rely on radioactive tracers whose synthesis can be complex and exposes patients to radiation. Here I present tools for imaging and control of bacteria that based on non-ionizing forms of energy that easily penetrate tissue: sound waves and magnetic fields.

The first two parts of my thesis focuses on imaging bacteria in vivo with ultrasound, which is a widely available imaging modality that does not use ionizing radiation and has tissue penetration depth of several centimeters. Bacteria can be imaged with ultrasound by expressing acoustic reporter genes (ARGs) which result in the production of gas vesicles (GVs), air-filled protein nanostructures that aquatic microbes use to regulate their buoyancy. However, the first-generation acoustic reporter genes expressed too poorly under in vivo conditions to enable ultrasound imaging of bacteria in therapeutically relevant contexts. Here, we present a new and improved ARG construct that produces high levels of robust gas vesicle expression in the probiotic bacterium *E. coli* Nissle (EcN), enabling ultrasound imaging of these cells with high sensitivity. This second-generation ARG construct, bARG$_{Ser}$, uses genes derived from *Serratia* sp. ATCC 39006 and was optimized for plasmid-based expression in EcN. We demonstrate that with bARG$_{Ser}$, we can visualize the spatial distribution of engineered EcN after they home to and colonize tumors upon systemic administration. We also demonstrate that the engineered EcN can be imaged with ultrasound when colonizing the gastrointestinal tract of mice after sensing dietary sugars as well as biomarkers of inflammation. By enabling monitoring of the precise spatial location of engineered probiotic bacteria inside the body, this technology could greatly improve the development and eventual clinical use of this emerging class of microbial cell-based theranostics.

The last part of my thesis focuses on control of bacteria in vivo with magnetic fields. Many bacteria have limited ability to selectively colonize specific targeted regions of the GI tract due to a lack of external control over their location and persistence. Magnetic fields are well suited to provide such control due to their ability to freely penetrate biological tissues, but

they are difficult to apply with enough strength to directly manipulate magnetically labeled cells within deep tissue or viscous environments such as in the GI tract. Here, we show that ingestible micron-sized magnetic particles, combined with an externally applied magnetic field, act as in vivo magnetic field gradient amplifiers, enabling the trapping and retention of orally administered probiotic *E. coli* within the mouse GI tract. This technology improves the ability of these probiotic agents to accumulate at specific locations and stably colonize without antibiotic treatment. By enhancing the ability of GI-targeted cellular agents to be at the right place at the right time, cellular localization assisted by magnetic particles (CLAMP) adds external physical control to an important emerging class of biotherapeutics.

PUBLISHED CONTENT AND CONTRIBUTIONS

Buss, M. T., Zhu, L., Kwon, J. & Shapiro, M. G. Ultrasound imaging of engineered diagnostic bacteria in the gastrointestinal tract. *Manuscript in preparation* (2024).

MTB contributed to the study design, experiments, data analysis, and writing.

Abundo, M. P., Tifrea, A. T., **Buss, M. T.**, Barturen-Larrea, P., Jin, Z., Malounda, D. & Shapiro, M.G. Ultrasound-actuated drug delivery with acoustic percolation switches. bioRxiv preprint at https://doi.org/10.1101/2024.05.10.593654 (2024).

MTB contributed to the experiments and data analysis performed in this study.

Hurt, R. C.#, **Buss, M. T.**#, Duan, M.#, Wong, K., You, M. Y., Sawyer, D. P., Swift, M. B., Dutka, P., Barturen-Larrea, P., Mittelstein, D. R., Jin, Z., Abedi, M. H., Farhadi, A., Deshpande, R. & Shapiro, M. G. Genomically mined acoustic reporter genes for real-time in vivo monitoring of tumors and tumor-homing bacteria. *Nat. Biotechnol.* **41**, 919–931 (2023). https://doi.org/10.1038/s41587-022-01581-y. # Equal contribution.

MTB contributed to the study design, experiments, data analysis, and writing.

Xiong L. L., Garrett, M. A., **Buss, M. T.**, Kornfield, J. A. & Shapiro, M.G. Tunable temperature-sensitive transcriptional activation based on Lambda repressor. *ACS Synth. Biol.* **11**, 2518 (2022). https://doi.org/10.1021/acssynbio.2c00093.

MTB contributed to the experiments performed in this study.

Abedi, M. H.#, Yao, M#, Mittelstein, D. R., Bar-Zion, A., Swift, M. B., Lee-Gosselin, A., Barturen-Larrea, P., **Buss, M. T.** & Shapiro, M. G. Ultrasound-controllable engineered bacteria for cancer immunotherapy. *Nat. Commun.* **13**, 1585 (2022). https://doi.org/10.1038/s41467-022-29065-2. # Equal contribution.

MTB contributed to the experiments performed in this study.

Bar-Zion, A., Nourmahnad, A., Mittelstein, D. R., Shivaei, S., Yoo, S., **Buss, M. T.**, Hurt, R. C., Malounda, D., Abedi, M. H., Lee-Gosselin, A., Swift, M. B., Maresca, D. & Shapiro, M. G. Acoustically triggered mechanotherapy using genetically encoded gas vesicles. *Nat. Nanotechnol.* **16**, 1403–1412 (2021). https://doi.org/10.1038/s41565-021-00971-8.

MTB contributed to the experiments performed in this study.

Buss, M. T.#, Ramesh, P.#, English, M. A., Lee-Gosselin, A. & Shapiro, M. G. Spatial control of probiotic bacteria in the gastrointestinal tract assisted by magnetic particles. *Adv. Mater.* **33**, 2007473 (2021). https://doi.org/10.1002/adma.202007473. # Equal contribution.

MTB contributed to the study design, experiments, data analysis, and writing.

TABLE OF CONTENTS

LIST OF FIGURES AND TABLES

FREQUENTLY USED ABBREVIATIONS

ARGs. Acoustic reporter genes.

bARG$_{Ser}$. Bacterial acoustic reporter genes derived from *Serratia* sp. ATCC 39006.

B-mode. Standard brightness mode ultrasound imaging using parabolic beams which shows anatomy.

BURST. Type of GV-specific ultrasound imaging technique based on collapse (bursting) of GVs. Stands for "Burst Ultrasound Reconstruction with Signal Templates" but BURST images can also be reconstructed via subtraction, SVD, or Pearson correlation.

CFUs. Colony forming units, used to assess viability and colonization of bacteria via plating.

dB. Decibels, where [Signal in dB] = 20*log10([linear signal]).

EcN. The widely used probiotic bacterium *Escherichia coli* Nissle 1917.

GI. Gastrointestinal.

GV. Gas vesicle.

pAM. Parabolic amplitude modulation. Type of GV-specific ultrasound imaging technique based on the use of amplitude modulation pulse sequences with parabolic beams to enhance GV-specific nonlinear contrast while canceling linear background scattering.

ROI. Region-of-interest.

SBR. Signal-to-background ratio, used for quantification of ultrasound images. Defined as the mean pixel intensity of the sample ROI divided by the mean pixel intensity of the background ROI.

xAM. Cross amplitude modulation. Type of GV-specific ultrasound imaging technique based on the use of cross-propagating plane waves to enhance GV-specific nonlinear contrast while canceling linear background scattering.

Chapter 1

INTRODUCTION

1.1 The importance of bacteria in human health and disease

The gut microbiome is a complex and diverse assortment of microbes that inhabit the gastrointestinal (GI) tract. It has been shown to play a central role in human health and disease, performing important functions ranging from regulating metabolism to modulating immune system development, and its disfunction has been implicated in diseases ranging from colitis to diabetes and obesity[1]. Because of its central role, there has been growing interest over the past decade in studying the microbiome to elucidate the complex mechanisms behind its influence on the host[2,3]. The gut microbiome has also been an attractive target for the development of new therapeutics, especially those involving genetically engineered microbes due to advances in synthetic biology[4]. For instance, probiotic bacterial strains such as *Escherichia coli* Nissle 1917 and *Lactococcus lactis* have been engineered to secrete anti-inflammatory molecules (e.g. cytokines and protease inhibitors) for the treatment of inflammatory bowel disease (IBD)[5] and to secrete certain molecules for the treatment of infections of the GI tract (e.g. secreting AI-2 to treat cholera infections)[6]. Probiotic bacterial strains have also been engineered to sense and respond to markers of disease in the GI tract, such as detecting inflammation from sensing nitric oxide[7] or tetrathionate[8], as new diagnostics.

The tumor microbiome also plays an important role in human health and disease by affecting the development and treatment of cancers through complex mechanisms such as modulating the host immune system or altering drug metabolism[9,10]. There are numerous on-going clinical trials aimed at elucidating the role of the tumor microbiome in various cancers[11]. Accordingly, in addition to the gastrointestinal (GI) tract, tumors are a major target of bacterial diagnostics and therapeutics. Using bacteria as cancer treatments dates back to the 1890s, when William Coley administered a mixture of strains called “Coley’s Toxins” that induced tumor regression by stimulating the immune system, one of the first examples of immunotherapies. Interest in bacterial cancer therapy then declined in favor of chemotherapy and radiation therapy, but recently there has been renewed interest due to developments in synthetic biology that enable complex engineering of bacteria[12]. Many bacteria, such as *Salmonella enterica* serovar Typhimurium (*S.* Typhimurium) and *E. coli* Nissle, are naturally capable of homing to and selectively growing in the core of tumors due to the hypoxic and immune-privileged environment there. To control the behavior of these bacteria and enhance their anti-tumor activity, they have been engineered using a variety of strategies including: displaying cell surface proteins to specifically target them to tumor cells, releasing cytotoxic molecules to kill cancer cells, and being activated by signals from the tumor microenvironment such as hypoxia[12,13]. Bacteria can also be used as cancer diagnostics, either by being engineered to produce a detectible signal when they sense a cancer biomarker[14] or by certain species of endogenous bacteria being correlated with the presence of cancer[9].

1.2 Existing methods for imaging and controlling bacteria in vivo

Despite the importance of bacteria in human health and disease and their potential as new cell-based therapeutics and diagnostics, currently there are very limited tools to control and monitor their activity *in vivo*. Optical methods for imaging and control, such as fluorescent/bioluminescent[15] reporter genes and optogenetics[16,17], are most commonly used in cell culture and rodent studies[18]. However, these optical methods are severely limited by the poor penetration depth of light into tissues, largely preventing their use in larger animals like humans[19]. Nuclear imaging methods like Single Photon Emission Computed Tomography (SPECT)[20] and Positron Emission Tomography (PET)[21] which use bacterial-specific radionuclides get around this depth penetration limitation and are capable of detecting very low concentrations of bacteria. However, nuclear methods are not commonly used for imaging bacteria because they rely on the use of radiotracers which present safety concerns and require specialized equipment to synthesize, and they often suffer from a high degree non-specificity as well as poor spatial resolution[22]. Other methods such as fluorescence *in situ* hybridization (FISH) and sequencing-based methods require invasive biopsies or sampling from blood or feces which lack much spatiotemporal information. Chemical inducers are commonly used to control gene expression in engineered bacteria in vivo but they can lack spatial precision especially when administered systemically. As a result, little is currently known about the spatiotemporal dynamics of bacterial passage through the gastrointestinal tract and in tumors, and it is difficult to control their function once they are in these areas. Non-invasive imaging and control methods, based on forms of non-ionizing energy that readily penetrate tissue such as sound waves and magnetic fields, can help address this gap.

1.3 Ultrasound imaging of bacteria

Ultrasound is an imaging modality based on the scattering and reflection of sound waves from inhomogeneities in tissue. Compared to other imaging methods, it is inexpensive, fast, portable, and widely available. Sound waves at MHz frequencies readily propagate through tissue, allowing imaging depths of several centimeters with micron-level spatial resolution. However, until the discovery that gas vesicles (GVs) can act as ultrasound contrast agents[23], there were no bacterial specific ultrasound contrast agents.

GVs are gas-filled protein nanostructures that are produced by some aquatic microorganisms like cyanobacteria that use them to control their buoyancy for better access to light and nutrients in the water column. Their size and shapes vary between different microbes, but generally they are cylindrically-shaped with widths of 45–250 nm and lengths of 100–600 nm[23]. They consist of two primary structural proteins: GvpA, which is an extremely hydrophobic protein that excludes water and forms the main shell, and GvpC, which binds on the outside of the GvpA shell to reinforce it. Several unique properties enable GV-specific ultrasound imaging. One key property is the collapse of GVs beyond a critical collapse pressure leading to loss of ultrasound contrast. This property enables the signal from gas vesicles to be isolated by subtracting the post-collapse image from the pre-collapsed image[23]. BURST imaging builds on this by using higher pressures that cause a transient increase in acoustic contrast during collapse, which can be isolated by subtracting collapsing

frames from each other. Additionally, the fact that the critical collapse pressure differs depending on which GV proteins make up the structure allows spectral unmixing of different populations of GVs, which is analogous to separating different colors of fluorescent proteins. Another key property of GVs is their nonlinear repose to acoustic pressure, which enables them to be selectively imaged using amplitude modulation (AM) pulse sequences[24]. An improvement that uses cross-propagating plane-wave transmissions called cross-amplitude modulation (xAM) eliminates many artifacts in AM imaging[25].

Gas vesicles are encoded by large clusters of genes, which we term acoustic reporter genes (ARGs) for their ability to confer acoustic contrast when expressed. Expressing ARGs in tumor-homing and intestinal bacteria would allow them to be noninvasively imaged in deep tissue with ultrasound. However, whether ARGs could be expressed in bacteria in an *in vivo* environment to a detectable extent to see ultrasound contrast was an open question. Bourdeau *et al*.[26] expressed ARGs in *E. coli* Nissle and *S. typhimurium* using a hybrid GV gene cluster from *Anabaena flos-aquae* and *Bacillus megaterium*. They were able to observe ultrasound contrast from ARG-expressing *E. coli* Nissle which was suspended in agarose and placed in a mouse colon, and from ARG-expressing *S. typhimurium* which was injected into tumors in mice. But in these cases, the bacteria were induced to express ARGs under ideal conditions in culture (rich LB medium with glucose and antibiotics, aerobically, and at 30ºC) before being injected. In order to image bacteria that had colonized tumors or areas in the gastrointestinal tract (rather than being injected into these areas), they would need to be able express enough GVs under *in vivo* conditions, which are often oxygen-poor and nutrient-poor in addition to having competition from host cells and potentially other microbial cells[27]. These conditions may be problematic for ARG expression because GVs are encoded by clusters of many genes, so high levels of expression are metabolically expensive for the cell. The burden creates a strong selective pressure against ARG-expressing cells, leading to mutations or loss of GV-encoding plasmids. Additionally, ARG expression in culture is typically best at lower temperatures such as 30ºC, but the mammalian environment is around 37ºC.

To overcome these challenges, we first aimed to develop next-generation ARGs that would give strong acoustic contrast even under challenging conditions (nutrient-poor, oxygen-limited, no antibiotics, and 37ºC). We chose *E. coli* Nissle (EcN) as the host because ARG expression has previously been attained in this organism and because it is tumor-homing and can colonize the murine gastrointestinal tract. Through a genomic mining approach, we found that ARGs from *Serratia sp. ATCC 39006* (termed bARG$_{Ser}$) express much better than previous ARGs in *E. coli*. After optimizing a plasmid-based system for bARG$_{Ser}$ expression in EcN, we characterized this strain in terms of GV expression under different conditions and optimal ultrasound imaging parameters. We then showed that the bARG$_{Ser}$-expressing EcN strain could be imaged with ultrasound after homing to and colonizing tumors in mice, the first ultrasound images showing the microscale distribution of tumor-homing bacteria in live mice. This work is described in **chapter 2**.

Furthermore, we colonized mice with the bARG$_{Ser}$-expressing EcN strain and developed imaging protocols to obtain 3-D ultrasound images of the spatial distribution of the EcN in the GI tract. We also developed strains of EcN that can sense inflammation biomarkers and trigger high levels of bARG$_{Ser}$ expression in response. We showed that these

strains can report on antibiotic-induced inflammation in mice via ultrasound. This work is described in **chapter 3**.

1.4 Ultrasound control of bacteria

Ultrasound can be used for controlling bacteria in vivo by delivering targeted sound energy to a specific region in the body. Because GVs collapse in response to high acoustic pressures, ultrasound could be used to trigger a spatially targeted response of GV-containing bacterial cells in the body. In particular, low-frequency ultrasound can turn GVs into cavitating bubbles, which unleashes strong local mechanical effects on the surrounding tissue[28]. When low-pressure focused ultrasound was applied to bARG$_{Ser}$-expressing EcN (described in section 1.3) while colonizing tumors in mice, the EcN cells and the surrounding tumor tissue were severely damaged, causing tumor regression in combination with the checkpoint inhibitors αCTLA-4 and αPD-L1[28]. Bacteria can also be triggered without the use of GVs due to the ability of focused ultrasound to locally heat tissue. Thermally activated circuits were implemented in EcN so that when cells are exposed to elevated temperatures they switch on production of a therapeutic payload (αCTLA-4 and αPD-L1 nanobodies). Performing focused ultrasound to locally heat tumors colonized by the thermally-activated EcN successfully suppressed tumor growth[29]. These results demonstrate the ability to modulate tumor-homing bacteria in vivo with ultrasound for therapeutic effect.

1.5 Magnetic imaging and control of bacteria

Like sound waves, magnetic fields readily penetrate tissue, making them ideal for the noninvasive imaging of bacteria in deep tissue. Magnetic resonance imaging (MRI) uses strong magnetic fields to produce images of the body by exploiting the fact that nuclear spins behave differently in different tissues. Several MRI methods based on endogenous chemical exchange saturation transfer (CEST) contrast of bacteria[30], on labeling bacteria with iron oxide nanoparticles[31,32], and on bacteria-targeted gadolinium probes[33] have been used to image bacteria in vivo. Genetically encoded reporters for MRI that are based on the expression of proteins that accumulate iron in a magnetic state in the cell have also been developed[34,35], which have the advantage of not being diluted out as the cell grows like the labeling methods do.

As for control, magnetic fields have been successfully used to localize magnetically-labeled bacteria cells to tumors in order to enhance existing anti-cancer therapies[36]. However, to our knowledge, magnetic fields have not been used to control bacteria in the GI tract. Magnetic control in the GI tract is more difficult due to its greater complexity and depth in the body than subcutaneous tumors, as magnetic fields and field gradients very rapidly attenuate from their source. To get around this issue, we developed cellular localization assisted by magnetic particles (CLAMP). CLAMP uses ingestible micron-sized magnetic particles, combined with an externally applied magnetic field, as in vivo magnetic field gradient amplifiers, enabling the trapping and retention of orally administered probiotics within the mouse GI tract. This technology improved the ability of EcN to accumulate at specific locations and stably colonize mice without antibiotic treatment. By enhancing the ability of GI-targeted bacterial agents to be at the right place at the right time, CLAMP adds

external physical control to this important emerging class of biotherapeutics. This work is described in **chapter 4**.

Chapter 2

ULTRASOUND IMAGING OF TUMOR-HOMING PROBIOTIC BACTERIA

Sections of this chapter have been adapted from:
Hurt, R. C.#, **Buss, M. T.**#, Duan, M.#, Wong, K., You, M. Y., Sawyer, D. P., Swift, M. B., Dutka, P., Barturen-Larrea, P., Mittelstein, D. R., Jin, Z., Abedi, M. H., Farhadi, A., Deshpande, R. & Shapiro, M. G. Genomically mined acoustic reporter genes for real-time in vivo monitoring of tumors and tumor-homing bacteria. *Nat. Biotechnol.* **41**, 919–931 (2023). https://doi.org/10.1038/s41587-022-01581-y. # Equal contribution.

2.1 Abstract

A major outstanding challenge in the fields of biological research, synthetic biology and cell-based medicine is the difficulty of visualizing the function of natural and engineered cells noninvasively inside opaque organisms. Ultrasound imaging has the potential to address this challenge as a widely available technique with a tissue penetration of several centimeters and a spatial resolution below 100 μm. Recently, the first genetically encoded reporter molecules were developed based on bacterial gas vesicles to link ultrasound signals to molecular and cellular function. However, the properties of these first-generation acoustic reporter genes (ARGs) resulted in limited sensitivity and specificity for imaging in the *in vivo* context. Here, we describe second-generation ARGs with greatly improved acoustic properties and expression characteristics. We identified these ARGs through a systematic phylogenetic screen of candidate gas vesicle gene clusters from diverse bacteria and archaea. The resulting constructs offer major qualitative and quantitative improvements, including the ability to produce nonlinear ultrasound contrast to distinguish their signals from those of background tissues, and a reduced burden of expression in probiotic hosts. We demonstrate the utility of these next-generation ARGs by imaging the *in situ* gene expression of tumor-homing probiotic bacteria, revealing the unique spatial distribution of tumor colonization by these cells noninvasively in living subjects.

2.2 Introduction

Basic biological research, *in vivo* synthetic biology and the development of cell-based medicine require methods to visualize the function of specific cells deep inside intact organisms. Within this context, widely used optical techniques based on fluorescent and luminescent proteins have limited utility due to the scattering and absorption of light by tissue.[37] In contrast, ultrasound is a widely used technique for deep-tissue imaging, providing sub-100 μm spatial resolution at a depth of several cm (ref. [38]). The relative simplicity and low cost of ultrasound make it widely accessible for both research and clinical medicine. Recently, the first genetically encodable reporters for ultrasound were introduced based on gas vesicles (GVs),[39] air-filled protein nanostructures encoded by clusters of 8-20+ genes, which evolved as flotation devices in a wide range of mostly aquatic bacteria and archaea.[40,41]

The low density and high compressibility of their air-filled interiors compared to surrounding tissues allow GVs to scatter sound waves and thereby produce ultrasound contrast when heterologously expressed as acoustic reporter genes (ARGs) in genetically engineered bacteria[42] or mammalian cells.[43]

Despite their promise, three major drawbacks have limited the utility of these first-generation ARGs in *in vivo* imaging. First, the GVs produced by existing ARGs scatter ultrasound linearly, making them difficult to distinguish from similar scattering by background tissues. Second, the existing bacterial ARGs express poorly at 37ºC. Third, the formation of the resulting GVs is too burdensome for long-term expression. The first of these limitations is currently addressed by destructive ultrasound pulse sequences that irreversibly collapse GVs for signal subtraction, resulting in one-time contrast and limiting dynamic imaging. The second and third limitations have prevented the use of ARGs to image *in situ* gene expression by bacteria inside a mammalian host.[42]

To overcome these limitations, we sought next-generation ARGs that, when expressed heterologously in bacterial strains widely used as *in vivo* probiotic agents, produce GVs with strong nonlinear ultrasound contrast and enable strong, sustained expression under physiological conditions. These qualities would provide greatly improved utility for *in vivo* imaging. We hypothesized that a genomic mining approach – previously applied to improving fluorescent proteins, optogenetic receptors and other biotechnology tools[44–48] – would yield ARGs with improved properties, which could be further optimized through genetic engineering. By cloning and screening 15 distinct polycistronic operons from a diverse set of GV-expressing species representing a broad phylogeny, we identified a gene cluster from *Serratia* sp. 39006 that produces strong nonlinear acoustic contrast and enables high levels of low-burden GV expression in *E. coli*. Engineering an optimized expression system for this gene cluster in the widely used probiotic species *E. coli* Nissle 1917 (EcN) resulted in ARGs with sufficient performance to enable the noninvasive imaging of mouse tumor colonization and subsequent gene expression by these probiotic agents, providing direct visualization of a critical aspect of this rapidly emerging class of anti-cancer therapy.

2.3 Results

Genomic mining of gas vesicle gene clusters reveals homologs with improved ultrasound performance in E. coli. GVs are encoded by polycistronic gene clusters comprising one or more copies of the primary structural gene *GvpA* and 7 to 20+ other genes encoding minor constituents, assembly factors or reinforcing proteins, which together help assemble the GVs' protein shell. Hundreds of organisms have GV genes in their genomes, but only a small subset have been shown to produce GVs. Given the labor involved in cloning and testing polycistronic clusters, we limited our phylogenetic search to organisms with confirmed GV production. From a list of 253 unique GV-producing species and 288 unique strains in the literature (**Table S2.1**), 117 have had their GV operons sequenced. We created a phylogenetic tree based on the 16S rDNA sequences of these organisms (**Fig. 2.1a** and **S2.1**) and used it to select 11 species, broadly sampling phylogenetic space, cluster architecture and organismal characteristics (*i.e.*, halophilic, thermophilic and mesophilic). We obtained each species from culture repositories, amplified GV operons from their genomes,

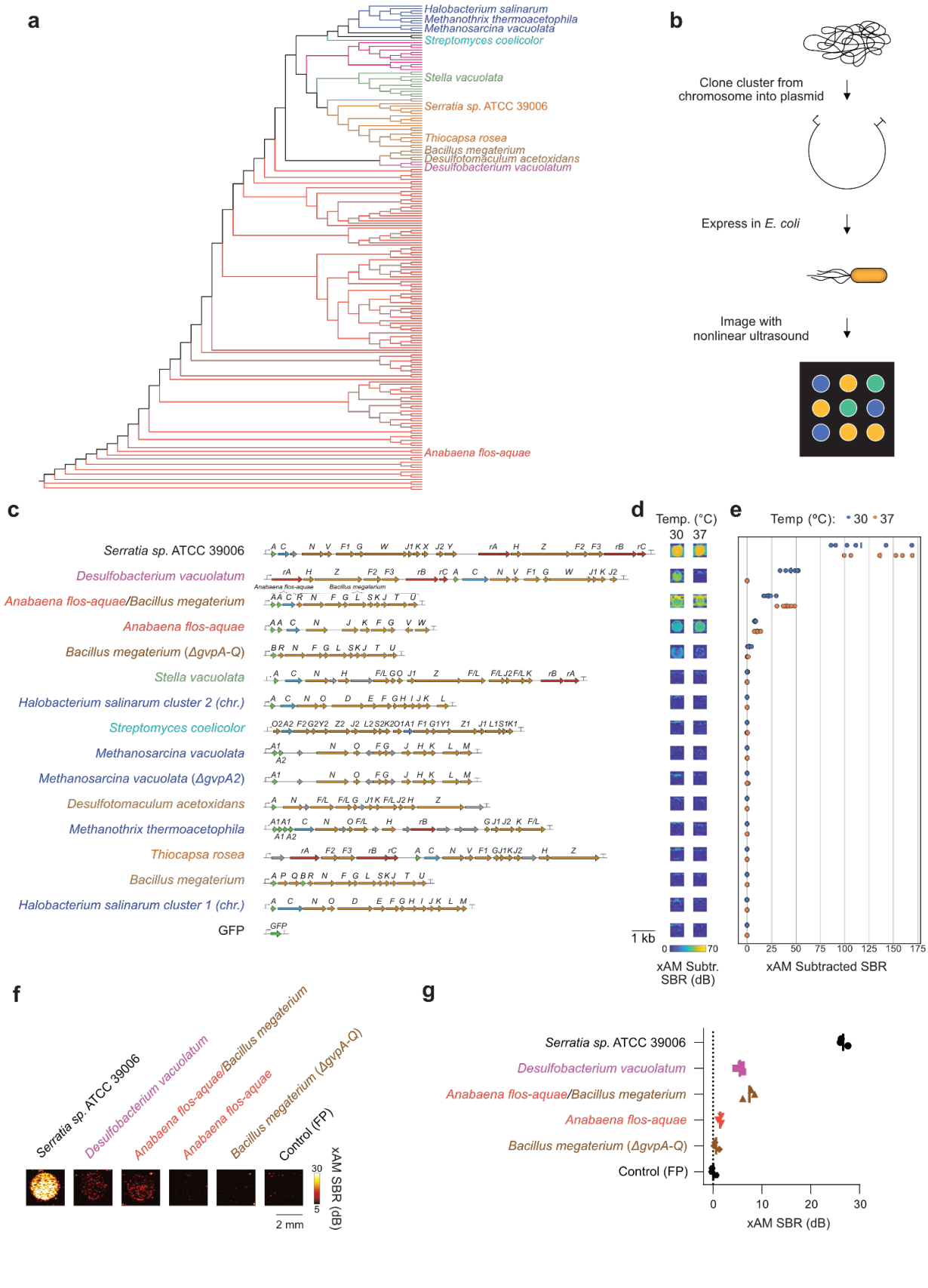
a
Halobacterium salinarum
Methanothrix thermoacetophila
Methanosarcina vacuolata
Streptomyces coelicolor
Stella vacuolata
Serratia sp. ATCC 39006
Thiocapsa rosea
Bacillus megaterium
Desulfotomaculum acetoxidans
Desulfobacterium vacuolatum
Anabaena flos-aquae
b
Clone cluster from chromosome into plasmid
Express in E. coli
Image with nonlinear ultrasound
c
Serratia sp. ATCC 39006
Desulfobacterium vacuolatum
Anabaena flos-aquae/Bacillus megaterium
Anabaena flos-aquae
Bacillus megaterium (ΔgvpA-Q)
Stella vacuolata
Halobacterium salinarum cluster 2 (chr.)
Streptomyces coelicolor
Methanosarcina vacuolata
Methanosarcina vacuolata (ΔgvpA2)
Desulfotomaculum acetoxidans
Methanothrix thermoacetophila
Thiocapsa rosea
Bacillus megaterium
Halobacterium salinarum cluster 1 (chr.)
GFP
d
Temp. (°C)
30 37
1 kb
0 70
xAM Subtr. SBR (dB)
e
Temp (°C): 30 37
0 25 50 75 100 125 150 175
xAM Subtracted SBR
f
Serratia sp. ATCC 39006
Desulfobacterium vacuolatum
Anabaena flos-aquae/Bacillus megaterium
Anabaena flos-aquae
Bacillus megaterium (ΔgvpA-Q)
Control (FP)
30
5
xAM SBR (dB)
2 mm
g
Serratia sp. ATCC 39006
Desulfobacterium vacuolatum
Anabaena flos-aquae/Bacillus megaterium
Anabaena flos-aquae
Bacillus megaterium (ΔgvpA-Q)
Control (FP)
0 10 20 30
xAM SBR (dB)

Figure 2.1 | Genomic mining of gas vesicle gene clusters reveals homologs with nonlinear ultrasound contrast in *E. coli*. (**a**) 16S phylogenic tree of known GV-producing organisms, with the species from which GV genes were cloned and tested in this study indicated by name. See **Fig. S2.1** for the fully annotated phylogenic tree. *B. megaterium* and *S. coelicolor* were not reported to produce GVs, but we tested their GV gene clusters here based on previous experiments in *E. coli*[3] and to broadly sample the phylogenetic space. (**b**) Workflow for testing GV clusters. Select GV gene clusters were expressed in BL21(DE3) *E. coli* by growing patches of cells on plates containing the inducer IPTG, and the patches were then imaged with nonlinear ultrasound (xAM). (**c-e**) Diagrams of the GV gene clusters tested in *E. coli* (c), pre-minus-post-collapse xAM images of representative patches (d), and quantification of the pre-minus-post-collapse xAM signal-to-background ratio (SBR) of the patches (n=6 biological replicates) (e). (**f-g**) Representative xAM images (f) and quantification of the xAM SBR (n=3 biological replicates, each with 2 technical replicates) (g) for the top 5 GV-producing clusters expressed in *E. coli* at 30ºC on solid media and normalized to 5 x 10^9 cells/mL in agarose phantoms, imaged at 1.74 MPa. See **Fig. S2.7a-b** for the ultrasound signal at varying acoustic pressures and **Fig. S2.7c** for the corresponding BURST data.

and cloned them into a bacterial expression vector.

We then expressed each operon in confluent *E. coli* patches at several temperatures and inducer concentrations (**Fig. 2.1b**), comparing them to two bacterial ARG constructs previously shown to work in *E. coli*[42] – bARG1 (*Anabaena flos-aquae/Bacillus megaterium* hybrid) and *Bacillus megaterium ΔgvpA-Q*, as well as the full *Bacillus megaterium* gene cluster (**Fig. 2.1c-g**, **S2.2a-e, S2.3a-c**, **S2.4-6**). We scanned these patches using a home-built robot-translated ultrasound imaging apparatus, applying a nonlinear ultrasound pulse sequence based on the transmission of cross-propagating waves for amplitude modulation (xAM).[49] This pulse sequence enhances signals specific to nonlinear contrast agents such as GVs while reducing background tissue scattering. Importantly, unlike other pulse sequences that rely on the irreversible collapse of GVs to obtain GV-specific contrast, xAM is nondestructive. In addition, we examined the optical opacity of the patches, which can be increased by sufficient levels of GV expression.

Of the 15 gene clusters tested, only 3 showed significant xAM signal when expressed at 37ºC, and 5 showed significant xAM signal at 30ºC (**Fig. 2.1c-e**). Only 3 clusters produced opaque patches at 30ºC, all of which also produced significant xAM signal at this temperature (**Fig. S2.2c and S2.5a-b**). Even though all operons tested are from organisms reported to produce GVs, only the *Anabaena flos-aquae*, *Bacillus megaterium ΔgvpA-Q*, bARG1, *Desulfobacterium vacuolatum*, and *Serratia sp.* 39006 (*Serratia*) clusters produced GVs in *E. coli*. Several other operons produced visible ultrasound contrast under certain conditions, which did not arise from GV expression but reflected an effect on patch morphology, likely due to cellular toxicity (**Fig. S2.3d)**. The failure of most tested gene clusters to produce GVs in *E. coli* reflects the complexity of polycistronic heterologous expression, which requires each component to fold and function properly in a new host with a potentially different cytoplasmic environment, growth temperature and turgor pressure.[50,51] In addition, it is possible that some genes included in the clusters act as cis-regulators,[41,50,52–54] limiting expression absent a specific trans input, or that some additional genes are required beyond the annotated operons.

In patch format, the strongest acoustic performance was observed with the genes from *Serratia*, bARG1, *A. flos-aquae*, *B. megateriaum*, and *D. vacuolatum*. Because patch experiments do not control for the density of cells in each sample, we further compared the

performance of these clusters in resuspended samples. Each operon was expressed on solid media at 30ºC – a temperature at which all five operons produced GVs – then scraped, resuspended, and normalized for cell concentration. These samples were imaged in hydrogels using xAM (**Fig. 2.1f-g and S2.7a-b**) and a more sensitive but destructive imaging method called BURST[55] (**Fig. S2.7c**), and examined optically with phase-contrast microscopy (PCM), which reveals the presence of GVs due to the refractive index difference between GVs and water[56,57] (**Fig. S2.7d**). Three of the clusters produced xAM signals, and all clusters produced BURST signals significantly stronger than the negative control. All clusters except *A. flos-aquae* exhibited sufficient GV expression to be visible by PCM.

Cells expressing the *Serratia* cluster produced the strongest ultrasound signals, 19.2 dB above the next brightest cluster, bARG1, under xAM imaging at an applied acoustic pressure of 1.74 MPa – a 9-fold gain in signal intensity (**Fig. 2.1f**). Additionally, PCM images (**Fig. S2.7d**) showed that cells expressing the *Serratia* cluster had the highest levels of GV expression, as also seen in whole-cell transmission electron microscopy (TEM) (**Fig. S2.7e**). Based on the large improvement in ultrasound contrast provided by the *Serratia* GV operon relative to the other gene clusters, we selected this operon for further optimization as a second-generation bacterial ARG.

Because overexpression of any protein imposes a finite metabolic demand on the host cell,[58–60] we reasoned that deletion of non-essential genes could improve GV expression from the *Serratia* cluster, and therefore the xAM signal. Previous work has shown that deletions of *gvpC, gvpW, gvpX, gvpY, gvpH*, or *gvpZ* preserve GV formation in the native organism.[50] We tested these deletions, as well as the deletion of an unannotated hypothetical protein (Ser39006_001280) encoded between the *gvpC* and *gvpN* coding sequences (**Fig. S2.8a**). When expressed in *E. coli*, deletions of *gvpC, gvpH, gvpW, gvpY,* or *gvpZ* reduced or eliminated xAM signal (**Fig. S2.8b-c**) and patch opacity (**Fig. S2.8d**). Deletion of *gvpX* increased xAM signal but decreased opacity, and deletion of Ser39006_001280 increased both xAM signal and opacity. Based on these results, we chose to use the *Serratia* ΔSer39006_001280 operon for subsequent *in vitro* and *in vivo* experiments. We call this genetic construct bARG$_{Ser}$ as a bacterial acoustic reporter gene derived from *Serratia*.

bARG$_{Ser}$ shows robust expression, contrast, and stability in E. coli Nissle. We next transferred bARG$_{Ser}$ into a strain of *E. coli* used widely in *in vivo* biotechnology applications. We selected the probiotic strain EcN because of its ability to persist in the gastrointestinal tract and colonize tumors.[61–63] Recently, EcN has been intensely investigated as the chassis for anti-tumor therapy delivery.[64–67] We first tested different inducible expression constructs in EcN on solid media at 37ºC, observing xAM ultrasound contrast and patch opacity as a function of inducer concentration. While the expression of bARG$_{Ser}$ from the T5-lac promoter and pTetR promoter was either leaky or toxic (**Fig. S2.9**), the pBAD promoter provided tight control over the formation of ultrasound contrast without obvious toxicity (**Fig. 2.2a-b**). At 0.1% and 1% (w/v) L-arabinose, patches produced the strongest optical opacity and xAM signal. Based on these results, we selected the pBAD-bARG$_{Ser}$ EcN strain for subsequent experiments.

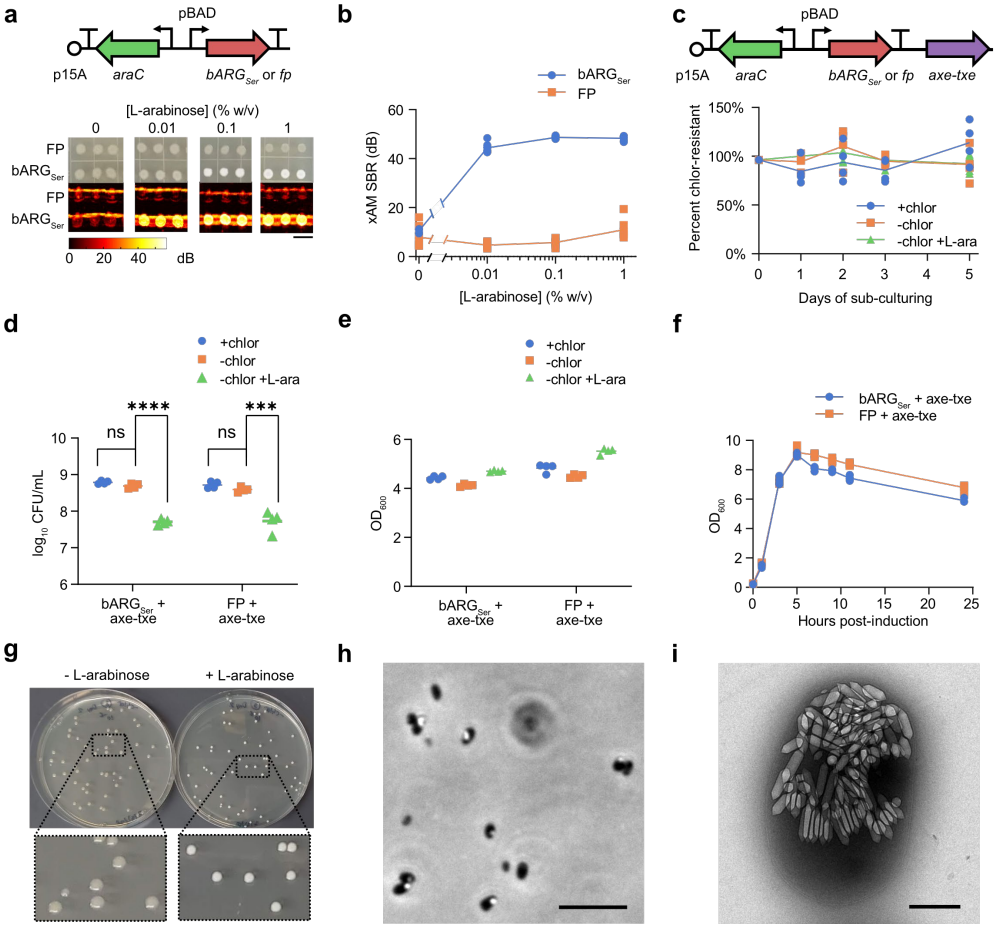

Figure 2.2 | Genetic engineering and expression of bARG$_{Ser}$ in the probiotic bacterium *E. coli* Nissle (EcN). (**a**) Diagram of the arabinose-inducible construct used to express bARG$_{Ser}$ in EcN (top), and optical and xAM images of bARG$_{Ser}$-expressing or FP-expressing patches of EcN on solid media with varying L-arabinose concentrations at 37°C (bottom). Scale bar is 1 cm. See **Fig. S2.9** for the corresponding results with IPTG-inducible and aTc-inducible constructs. (**b**) Quantification of the xAM SBR of all patches from the experiment in (a) versus the L-arabinose concentration (n=8). (**c**) Diagram of the construct from (a) with Axe-Txe[29] added to enable plasmid maintenance in the absence of antibiotics (top), and verification of plasmid maintenance *in vitro* (bottom). Conditions were with chloramphenicol (+chlor), without chloramphenicol (-chlor), or without chloramphenicol and with 0.1% L-arabinose (-chlor +L-ara) using pBAD-bARG$_{Ser}$-AxeTxe EcN (n=4). (**d-e**) Log10 of the colony forming units (CFUs) on chloramphenicol plates per mL of culture (d) and optical density at 600 nm (e) of pBAD-bARG$_{Ser}$-AxeTxe EcN and pBAD-FP-AxeTxe EcN cultures 24 hours after sub-culturing into LB media with the same conditions as in (c). Asterisks indicate statistical significance by unpaired t-tests (**** = $p < 0.0001$, *** = $p < 0.001$, ns = no significance); n=4. (**f**) OD_{600} versus time after inducing pBAD-bARG$_{Ser}$-AxeTxe (bARG$_{Ser}$ + axe-txe) and pBAD-FP-AxeTxe (FP + axe-txe) EcN strains with 0.1% (w/v) L-arabinose in liquid culture at 37°C (n=4). Between 5 and 24 hours post-induction, when the OD_{600} of all cultures decreased, the OD_{600} of FP-expressing cultures was slightly higher than that of the bARG$_{Ser}$-expressing cultures, likely due to expression of red fluorescent protein which is known to absorb light at 600 nm.[42] (**g**) Representative image of colonies from the experiment in (c) on chloramphenicol plates with (right) and without (left) 0.1% (w/v) L-arabinose. The opacity of the colonies on plates with L-arabinose indicates bARG$_{Ser}$ expression and was used to screen for mutants deficient in bARG$_{Ser}$ expression (see **Fig. S2.11**). (**h-i**) Representative phase contrast microscopy (h) and transmission electron microscopy (i) images of pBAD-bARG$_{Ser}$-AxeTxe EcN cells grown on plates with 0.1% (w/v) L-arabinose at 37°C. Scale bars are 10 µm (h) and 500 nm (i).

To ensure that the pBAD-bARG$_{Ser}$ plasmid is maintained in the absence of antibiotic selection, as required in certain *in vivo* applications, we added the toxin-antitoxin stability cassette Axe-Txe.[68] This enabled the pBAD-bARG$_{Ser}$-AxeTxe plasmid to be maintained in EcN for up to 5 days of daily sub-culturing in liquid media without antibiotics, both with and without induction of ARG expression using 0.1% (w/v) L-arabinose (**Fig. 2.2c**).

The expression of most heterologous genes, including widely used reporter genes such as fluorescent proteins, results in some degree of metabolic burden on engineered cells.[59,60,69] Consistent with this expectation, the induction of pBAD-bARG$_{Ser}$ EcN with 0.1% (w/v) L-arabinose resulted in reduced colony formation to an extent similar to the expression of a fluorescent protein (FP) (**Fig. 2.2d and S2.10a**), even as the culture density measured by OD_{600} remained relatively unchanged (**Fig. 2.2e and S2.10b**). When the OD_{600} was measured after inducing cultures with L-arabinose, the growth curves of bARG$_{Ser}$-expressing and FP-expressing EcN were indistinguishable during the growth phase (0 to 5 hours), indicating that the two strains have similar growth rates (**Fig. 2.2f**). Collectively, these results suggest that overexpression of bARG$_{Ser}$ using the pBAD expression system in EcN is not significantly more burdensome than that of FPs, which are widely accepted as relatively non-perturbative indicators of cellular function.

To further examine the genetic stability of bARG$_{Ser}$ constructs, we plated cells from daily sub-cultures onto agar with 0.1% (w/v) L-arabinose and examined colony opacity (**Fig. 2.2g**) as a measure of retained GV expression. Of a total of 3824 colonies, nearly all were opaque (**Fig. 2.2g**), with GV expression confirmed by PCM and TEM (**Fig. 2.2h-i**). Only 11 colonies (<0.3% after ~35 cell generations) exhibited a reduction in opacity and were instead grey in appearance (**Fig. S2.11a**), representing a mutated phenotype confirmed by growing these cells on fresh media (**Fig. S2.11b**). PCM revealed that these rare grey mutants still produced GVs, but at lower levels than non-mutants. These results indicate that mutational escape from GV production is not a major issue for pBAD-bARG$_{Ser}$-AxeTxe EcN under typical conditions.

After establishing construct stability, we characterized the acoustic properties of bARG$_{Ser}$-expressing EcN. For cells induced with 0.1% (w/v) L-arabinose for 24 hours and suspended at 10^9 cells/mL in agarose phantoms, an xAM signal was detected at pressures above 0.72 MPa, rising with increasing acoustic pressure up to the maximum tested pressure of 1.74 MPa (**Fig. 2.3a**). To characterize the physical stability of GVs in these cells during ultrasound exposure, we measured the xAM signal over time at a series of increasing acoustic pressures (**Fig. 2.3b**). The xAM signal was steady at pressures up to 0.96 MPa, at which point we observed a slow decrease in the xAM SBR, indicating that some of the GVs slowly collapsed despite sustained high xAM signals. We also imaged the cells with parabolic pulses, which can transmit higher pressures than xAM, and thus can be helpful *in vivo* to compensate for attenuation at tissue interfaces. When imaged with parabolic B-mode at varying acoustic pressures, the GVs started to collapse slowly at 1.02 MPa and more rapidly at 1.33 MPa and above (**Fig. 2.3c**). Based on these results, an acoustic pressure of 1.29 MPa was selected for xAM imaging and 1.02 MPa was chosen for parabolic AM (pAM) imaging in subsequent experiments to obtain the strongest signals while minimizing GV collapse.

Next, to characterize the dynamics and inducibility of bARG$_{Ser}$ in EcN and determine the ultrasound detection limit of bARG$_{Ser}$-expressing EcN, we measured xAM signal as a

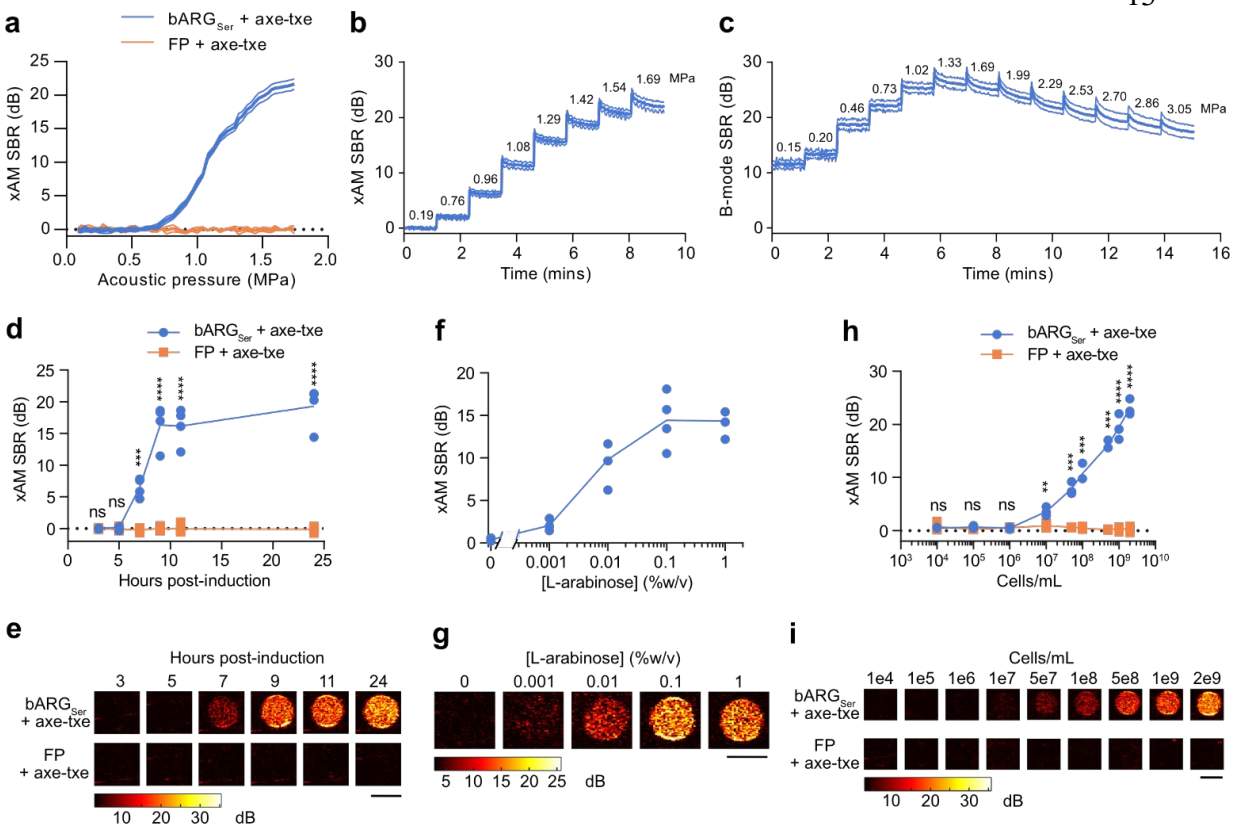

Figure 2.3 | Acoustic characterization of bARG$_{Ser}$-expressing EcN *in vitro*. (**a**) xAM SBR as a function of transmitted acoustic pressure for bARG$_{Ser}$-expressing and FP-expressing EcN. (**b-c**) xAM (b) and parabolic B-mode (c) SBRs measured over time when the transmitted acoustic pressure was increased approximately every 70 sec as indicated by the numbers above the curve for bARG$_{Ser}$-expressing EcN. Ultrasound was applied at a pulse repetition rate of 86.8 Hz. For (a-c), pBAD-bARG$_{Ser}$-AxeTxe EcN were induced with 0.1% (w/v) L-arabinose for 24 hours at 37°C in liquid culture, and were then normalized to 10^9 cells/mL in agarose phantoms for ultrasound imaging. Bold lines represent the mean and thin lines represent ± standard deviation; n=3 biological replicates, each with 2 technical replicates. (**d-e**) xAM ultrasound SBR (d) and corresponding representative ultrasound images (e) at several time points after inducing pBAD-bARG$_{Ser}$-AxeTxe (bARG$_{Ser}$ + axe-txe) and pBAD-FP-AxeTxe (FP + axe-txe) EcN strains with 0.1% (w/v) L-arabinose in liquid culture at 37°C. (**f-g**) xAM ultrasound SBR (f) and corresponding representative ultrasound images (g) using varying L-arabinose concentrations to induce pBAD-bARG$_{Ser}$-AxeTxe EcN in liquid culture at 37°C for 24 hours. (**h-i**) xAM ultrasound SBR (h) and corresponding representative ultrasound images (i) of varying concentrations of pBAD-bARG$_{Ser}$-AxeTxe or pBAD-FP-AxeTxe EcN cells induced for 24 hours at 37°C with 0.1% (w/v) L-arabinose in liquid culture. For (e, g, i) scale bars are 2 mm. For (d-g), cells were normalized to 10^9 cells/mL in agarose phantoms for ultrasound imaging. For (d, f, h), each point is a biological replicate (n=4 for d and f; n=3 for h) that is the average of at least 2 technical replicates. Asterisks represent statistical significance by unpaired t-tests (**** = $p<0.0001$, *** = $p<0.001$, ** = $p<0.01$, ns = no significance).

function of induction time, inducer concentration, and cell concentration. At a density of 10^9 cells/mL, xAM signal could first be observed 7 hours after induction with 0.1% L-arabinose and leveled off by 9 hours post-induction (**Fig. 2.3d-e**). Keeping the induction time constant at 24 hours while varying the L-arabinose concentration, GV expression was detected with as little as 0.001% L-arabinose, and the highest ultrasound signal was observed for 0.1-1%

L-arabinose (**Fig. 2.3f-g**). When cells induced for 24 hours with 0.1% L-arabinose were diluted, they were detectable by ultrasound down to 10^7 cells/mL (**Fig. 2.3h-i**). Critically, this detection was achieved non-destructively with nonlinear imaging, compared to previous bacterial ARGs, which required a destructive linear imaging approach.[42] The bARG$_{Ser}$ xAM signal was proportional to the cell concentration between 10^7 cells/mL and 2 x 10^9 cells/mL (**Fig. 2.3h-i**). We also imaged the cells using BURST imaging, which provides greater sensitivity at the cost of collapsing the GVs.[55] BURST enabled bARG$_{Ser}$-expressing EcN to be detected as early as 3 hours post-induction (**Fig. S2.12a-b**), with as little as 0.001% L-arabinose (**Fig. S2.12c-d**), and at density as low as 10^5 cells/mL (**Fig. S2.12e-f**). Taken together, our *in vitro* experiments indicated that the reporter gene construct pBAD-bARG$_{Ser}$-AxeTxe is robust and stable in EcN and enables gene expression in these cells to be imaged with high contrast and sensitivity.

bARG$_{Ser}$ enables in situ imaging of tumor-colonizing bacteria. Tumor-homing bacteria are a major emerging class of cancer therapy, which take advantage of the ability of cells such as EcN to infiltrate tumors and grow in their immunosuppressed microenvironment. Major synthetic biology efforts have been undertaken to turn tumor-homing EcN cells into effective therapies for solid tumors.[64–67] However, despite the promise of this technology and the importance of appropriate microscale biodistribution of the bacteria inside tumors, no effective methods currently exist to visualize this biodistribution *in situ* in living animals.

To test the ability of bARG$_{Ser}$ to overcome this limitation, we formed MC26 tumors in mice and, when the tumors reached a substantial size, intravenously injected EcN containing the pBAD-bARG$_{Ser}$-AxeTxe plasmid, giving the bacteria 3 days to home to and colonize the tumors. We then induced GV expression and imaged the tumors with ultrasound (**Fig. 2.4a**). In all tumors colonized by bARG$_{Ser}$-expressing EcN, pAM, BURST, and xAM ultrasound signals were observed 1 day after injection with L-arabinose (**Fig. 2.4b** and **S2.13a**). The signals were localized to the core of the tumor and concentrated at the interface between live and necrotic tissue,[62] where the EcN primarily colonized as confirmed with subsequent tissue histology (**Fig. 2.4f-h** and **S2.14**).

Furthermore, after applying 3 MPa acoustic pressure throughout the tumor to collapse all the GVs, re-injecting mice with L-arabinose inducer, and allowing ≥ 24 hours for re-expression, similar ultrasound signals were observed in all tumors colonized by bARG$_{Ser}$-expressing EcN (**Fig. 2.4c** and **S2.13b**). This result indicates that bARG$_{Ser}$ can be used to visualize gene expression at multiple timepoints. Absent L-arabinose induction, no xAM or pAM ultrasound signals were observed from bARG$_{Ser}$-containing EcN (**Fig. 2.4d** and **S2.13c**); likewise, no xAM or pAM ultrasound signals were seen in tumors colonized by FP-expressing EcN (**Fig. 2.4e,j** and **S2.13d-e**). Low levels of BURST signal were observed in uninduced animals (**Fig. 2.4k**), likely due to small amounts of L-arabinose present in the diet combined with BURST's high sensitivity.

To quantify tumor colonization, at the end of the experiment (day 20 in **Fig. 2.4a**) all mice were euthanized and their tumors were homogenized and plated on selective media. Tumors from all groups of mice (n=5 for induced and re-expressed bARG$_{Ser}$, n=5 for uninduced bARG$_{Ser}$, and n=5 for FP) contained more than 7 x 10^8 CFU/g tissue (**Fig. 2.4l**), indicating that the EcN can persist at high levels in tumors for at least 6 days after IV injection

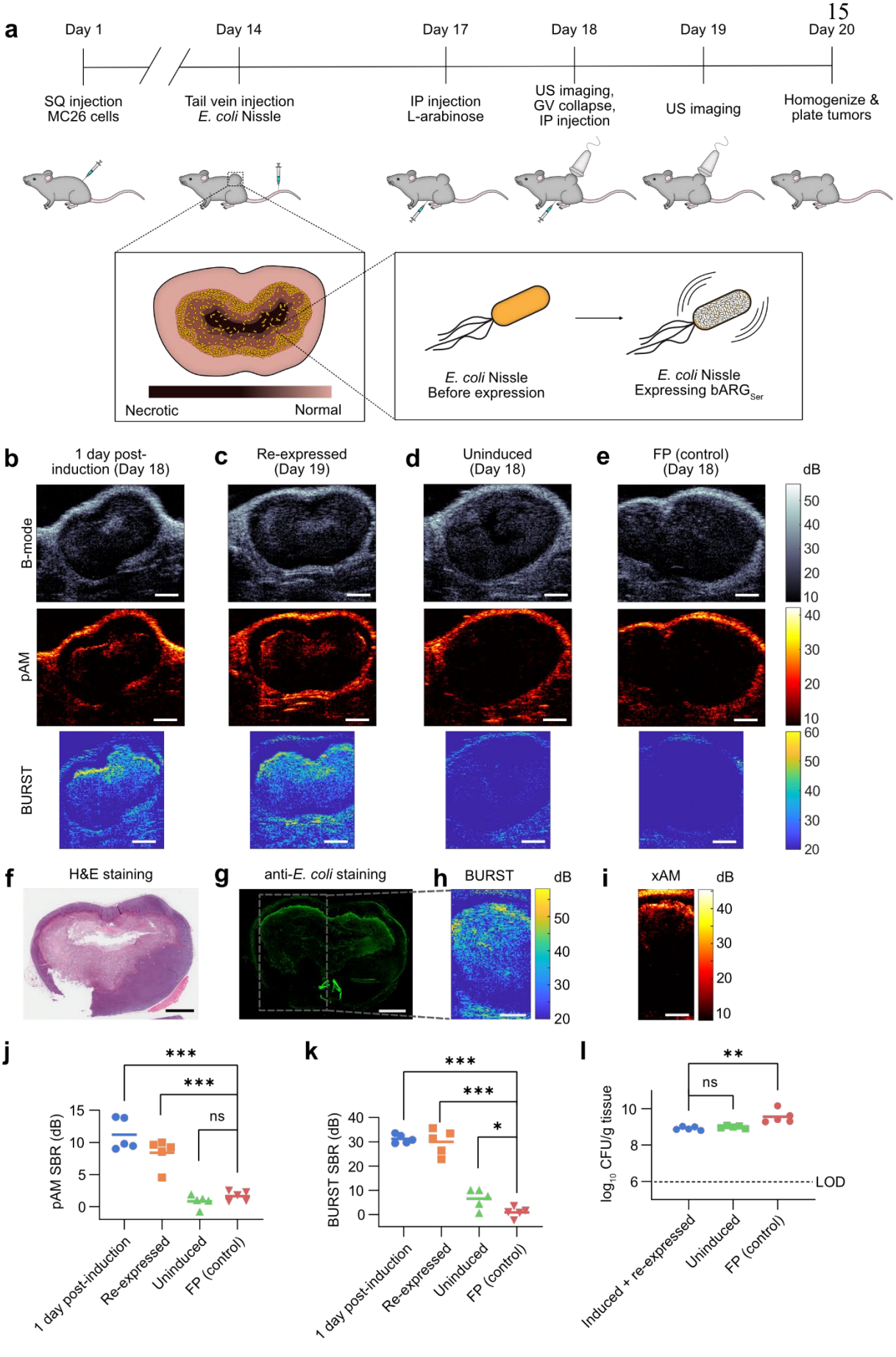
a
Day 1
Day 14
Day 17
Day 18
Day 19
Day 20
SQ injection MC26 cells
Tail vein injection E. coli Nissle
IP injection L-arabinose
US imaging, GV collapse, IP injection
US imaging
Homogenize & plate tumors
Necrotic
Normal
E. coli Nissle Before expression
E. coli Nissle Expressing bARG Ser
b
1 day post-induction (Day 18)
c
Re-expressed (Day 19)
d
Uninduced (Day 18)
e
FP (control) (Day 18)
dB
B-mode
pAM
BURST
f
H&E staining
g
anti-E. coli staining
h
BURST
i
xAM
j
pAM SBR (dB)
1 day post-induction
Re-expressed
Uninduced
FP (control)
k
BURST SBR (dB)
l
log10 CFU/g tissue
LOD
Induced + re-expressed
ns

Figure 2.4 | *In situ* bARG$_{Ser}$ expression enables ultrasound imaging of tumor colonization by EcN. (**a**) Diagram of the *in vivo* protocol for assessing *in situ* bARG$_{Ser}$ expression in tumors. Mice were injected subcutaneously (SQ) with MC26 cancer cells on day 1 and the tumors were allowed to grow for 14 days. Mice were then injected with *E. coli* Nissle (EcN) carrying either pBAD-bARG$_{Ser}$-AxeTxe or pBAD-FP-AxeTxe plasmids via the tail vein. After allowing 3 days for the EcN to colonize the tumors, bARG$_{Ser}$ or FP expression was induced by injecting L-arabinose intraperitoneally (IP) on day 17. The next day, at least 24 hours after induction, tumors were imaged with ultrasound. Subsequently, all the GVs in the tumors were collapsed by applying maximum acoustic pressure (3.0 MPa) throughout the tumor. L-arabinose was then injected again to re-induce bARG$_{Ser}$ expression, and tumors were again imaged with ultrasound at least 24 hours later. The next day (day 20), all mice were sacrificed, and their tumors were homogenized and plated on selective media to quantify the levels of EcN colonization. In separate experiments for histological analysis, mice were sacrificed on day 18 directly after ultrasound imaging. (**b-d**) Representative B-mode, parabolic AM (pAM), and BURST ultrasound images of tumors colonized by pBAD-bARG$_{Ser}$-AxeTxe EcN at least 24 hours after induction with L-arabinose on day 18 (b), at least 24 hours after collapse and re-induction (day 19) (c), or uninduced on day 18 (d). (**e**) Representative B-mode, pAM, and BURST ultrasound images of tumors colonized by pBAD-FP-AxeTxe EcN at least 24 hours after induction with L-arabinose on day 18. (**f-g**) Optical images of tissue sections stained with H&E (f) or anti-*E. coli* antibodies (g) from a tumor colonized by bARG$_{Ser}$-expresssing EcN after ultrasound imaging on day 19. (**h-i**) BURST (h) and xAM (i) ultrasound images of the same tumor as in (f-g), with the boxed region showing the approximate BURST imaging region in the tissue section. Scale bars in (b-i) represent 2 mm. (**j-k**) Quantification of the pAM (j) and BURST (k) SBR for the same conditions in (b-e); each group is n=5 mice. (**l**) Log10 of the colony forming units (CFUs) per gram of tissue from tumors homogenized and plated on day 20. The dotted line indicates the limit of detection (LOD). Asterisks represent statistical significance by unpaired t-tests (*** = $p<0.001$, ** = $p<0.01$, * = $p<0.05$, ns = no significance). See **Fig. S2.13** for representative xAM ultrasound images for the conditions in (b-d), and **Fig. S2.14** for more histological images of tissue sections from tumors colonized with pBAD-bARG$_{Ser}$-AxeTxe EcN.

regardless of bARG$_{Ser}$ expression, collapse, and re-expression. The somewhat higher density of FP-expressing EcN suggested that maintenance of the smaller pBAD-FP-AxeTxe plasmid (7.2 kb versus 23.2 kb for pBAD-bARG$_{Ser}$-AxeTxe) may be easier in this *in vivo* context.

To test if there were any mutations causing a reduction in the ability of the cells to produce GVs, tumors were plated on selective media with 0.1% L-arabinose and screened for colony opacity (**Fig. S2.15a**). Out of a total of 6,097 colonies screened from ten mice, only seven colonies were not opaque (**Fig. S2.15b-c**), suggesting a very low level of mutational silencing. Taken together, our *in vivo* experiments with EcN demonstrate that bARG$_{Ser}$ expression enables stable, non-destructive acoustic visualization of the microscale distribution of these probiotic agents in a biotechnology-relevant context.

2.4 Discussion

Our results establish a new second-generation ARG construct, bARG$_{Ser}$, that provides unprecedented US detection sensitivity and specificity when expressed in probiotic *E. coli*. The cluster, selected through a systematic phylogenetic screen and optimized through genetic engineering, produces bright nonlinear US signal[49] when expressed *in situ* by bacterial agents colonizing the necrotic core of a tumor. Through the use of a highly sensitive and specific non-destructive US imaging paradigm, this nonlinear signal enables real-time monitoring of the precise locations of these cells in the tumor and is sufficiently stable to image tissue biodistribution and gene expression functionality over multiple days. These results represent a major improvement over previous work with heterologous GV expression in bacteria,

which required the bacteria to be cultured and pre-express GVs under ideal laboratory conditions before *in vivo* injection for transient imaging.[42]

With these major improvements, we anticipate that ARGs will be useful for many applications that demand the long-term, noninvasive imaging of bacteria deep inside the body. Potential applications involve tracking therapeutic bacteria as they home to and attack tumors or travel through the gastrointestinal (GI) tract and report on its inflammatory state.[70,71] Further, the nonlinear signal generation of these ARGs mean that they could form the basis for acoustic biosensors of more dynamic cellular signals such as enzyme activity.[72]

While these results represent an important step in the development of ARGs, additional improvements could further expand their utility in biotechnology. First, the expression kinetics of ARGs are significantly slower than those of fluorescent proteins in *E. coli*,[73] and faster expression would facilitate the imaging of more dynamic genetic outputs. Second, the ability to multiplex different "colors" of ARGs nondestructively in vivo would enable discrimination of different strains of engineered bacteria in a consortium.[74–76] Additionally, the *Serratia* gene cluster is relatively large, making it more challenging to clone and incorporate with other genetic elements. The engineering of a shorter cluster with similar acoustic properties would simplify these efforts.

Our phylogenetic screening approach was successful in identifying $bARG_{Ser}$ as a vastly improved ARG construct for expression in *E. coli*. However, out of practical necessity, this screen only subsampled the available phylogenetic space. Future mining of additional GV-encoding gene clusters could thus lead to the discovery of ARGs with further new and improved properties. Improvements can also be made in the screening strategy. It is challenging to identify all of the gvp genes in a given genome (see methods), and there is considerable regulation of GV cluster transcription by factors inside[41,52] or outside[53] the clusters. In a given cloned cluster, it is possible that either essential genes are missing or cryptic regulatory elements are included.[41,50,54] These issues could be resolved by synthesizing multiple versions of each putative gene cluster and screening a larger number of them in higher throughput. Even with optimal genetic constructs, it is likely that gene clusters from some species will not successfully form GVs in a given heterologous host due to differences in growth temperature, turgor pressure or the presence or absence of specific host factors. The phylogenetic screening strategy used in this study could thus be adapted to find optimal ARGs for use in other bacterial species of interest to the mammalian microbiome and probiotic research communities.

Just as improvements in and adaptations of fluorescent proteins enabled a wide range of microscopy applications that were mere speculations when GFP was first harnessed as a biotechnology, the systematic development of next-generation ARGs will help bring to reality the promise of sensitive, high-resolution noninvasive imaging of cellular function inside intact mammals.

2.5 Methods

Genomic mining of ARG clusters

A literature search was conducted to find papers reporting the production of gas vesicles in any species. Search terms included "gas vesicle," "gas vacuole," "aerotope," and "aerotype." All species found are listed in **Table S2.1**. If the report did not include a strain name, then

any available 16S rRNA gene sequence used (as it was assumed that any other strain of the same species would fall in the same place on the phylogenetic tree), but no GV gene cluster sequence was used (even if it was available for one or more strains of that species) because it was found during our analysis that: 1) several reports describe species for which some strains produce GVs but others do not, and 2) comparison of GV gene cluster sequences of multiple strains of the same species almost always showed differences—often very significant ones. Further, even if a reference stating that a given organism produced GVs was not available, 16S rRNA gene sequences from all members of the following genera were included because GV production is a diacritical taxonomic feature for these genera: *Dolichospermum*,[77] *Limnoraphis*[78] and *Planktothrix*.[79]

GV clusters were identified in genomes through a combination of annotations and sequence similarity to known *gvp* genes. However, there were two challenges in identifying all *gvp*s in a given genome: 1) there is little to no annotation for many *gvp*s, and 2) GV gene clusters are not always contiguous in genomes, and *gvp*s can occasionally be found hundreds of kb away from the main cluster(s). We attempted to only select "well-behaved" GV clusters for testing (*i.e.*, ones in which all *gvp*s identified in that genome were present in clusters, and these clusters contained a minimum of non-*gvp* genes, which could increase the metabolic burden of cluster expression without increasing GV yield), but it is possible that even for these clusters, some *gvp*s were not cloned.

Of our list of 288 strains reported to form gas vesicles, 270 had 16S rRNA gene sequences available (**Table S2.1**). These were downloaded from NCBI using a custom Python script, and a multiple sequence alignment was constructed using Clustal Omega.[80] This alignment was used to generate a phylogenetic tree file using ClustalW2,[81] which was rendered using EvolView.[82] Only unique species are displayed in the phylogenetic trees in **Fig. 2.1a** and **Fig. S2.1**.

Plasmid construction and molecular biology

Organisms were obtained from commercial distributors as indicated in **Table S2.2**. If an organism was shipped as a liquid culture, the culture was centrifuged and the pellet resuspended in ddH2O, as it was found that even trace amounts of certain culture media could completely inhibit PCR. Fragments were amplified by PCR using Q5 polymerase and assembled into a pET28a(+) vector (Novagen) via Gibson Assembly using reagents from New England Biolabs (NEB). Sub-cloning and other modifications to plasmids were also performed with Gibson Assembly using reagents from NEB. Assemblies were transformed into NEB Stable *E. coli*. All constructs were verified by Sanger sequencing.

Halobacterium salinarum has two chromosomal GV gene clusters (plus additional plasmid-borne ones), which were cloned and tested separately. *Methanosarcina vacuolata* has only one cluster, but while its genome sequence in the NCBI database has two copies of *GvpA1* and one copy of *GvpA2*, our genomic PCR yielded a product with only one copy of *GvpA1*. In a second cloning step, we added a copy of *GvpA2* to the cloned cluster. While we were able to PCR *GvpA2* from the genome, it was not contiguous with the rest of the cluster. Therefore, we speculate that either there was an error in the assembly of the genome sequence (likely caused by the high sequence similarity of the *GvpA* genes), or that the genotype of our strain differs slightly from that of the strain sequenced.

In vitro bacterial expression of ARGs

For initial testing, all constructs were expressed in BL21(DE3) *E. coli* (NEB). Fifty μL of electrocompetent *E. coli* were transformed with 1.5 μL of purified plasmid DNA (Econospin 96-well filter plate, Epoch Life Science), and 1 mL of SOC medium (NEB) was added immediately after electroporation. These cultures were incubated at 37ºC for 2 hr, and 150 uL was inoculated into larger 1.5 mL LB cultures containing 100 ug/mL kanamycin and 1% (w/v) glucose in a deep-well 96-well plate and grown overnight in a shaking incubator at 30ºC. Square dual-layer LB agar plates were prepared as described previously,[42] with varying concentrations of IPTG and 100 ug/mL kanamycin in the bottom layer, and 1% (w/v) glucose and 100 ug/mL kanamycin in the top layer. LB agar was incubated at 60ºC for 12-36 hr after dissolution to allow it to degas. After the agar solidified, plates were dried at 37ºC to remove all condensation on the top layer that would cause the bacterial patches to run together. A multichannel pipette was used to thoroughly mix overnight cultures and drop 1 μL of each culture onto the surface of the dual-layer plates, with care taken to avoid puncturing the agar which results in artifacts during ultrasound scans. Importantly, low-retention pipette tips were used, as it was found that the small volumes of culture would wet the outsides of standard pipette tips, resulting in inaccurate volume dispensing. Patches were allowed to dry completely before plates were flipped and incubated at 37ºC for 24 hr or 30ºC for 48 hr.

For *in vitro* expression experiments in EcN, the appropriate plasmids were first transformed via electroporation and the outgrowth was plated on LB (Miller)-agar plates with the appropriate antibiotic (25 μg/mL chloramphenicol or 50 μg/mL kanamycin) and 1% (w/v) glucose. The resulting colonies were used to inoculate 2 mL LB (Miller) medium with the appropriate antibiotic and 1% (w/v) glucose, and these cultures were incubated at 250 rpm and 37ºC overnight. Glycerol stocks were prepared by mixing the overnight cultures in a 1:1 volume ratio with 50% (v/v) glycerol and storing at -80ºC. The night before expression experiments, glycerol stocks were used to inoculate overnight cultures (2 mL LB medium with the appropriate antibiotic and 1% (w/v) glucose) which were incubated at 37ºC and shaken at 250 rpm. For expression on solid media, 1 μL of overnight culture was dropped onto square dual-layer LB agar plates with 2X the final inducer (IPTG, aTc, or L-arabinose) concentration in the bottom layer, 1% (w/v) glucose in the top layer, and the appropriate antibiotic in both layers (50 μg/mL chloramphenicol or 100 μg/mL kanamycin). Plates were allowed to dry, and then inverted and incubated at 37ºC for 24 hours before imaging with ultrasound. For expression in liquid media, 500 μL of each overnight culture was used to inoculate 50 mL LB supplemented with 0.4% (w/v) glucose and 25 μg/mL chloramphenicol in 250 mL baffled flasks. Cultures were incubated at 37ºC and 250 rpm until reaching at OD_{600} of 0.1 - 0.3. At this point, cultures were induced by addition of L-arabinose and placed back at 37ºC and 250 rpm. For time titration experiments, 0.1% (w/v) L-arabinose was used for induction and 0.5 mL of each culture was removed at 0, 1, 3, 5, 7, 9, 11, and 24 hours post-induction for OD_{600} and ultrasound measurements. For L-arabinose titration experiments, L-arabinose concentrations ranging from 0 to 1% (w/v) were used for induction, and cultures were incubated for 24 hours at 37ºC and 250 rpm after addition of L-arabinose before ultrasound imaging. For cell concentration titration experiments, cultures were incubated for 24 hours at 37ºC and 250 rpm after addition of 0.1% (w/v) L-arabinose

before ultrasound imaging. All cultures were stored at 4ºC or on ice until casting in phantoms and imaging with ultrasound. In all liquid culture experiments, cultures were prescreened for the presence of GVs by phase contrast microscopy before being imaged with ultrasound.

To assess plasmid stability of pBAD-bARG$_{Ser}$-AxeTxe in EcN, the glycerol stock of this strain was used to inoculate 2 mL LB (Miller) supplemented with 25 μg/mL chloramphenicol and 1% (w/v) glucose, and this culture was incubated at 37ºC and 250 rpm overnight. Twenty μL of the overnight culture was subcultured into 2 mL LB with 25 μg/mL chloramphenicol, 2 mL LB without antibiotics, and 2 mL LB without antibiotics and with 0.1% (w/v) L-arabinose, each in quadruplicate. Every 24 hours, 20 μL of each culture was sub-cultured into fresh media of the same conditions. All cultures were incubated at 37ºC and 250 rpm. On days 1-3, 5, and 7, serial dilutions of each culture were plated on LB-agar without antibiotics, LB-agar with 25 μg/mL chloramphenicol, and LB-agar with 25 μg/mL chloramphenicol + 0.1% (w/v) L-arabinose + 0.4% (w/v) glucose. Plates were incubated at 37ºC for at least 16 hours and colonies were counted and screened manually. Plasmid retention was assessed by taking the ratio of CFUs on LB-agar plates with chloramphenicol to CFUs on LB-agar plates without antibiotics. The presence of mutations that disrupt the ability to express functional bARG$_{Ser}$ was assessed by a loss of colony opacity on LB-agar plates with 25 μg/mL chloramphenicol + 0.1% (w/v) L-arabinose + 0.4% (w/v) glucose.

In vitro ultrasound imaging of bacteria expressing ARGs on solid media

Ultrasound imaging of bacterial patches was performed using a Verasonics Vantage programmable ultrasound scanning system and an L10-4v 128-element linear array transducer (Verasonics) with a center frequency of 6 MHz and an element pitch of 300 μm. Image acquisition was performed using a custom imaging script with a 64-ray-lines protocol and a synthetic aperture of 65 elements. The transmit waveform was set to a voltage of 50 V and a frequency of 10 MHz, with 1 waveform cycle and 67% intra-pulse duty cycle. In xAM mode, a custom sequence detailed previously[49] was used with an angle of 19.5°. RF data from 4 repeated acquisitions was coherently averaged prior to beamforming for each image plane.

Agar plates containing bacterial patches were coated with a thin layer of LB agar and immersed in PBS to allow acoustic coupling to the L10-4v transducer. The transducer was connected to a BiSlide computer-controlled 3D translatable stage (Velmex) and positioned above the plane of the plate at an angle of 15° from the vertical (to minimize specular reflection from the plastic dishes and agar) and a distance of 20 mm from the bacterial patches. The imaging sequence was applied sequentially to acquire image planes covering the full area of all plates. A custom script was used to automate the scan by controlling the motor stage in tandem with the ultrasound system, translating 0.5 mm in the azimuthal direction between rows and 19.5 mm in the lateral direction between columns. In the case of pre-minus-post-collapse scans, the full scan sequence was repeated after returning the motor stage to its origin and adjusting the voltage of the transducer.

For image processing and analysis, custom beamforming scripts were applied on-line to reconstruct image planes from the acquired RF data at each location. The intensity data for each plane was saved for off-line processing. All image planes were concatenated to form

a 3D volume with all plates and colonies. A 2D image of the colonies was extracted from the 3D volume by taking the maximum intensity over a manually-defined depth range for all voxel columns. 2D pre-minus-post-collapse images were obtained by subtracting the post-collapse 2D image from the pre-collapse 2D image. Bacterial patch intensities were then quantified from these 2D images. Sample ROIs were drawn around the center of each patch to avoid artefacts from the edges, and background ROIs were drawn around representative regions without patches. The signal-to-background ratio (SBR) was calculated as the mean pixel intensity of the sample ROI divided by the mean pixel intensity of the background. Conversion to decibels (dB) was calculated as 20*log10(SBR). For display, images were normalized by dividing by the average background signal of all images being compared and setting the lower and upper limits of the colormaps to be the same, where the lower limit was equal to a constant A times the average background and the upper limit was equal to a constant B times the maximum pixel intensity out of all images being compared; images were then converted to dB. For xAM and pre-minus-post-collapse xAM images of bacterial patches, A was set to 1 and B was set to 0.5.

In vitro ultrasound imaging of bacteria expressing ARGs suspended in agarose phantoms
To create phantoms for ultrasound imaging of bacteria from liquid cultures or suspended in PBS from patches on solid media, wells were cast with a custom 3D-printed mold using 1% (w/v) agarose in PBS, which was degassed by incubating at 60ºC for at least 16 hours. Cultures or cell suspensions to be analyzed were diluted in ice-cold PBS to 2x the final desired cell concentration (calculated from the measured OD_{600}), incubated at 42ºC for one minute, and mixed 1:1 with 1% (w/v) agarose in PBS at 42ºC for a final concentration of 1x. This mixture was then loaded into the wells in duplicate and allowed to solidify. Care was taken not to introduce bubbles during this process. The phantoms were submerged in PBS, and ultrasound images were acquired using a Verasonics Vantage programmable ultrasound scanning system and an L22-14v 128-element linear array transducer with a center frequency of 18.5 MHz with 67%-6-dB bandwidth, an element pitch of 100 μm, an elevation focus of 8 mm, and an elevation aperture of 1.5 mm. The transducer was attached to a custom-made manual translation stage to move between samples. B-mode and xAM images were acquired using the same parameters as described previously[72]: the frequency and transmit focus were set to 15.625 MHz and 5 mm, respectively, and each image was an average of 50 accumulations. B-mode imaging was performed with a conventional 128-ray-lines protocol, where each ray line was a single pulse transmitted with an aperture of 40 elements. xAM imaging was performed using a custom sequence detailed previously[49] with an angle of 19.5º and an aperture of 65 elements. The transmitted pressure at the focus was calibrated using a Fibre-Optic Hydrophone (Precision Acoustics), and the peak positive pressure was used as the "acoustic pressure" in **Fig. 2.3**.

To measure the xAM signal at varying acoustic pressures, an automated voltage ramp imaging script was used to acquire an xAM image at each voltage step (0.5 V increments from 2 to 25 V), immediately followed by a B-mode acquisition at a constant voltage of 1.6 V (0.15 MPa) before another xAM acquisition at the next voltage step; the voltage was held constant for 10 seconds at each step before the image was saved. To measure the xAM and B-mode signals over time at various acoustic pressures, another script was used to

automatically save an xAM or B-mode image every second while the voltage was automatically increased by 2 V approximately every 70 seconds. Each frame consisted of 64 ray lines, which took 180 μs each to acquire, giving a pulse repetition rate of 86.8 Hz. Based on these results, all subsequent *in vitro* xAM images of bARG$_{Ser}$-expressing EcN were acquired at 18V (1.29 MPa).

Image processing and analysis were performed as described above, except that custom beamforming scripts were applied off-line to reconstruct images from the saved RF data for each sample, no 3D reconstruction was performed as images captured at single locations, circular ROIs were drawn around sample and background regions (taking care to avoid bubbles) to calculate SBRs, and values of A=1.4 and B=0.5 were used to normalize images for display.

Microscopy

For TEM imaging, cells expressing GVs were diluted to OD_{600} ~1 in 10 mM HEPES (pH 7.5) or culture media. 3 μL of the sample was applied to a freshly glow-discharged (Pelco EasiGlow, 15 mA, 1 min) Formvar/carbon-coated, 200 mesh copper grid (Ted Pella) for 1 min before being reduced to a thin film by blotting. Grids with cells were washed three times in 10 mM HEPES (pH 7.5), blotted, air-dried, and imaged without the stain. Image acquisition was performed using a Tecnai T12 (FEI, now Thermo Fisher Scientific) electron microscope operated at 120 kV, equipped with a Gatan Ultrascan 2k X 2k CCD. For phase contrast microcopy (PCM) imaging, cells expressing GVs were scraped off from plates and re-suspended in PBS at an OD_{600} of 1-2. Suspensions were transferred to glass slides and PCM images were acquired using a Zeiss Axiocam microscope with a 40X Ph2 objective.

In vivo bacterial ARG expression and ultrasound imaging

All *in vivo* experiments were performed under a protocol approved by the Institutional Animal Care and Use of Committee (IACUC) of the California Institute of Technology. For experiments involving tumor colonization with EcN, MC26 cells were grown in DMEM media in T225 flasks. After trypsinization and resuspension in PBS + 0.1 mg/mL DNAseI, 5 x 10^6 MC26 cells were injected subcutaneously into the right flank of 6-8 week-old female Balb/cJ mice. Tumors were allowed to grow for 14 days (reaching sizes of 200-300 mm^3) before injecting 10^8 EcN cells suspended in PBS via the lateral tail vein. The day before injection of EcN, Ibuprofen was added to the drinking water at 0.2 mg/mL to ameliorate side effects of EcN injections. To prepare the EcN for injection, the appropriate glycerol stocks were used to inoculate 2 mL LB + 1% (w/v) glucose + 25 ug/mL chloramphenicol which was incubated at 37ºC and 250 rpm overnight. The overnight culture (500 μL) was used to inoculate 50 mL LB + 0.4% (w/v) glucose + 25 μg/mL chloramphenicol in 250 mL baffled flasks, which was grown at 37ºC and 250 rpm until reaching an OD_{600} of 0.3 - 0.6. This culture was pelleted, washed 4 times with PBS, resuspended in PBS at an OD_{600} of 0.625, and used for injection. Three days after injection of EcN, mice were injected intraperitoneally with 120 mg L-arabinose to induce the EcN. Starting 24 hours after induction, ultrasound images of tumors were acquired as described below. After imaging, 3.0 MPa acoustic pressure was applied throughout the tumor to collapse GVs, and mice were injected again intraperitoneally with 120 mg L-arabinose. The next day, mice were imaged again with

ultrasound for re-expression of GVs. The following day, all mice were euthanized and tumors were excised, homogenized, serially diluted, and plated on selective media (LB-agar + 25 μg/mL chloramphenicol) as well as on induction plates (LB-agar + 25 μg/mL chloramphenicol + 0.4% (w/v) glucose + 0.1% (w/v) L-arabinose). Colonies on plates with chloramphenicol were manually counted to quantify the levels of colonization, and colonies on induction plates were screened for a non-opaque mutant phenotype.

For ultrasound imaging, mice were anesthetized with 2% isoflurane and maintained at 37ºC using a heating pad. Images were acquired using the L22-14v transducer attached to a manual translation stage described above. Any hair on or around the tumors was removed with Nair, and Aquasonic 100 ultrasound transmission gel was used to couple the transducer to the skin. B-mode and parabolic AM (pAM) images were first acquired using a custom 128 ray line script. Each image was formed from 96 focused beam ray lines, each with a 32-element aperture and 6 mm focus. The transmit waveform was set to a voltage of 1.6V in B-mode or 8V in pAM and a frequency of 15.625 MHz, with 1 waveform cycle and 67% intra-pulse duty. In B-mode, each ray line was a single transmit with all 32 elements, and in pAM each ray line consisted of one transmit with all 32 elements followed by 2 transmits in which first the odd and then the even-numbered elements are silenced.[83] Subsequently, xAM images and additional B-mode images were acquired at the same location without moving the transducer using the same parameters as described above for the *in vitro* experiments (e.g. 18V for xAM and 1.6V for B-mode). At least two separate locations spaced at least 2 mm apart in each tumor were imaged with B-mode, pAM, and xAM. Ultrasound images of tumors were quantified as described above where the sample ROIs were drawn around the necrotic cores in the tumors and the background ROIs were drawn around regions in the gel above the mouse. Images were normalized and plotted on a dB scale as described above except the scaling factors were A=2.5 and B=1 for pAM and the corresponding B-mode tumor images, and A=3.5 and B=1 for xAM and the corresponding B-mode tumor images.

Histology

Tumors were colonized with pBAD-bARG$_{Ser}$-AxeTxe EcN following the same protocol as described above. The day after inducing GV expression with IP injections of L-arabinose, xAM and B-mode images of tumors were acquired as described above. Shortly after imaging, mice were euthanized by sedation with isoflurane and cervical dislocation. Tumors were resected, placed in 10% buffered formalin for 48 hours, and then washed and stored in 70% ethanol. Tumors were then cut in half along the approximate plane of imaging, placed in tissue cassettes, and sent to the Translational Pathology Core Laboratory at UCLA, which embedded samples in paraffin and performed H&E staining, immunohistochemistry, and microscopy imaging. Immunohistochemistry was performed using Opal IHC kits (Akoya Biosciences) according to the manufacturer's instructions. Tissue sections were incubated with either polyclonal rabbit anti-*E. coli* antibody (Virostat; catalogue number 1001) or non-reactive rabbit IgG isotype control antibody as a negative control. All sections were then incubated with an Opal 520 polymer anti-rabbit HRP antibody (Akoya Biosciences) and counterstained with DAPI. Sections were imaged in the appropriate fluorescence or brightfield channels using a high throughput scanning system (Leica Aperio VERSA) with 40 μm resolution.

Data and code availability

Plasmids are available through Addgene and select ultrasound data acquisition and analysis scripts are available on the Shapiro Lab GitHub at https://github.com/shapiro-lab. All other materials and data are available from the corresponding author upon reasonable request.

2.6 Acknowledgements

The authors would like to thank Dianne Newman for a sample of *Streptomyces coelicolor* A3(2), and Yunfeng Li and Avinoam Bar-Zion for help with tissue histology. Electron microscopy was performed in the Beckman Institute Resource Center for Transmission Electron Microscopy at Caltech. R.C.H. was supported by the Caltech Center for Environmental Microbial Interactions. M.T.B. was supported by an NSF GRFP fellowship. This research was supported by the National Institutes of Health (R01-EB018975 to M.G.S.) and Pew Charitable Trust. Related research in the Shapiro Laboratory is supported by the David and Lucille Packard Foundation, the Burroughs Wellcome Fund and the Heritage Medical Research Institute.

2.7 Supplementary information

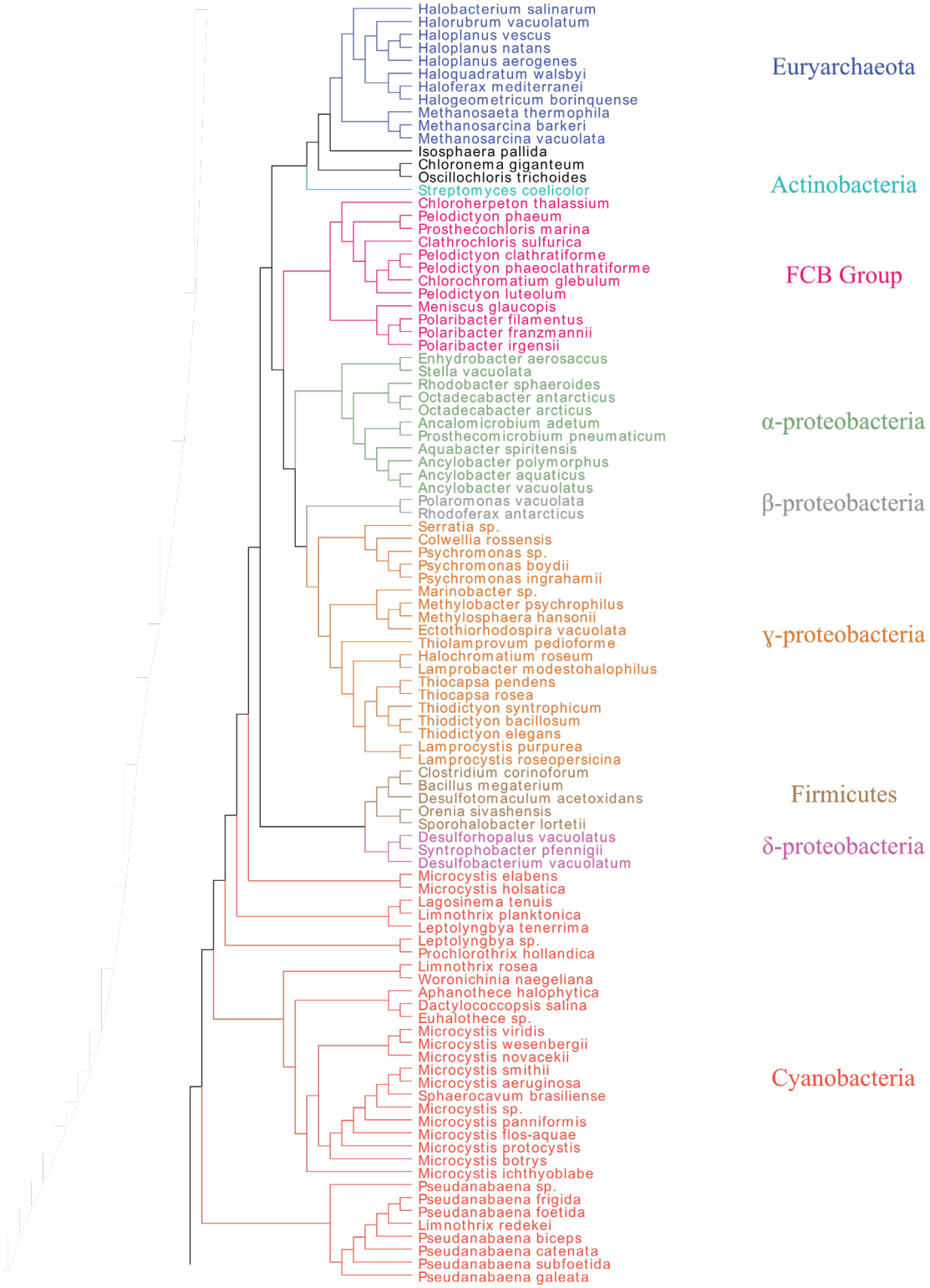

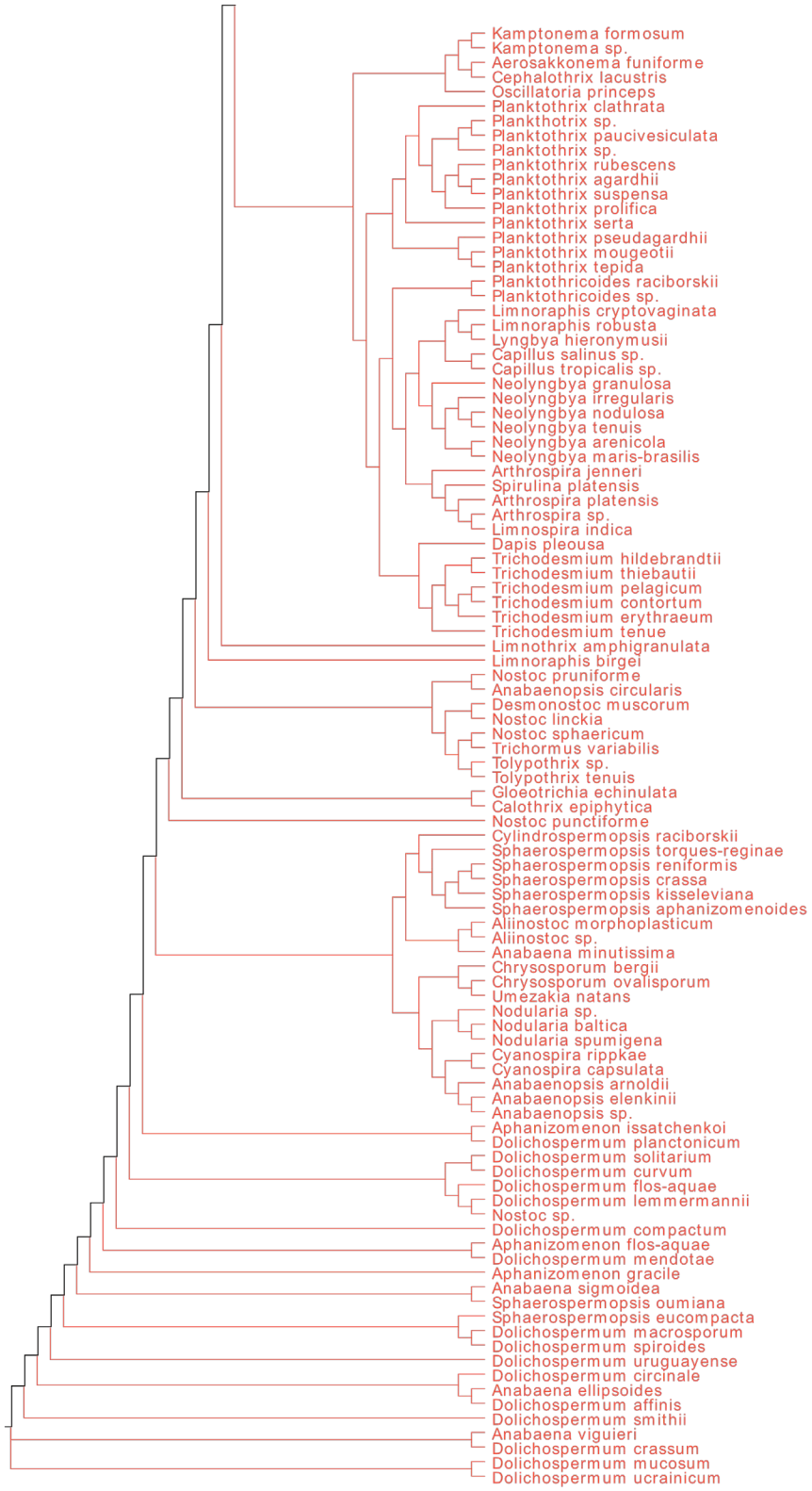

Cyanobacteria

Figure S2.1 | 16S phylogenetic tree of all reported GV-producing organisms. Colors indicate groupings of phylogenetically similar organisms. Organisms from which GV genes were tested in *E. coli* are shown in **Fig. 2.1a**.

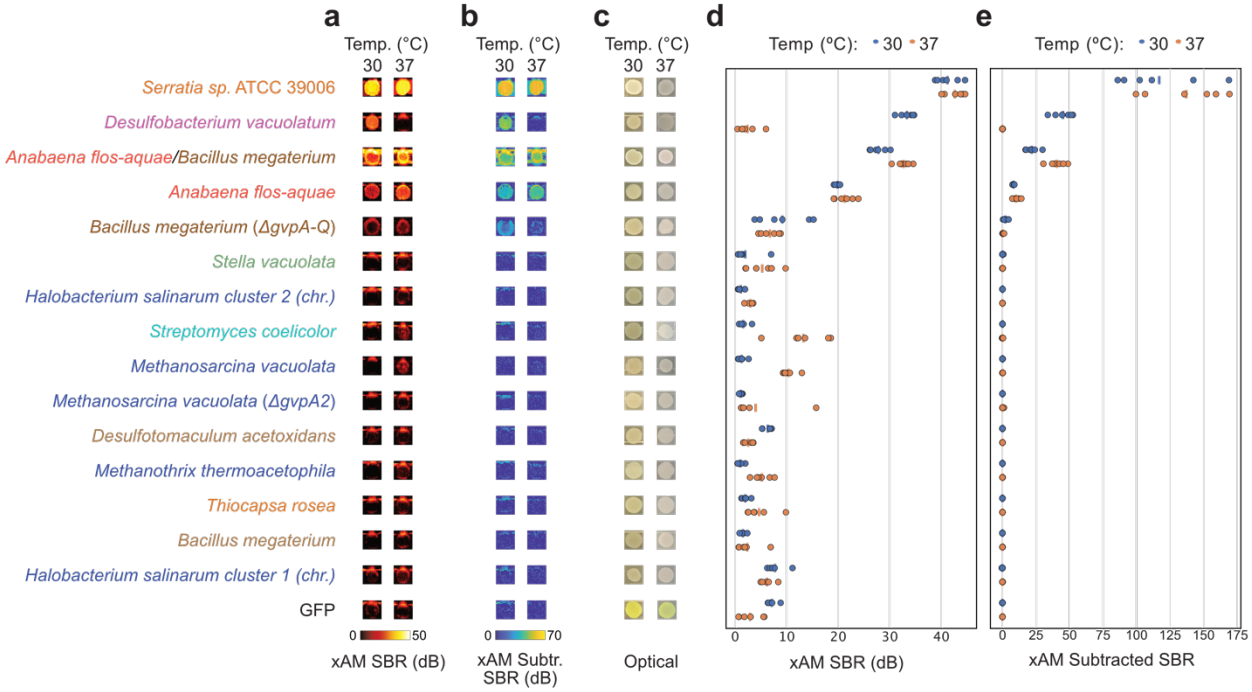

Figure S2.2 | Additional images and quantification of *E. coli* patches expressing select GV gene clusters. (a-c) xAM images (a), pre-minus-post-collapse xAM images (b), and optical images showing opacity (c) of patches of *E. coli* expressing various GV gene clusters from the organisms listed on the left. (**d-e**) Quantification of the xAM (d) and pre-minus-post-collapse xAM (e) signals from images in (a-b) (n=6). SBR, signal-to-background ratio.

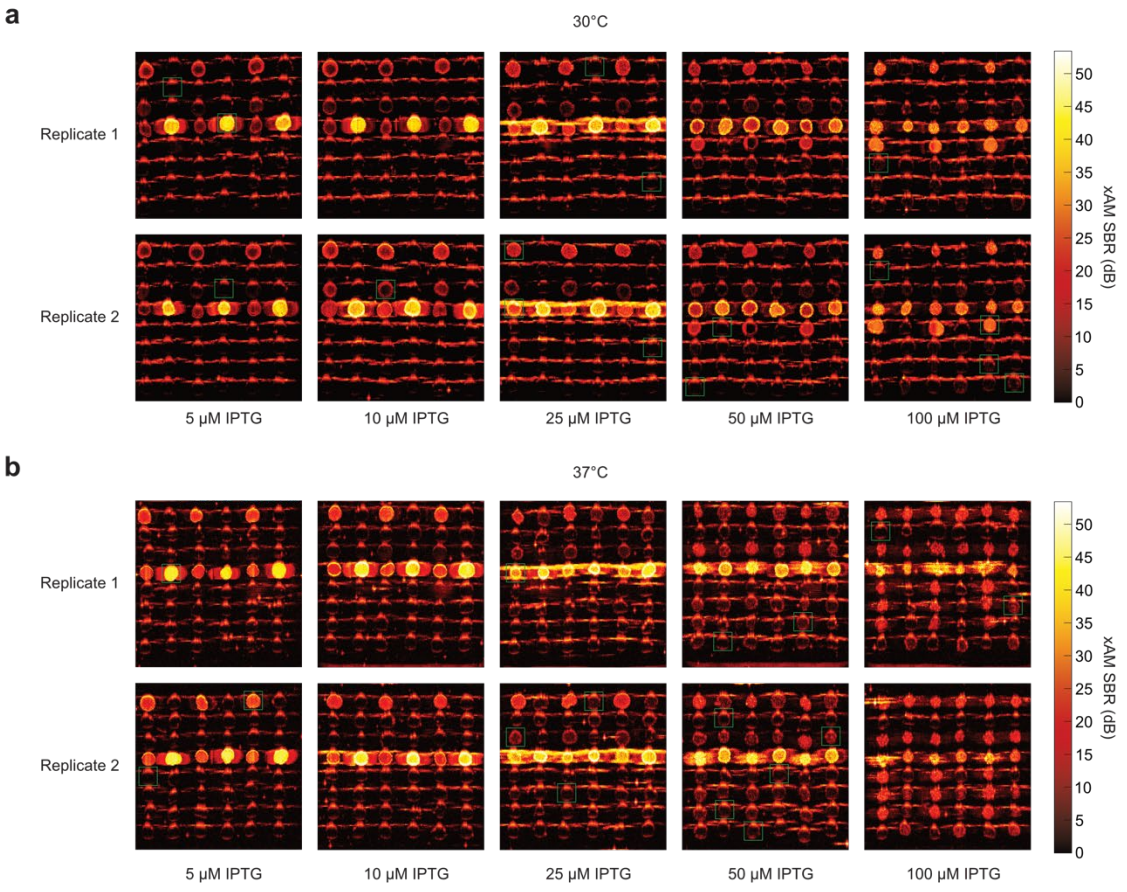
a
30°C
Replicate 1
Replicate 2
5 μM IPTG
10 μM IPTG
25 μM IPTG
50 μM IPTG
100 μM IPTG
xAM SBR (dB)
50
45
40
35
30
25
20
15
10
5
0
b
37°C
Replicate 1
Replicate 2
5 μM IPTG
10 μM IPTG
25 μM IPTG
50 μM IPTG
100 μM IPTG
xAM SBR (dB)
50
45
40
35
30
25
20
15
10
5
0
c
Anabaena flos-aquae
Bacillus megaterium
Bacillus megaterium (ΔgvpA-Q)
Anabaena flos-aquae/Bacillus megaterium
Desulfobacterium vacuolatum
Desulfotomaculum acetoxidans
Halobacterium salinarum cluster 1 (chr.)
Halobacterium salinarum cluster 2 (chr.)
Methanothrix thermoacetophila
Methanosarcina vacuolata (ΔgvpA2)
Methanosarcina vacuolata
Serratia sp. ATCC 39006
Stella vacuolata
Streptomyces coelicolor
Thiocapsa rosea
GFP
d
Uniform, +GVs
Uniform, -GVs
Punctate, +GVs
Punctate, -GVs
Normal OD, -GVs
Reduced OD, -GVs

Figure S2.3 | Optimization of expression conditions for all tested clusters in BL21(DE3) *E. coli.* (**a-b**) xAM images of bacterial patches expressing each GV cluster at varying inducer concentrations and temperatures. Green boxes indicate the patches shown in **Fig. S2.2a**. The IPTG concentration selected was the one that resulted in the highest xAM pre-minus-post-collapse difference signal (**Fig. S2.6**) while not creating toxicity, as determined by whether the patch was uniform or punctate (**Fig. S2.5a-b**). Some of the IPTG concentrations that led to toxicity also created significant xAM signal, but this signal did not originate from GVs, as indicated by the lack of xAM pre-minus-post-collapse signal difference (**Fig. S2.6**). Further, there were some IPTG concentrations for certain genotypes that created significant xAM signal but no xAM pre-minus-post-collapse signal difference, and no visible toxicity (e.g., *Streptomyces coelicolor*, *Thiocapsa rosea*, and GFP at 37˚C, 100 μM IPTG). This discrepancy was likely caused by subtle toxicity that is not apparent in optical images, but altered the texture of the patch enough to be detectable by US. (**c**) Key for genotypes tested in (a-b), with this pattern repeated in three pairs of columns replicated on each plate. (**d**) Examples of the effects of toxic genotypes on bacterial patches, and of artifacts that can appear in bacterial patch scan images. Bacteria themselves can produce significant xAM signal (especially when present in extremely high concentrations, as they are in the confluent patches imaged here), which can be seen in the forms of rings around all patches, regardless of GV expression status. Further, expression of toxic proteins (or of large amounts of otherwise non-toxic proteins, such as GFP) can interfere with bacterial growth; in extreme cases this results in significant cell death and a punctate appearance, and in less extreme cases it simply reduces the optical density of patches. GV expression can increase the optical density of patches, but only at high levels of GV expression. Punctate patches produce considerably more xAM signal than uniform ones, even in the absence of GV expression. The xAM pre-minus-post-collapse difference can be used to qualitatively determine if a patch produces GVs, but because collapse is incomplete in some cases, it is not an ideal method for quantitatively comparing genotypes.

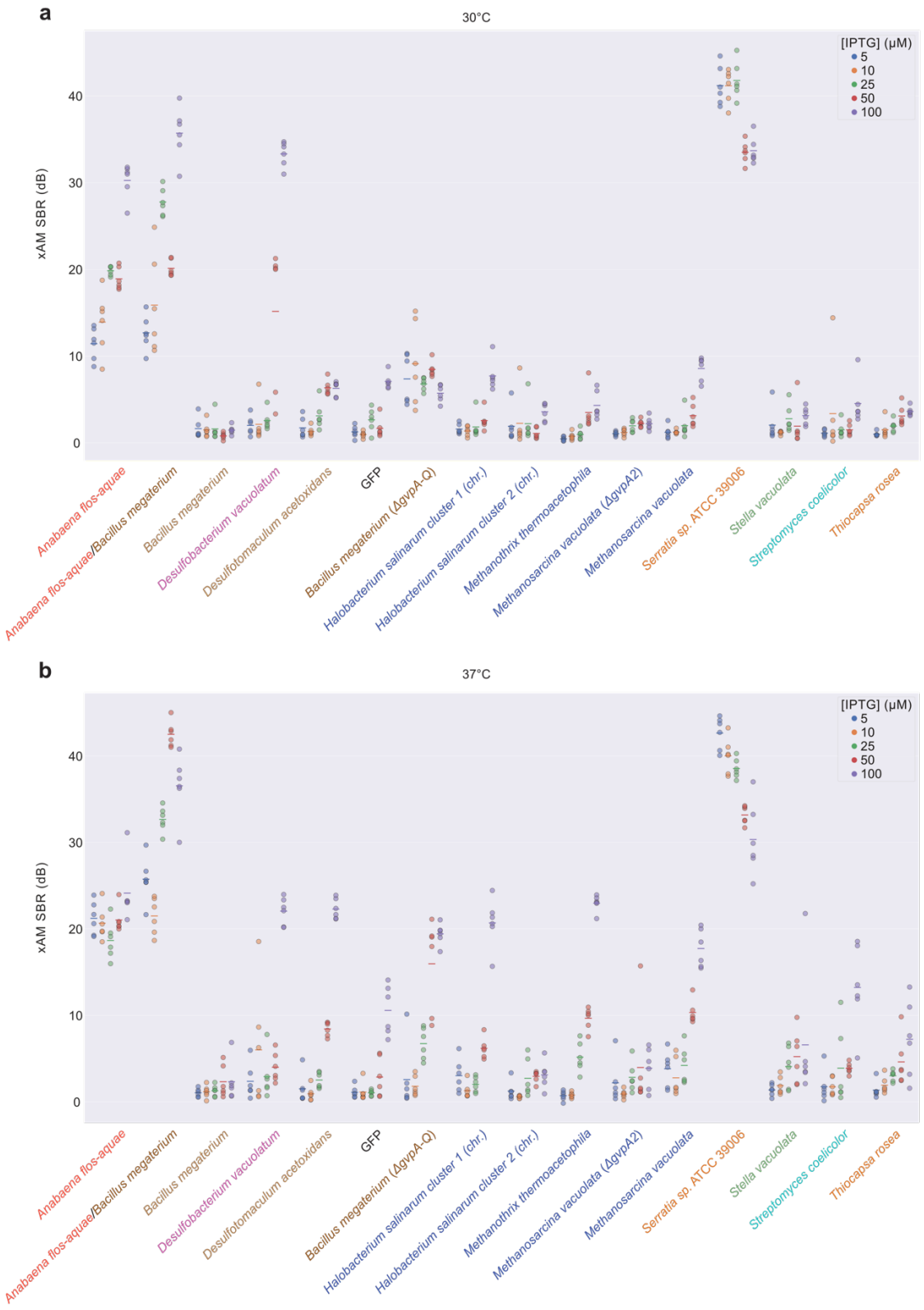
a
30°C
xAM SBR (dB)
[IPTG] (μM)
5
10
25
50
100
Anabaena flos-aquae
Anabaena flos-aquae/Bacillus megaterium
Bacillus megaterium
Desulfobacterium vacuolatum
Desulfotomaculum acetoxidans
GFP
Bacillus megaterium (ΔgvpA-Q)
Halobacterium salinarum cluster 1 (chr.)
Halobacterium salinarum cluster 2 (chr.)
Methanothrix thermoacetophila
Methanosarcina vacuolata (ΔgvpA2)
Methanosarcina vacuolata
Serratia sp. ATCC 39006
Stella vacuolata
Streptomyces coelicolor
Thiocapsa rosea
b
37°C
xAM SBR (dB)
[IPTG] (μM)
5
10
25
50
100
Anabaena flos-aquae
Anabaena flos-aquae/Bacillus megaterium
Bacillus megaterium
Desulfobacterium vacuolatum
Desulfotomaculum acetoxidans
GFP
Bacillus megaterium (ΔgvpA-Q)
Halobacterium salinarum cluster 1 (chr.)
Halobacterium salinarum cluster 2 (chr.)
Methanothrix thermoacetophila
Methanosarcina vacuolata (ΔgvpA2)
Methanosarcina vacuolata
Serratia sp. ATCC 39006
Stella vacuolata
Streptomyces coelicolor
Thiocapsa rosea

Figure S2.4 | Quantification of ultrasound signal for all samples shown in Fig. S2.3a-b. (**a-b**) xAM SBR of the patches at 30ºC (a) and 37ºC (b) shown in **Fig. S2.3a-b**.

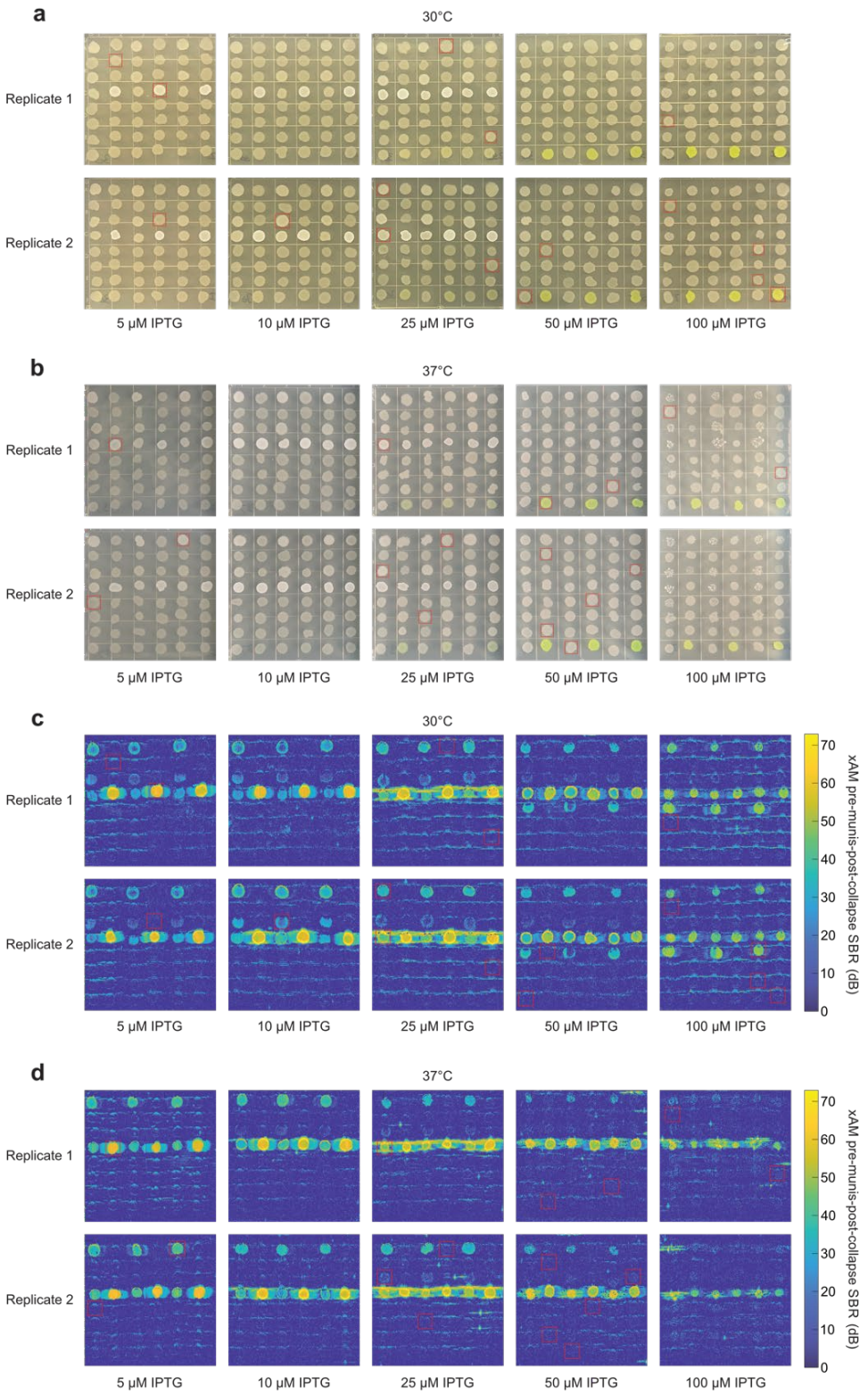
a
30°C
Replicate 1
Replicate 2
5 μM IPTG
10 μM IPTG
25 μM IPTG
50 μM IPTG
100 μM IPTG
b
37°C
Replicate 1
Replicate 2
5 μM IPTG
10 μM IPTG
25 μM IPTG
50 μM IPTG
100 μM IPTG
c
30°C
Replicate 1
Replicate 2
5 μM IPTG
10 μM IPTG
25 μM IPTG
50 μM IPTG
100 μM IPTG
xAM pre-munis-post-collapse SBR (dB)
70
60
50
40
30
20
10
0
d
37°C
Replicate 1
Replicate 2
5 μM IPTG
10 μM IPTG
25 μM IPTG
50 μM IPTG
100 μM IPTG
xAM pre-munis-post-collapse SBR (dB)
70
60
50
40
30
20
10
0

Figure S2.5 | Optical and xAM pre-minus-post-collapse difference images of all samples shown in Fig. S2.3. (**a-b**) Optical images of patches at 30ºC (a) and 37ºC (b) shown in **Fig. S2.3a-b**. (**c-d**) xAM pre-minus-post-collapse difference patches of samples at 30ºC (a) and 37ºC (b) shown in **Fig. S2.3a-b**. Red boxes indicate the patches shown in **Fig. S2.2b-c**.

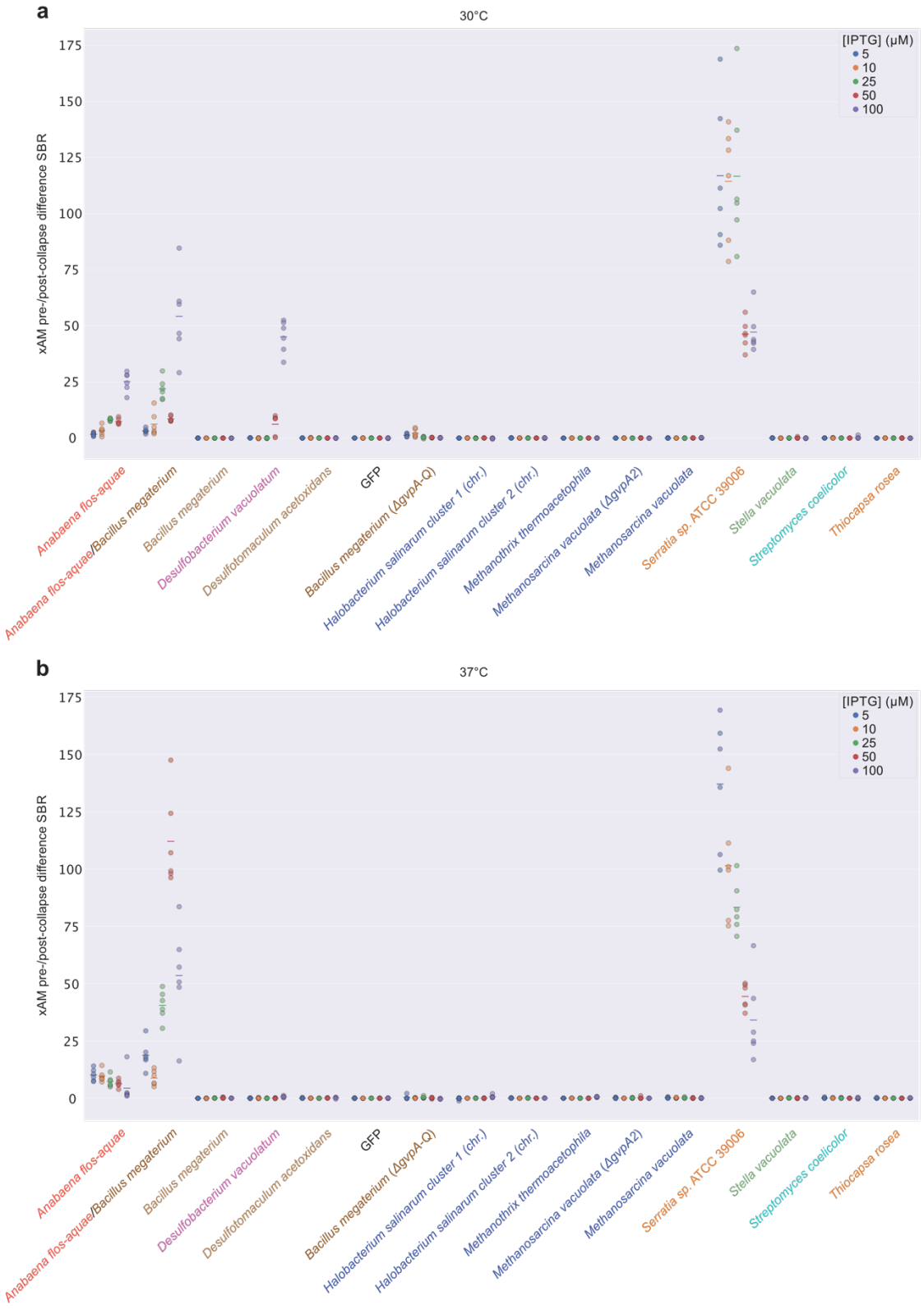
a
30°C
xAM pre-/post-collapse difference SBR
[IPTG] (μM)
5
10
25
50
100
Anabaena flos-aquae
Anabaena flos-aquae/Bacillus megaterium
Bacillus megaterium
Desulfobacterium vacuolatum
Desulfotomaculum acetoxidans
GFP
Bacillus megaterium (ΔgvpA-Q)
Halobacterium salinarum cluster 1 (chr.)
Halobacterium salinarum cluster 2 (chr.)
Methanothrix thermoacetophila
Methanosarcina vacuolata (ΔgvpA2)
Methanosarcina vacuolata
Serratia sp. ATCC 39006
Stella vacuolata
Streptomyces coelicolor
Thiocapsa rosea
b
37°C
xAM pre-/post-collapse difference SBR
[IPTG] (μM)
5
10
25
50
100
Anabaena flos-aquae
Anabaena flos-aquae/Bacillus megaterium
Bacillus megaterium
Desulfobacterium vacuolatum
Desulfotomaculum acetoxidans
GFP
Bacillus megaterium (ΔgvpA-Q)
Halobacterium salinarum cluster 1 (chr.)
Halobacterium salinarum cluster 2 (chr.)
Methanothrix thermoacetophila
Methanosarcina vacuolata (ΔgvpA2)
Methanosarcina vacuolata
Serratia sp. ATCC 39006
Stella vacuolata
Streptomyces coelicolor
Thiocapsa rosea

Figure S2.6 | Quantification of ultrasound signal for samples shown in Fig. S2.5c-d. (**a-b**) xAM SBR for the patches at 30ºC (a) and 37ºC (b) shown in **Fig. S2.5c-d**.

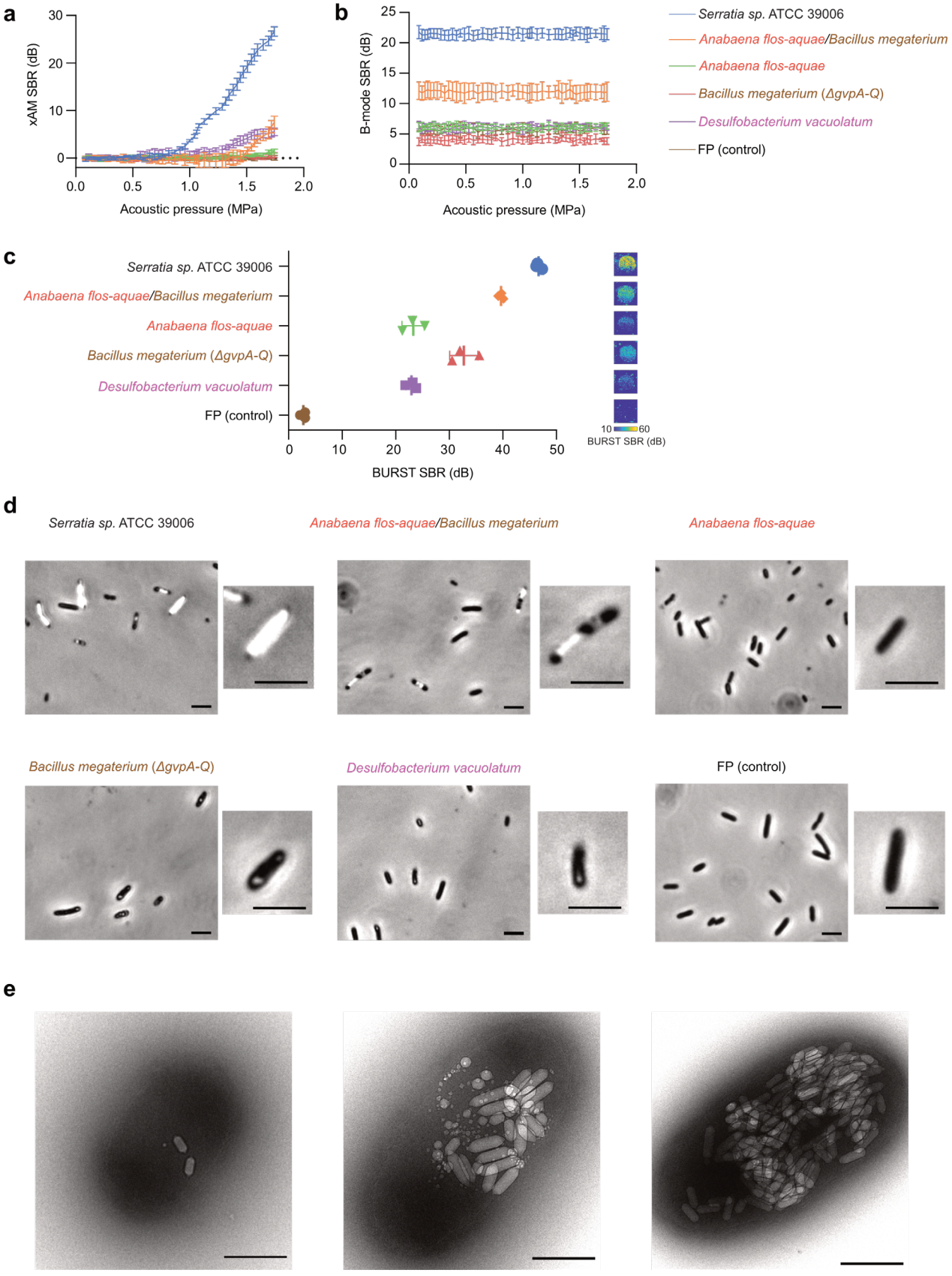
a
xAM SBR (dB)
Acoustic pressure (MPa)
b
B-mode SBR (dB)
Acoustic pressure (MPa)
Serratia sp. ATCC 39006
Anabaena flos-aquae/Bacillus megaterium
Anabaena flos-aquae
Bacillus megaterium (ΔgvpA-Q)
Desulfobacterium vacuolatum
FP (control)
c
BURST SBR (dB)
d
e

Figure S2.7 | Characterization of working GV clusters in BL21(DE3) *E. coli*. (**a-d**) xAM signal-to-background ratio (SBR) as a function of acoustic pressure (a), B-mode SBR at a constant pressure of 0.15 MPa after each increase in acoustic pressure in a (b), BURST SBRs and corresponding representative images (c), and representative phase contrast microscopy (PCM) images (d) of the working GV clusters expressed in BL21(DE3) *E. coli* at 30ºC on solid media. For ultrasound imaging (a-c), samples were normalized to 5 x 10^9 cells/mL in agarose phantoms. Curves and error bars represent the mean (n=3 biological replicates each with 2 technical replicates) ± SD. (a-b) have the same legend. GV clusters in cells are visible by PCM for all clusters except for the cluster from *Anabaena flos-aquae* and the fluorescent protein (FP) control (d). (**e**) Representative TEM images of BL21(DE3) *E. coli* cells expressing Serratia GVs at varying levels of expression. Scale bars are 5 μm in (d) and 500 nm in (e).

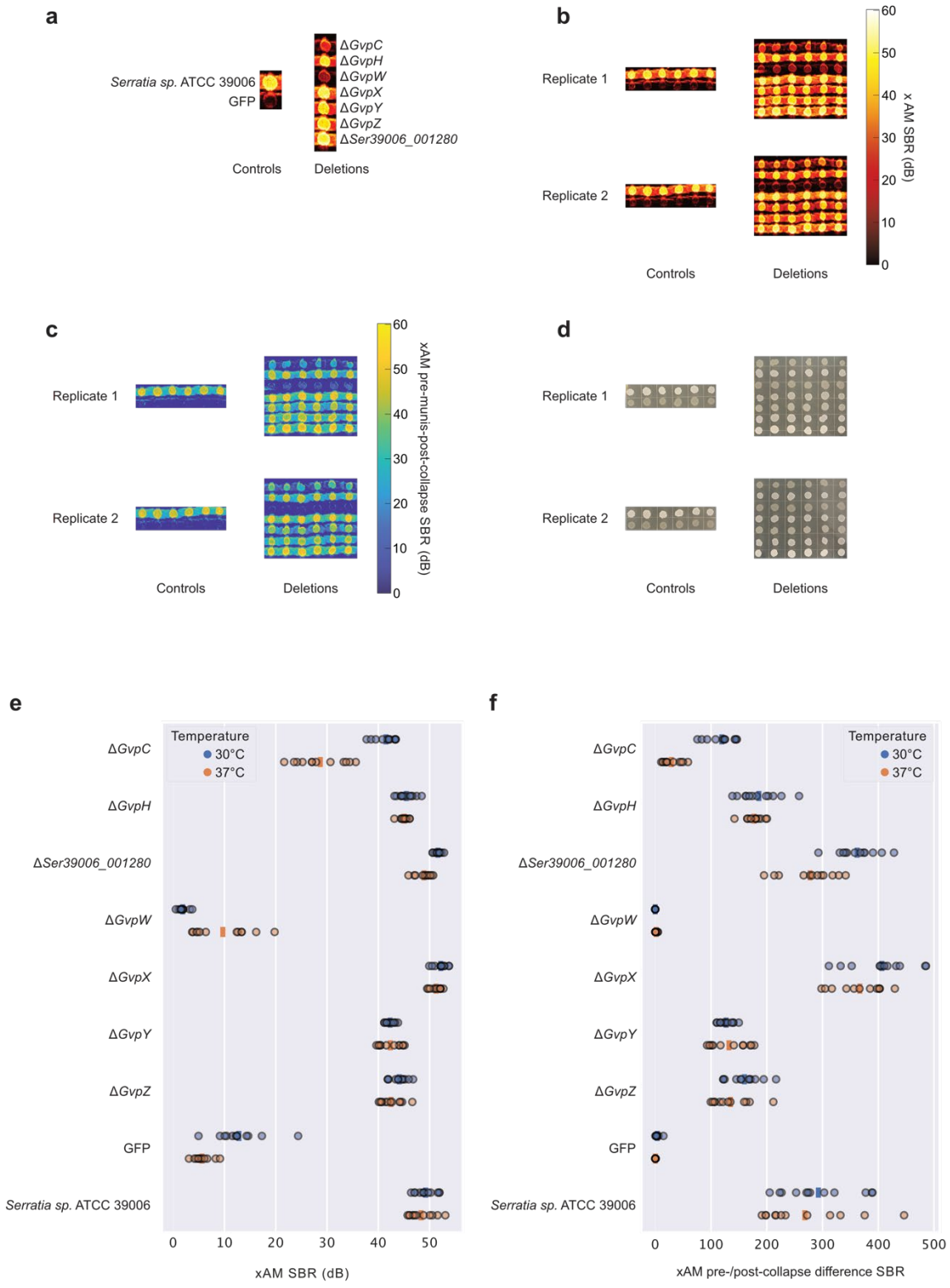
a
Serratia sp. ATCC 39006
GFP
ΔGvpC
ΔGvpH
ΔGvpW
ΔGvpX
ΔGvpY
ΔGvpZ
ΔSer39006_001280
Controls
Deletions
b
Replicate 1
Replicate 2
Controls
Deletions
x AM SBR (dB)
60
50
40
30
20
10
0
c
Replicate 1
Replicate 2
Controls
Deletions
xAM pre-munis-post-collapse SBR (dB)
60
50
40
30
20
10
0
d
Replicate 1
Replicate 2
Controls
Deletions
e
Temperature
30°C
37°C
ΔGvpC
ΔGvpH
ΔSer39006_001280
ΔGvpW
ΔGvpX
ΔGvpY
ΔGvpZ
GFP
Serratia sp. ATCC 39006
0
10
20
30
40
50
xAM SBR (dB)
f
Temperature
30°C
37°C
ΔGvpC
ΔGvpH
ΔSer39006_001280
ΔGvpW
ΔGvpX
ΔGvpY
ΔGvpZ
GFP
Serratia sp. ATCC 39006
0
100
200
300
400
500
xAM pre-/post-collapse difference SBR

Figure S2.8 | Effects of single-gene deletions on GV expression by the *Serratia* cluster. (**a**) Key for genotypes tested, repeated in 6 replicate columns on each plate. (**b-d**) xAM images (b), pre-minus-post-collapse xAM images (c), and optical images (d) of bacterial patches expressing single-gene deletions of the Serratia cluster. (**e-f**) Quantification of the xAM images (e) and pre-minus-post-collapse xAM images (f) shown in (b-c).

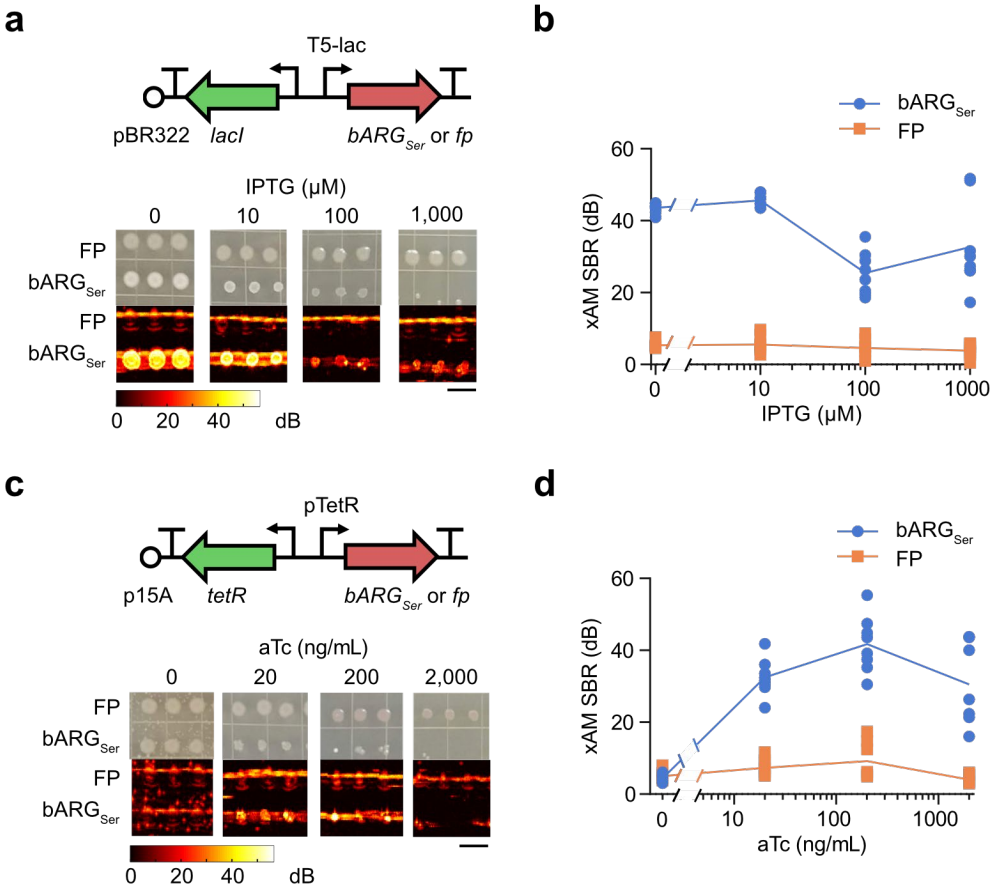

Figure S2.9 | Testing bARG$_{Ser}$ expression in EcN with IPTG- and aTc-inducible gene circuits. (**a**) Diagram of the IPTG-inducible construct used to express bARG$_{Ser}$ in EcN (top), and representative optical and xAM images of bARG$_{Ser}$-expressing or fluorescent protein (FP)-expressing patches of EcN on solid media with varying IPTG concentrations at 37°C (bottom). (**b**) Quantification of the xAM SBR of all patches from the experiment in (a) (n=8). (**c-d**) Same as in (a-b) but for the aTc-inducible construct. The scale bars in (a,c) represent 1 cm.

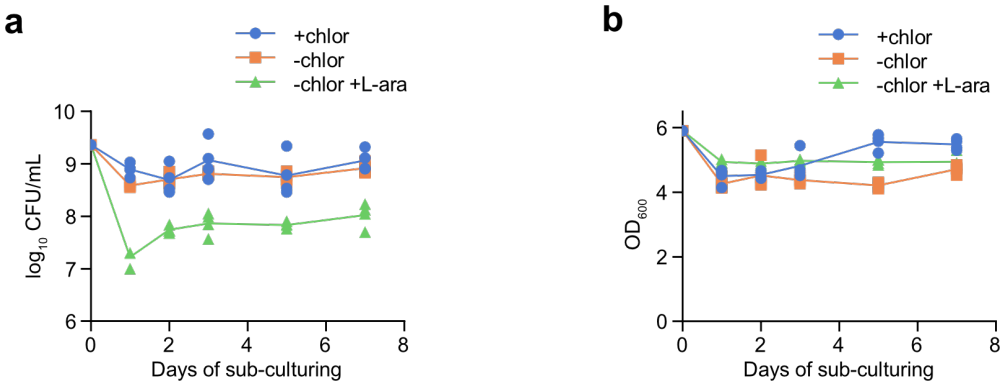

Figure S2.10 | Effect of induction on viability and OD_{600} for $bARG_{Ser}$-expressing EcN in liquid culture. (**a-b**) Colony forming units (CFU) per mL of culture (a) and optical density at 600 nm (b) during daily sub-culturing into LB media with 25 µg/mL chloramphenicol (+chlor), without chloramphenicol (-chlor), or without chloramphenicol and with 0.1% (w/v) L-arabinose (-chlor +L-ara) using pBAD-$bARG_{Ser}$-AxeTxe EcN.

a

			Non-white mutants / total colonies screened			
Condition	**Replicate**	**Starter**	**Day 1**	**Day 2**	**Day 3**	**Day 5**
+chlor	#1	0/226	0/68	0/69	0/60	0/40
+chlor	#2		0/55	0/47	0/355	0/54
+chlor	#3		0/48	0/39	0/98	0/42
+chlor	#4		0/56	0/21	0/49	0/233
-chlor	#1		0/39	0/54	0/70	0/64
-chlor	#2		0/28	0/46	0/65	0/46
-chlor	#3		0/47	0/57	0/75	0/52
-chlor	#4		0/36	0/57	0/57	0/38
-chlor +ara	#1		0/2	0/68	0/53	0/44
-chlor +ara	#2		0/2	0/62	2/86	0/68
-chlor +ara	#3		ND*	0/67	3/102	6/70
-chlor +ara	#4		0/1	0/76	0/34	0/56

*ND: no data because there were no colonies

b

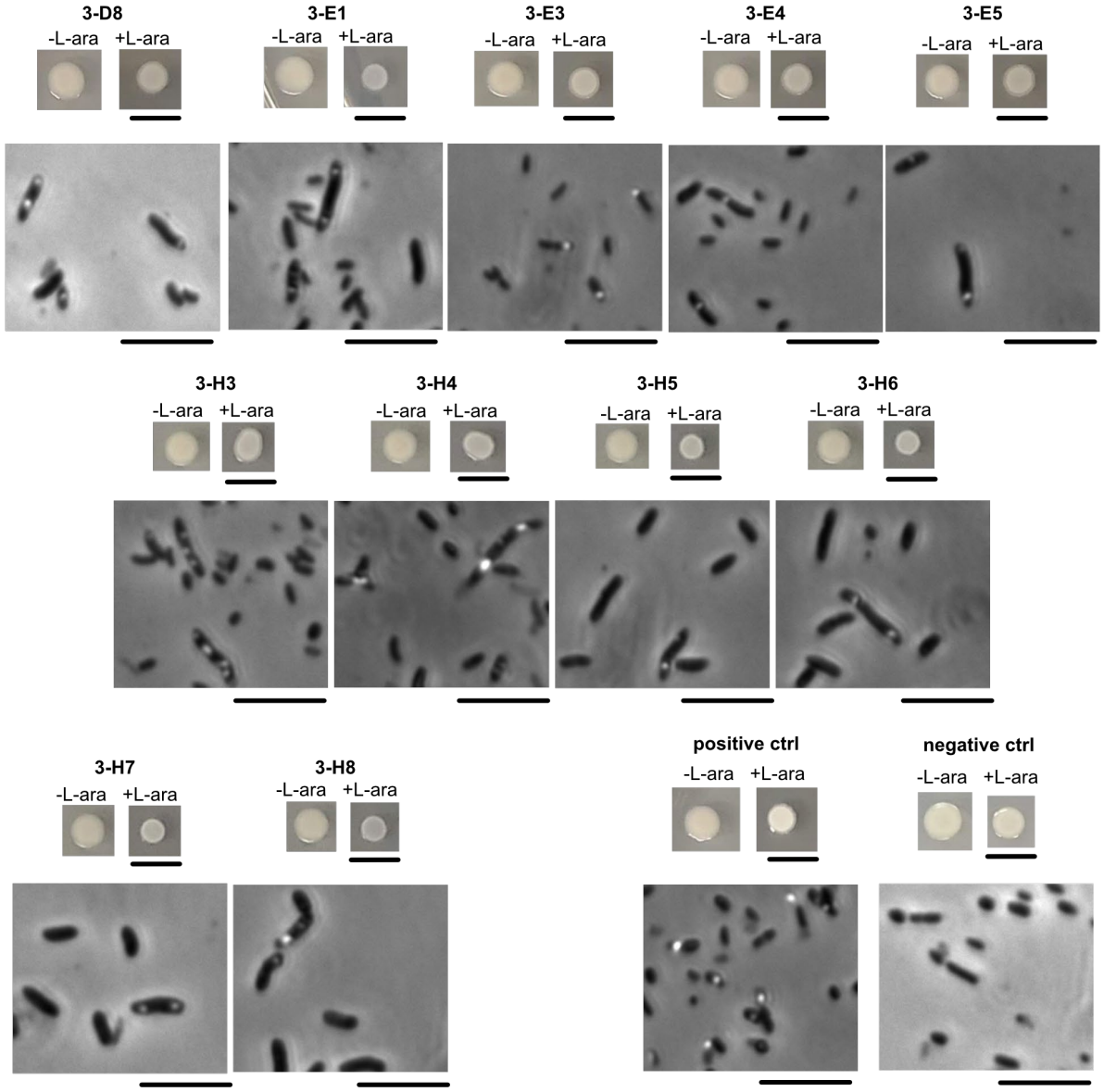

Figure S2.11 | Quantification and characterization of EcN mutants deficient in bARG$_{Ser}$ expression isolated from daily subculturing *in vitro*. (**a**) Numbers of non-white mutant colonies and total colonies screened on plates with 0.1% (w/v) L-arabinose from daily sub-culturing into LB media with 25 μg/mL chloramphenicol (+chlor), without chloramphenicol (-chlor), or without chloramphenicol and with 0.1% (w/v) L-arabinose (-chlor +L-ara) using pBAD-bARG$_{Ser}$-AxeTxe EcN. Cultures where mutants were found are indicated in red. (**b**) Optical images of patches (top rows) on fresh plates with 0.1% (w/v) L-arabinose (+L-ara) and without L-arabinose (-L-ara), and phase contrast microscopy images (bottom rows) from the 11 mutant colonies in (a). Mutants 3-D3 and 3-E1 were from the culture -chlor +ara, replicate #2, day 3; mutants 3-E3, 3-E4, and 3-E5 were from the culture -chlor +ara, replicate #3, day 3; and mutants 3-H3 through 3-H8 were from the culture -chlor +ara, replicate #3, day 5. The positive and negative controls were wild-type pBAD-bARG$_{Ser}$-AxeTxe EcN and pBAD-FP-AxeTxe EcN, respectively. Scale bars are 1 cm for images of patches and 10 μm for microscopy images.

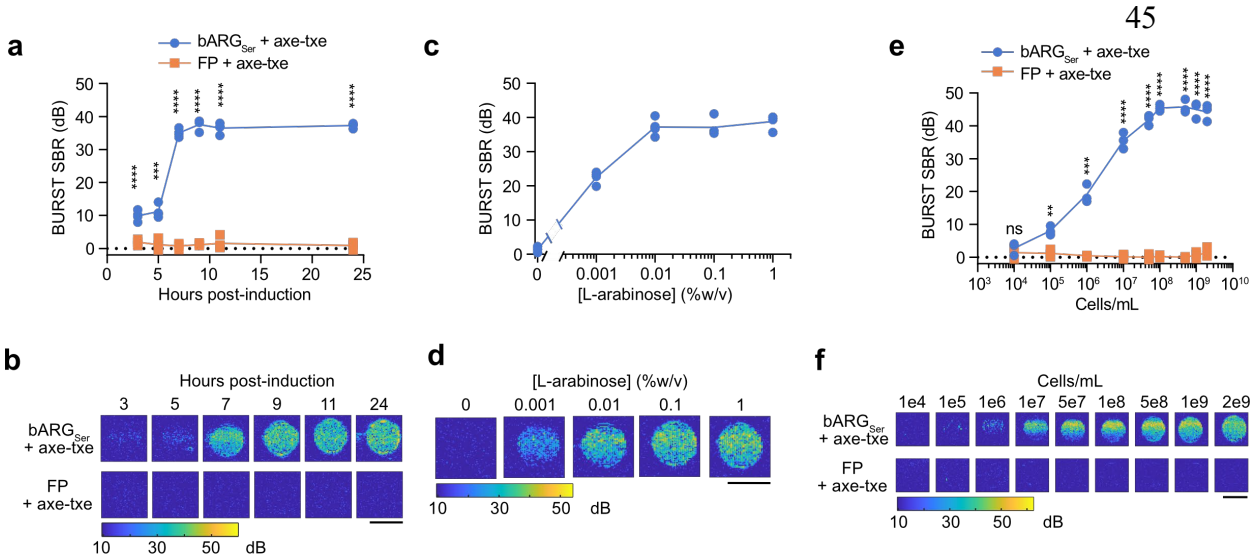

Figure S2.12 | *In vitro* characterizations of bARG$_{Ser}$-expressing EcN with BURST ultrasound imaging. (**a-b**) BURST ultrasound signal-to-background ratio (SBR) versus time after inducing pBAD-bARG$_{Ser}$-AxeTxe and pBAD-FP-AxeTxe EcN strains with 0.1% L-arabinose in liquid culture at 37ºC (a) and the corresponding representative BURST images (b). (**c-d**) BURST ultrasound SBR versus L-arabinose concentration used to induce pBAD-bARG$_{Ser}$-AxeTxe EcN in liquid culture at 37ºC for 24 hours (c) and the corresponding representative BURST images. (**e-f**) BURST ultrasound SBR versus concentration of pBAD-bARG$_{Ser}$-AxeTxe or pBAD-FP-AxeTxe EcN cells induced for 24 hours at 37ºC with 0.1% L-arabinose in liquid culture (e) and the corresponding representative BURST images (f). Note that the BURST SBR saturated at 7 hours post-induction, 0.01% (w/v) L-arabinose, and 10^8 cells/mL. All scale bars are 2 mm. For (a-d), cells were normalized to 10^9 cells/mL in agarose phantoms for ultrasound imaging. For (a, c, e), each point is a biological replicate (n=4 for a and c; n=3 for e) that is the average of at least 2 technical replicates. Asterisks represent statistical significance by unpaired t-tests (**** = $p<0.0001$, *** = $p<0.001$, ** = $p<0.01$, ns = no significance).

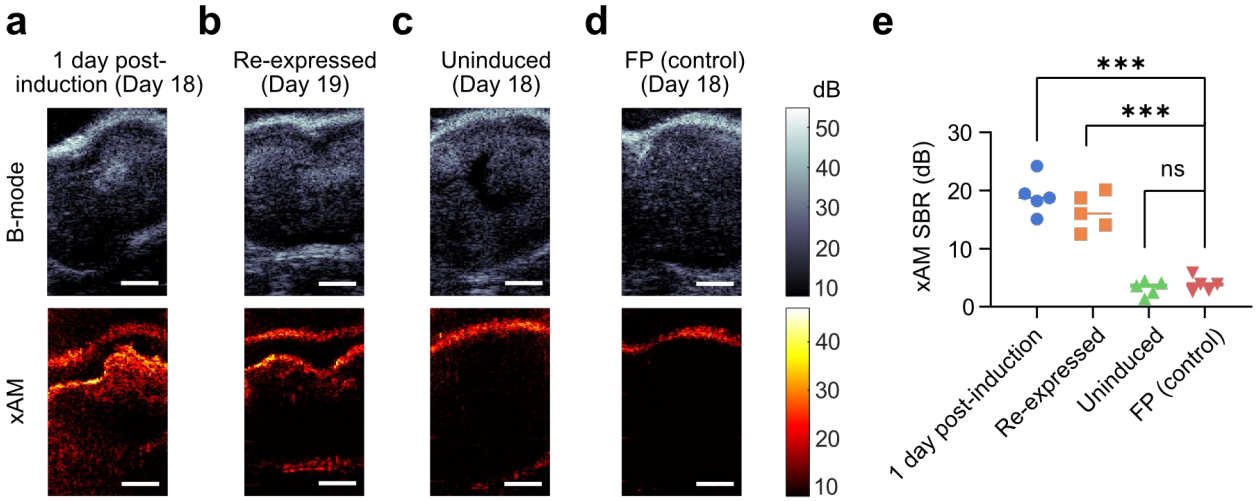

Figure S2.13 | xAM ultrasound imaging of mouse tumors colonized by EcN. (**a-c**) Representative B-mode (top, grayscale) and xAM (bottom, hot-scale) ultrasound images of tumors colonized by pBAD-bARG$_{Ser}$-AxeTxe EcN at least 24 hours after induction with L-arabinose on day 18 (a), at least 24 hours after collapse and re-induction (day 19) (b), or uninduced on day 18 (c). (**d**) Representative ultrasound images of tumors colonized by pBAD-FP-AxeTxe EcN at least 24 hours after induction with L-arabinose on day 18. Scale bars in (a-d) represent 2 mm. (**e**) Quantification of the xAM SBR for the same conditions in (a-d). Each group is N=5. Asterisks represent statistical significance by unpaired t-tests (*** = $p<0.001$, ns = no significance). See **Fig. 2.4a** for the corresponding *in vivo* protocol.

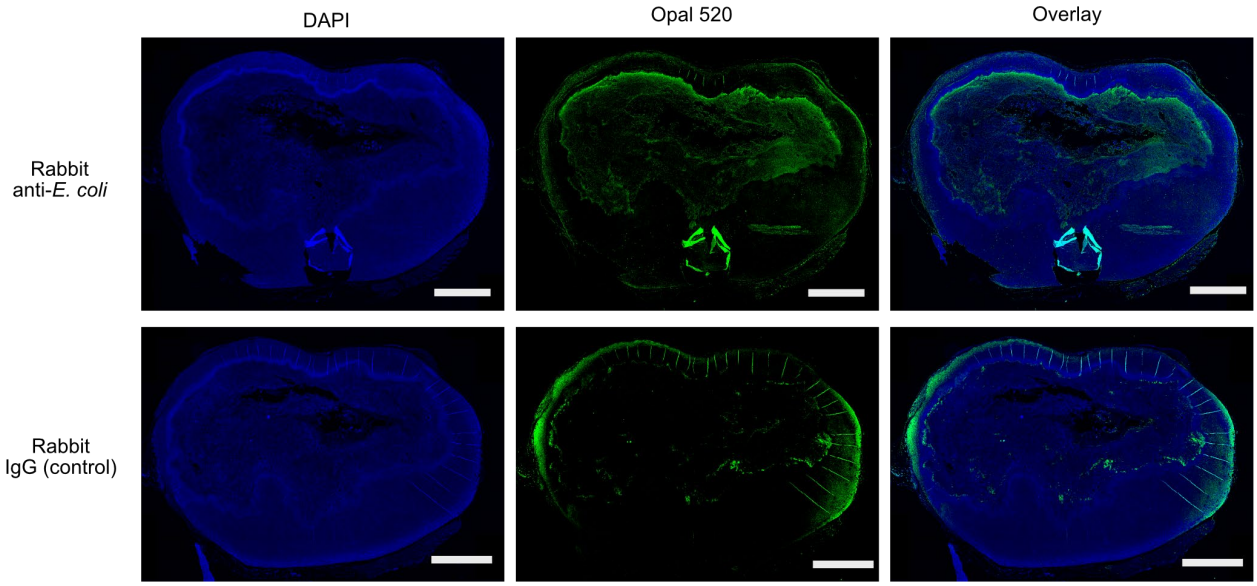

Figure S2.14 | Histology of MC26 tumor colonized with bARG$_{Ser}$-expressing EcN. Fluorescent images of tissue sections after ultrasound imaging on day 19 (see **Fig. 2.4a**). Sections were incubated with either polyclonal rabbit anti-*E. coli* antibodies (top row) or non-reactive rabbit IgG isotype control antibody (bottom row) as a negative control. All sections were then incubated with an Opal 520 polymer anti-rabbit HRP antibody (Akoya biosciences) and counterstained with DAPI. The EcN are visible in the necrotic core in the Opal 520 channel (top middle panel); the edges of the tissue exhibit a high degree of background staining (bottom middle panel).

a

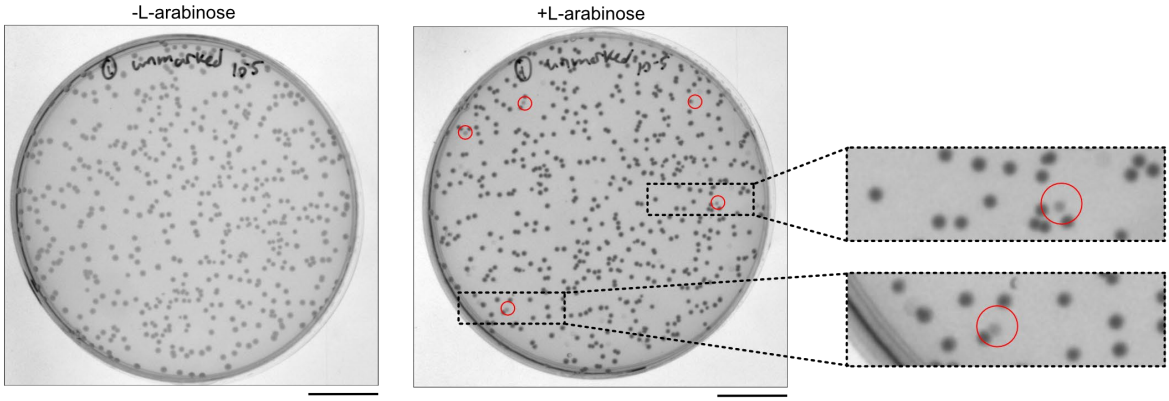

b

Mouse	Condition	Non-white mutants / total colonies screened
#1	Induced	0/687
#2	Induced	2/807
#3	Induced	0/341
#4	Induced	0/478
#5	Induced	5/585
#6	Uninduced	0/660
#7	Uninduced	0/567
#8	Uninduced	0/553
#9	Uninduced	0/556
#10	Uninduced	0/863
Total		7/6097 ~ 0.1%

c

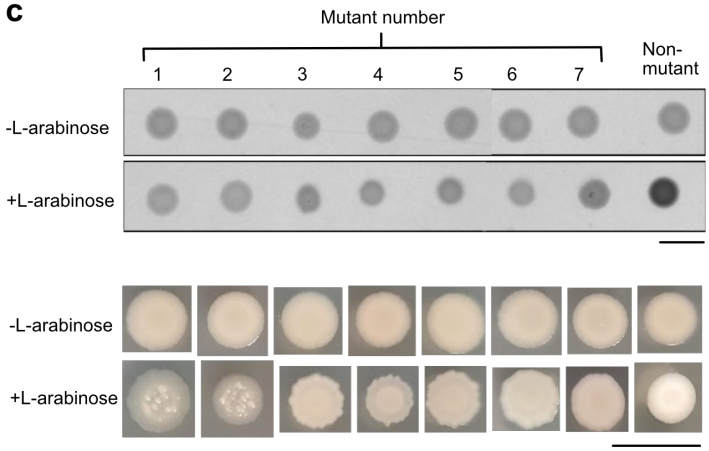

Figure S2.15 | Screening for EcN mutants defective in bARG$_{Ser}$ expression isolated from colonized tumors. (**a**) White light transmission images of plates with 0.1% (w/v) L-arabinose and without L-arabinose from plating a tumor (from mouse #5 in (b)) colonized by bARG$_{Ser}$-expressing EcN. Mutant colonies on the +L-arabinose plate appear lighter (more translucent) than wild-type opaque colonies and are indicated by red circles. (**b**) Numbers of non-white mutant colonies and total colonies screened on plates with 0.1% (w/v) L-arabinose for the ten mice injected with pBAD-bARG$_{Ser}$-AxeTxe EcN. **c**, White light transmission images (top) and photographs (bottom) of patches on fresh plates with 0.1% (w/v) L-arabinose and without L-arabinose made from the seven translucent mutant colonies in red in (b) and an opaque non-mutant colony as a control. Mutants 1-2 were from mouse #2 and mutants 3-7 were from mouse #5. Scale bars are 2 cm in (a) and 1 cm in (c).

Table S2.1 | GV-producing species.

Reference	Species	Strain	Cluster_Accession	Cluster_Coordinates	16S_Accession	16S_Coordinates	16S_Locus
10.2216/11-130.1	*Aerosakkonema funiforme*	NIES 2861, Lao26			AB686261	1, end	N/A
10.1099/ijsem.0.002112	*Aliinostoc morphoplasticum*	NOS			KY403996	1, end	N/A
10.1101/2020.12.12.422513	*Aliinostoc sp.*	PMC 882.14			MT984289	1, end	N/A
10.1099/ijsem.0.002112	*Aliinostoc sp.*	PCC 8112			AM711537	1, end	N/A
10.1023/A:1004170230774	*Anabaena danica*	TAC453			N/A	N/A	N/A
10.1023/A:1004170230774	*Anabaena ellipsoides*	Ana HB			AY701560	1, end	N/A
10.1080/00288825X.2005.9512969	*Anabaena minderi (Anabaena bergii var. limnetica) (Anabaena bergii var. minor)*				N/A	N/A	N/A
Walsby, A.E., Reynolds, C.S., Oliver, R.L. and Kromkamp, J., 1989. The role of gas vacuoles and carbohydrate content in the buoyancy and vertical distribution of Anabaena minutissima in Lake Rotongaio, New Zealand.	*Anabaena minutissima*	var. attenuata			MN453281	1, end	N/A
10.1099/ijs.0.63276-0	*Anabaena sigmoidea*	0tu36s7			AJ630434	1, end	N/A
10.1023/A:1004170230774	*Anabaena viguieri*	TAC433			AY701559	1, end	N/A
Komárek, J. (2005) Phenotype diversity of the heterocytous cyanoprokaryotic genus Anabaenopsis. Czech Phycology, Olomouc 5: 1–35.	*Anabaenopsis arnoldii*				MH160831	1, end	N/A
10.1099/0022128 7-111-1-1	*Anabaenopsis circularis*	M4, PCC 6720, NIES 21, ATCC 27895, CCAP 1402/1	AP018174	1063488, 1079019	DQ185240	1, end	N/A
ISBN 9782726002100	*Anabaenopsis elenkinii*	PCC 9420			AM773308	1, end	N/A
10.1099/0022128 7-148-2-481	*Anabaenopsis sp.*	PCC 9215			AY038033	1, end	N/A
ISBN 9782726002100	*Anabaenopsis sp.*	PCC 9216			N/A	N/A	N/A
ISBN 9782726002100	*Anabaenopsis sp.*	PCC 9608			N/A	N/A	N/A
ISBN 978-0-387-21609-6	*Ancalochloris perfilievii*				N/A	N/A	N/A
10.1128/JB.95.5.1921-1942.1968 ; 10.1128/JB.95.5.1921-1942.1968	*Ancalomicrobium adetum*	4a, DSM 4722, ATCC 23632			NR_104726	1, end	N/A
https://www.ncbi.nlm.nih.gov/pmc/articles/PMC247056/	*Ancylobacter aquaticus (Micrococcus aquaticus)*	M, ATCC 27068, DSM 334			N/A	N/A	N/A
10.1099/00207713-26-4-528	*Ancylobacter aquaticus (Micrococcus aquaticus)*	ATCC 25396, DSM 101, CCM 1786, NCIB 9271, CCUG 30551, JCM 20518, JCM 6888			M62790	1, end	N/A
https://www.ncbi.nlm.nih.gov/pmc/articles/PMC247056/	*Ancylobacter aquaticus (Micrococcus aquaticus)*	B, ATCC 27069, DSM 2454			N/A	N/A	N/A

10.1099/00221287-136-7-1259	*Ancylobacter aquaticus (Microcyclus aquaticus)*	M100, S1	AF087458	1, 2774	N/A	N/A	N/A
10.1099/ijs.0.64118-0	*Ancylobacter polymorphus*	DSM 2457, AS 1.2800, NCIMB 10516			AY211516	1, end	N/A
10.1134/S002626171201016X	*Ancylobacter vacuolatus (Renobacter vaculatum)*	DSM 1277			NR_042794	1, end	N/A
10.1099/ijs.0.02270-0	*Aphanizomenon flos-aquae*	NIES 81	KI928192	2184412, 2197170	AJ293131	1, end	N/A
10.1099/00221287-138-6-1243	*Aphanizomenon flos-aquae*	CCAP 1401/1			N/A	N/A	N/A
10.1111/j.1529-8817.1987.tb04428.x	*Aphanizomenon flos-aquae*	PCC 7905			AJ133154	1, end	N/A
10.1099/ijs.0.02270-0	*Aphanizomenon gracile*	PH271			AJ293125	1, end	N/A
10.1099/ijs.0.02270-0	*Aphanizomenon gracile*	PH219			AJ293124	1, end	N/A
10.1099/ijs.0.02270-0	*Aphanizomenon gracile*	PMC 9402			AJ293127	1, end	N/A
10.2216/06-92.1	*Aphanizomenon issatchenkoi (Cuspidothrix issatschenkoi)*	0tu37s7			AJ630446	1, end	N/A
10.1590/S0100-84042004000200002	*Aphanothece conglomerata*	SPC 515			N/A	N/A	N/A
10.1016/j.micres.2018.04.001	*Aphanothece halophytica (Halothece)*	PCC 7418	CP003945	542576, 548472	AF296872	1, end	N/A
https://isb.emnuvens.com.br/iheringia/article/view/396	*Aphanothece smithii (Anathece smithii)*				N/A	N/A	N/A
ISBN 978-0-387-29298-4	*Aquabacter spiritensis*	SPL-1, ATCC 43981, DSM 9035, LMG 8611	SMAI01000014	114270, 131868	NR_104747	1, end	N/A
10.1038/s41598-018-36831-0	*Arthrospira jenneri*				GQ184185	1, end	N/A
10.1093/oxfordjournals.pcp.a029507	*Arthrospira platensis (Spirulina platensis)*	C1, PCC 9438	NZ_CM001632	50151, 54585; 827532, 828570; 5846728, 5848716	NZ_CM001632	5880927, 5882415	SPLC1_RS25395
10.1080/09670262.2012.692817	*Arthrospira platensis (Spirulina platensis)*	PCC 7345, UTEX 1928	HQ641414	1, 1287	NR_125599	1, end	N/A
10.1080/09670262.2012.692817	*Arthrospira platensis (Spirulina platensis)*	PCC 7345, UTEX 1928	HQ641410	1, 2352	N/A	N/A	N/A
10.1080/09670262.2012.692817	*Arthrospira platensis (Spirulina platensis)*	PCC 9108			DQ393284	1, end	N/A
10.1590/S2236-89062007000100002	*Arthrospira santannae*				N/A	N/A	N/A
10.1080/09670262.2012.692817	*Arthrospira sp.*	PCC 9444, PCC 9223	HQ641412	1, 2352	DQ393285	1, end	N/A
10.1080/09670262.2012.692817	*Arthrospira sp.*	PCC 9444, PCC 9223	HQ641416	1, 1286	N/A	1, end	N/A
10.1080/09670262.2012.692817	*Arthrospira sp.*	Moz. 2.1	HQ641413	1, 2352	N/A	N/A	N/A
10.1080/09670262.2012.692817	*Arthrospira sp.*	Moz. 2.1	HQ641417	1, 1286	N/A	N/A	N/A
https://www.ncbi.nlm.nih.gov/pmc/articles/PMC107188/	*Bacillus megaterium*	ATCC 19213, VT1660	AF053765	151, 7051	FJ969754	1, end	N/A
10.1007/BF02512379	*Brachyarcus thiophilus*	Skuja			N/A	N/A	N/A
Canabaeus, L. 1929. Über die Heterocysten und Gasvakuolen der Blaualgen und ihre Beziehung zueinander. Pflanzenforschung 13:1–48.	*Calothrix epiphytica*				MN062680	1, end	N/A

10.4490/algae.2018.33.11.25	*Capillus salinus sp.*	ALCB 114379			KY824052	1, end	N/A
10.4490/algae.2018.33.11.25	*Capillus tropicalis sp.*	ALCB 114392			MF190468	1, end	N/A
10.11646/phytotaxa.387.4.1	*Cephalothrix lacustris*	LEGE 15492			MF629809	1, end	N/A
ISBN 978-0-387-21609-6	*Chlorochromatium glebulum*				AJ272092	1, end	N/A
10.1007/bf00413007	*Chloroherpeton thalassium*	ATCC 35110		no GV genes	AF170103.1	1, end	N/A
PMID: 125847	*Chloronema giganteum*				AF345825	1, end	N/A
PMID: 125847	*Chloronema spiroideum*				N/A	N/A	N/A
ISBN 9781441915283	*Chloroplana vacuolata*				N/A	N/A	N/A
10.1007/s10750-012-1034-z	*Chrysosporum bergii (Anabaena bergii)*	44441			JQ237772	1, end	N/A
10.1016/j.ecoenv.2011.08.022	*Chrysosporum ovalisporum (Aphanizomenon ovalisporum)*	UAM MAO	CDHJ01000157	6022, 17213	CDHJ01007043	1, end	N/A
10.1007/978-0-387-21609-6	*Clathrochloris sulfurica*				X53184	1, end	N/A
10.1007/bf00406471	*Clostridium corinoforum*				X76742	1, end	N/A
ISBN 9780123858771	*Coelomoron minimum*				N/A	N/A	N/A
ISBN 978-0-387-28022-6	*Colwellia rossensis*	S51-W(gv)1, ACAM 608			U14581	1, end	N/A
ISBN 978-0-387-21609-6	*Cyanospira capsulata*	PCC 9502			FR774777	1, end	N/A
10.1099/00221287-148-2-481	*Cyanospira rippkae*	PCC 9501			AY038036	1, end	N/A
10.1371/journal.pone.0074238	*Cylindrospermopsis raciborskii (Raphidiopsis raciborskii) (Anabaena raciborskii)*	CENA302	NZ_MTPU01000056	3472, 15205	JQ707291	1, end	N/A
10.1371/journal.pone.0074238	*Cylindrospermopsis raciborskii (Raphidiopsis raciborskii) (Anabaena raciborskii)*	CENA303	NZ_NBYN01000060	18659, 30581	JQ707292	1, end	N/A
10.1016/j.micres.2018.04.001	*Dactylococcopsis salina*	PCC 8305	NC_019780	1399778, 1408377	NR_102465	1, end	N/A
10.1099/00221287-138-6-1243	*Dactylococcopsis salina*	CCAP 1417/1			N/A	N/A	N/A
10.1111/jpy.12752	*Dapis pleousa*	FFP12-7			MF061799	1, end	N/A
10.1099/00221287-134-10-2635	*Desmonostoc muscorum (Nostoc muscorum)*	ATCC 29105, PCC 6719			AJ630451	1, end	N/A
ISBN 978-1-4757-2191-1	*Desulfobacterium vacuolatum*	DSM 3385	FWXY01000008	1268, 24724	NR_041854	1, end	N/A
10.1007/s002030050371	*Desulforhopalus vacuolatus*	ltk10			NR_044653	1, end	N/A
10.1007/BF00406471	*Desulfotomaculum acetoxidans*	5575, DSM 771, ATCC 49208, VKM B-1644, KCTC 5769	CP001720	3216181, 3228274	NR_102777	1, end	N/A
10.1023/A:1004170230774	*Dolichospermum affinis (Anabaena affinis)*	NIES 40			AY701541	1, end	N/A
10.1023/A:1004170230774	*Dolichospermum circinale (Anabaena circinalis)*	Ana Da			AB042859	1, end	N/A
10.1099/ijs.0.63276-0	*Dolichospermum compactum (Anabaena compacta)*	ANACOM-KOR			AJ630418	1, end	N/A
10.1023/A:1004170230774	*Dolichospermum compactum (Anabaena compacta)*	CCAP 1403/24			AY701569	1, end	N/A
10.1099/ijs.0.02270-0	*Dolichospermum crassum (Anabaena crassa)*	PH215			AJ293112	1, end	N/A
10.1023/A:1004170230774	*Dolichospermum crassum*	TAC436			AB551442	1, end	N/A

	(Anabaena crassa)						
10.1023/A:1004170230774	*Dolichospermum crassum (Anabaena crassa)*	TAC443			AB551446	1, end	N/A
10.1023/A:1004170230774	*Dolichospermum curvum (Anabaena curva)*	Ana Ao			FN691914	1, end	N/A
ISBN 9782726002100	*Dolichospermum flos-aquae (Anabaena flos-aquae)*	PCC 9349, CCAP 1403/23			HE975016	1, end	N/A
10.1099/00221287-134-10-2635	*Dolichospermum flos-aquae (Anabaena flos-aquae)*	PCC 9332, CCAP 1403/13f	CP051206	266192, 276665	AY887021	1, end	N/A
10.1099/00221287-148-2-481	*Dolichospermum flos-aquae (Anabaena flos-aquae)*	PCC 9302, NRC-525-17			AY038032	1, end	N/A
10.5507/fot.2009.005	*Dolichospermum lemmermannii (Anabaena lemmermannii)*	202A2			AJ293104	1, end	N/A
10.1023/A:1004170230774	*Dolichospermum lemmermannii (Anabaena lemmermannii)*	Ana Dalai			AY701571	1, end	N/A
10.1099/ijs.0.02270-0	*Dolichospermum macrosporum (Anabaena macrospora)*	PMC 9301			AJ293115	1, end	N/A
10.1099/ijs.0.02270-0	*Dolichospermum mendotae (Anabaena mendotae)*	PH57			AJ293107	1, end	N/A
10.1099/ijs.0.63276-0	*Dolichospermum mucosum (Anabaena mucosa)*	1tu35s5			AJ630425	1, end	N/A
10.1023/A:1004170230774	*Dolichospermum mucosum (Anabaena mucosa)*	TAC425			AB551440	1, end	N/A
10.1099/ijs.0.02270-0	*Dolichospermum planctonicum (Anabaena planktonica) (Anabaena planctonica) (Anabaena solitaria f. planktonica) (Anabaena limnetica)*	PH71			AJ293108	1, end	N/A
10.1023/A:1004170230774	*Dolichospermum smithii (Anabaena smithii) (Anabaena solitaria f. smithii)*	TAC432			AY701555	1, end	N/A
10.1099/ijs.0.02270-0	*Dolichospermum solitarium (Anabaena solitaria)*	82			AJ293105	1, end	N/A
10.1023/A:1004170230774	*Dolichospermum solitarium (Anabaena solitaria)*	NIES 80			AY701552	1, end	N/A
10.1099/ijs.0.02270-0	*Dolichospermum spiroides (Anabaena spiroides)*	PMC 9403			AJ293116	1, end	N/A
10.1099/ijs.0.02270-0	*Dolichospermum spiroides (Anabaena spiroides)*	PMC 9702			AJ293118	1, end	N/A
10.1023/A:1004170230774	*Dolichospermum ucrainicum (Anabaena ucrainica)*	TAC448			AY701565	1, end	N/A
10.1023/A:1004170230774	*Dolichospermum ucrainicum (Anabaena ucrainica)*	TAC449			AB551448	1, end	N/A

10.5507/fot.2016.009	*Dolichospermum uruguayense*	7			KC297495	1, end	N/A
10.1007/bf00459526	*Ectothiorhodospira vacuolata*	BN 9512, DSM 2111, ATCC 43036			FR733667	1, end	N/A
ISBN 978-0-387-28022-6	*Enhydrobacter aerosaccus*	ATCC 27094, DSM 8914, LMG 81277	NZ_FUWJ01000001	1801118, 1810562	FUWJ01000012	96347, 94977	SAMN02745126_05622
10.1016/j.micres.2018.04.001	*Euhalothece sp.*	KZN 001	MDVL01001001	1, 6402	MDVL01000965	1, 1027	BEN50_00145
10.1007/BF00408695	*Gloeotrichia echinulata*	CCAP 1432/1			AF527469	1, end	N/A
10.1111/j.1529-8817.1970.tb02377.x	*Gloeotrichia ghosei*	Singh			N/A	N/A	N/A
ISBN 9780123858771	*Gomphosphaeria wichurae*				N/A	N/A	N/A
10.1016/j.femsle.2005.09.017	*Halobacterium salinarum (Halobacterium halobium)*	NRC-1, ATCC 700922	NC_001869	16352, 25404	AB663363	1, end	N/A
10.1016/j.femsle.2005.09.017	*Halobacterium salinarum (Halobacterium halobium)*	NRC-1, ATCC 700922	NC_002608	16352, 25404; 186102, 194522	N/A	N/A	N/A
10.1099/ijs.0.65034-0	*Halochromatium roseum*	JA134, ATCC BAA-1363, DSM 18859, JCM 14151			NR_042529	1, end	N/A
10.1016/S0723-2020(83)80021-6	*Haloferax mediterranei (Halobacterium mediterranei)*	ATCC 33500, DSM 1411, JCM 8866, NBRC 14739, NCIMB 2177, R-4	NC_017941	1616906, 1626364	AB663379	1, end	N/A
10.1099/002077-48-4-1305	*Halogeometricum borinquense*	DSM 11551, ATCC 700274	NC_014735	324827, 334073	NR_102892	1, end	N/A
10.1099/ijs.0.025023-0	*Haloplanus aerogenes*	TBN37, JCM 16430		no GV genes	AB663395	1, end	N/A
10.1099/ijs.0.64648-0	*Haloplanus natans*	RE-101, DSM 17983, JCM 14081	ATYM01000003	230153, 239037	AB663396	1, end	N/A
10.1099/ijs.0.018564-0	*Haloplanus vescus*	RO5-8, JCM 16055, CGMCC 1.8712		no GV genes	NR_113462	1, end	N/A
10.1099/ijs.0.64690-0	*Haloquadratum walsbyi*	C23, DSM 16854	NC_017459	971563, 982017	AY676200	1, end	N/A
10.1099/ijs.0.64690-0	*Haloquadratum walsbyi*	HBSQ001, DSM 16790	NC_008212	951771, 963172	NC_008212	67537, 69008	HQ_RS00290
10.1099/002077-43-3-401	*Halorubrum vacuolatum (Natronobacterium vacuolata)*	DSM 8800, NCIMB 13189, JCM 9060	FZNQ01000042	1, 7671	NR_113490	1, end	N/A
10.1007/BF02512379	*Hyalobonys hypolimnicus*	Skuja			N/A	N/A	N/A
10.4056/sigs.1533840	*Isosphaera pallida*	IS1B, ATCC 43644, DSM 9630	CP002353	1073765, 1080713	AJ231195	1, end	N/A
ISBN 978-0-387-21609-6	*Kamptonema formosum*	PCC 6407, ATCC 27906	NZ_KB235903	573051, 584292; 1589152, 1595268	AM398782	1, end	N/A
10.1128/JB.00704-10	*Kamptonema sp. (Oscillatoria sp.)*	PCC 6506, PCC 9029, UTEX 1547	CACA01000341	696, 7694	AY768397	1, end	N/A
10.1128/JB.00704-10	*Kamptonema sp. (Oscillatoria sp.)*	PCC 6506, PCC 9029, UTEX 1547	CACA01000221	10767, 15710	N/A	1, end	N/A
10.2307/3668091	*Katagnymene mucigera*				N/A	N/A	N/A
10.1111/j.1529-8817.2011.01096.x	*Katagnymene spiralis*	ZK			N/A	N/A	N/A
10.5507/fot.2018.012	*Lagosinema tenuis*	NGPC151			KU321243	1, end	N/A
10.1134/S0026261714060071	*Lamprobacter modestohalophilus*	Sivash, DSM 25653			HQ877095	1, end	N/A
10.1099/002077-51-5-1699	*Lamprocystis purpurea (Amoebobacter purpureus)*	DSM 4197, BN 4450, ThSch12	KB902538	1, 7956	AJ223235	1, end	N/A
10.1099/002077-51-5-1699	*Lamprocystis purpurea (Amoebobacter purpureus)*	DSM 4197, BN 4450, ThSch12	KB902499	1, 8518	N/A	1, end	N/A
10.1016/j.syapm.2012.01.001	*Lamprocystis roseopersicina*	DSM 229			NR_025288	1, end	N/A

10.1101/2020.12.12.422513	*Laspinema sp.*	PMC 878.14			MT984288	1, end	N/A
10.1099/00221287-111-1-1	*Leptolyngbya sp.*	ATCC 29125, PCC 7406			N/A	N/A	N/A
10.1099/00221287-111-1-1	*Leptolyngbya sp.*	ATCC 29165, PCC 7404			N/A	N/A	N/A
10.1099/00221287-111-1-1	*Leptolyngbya sp.*	ATCC 27913, PCC 7004			N/A	N/A	N/A
10.1099/00221287-111-1-1	*Leptolyngbya sp.*	ATCC 29122, PCC 7123			KJ708585	1, end	N/A
10.1099/00221287-111-1-1	*Leptolyngbya sp.*	ATCC 29123, PCC 7124			KJ708584	1, end	N/A
10.1111/jam.12961	*Leptolyngbya sp.*	KIOST-1	NZ_JQFA01000002	2009479, 2017739	JX401929	1, end	N/A
10.1099/00221287-111-1-1	*Leptolyngbya sp. (Pseudanabaena sp.)*	ATCC 29118, PCC 6406	NZ_KI913949	5007460, 5015106	NZ_KI913949	634665, 636157	LEP6406_RS02022910
Meffert, M.E., 1987. Planktic unsheathed filaments (Cyanophyceae) with polar and central gas-vacuoles. I: Their morphology and taxonomy. Archiv für Hydrobiologie. Supplementband. Monographische Beiträge, 76(4), pp.315-346.	*Leptolyngbya tenerrima (Oscillatoria tenerrima)*				AF218368	1, end	N/A
10.1080/01490458009377749	*Leptothrix pseudovacuolata (Spirothrix pseudovacuolata)*				N/A	N/A	N/A
10.5507/fot.2013.004	*Limnoraphis birgei*				EU586053	1, end	N/A
10.5507/fot.2013.004	*Limnoraphis cryptovaginata (Planktothrix cryptovaginata)*	3/Kutnar09			JN854139	1, end	N/A
10.5507/fot.2013.004	*Limnoraphis robusta (Lyngbya hieronymusii f. robusta)*	CCALA 966	LATL02000226	7952, 18451	JN854138	1, end	N/A
10.1080/09670262.2012.692817	*Limnospira indica*	PCC 8005	NZ_FO818640	2020403, 2025039; 2337062, 2338636; 2748477, 2748815	FO818640	809473, 810949	ARTHRO_16s_rRNA_1
10.1007/s10811-018-1392-7	*Limnothrix amphigranulata (Pseudanabaena amphigranulata) (Oscillatoria amphigranulata)*				KY550461	1, end	N/A
10.1007/s10750-012-1127-8	*Limnothrix planktonica*	CHAB709			JQ004021	1, end	N/A
10.1099/00207713-52-5-1577	*Limnothrix redekei (Oscillatoria redekei)*	NIVA CYA 277/1, NIES 847			AB045929	1, end	N/A
Meffert, M.E., 1988. Limnothrix Meffert nov. gen. The unsheathed planktic cyanophycean filaments with polar and central gas vacuoles. Algological Studies/Archiv für Hydrobiologie, Supplement Volumes, pp.269-276	*Limnothrix rosea (Oscillatoria rosea)*			no GV genes	AB003164	1, end	N/A
Meffert, M.E., 1987. Planktic	*Lyngbia brachynema*	Skuja			N/A	N/A	N/A

unsheathed filaments (Cyanophyceae) with polar and central gas-vacuoles. I: Their morphology and taxonomy. Archiv für Hydrobiologie. Supplementband. Monographische Beiträge, 76(4), pp.315-346.							
10.1590/S2236-89062007000100002	*Lyngbya hieronymusii (Limnoraphis hieronymusii)*	N-929			JN854140	1, end	N/A
10.1101/2020.12.12.422513	*Lyngbya martensiana*	PMC 880.14			MT984286	1, end	N/A
http://www.journalcra.com/sites/default/files/issue-pdf/8654.pdf	*Lyngbya vacuolifera*	Skuja, BTA-1051			N/A	N/A	N/A
https://aem.asm.org/content/61/9/3486.long	*Marinobacter sp.*	S36-W<gv>1			U14584	1, end	N/A
10.1099/00207713-27-1-38	*Meniscus glaucopis*	V, ATCC 29398			NR_104837	1, end	N/A
ISBN 978-0-387-21609-6	*Methanosaeta thermophila (Methanothrix thermoacetophila)*	PT, DSM 6194, OCM 780	CP000477	46739, 61479	NR_074214	1, end	N/A
10.1099/00221287-130-1-167	*Methanosarcina barkeri*	DSM 804, Fusaro	NC_007355	384816, 395668	NC_007355	1142958, 1141481	MBAR_RS05085
10.1099/00207713-37-3-281	*Methanosarcina vacuolata*	Z-761, DSM 1232, OCM 85, ATCC 35090	NZ_CP009520	3958045, 3967318	NR_104728	1, end	N/A
ISBN 978-0-387-28022-6	*Methylobacter psychrophilus*	Z-0021, VKM B-2103			AF152597	1, end	N/A
ISBN 978-0-387-28022-6	*Methylosphaera hansonii*	AM6, ACAM 549			U67929	1, end	N/A
10.1101/2020.12.12.422513	*Microcoleus vaginatus*	PMC 879.14			MT984285	1, end	N/A
10.1128/AEM.72.2.1239-1247.2006	*Microcystis aeruginosa*	NIES 298	CP046058	3147505, 3162702	AB023261	1, end	N/A
10.1007/s11270-018-4010-z	*Microcystis aeruginosa*	NIES 843	NC_010296	3398250, 3411674	NR_074314	1, end	N/A
10.1128/JB.186.8.2355-2365.2004 ; 10.1016/j.femsle.2005.04.026	*Microcystis aeruginosa*	PCC 7806	NZ_CP020771	1899779, 1908527	AF139299	1, end	N/A
10.1128/AEM.02634-16	*Microcystis aeruginosa*	PCC 7941	HE973144	71994, 79394	AJ133171	1, end	N/A
10.1007/s12640-010-9177-z	*Microcystis aeruginosa*	SPC 777	NZ_ASZQ01000261	11049, 18730	EF121241	1, end	N/A
10.1099/00207713-47-3-693	*Microcystis aeruginosa*	NIES 89			U03403	1, end	N/A
10.1099/00207713-47-3-693	*Microcystis aeruginosa*	NIES 98	NZ_MDZH01000371	78000, 85110	D89032	1, end	N/A
10.1099/00207713-47-3-693	*Microcystis aeruginosa*	PCC 7820			AF139300	1, end	N/A
10.1128/JB.186.8.2355-2365.2004	*Microcystis aeruginosa*	PCC 9354			N/A	N/A	N/A
10.1590/S0100-84042004000200002	*Microcystis botrys*	SPC 758			KJ818202	1, end	N/A
10.1099/00207713-47-3-693	*Microcystis elabens*	NIES 42			U40335	1, end	N/A
10.1093/plankt/fbm054	*Microcystis flos-aquae*				AF139327	1, end	N/A
10.1099/00207713-47-3-693	*Microcystis holsatica*	NIES 43			U40336	1, end	N/A
10.1038/srep37056	*Microcystis ichthyoblabe*				AB012339	1, end	N/A
10.5829/idosi.ejbs.2015.7.04.1109	*Microcystis marginata*				N/A	N/A	N/A
10.1590/S0100-84042004000200002	*Microcystis novacekii*	SPC 503			AB012336	1, end	N/A

10.1590/S0100-84042004000200002	*Microcystis panniformis*	SPC 686			AB666074	1, end	N/A
https://www.researchgate.net/profile/Jaroslava_Komarkova/publication/284263344_Review_of_the_European_Microcystis-morphospecies_Cyanoprokaryotes_from_nature/links/572b6a2808ae057b0a095174/Review-of-the-European-Microcystis-morphospecies-Cyanoprokaryotes-from-nature.pdf	*Microcystis panniformis*	SPC 702			N/A	N/A	N/A
https://www.researchgate.net/profile/Jaroslava_Komarkova/publication/284263344_Review_of_the_European_Microcystis-morphospecies_Cyanoprokaryotes_from_nature/links/572b6a2808ae057b0a095174/Review-of-the-European-Microcystis-morphospecies-Cyanoprokaryotes-from-nature.pdf	*Microcystis protocystis*	CCALA 106-1			N/A	N/A	N/A
https://www.researchgate.net/profile/Jaroslava_Komarkova/publication/284263344_Review_of_the_European_Microcystis-morphospecies_Cyanoprokaryotes_from_nature/links/572b6a2808ae057b0a095174/Review-of-the-European-Microcystis-morphospecies-Cyanoprokaryotes-from-nature.pdf	*Microcystis protocystis*	SPC 618			N/A	N/A	N/A
10.1590/S0100-84042004000200002	*Microcystis protocystis*	SPC 698, SPC 522			AB666054	1, end	N/A
10.1080/0028825X.2005.9512969	*Microcystis smithii*				GQ496076	1, end	N/A
10.1099/002212877-138-6-1243	*Microcystis sp.*	CCAP 1450/13			HE975021	1, end	N/A
10.1016/j.femsle.2005.04.026	*Microcystis sp.*	BC 8401, CCAP 1450/30	AY965344	1, 7153	N/A	N/A	N/A
10.1002/1873-3468.12370	*Microcystis sp.*	FACHB-930	DQ888810	1, 2480	N/A	N/A	N/A
10.1099/002077137-47-3-693	*Microcystis viridis*	NIES 102	AP019314	1312632, 1320126	DQ648027	1, end	N/A
10.1590/S0100-84042004000200002	*Microcystis wesenbergii*	Komárek			AB012334	1, end	N/A
10.1099/002077137-47-3-693	*Microcystis wesenbergii*	NIES 107			U40333	1, end	N/A
10.1099/002077137-47-3-693	*Microcystis wesenbergii*	NIES 112			U40334	1, end	N/A
10.1016/j.vmpev.2017.12.009	*Neolyngbya arenicola*	ALCB 114386			MF190466	1, end	N/A
10.1016/j.vmpev.2017.12.009	*Neolyngbya granulosa*	ALCB 114378			KY824053	1, end	N/A

10.1016/j.ympev.2017.12.009	*Neolyngbya irregularis*	ALCB 114382			KY824054	1, end	N/A
10.1016/j.ympev.2017.12.009	*Neolyngbya maris-brasilis*	ALCB 114380			KY824056	1, end	N/A
10.1016/j.ympev.2017.12.009	*Neolyngbya nodulosa*	ALCB 114383			KY824057	1, end	N/A
10.1016/j.ympev.2017.12.009	*Neolyngbya tenuis*	ALCB 114390			MF190467	1, end	N/A
10.2216/06-92.1	*Nodularia baltica*	BY1			AJ133177	1, end	N/A
10.1128/AEM.67.10.4638-4647.2001	*Nodularia litorea*				N/A	N/A	N/A
10.1099/00221287-148-2-481	*Nodularia sp.*	PCC 9350			AY038034	1, end	N/A
10.1099/00221287-148-2-481	*Nodularia sp.*	BCNOD9427			AJ224447	1, end	N/A
10.1099/00221287-148-2-481	*Nodularia sp.*	NSPI-05			AJ133179	1, end	N/A
10.1371/journal.pone.0060224	*Nodularia spumigena*	CCY9414	NZ_CP007203	1573331, 1579947	CP007203	5061534, 5060053	NSP_49810
Canabaeus, L. 1929. Über die Heterocysten und Gasvakuolen der Blaualgen und ihre Beziehung zueinander. Pflanzenforschung 13:1–48.	*Nostoc linckia*				AB074503	1, end	N/A
10.1111/j.0022-3646.1995.00002.x	*Nostoc pruniforme*				KY550450	1, end	N/A
10.1099/00221287-111-1-1	*Nostoc punctiforme*	ATCC 29133, PCC 73102	CP001037	2617497, 2629446	NR_074317	1, end	N/A
10.1099/00221287-111-1-1	*Nostoc sp.*	ATCC 29105, PCC 6719, CCAP 1453/32			HF678482	1, end	N/A
10.1128/jb.171.3.1445-1452.1989	*Nostoc sp.*	PCC 8009			N/A	N/A	N/A
10.1099/00221287-111-1-1	*Nostoc sp.*	ATCC 29131, PCC 6705			N/A	N/A	N/A
10.1099/ijs.0.02270-0	*Nostoc sp. (Anabaena sp.)*	299			AJ293106	1, end	N/A
10.1099/ijs.0.02270-0	*Nostoc sp. (Anabaena sp.)*	IC-1			AJ293120	1, end	N/A
10.1186/s12866-020-01805-8	*Nostoc sp. (Anabaena sp.)*	PCC 6411, ATCC 27898			N/A	N/A	N/A
10.1186/s12866-020-01805-8	*Nostoc sp. (Anabaena sp.)*	PCC 7118, ATCC 27892			N/A	N/A	N/A
10.1186/s12866-020-01805-8	*Nostoc sp. (Anabaena sp.)*	PCC 7119, ATCC 29151			N/A	N/A	N/A
10.1186/s12866-020-01805-8	*Nostoc sp. (Anabaena sp.)*	PCC 7120, ATCC 27347, FACHB-418	BA000019	2700304, 2707131	AF317631	1, end	N/A
10.1016/S0022-5320(69)90027-6	*Nostoc sphaericum*				MH702223	1, end	N/A
https://aem.asm.org/content/61/9/3486.long	*Octadecabacter antarcticus*	307, CIP 106732	NC_020911	3023786, 3033322	NR_102908	1, end	N/A
ISBN 978-0-387-29298-4	*Octadecabacter arcticus*	238	NC_020910	62360, 71931	NR_102905	1, end	N/A
10.1007/b92997	*Orenia sivashensis*	Z-7191, DSM 12596			NR_028752	1, end	N/A
10.1080/00071618100650091	*Oscillatoria acutissima*	Kuff			N/A	N/A	N/A
10.1007/BF02512379	*Oscillatoria breviarticulata*				N/A	N/A	N/A
10.2307/3668091	*Oscillatoria lacustris (Trichodesmium lacustre)*	Kleb			N/A	N/A	N/A
Meffert, M.E., 1987. Planktic unsheathed filaments (Cyanophyceae) with polar and central gas-vacuoles. I: Their morphology and taxonomy. Archiv für Hydrobiologie. Supplementban	*Oscillatoria lauterbornii*				N/A	N/A	N/A

d. Monographische Beiträge, 76(4), pp.315-346.							
10.1080/00071618100650091	*Oscillatoria obliqueacuminata (Limnothrix obliqueacuminata)*	Skuja			N/A	N/A	N/A
Shinke, N., and K. Ueda, 1956. A cytomorphological and cytochemical study of Cyanophyta. 1. An electronn microscope study of Oscillatoria princeps. Mem. Coll. Sci. Univ. Kyoto, Ser. B 13:101-104	*Oscillatoria princeps*	NIVA CYA 150			AB045961	1, end	N/A
10.1080/00071618100650091	*Oscillatoria putrida*	Schmidle			N/A	N/A	N/A
10.1128/jb.171.3.1445-1452.1989	*Oscillatoria sp.*	PCC 6412, ATCC 29205			N/A	N/A	N/A
ISBN 978-0-387-21609-6	*Oscillochloris chrysea*				N/A	N/A	N/A
10.1099/00207713-50-4-1529	*Oscillochloris trichoides*	DG-6	GL501404	1828463, 1835489	AF093427	1, end	N/A
10.1099/ijs.0.02403-0	*Pelodictyon clathratiforme (Chlorobium clathratiforme)*	PG			Y08106	1, end	N/A
10.1099/ijs.0.02403-0	*Pelodictyon luteolum (Chlorobium luteolum)*	2532, DSM 273	NC_007512	802617, 820127	NR_074096	1, end	N/A
10.1007/BF02512379	*Pelodictyon parallelum*				N/A	N/A	N/A
10.1007/BF00245331	*Pelodictyon phaeoclathratiforme*	BU-1, DSM 5477	NC_011060	1909025, 1922810	NR_074365	1, end	N/A
ISBN 978-0-387-21609-6	*Pelodictyon phaeum*	WS-6, DSM 728			AJ291828	1, end	N/A
10.1007/BF02512379	*Pelonema pseudovacuolatum*	Lauterborn			N/A	N/A	N/A
10.1007/BF02512379	*Pelonema spirale*	Lauterborn			N/A	N/A	N/A
10.1007/BF02512379	*Pelonema subtilissimum*	Skuja			N/A	N/A	N/A
10.1007/BF02512379	*Peloploca taeniata*	Lauterborn			N/A	N/A	N/A
10.1007/BF02512379	*Peloploca undulatum*				N/A	N/A	N/A
10.1038/srep41181	*Plankthotrix sp.*	PCC 11201	NZ_LT797710	41379, 44905	CZCT02000086	40493, 41971	PL11201_16S_RRNA_5
10.1590/S2236-89062007000100002	*Planktothricoides attenuata*				N/A	N/A	N/A
10.1101/2020.12.12.422513	*Planktothricoides raciborskii (Oscillatoria raciborskii)*	PMC 877.14			MT984287	1, end	N/A
10.1099/00207713-52-5-1577	*Planktothricoides raciborskii (Oscillatoria raciborskii)*	NIES 207, CCAP 1465/1			AB045960	1, end	N/A
10.1186/s40793-017-0247-1	*Planktothricoides sp.*	SR001	LIUQ01000005	93290, 97610	LIUQ01000113	5065, 3569	AM228_28330
10.1186/s40793-017-0247-1	*Planktothricoides sp.*	SR001	LIUQ01000135	1, 2389	N/A	N/A	N/A
10.1038/srep41181	*Planktothrix agardhii (Oscillatoria agardhii)*	PCC 7805, NIVA-CYA 68	LO018304	1665879, 1668157; 3563076, 3566188	GQ351563	1, end	N/A
10.1099/00207713-52-5-1577	*Planktothrix agardhii (Oscillatoria agardhii)*	NIES 204, CCAP 1460/5, PCC 10704	AP017991	2814932, 2825057; 3326168, 3327407; 3673205, 3677503	AB045954	1, end	N/A

10.1016/j.syapm.2015.02.004	*Planktothrix agardhii (Oscillatoria agardhii)*	NIES 905, CCAP 1459/11A	BJCD01000030	48795, 51951	LC455659	1, end	N/A
10.1016/j.syapm.2015.02.004	*Planktothrix agardhii (Oscillatoria agardhii)*	NIES 905, CCAP 1459/11A	BJCD01000057	57907, 58593	N/A	N/A	N/A
10.1016/j.syapm.2015.02.004	*Planktothrix agardhii (Oscillatoria agardhii)*	NIES 905, CCAP 1459/11A	BJCD01000062	111, 461	N/A	N/A	N/A
10.1016/j.syapm.2015.02.004	*Planktothrix agardhii (Oscillatoria agardhii)*	NIES 905, CCAP 1459/11A	BJCD01000096	3870, 5085	N/A	N/A	N/A
10.1016/j.syapm.2015.02.004	*Planktothrix agardhii (Oscillatoria agardhii)*	NIES 905, CCAP 1459/11A	BJCD01000124	151, 690	N/A	N/A	N/A
10.1016/j.syapm.2015.02.004	*Planktothrix agardhii (Oscillatoria agardhii)*	NIES 905, CCAP 1459/11A	BJCD01000139	62, 412	N/A	N/A	N/A
10.1099/00221287-138-6-1243	*Planktothrix agardhii (Oscillatoria agardhii)*	NIVA-CYA 29	AJ253130	1, 591	AB045931	1, end	N/A
10.1099/00221287-138-6-1243	*Planktothrix agardhii (Oscillatoria agardhii)*	NIVA-CYA 29	AJ494992	221, 943	N/A	N/A	N/A
10.1099/00221287-138-6-1243	*Planktothrix agardhii (Oscillatoria agardhii)*	CCAP 1459/36			AB045903	1, end	N/A
10.1099/00221287-146-8-2009	*Planktothrix agardhii (Oscillatoria agardhii)*	NIVA-CYA 15	NZ_KE734694	1535278, 1538652	AB045923	1, end	N/A
10.1016/j.syapm.2015.02.004	*Planktothrix agardhii (Oscillatoria agardhii)*	PCC 10110			GQ351573	1, end	N/A
10.1016/j.syapm.2015.02.004	*Planktothrix agardhii (Oscillatoria agardhii)*	PCC 10606			GQ995002	1, end	N/A
10.1016/j.syapm.2015.02.004	*Planktothrix agardhii (Oscillatoria agardhii)*	PCC 10607			GQ995003	1, end	N/A
10.1016/j.syapm.2015.02.004	*Planktothrix agardhii (Oscillatoria agardhii)*	PCC 7811			AY768402	1, end	N/A
10.1016/j.syapm.2015.02.004	*Planktothrix agardhii (Oscillatoria agardhii)*	PCC 9239			GQ351567	1, end	N/A
10.1016/j.syapm.2015.02.004	*Planktothrix agardhii (Oscillatoria agardhii)*	PCC 9625			GQ351568	1, end	N/A
10.1016/j.syapm.2015.02.004	*Planktothrix agardhii (Oscillatoria agardhii)*	PCC 9637			GQ351569	1, end	N/A
10.1016/j.syapm.2015.02.004	*Planktothrix agardhii (Oscillatoria agardhii)*	PCC 9702			GQ351570	1, end	N/A
10.1016/j.syapm.2015.02.004	*Planktothrix agardhii (Oscillatoria agardhii)*	PCC 9801			GQ351571	1, end	N/A
10.1007/s12038-014-9458-4	*Planktothrix clathrata*	PUPCCC 108.8			KM384750	1, end	N/A
10.1099/ijs.0.01834-0	*Planktothrix mougeotii*	TR1-5, NIES 844, CCAP 1460/6			NR_112129	1, end	N/A
10.1016/j.syapm.2015.02.004	*Planktothrix paucivesiculata*	PCC 9631	NZ_LR735018	445911, 449537	GQ351578	1, end	N/A
10.1016/j.syapm.2015.02.004	*Planktothrix paucivesiculata*	PCC 9631	LR735026	45660, 48299; 186188, 187253	N/A	1, end	N/A
10.1016/j.syapm.2015.02.004	*Planktothrix paucivesiculata*	M201, PCC 8926, NIES 2668			GQ351574	1, end	N/A

10.1016/j.syapm.2015.02.004	*Planktothrix paucivesiculata*	PCC 8954			GQ351576	1, end	N/A
Komárek, J., & Komárková, J. (2004). Taxonomic review of the cyanoprokaryotic genera Planktothrix and Planktothricoides . Fottea, 4(1), 1-18.	*Planktothrix prolifica (Oscillatoria prolifica)*				Z82798	1, end	N/A
10.1099/002077-13-52-5-1577	*Planktothrix pseudagardhii*	T1-8-4, NIES 845, CCAP 1460/7			AB045968	1, end	N/A
10.1099/002212-87-146-8-2009	*Planktothrix rubescens*	PCC 7821, NIVA-CYA 18, CCAP 1459/22, NIES 610	CZCZ01000006	559374, 562384	AB045901	1, end	N/A
10.1016/j.syapm.2015.02.004	*Planktothrix rubescens*	PCC 10106			GQ351572	1, end	N/A
10.1016/j.syapm.2015.02.004	*Planktothrix rubescens*	CCAP 1459/30			GQ994995	1, end	N/A
10.1016/j.syapm.2015.02.004	*Planktothrix rubescens*	CCAP 1459/40			HE974999	1, end	N/A
10.1016/j.syapm.2015.02.004	*Planktothrix rubescens*	CCAP 1460/10			GQ994997	1, end	N/A
10.1016/j.syapm.2015.02.004	*Planktothrix rubescens*	CCAP 1460/18			HF678490	1, end	N/A
10.1016/j.syapm.2015.02.004	*Planktothrix rubescens*	NIES 1266			GQ995001	1, end	N/A
10.1016/j.syapm.2015.02.004	*Planktothrix rubescens*	NIES 928, CCAP 1459/14			GQ995000	1, end	N/A
10.1016/j.syapm.2015.02.004	*Planktothrix serta*	M220, PCC 8927, NIES 2869	CZCU02000129	41851, 47847	GQ351575	1, end	N/A
10.1016/j.syapm.2015.02.004	*Planktothrix serta*	M220, PCC 8927, NIES 2869	CZCU02000130	153908, 156179	N/A	N/A	N/A
10.1016/j.syapm.2015.02.004	*Planktothrix serta*	M220, PCC 8927, NIES 2869	CZCU02000137	77575, 78264	N/A	N/A	N/A
10.1016/j.syapm.2015.02.004	*Planktothrix sp.*	PCC 9018			GQ351577	1, end	N/A
https://pubs.usgs.gov/of/2017/1054/ofr20171054.pdf	*Planktothrix suspensa*				LC037449	1, end	N/A
10.1016/j.syapm.2015.02.004	*Planktothrix tepida*	4d.1, PCC 9214, NIES 2870	CZDF01000171	618285, 625167	GQ351566	1, end	N/A
10.1016/j.syapm.2015.02.004	*Planktothrix tepida*	4d.1, PCC 9214, NIES 2870	CZDF01000172	647761, 649593	N/A	N/A	N/A
10.1016/j.syapm.2015.02.004	*Planktothrix tepida*	4d.1, PCC 9214, NIES 2870	CZDF01000132	466050, 469171	N/A	N/A	N/A
Komárek, J., & Komárková, J. (2004). Taxonomic review of the cyanoprokaryotic genera Planktothrix and Planktothricoides . Fottea, 4(1), 1-18.	*Planktothrix zahidii (Oscillatoria zahidii)*				N/A	N/A	N/A
10.1099/002077-13-48-1-223	*Polaribacter filamentus*	215, ATCC 700397	MQUA01000013	1735921, 1756703	NR_026041	1, end	N/A
10.1099/002077-13-48-1-223	*Polaribacter franzmannii*	301, ATCC 700399			U14586	1, end	N/A
10.1099/002077-13-48-1-223	*Polaribacter irgensii*	23-P, ATCC 700398	AAOG01000001	187691, 209325	NR_044733	1, end	N/A
10.1099/002077-13-46-3-822	*Polaromonas vacuolata*	34-P, ATCC 51984, KCTC 22033	CP051461	2063927, 2077871	NR_025958	1, end	N/A
10.3389/fmicb.2012.00173	*Prochlorothrix hollandica*	PCC 9006, CALU 1027, SAG 10.89	AJTX02000006	784832, 793067	NR_126312	1, end	N/A
10.1007/s00203-019-01707-y	*Prosthecochloris marina*	V1	NZ_PDNZ01000003	193529, 205094	MF423475	1, end	N/A
10.1007/BF00425125	*Prosthecomicrobium pneumaticum*	DSM 16268, 3a, ATCC 23633			NR_040791	1, end	N/A
10.1099/002212-87-111-1-1	*Pseudanabaena biceps*	ATCC 29536, PCC 7429	ALWB01000068	21090, 23750	ALWB01000102	7448, 8921	Pse7429DRAFT_R0029
10.1099/002212-87-111-1-1	*Pseudanabaena biceps*	ATCC 29536, PCC 7429	ALWB01000008	31589, 32341	N/A	N/A	N/A
10.1099/002212-87-111-1-1	*Pseudanabaena biceps*	ATCC 29536, PCC 7429	ALWB01000015	17755, 18222	N/A	N/A	N/A

10.1099/00221287-111-1-1	*Pseudanabaena biceps*	ATCC 29536, PCC 7429	ALWB01000027	1967, 2194	N/A	N/A	N/A
10.1099/00221287-111-1-1	*Pseudanabaena biceps*	ATCC 29536, PCC 7429	ALWB01000029	2577, 3269	N/A	N/A	N/A
10.1099/00221287-111-1-1	*Pseudanabaena biceps*	ATCC 29536, PCC 7429	ALWB01000113	17223, 17579	N/A	N/A	N/A
10.1099/00221287-111-1-1	*Pseudanabaena biceps*	ATCC 29536, PCC 7429	ALWB01000158	6137, 6505	N/A	N/A	N/A
10.2216/10-097.1	*Pseudanabaena catenata*	SAG 254.80			KM020004	1, end	N/A
10.1080/00071618100650091	*Pseudanabaena constricta*				N/A	N/A	N/A
10.5507/fot.2016.006	*Pseudanabaena foetida*	PTG			LC016773	1, end	N/A
10.1007/s12038-014-9458-4	*Pseudanabaena frigida*	PUPCCC 106.7			KJ705103	1, end	N/A
10.1002/9781118960608.gbm00444	*Pseudanabaena galeata*	ATCC 27263, PCC 6901	X57731	1, 2885	N/A	N/A	N/A
10.1002/9781118960608.gbm00444	*Pseudanabaena galeata*	ATCC 27190, PCC 6903			AB039017	1, end	N/A
10.1002/9781118960608.gbm00444	*Pseudanabaena galeata*	ATCC 29207, PCC 7402			N/A	N/A	N/A
10.2166/ws.2016.068	*Pseudanabaena galeata*	CCCOL-75-PS			HQ658458	1, end	N/A
10.1099/00221287-111-1-1	*Pseudanabaena sp.*	ATCC 27183, PCC 6802	NZ_KB235914	781295, 781534; 1216721, 1217464; 2179661, 2182870; 2870858, 2874046	AB039016	1, end	N/A
10.1099/00221287-111-1-1	*Pseudanabaena sp.*	ATCC 29210, PCC 7403			AB039019	1, end	N/A
10.1128/jb.171.3.1445-1452.1989	*Pseudanabaena sp.*	PCC 7955			N/A	N/A	N/A
10.1099/00221287-111-1-1	*Pseudanabaena sp. (Calotaxis gracile)*	ATCC 29137, PCC 7367	CP003592	309523, 309768; 1028155, 1032152; 1138919, 1139368; 1766647, 1767330; 2490950, 2491687	AB039018	1, end	N/A
10.5507/fot.2016.006	*Pseudanabaena subfoetida*	PS1306			LC016779	1, end	N/A
10.1099/ijs.0.007773-0	*Psychromonas boydii*	174, DSM 17665, CCM 7498			NR_116830	1, end	N/A
10.1099/ijs.0.64068-0	*Psychromonas ingrahamii*	37	NC_008709	1553442, 1570477; 2124885, 2134437	NR_074862	1, end	N/A
https://aem.asm.org/content/61/9/3486.long	*Psychromonas sp.*	90-P(gv)1			U14582	1, end	N/A
10.1590/S0100-84042004000200002	*Radiocystis fernandoi*	Komárek			N/A	N/A	N/A
10.2216/17-2.1	*Raphidiopsis mediterranea*				N/A	N/A	N/A
10.1590/S0100-84042004000200002	*Rhabdoderma lineare (Synechococcus linearis)*	Lauterborn			N/A	N/A	N/A
10.1128/JB.00678-19	*Rhodobacter sphaeroides*	WS8N	NZ_CM001162	920504, 930876	NZ_CM001161	2607969, 2609435	RSWS8N_RS12465
10.1007/s00203-004-0719-8	*Rhodoferax antarcticus*	Fryx1			AY609198	1, end	N/A
10.1111/1462-2920.13203	*Serratia sp.*	ATCC 39006	CP025084	259501, 276334	NZ_CP025084	206120, 204578	Ser39006_000940
10.1590/S0100-84042004000200002	*Sphaerocavum brasiliense*	SPC 484			KY460542	1, end	N/A
10.1111/j.1529-8817.2009.00758.x	*Sphaerospermopsis aphanizomenoides (Aphanizomenon aphanizomenoides)*	04-43			FM161350	1, end	N/A
10.2216/16-70.1	*Sphaerospermopsis crassa*	CHAB 4404			KT583658	1, end	N/A
10.1023/A:1004170230774	*Sphaerospermopsis eucompacta*	Ana Chiba			GU197646	1, end	N/A

	(Anabaena eucompacta)						
10.1023/A:1004170230774	*Sphaerospermopsis kisseleviana (Anabaena kisseleviana)*	NIES 74	NZ_AP018314	1529964, 1540809	NZ_AP018314	1832860, 1834353	CA728_RS08370
10.1023/A:1004170230774	*Sphaerospermopsis kisseleviana (Anabaena kisseleviana)*	TAC34			AY701557	1, end	N/A
10.1023/A:1004170230774	*Sphaerospermopsis oumiana (Anabaena oumiana)*	NIES 73			GU197635	1, end	N/A
10.1111/j.1529-8817.2009.00758.x	*Sphaerospermopsis reniformis (Anabaena reniformis) (Sphaerospermum reniforme)*	06-01, SAG 2284, CCALA 862			FM161348	1, end	N/A
10.2216/11-32.1	*Sphaerospermopsis torques-reginae*	ITEP-024			HQ730086	1, end	N/A
10.2216/11-32.1	*Sphaerospermopsis torques-reginae*	ITEP-026			HQ730087	1, end	N/A
PMID: 17483796	*Spirulina platensis (Arthrospira platensis)*	NIES 39, IAM M-135, IAM M-222	NC_016640	2356082, 2375411; 3210401, 3236987; 5355891, 5365254	DQ393279	1, end	N/A
PMID: 17483796	*Spirulina platensis (Arthrospira platensis)*	NIES 46, IAM M-185	NZ_BIMW01000127	464, 1147	LC455668	1, end	N/A
PMID: 17483796	*Spirulina platensis (Arthrospira platensis)*	NIES 46, IAM M-185	NZ_BIMW01000189	1668, 3242	N/A	N/A	N/A
PMID: 17483796	*Spirulina platensis (Arthrospira platensis)*	NIES 46, IAM M-185	NZ_BIMW01000238	419, 637	N/A	N/A	N/A
PMID: 17483796	*Spirulina platensis (Arthrospira platensis)*	NIES 46, IAM M-185	NZ_BIMW01000067	180, 2338	N/A	N/A	N/A
10.1099/00221287-138-6-1243	*Spirulina sp.*	CCAP 1475/10			N/A	N/A	N/A
10.1007/bf00415608	*Sporohalobacter lortetii (Clostridium lortetii)*	MD-2, ATCC 35059, DSM 3070			NR_117602	1, end	N/A
10.1099/002077-13-35-4-518	*Stella vacuolata*	ATCC 43931, DSM 5901, INMI 229, VKM B-1552	AP019702	1386832, 1401316	NR_025583	1, end	N/A
10.1007/s00253-019-09891-z	*Streptomyces sp.*	CB03234	NZ_LIYH01000003	96350, 99749	KT722842	1, end	N/A
10.1007/s002030050273	*Syntrophobacter pfennigii*	KoProp1, DSM 10092			NR_026232	1, end	N/A
10.1016/j.syapm.2012.01.001	*Thiocapsa pendens (Amoebobacter pendens)*	DSM 236			NR_114686	1, end	N/A
10.1016/j.syapm.2012.01.001	*Thiocapsa rosea (Amoebobacter roseus, Rhodothece conspicua)*	DSM 235	NZ_RBXL01000001	3920612, 3935908	NR_114687	1, end	N/A
10.1016/j.syapm.2012.01.001	*Thiodictyon bacillosum (Amoebobacter bacillosus, Rhodocapsa suspensa, Rhabdomonas gracilis)*	DSM 234			NR_044364	1, end	N/A
10.1016/j.syapm.2012.01.001	*Thiodictyon elegans*	DSM 232			NR_044363	1, end	N/A
10.1016/j.syapm.2012.01.001	*Thiodictyon syntrophicum*	Cad16	CP020370	2823407, 2834709; 4492646, 4496420	AJ511274	1, end	N/A
10.1007/bf00403233	*Thiolamprovum pedioforme*	CML2, DSM 3802			NR_026414	1, end	N/A

ISBN 978-0-387-28022-6	*Thiopedia rosea*	4711, DSM 1236			N/A	N/A	N/A
Canabaeus, L. 1929. Über die Heterocysten und Gasvakuolen der Blaualgen und ihre Beziehung zueinander. Pflanzenforschung 13:1–48.	*Tolypothrix rivularis*				N/A	N/A	N/A
10.1099/00221287-111-1-1	*Tolypothrix sp.*	ATCC 29158, PCC 7504			AM230669	1, end	N/A
10.1099/00221287-134-10-2635	*Tolypothrix sp. (Fremyella diplosiphon)*	PCC 7601, UTEX 481	JH930362	402591, 408790	NZ_JH930368	243192, 244681	FDUTEX481_03748
10.1099/00221287-111-1-1	*Tolypothrix tenuis*	ATCC 27914, PCC 7101	AP018248	3367189, 3369533; 5949288, 5959254	AB325535	1, end	N/A
10.1590/2175-7860201869433	*Trichodesmium brasiliense*				N/A	N/A	N/A
10.1590/S2236-89062007000100002	*Trichodesmium cf. lacustre*				N/A	N/A	N/A
10.1111/j.1529-8817.2011.01096.x	*Trichodesmium contortum*	20-70			HM486742	1, end	N/A
10.1111/j.1529-8817.2011.01096.x	*Trichodesmium contortum*	21-74			HM486743	1, end	N/A
10.1111/j.1529-8817.2011.01096.x	*Trichodesmium erythraeum*	21-75	available, new one expected		HM486748	1, end	N/A
10.1111/j.1529-8817.2011.01096.x	*Trichodesmium erythraeum*	IMS101	NC_008312	3597390, 3616766	AF013030	1, end	N/A
10.1111/j.0022-3646.1995.00463.x	*Trichodesmium hildebrandtii*				AF091322	1, end	N/A
10.1111/j.1529-8817.2011.01096.x	*Trichodesmium pelagicum*	20-71			AF518769	1, end	N/A
10.1111/j.1529-8817.2011.01096.x	*Trichodesmium tenue*	Z-1			AF013029	1, end	N/A
10.1111/j.1529-8817.2011.01096.x	*Trichodesmium thiebautii*	H9-4	LAMW01000069	1, 20609	AF013027	1, end	N/A
ISBN 978-0-387-21609-6, ISBN 978-3-642-32781-0	*Trichormus variabilis (Anabaena variabilis)*	ATCC 29413, PCC 7937	NC_007413	93053, 101815	HF678501	1, end	N/A
10.5507/fot.2011.016	*Umezakia natans*	TAC611, NIES 2665			AB608023	1, end	N/A
10.1515/pbj-2017-0020	*Woronichinia karelica*				N/A	N/A	N/A
ISBN 9780123858771	*Woronichinia klingae*				N/A	N/A	N/A
10.1111/j.1529-8817.2006.00179.x	*Woronichinia naegeliana (Coelosphaerium naegelianum)*	0LE35S01			AJ781043	1, end	N/A

Table S2.2 | Genomic primers

Organism Name	Source	NCBI Accession Number	Primer Name	Primer Sequence
Anabaena flos-aquae (Dolichospermum flos-aquae)	CCAP 1403/13F	CP051206.1	pET28a-Anabaena flos-aquae_F1	GTGAGCGGATAACAATTCCcatgactcatatttatagttattctcctcatttccc
			pET28a-Anabaena flos-aquae_R1	GAGGCCCCAAGGGGTTATGCTAGctaaataaagtggtaaggaggaagacaatctc
Bacillus megaterium	ATCC 19213	CP047699.1	pET28a-Bacillus megaterium_F1	GGGGAATTGTGAGCGGATAACAATTCCgttaagcaggttcattagtagcatcattc
			pET28a-Bacillus megaterium_R1	CCCGTTTAGAGGCCCCAAGGGGTTATGCTAGgctgcacatctcatcacatcac
Desulfobacterium vacuolatum	DSM 3385	FWXY01000008.1	pET28a-Desulfobacterium vacuolatum_F1	TCACTATAGGGGAATTGTGAGCGGATAACAATTCCgccatgggccagaagtttc
			pET28a-Desulfobacterium vacuolatum_R1	caatcctcttcaagggcttttc
			pET28a-Desulfobacterium vacuolatum_F2	cagagatgatcctgcaatcagaaaag
			pET28a-Desulfobacterium vacuolatum_R2	GACCCGTTTAGAGGCCCCAAGGGGTTATGCTAGggttagatgccatgataaattcctcc
Desulfotomaculum acetoxidans	DSM 771	CP001720.1	pET28a-Desulfotomaculum acetoxidans_F1	CTATAGGGGAATTGTGAGCGGATAACAATTCCaggaggggagcaatatatgcaatatacc
			pET28a-Desulfotomaculum acetoxidans_R1	gcgggggtcaacctcatatctttcatacttcccatcttatctacctc
			pET28a-Desulfotomaculum acetoxidans_F2	gatgggaagtatgaaagatatgaggttgaccccccgc
			pET28a-Desulfotomaculum acetoxidans_R2	GACCCGTTTAGAGGCCCCAAGGGGTTATGCTAGttccatttcatcaccggagcttatac
Halobacterium salinarum_cluster 1	DSM 670	AE004438.1	pET28a-Halobacterium-salinarum-cluster-1_F1	CACTATAGGGGAATTGTGAGCGGATAACAATTCCgactgtctaagaagctttacactctc
			pET28a-Halobacterium-salinarum-cluster-1_R1	ggtgaggctttcttcgcttcactacggtcagtcgatgggccatatc
			pET28a-Halobacterium-salinarum-cluster-1_F2	ggcccatcgactgaccgtagtgaagcgaagaaagcctcacctac
			pET28a-Halobacterium-salinarum-cluster-1_R2	CAAGACCCGTTTAGAGGCCCCAAGGGGTTATGCTAGaccgctgtgattcaacatatcc
Halobacterium salinarum_cluster 2	DSM 670	AE004438.1	pET28a-Halobacterium-salinarum-cluster-2_F1	CACTATAGGGGAATTGTGAGCGGATAACAATTCCgtacaaatcagcgaactattacgagc
			pET28a-Halobacterium-salinarum-cluster-2_R1	cgactaccattacaagtgttgtgcatcactgtcgcgttcac
			pET28a-Halobacterium-salinarum-cluster-2_F2	cgcgacagtgatgcacaacacttgtaatggtagtcgaactg
			pET28a-Halobacterium-salinarum-cluster-2_R2	CAAGACCCGTTTAGAGGCCCCAAGGGGTTATGCTAGcgtcgaatatgccgtattcgg
Methanothrix thermoacetophila (Methanosaeta thermophila)	DSM 6194	CP000477.1	pET28a-Methanothrix thermoacetophila_F1	CGACTCACTATAGGGGAATTGTGAGCGGATAACAATTCCgataccgtcttcgccctc
			pET28a-Methanothrix thermoacetophila_R1	ctgtgtacatctgcatggatggtcaaactgggactgtgtgctttc
			pET28a-Methanothrix thermoacetophila_F2	gcacacagtcccagtttgaccatccatgcagatgtacac
			pET28a-Methanothrix thermoacetophila_R2	CAAGACCCGTTTAGAGGCCCCAAGGGGTTATGCTAGgctgatctacctgccctcaatggg
Methanosarcina vacuolata	DSM 1232	CP009520.1	pET28a-Methanosarcina vacuolata_F1	CTATAGGGGAATTGTGAGCGGATAACAATTCCagaagagcaactatagtaaggtataccg
			pET28a-Methanosarcina vacuolata_R1	GACCCGTTTAGAGGCCCCAAGGGGTTATGCTAGaactgcctgatcacatgatccc
Serratia sp.	ATCC 39006	CP025084.1	pET28a-Serratia sp_F1	GGGAATTgtgagcggataacaattccttcattgtggtggatttattaacattaatagagc
			pET28a-Serratia sp_R1	ctaaatactttcccctcctgggg
			pET28a-Serratia sp_F2	tcaaccgttaggtaaaccccc
			pET28a-Serratia sp_R2	GACCCGTTTAGAGGCCCCAAGGGGTTATGCTAGacgctaacgataaaacaccatttgc
Stella vacuolata	ATCC 43931	AP019702.1	pET28a-Stella vacuolata_F1	CACTATAGGGGAATTGTGAGCGGATAACAATTCCcagaatctgctaactaatgaattcgg
			pET28a-Stella vacuolata_R1	ctcccggaaaaggccg
			pET28a-Stella vacuolata_F2	gattcgggacaatcagggtcc

			pET28a-Stella vacuolata_R2	ctacccgccgctaccgtatcggactatctgggcggc
			pET28a-Stella vacuolata_F3	gccgcccagatagtccgatacggtagcggcgg
			pET28a-Stella vacuolata_R3	CAAGACCCGTTTAGAGGCCCCAAGGGGTTATGCTA Gggcgtttcctgactggc
Streptomyces coelicolor	DSM 40783	CP042324.1	pET28a-Streptomyces coelicolor_F1	TCACTATAGGGGAATTGTGAGCGGATAACAATTCC gccgcacctcttcctgc
			pET28a-Streptomyces coelicolor_R1	cgccaaacctcgtcgggttgcgcaatcaggtctccccacccgag
			pET28a-Streptomyces coelicolor_F2	gaacattctcgggtggggagacctgattgcgcaacccgacgag
			pET28a-Streptomyces coelicolor_R2	CAAGACCCGTTTAGAGGCCCCAAGGGGTTATGCTA Gacgcacgacggatgac
Thiocapsa rosea	DSM 235	NZ_RBXL01000001.1	pET28a-Thiocapsa-rosea_F1	TCACTATAGGGGAATTGTGAGCGGATAACAATTCC gaattcaagcctgaatgcgtgc
			pET28a-Thiocapsa-rosea_R1	ggcctgtaacggcatcgac
			pET28a-Thiocapsa-rosea_F2	gccttcgtggccgacatc
			pET28a-Thiocapsa-rosea_R2	CAAGACCCGTTTAGAGGCCCCAAGGGGTTATGCTA Gaccaaccgaaccgccg
pET-28a(+)	EMD Millipore	MK948096.1	pET28a_FB	CTAGCATAACCCCTTGGGGCC
			pET28a_RB	GGAATTGTTATCCGCTCACAATTCCCCTATAG

Chapter 3

ULTRASOUND IMAGING OF ENGINEERED DIAGNOSTIC BACTERIA IN THE GATROINTESTINAL TRACT

Sections of this chapter have been adapted from:

Buss, M. T., Zhu, L., Kwon, J. & Shapiro, M. G. Ultrasound imaging of engineered diagnostic bacteria in the gastrointestinal tract. *Manuscript in preparation* (2024).

3.1 Abstract

Inflammatory bowel diseases (IBD) affect millions of people globally, result in severe symptoms, and are difficult to diagnose and monitor, often necessitating the use of invasive and unpleasant methods like colonoscopies and biopsies. Engineered probiotic bacteria offer a promising solution due to their ability to persist in the gastrointestinal (GI) tract and to sense and respond to specific environmental signals. Bacteria have been engineered to sense and report on a range of inflammatory and other disease biomarkers in the Gl tract, but most sensor strains rely on the use of fluorescent or bioluminescent reporter genes which cannot be imaged in situ in large animals or humans due to the poor penetration depth of light in tissue. To overcome this limitation, we propose to image bacterial sensor strains in situ using ultrasound, which is a widely available and relatively inexpensive imaging modality with an imaging depth of up to several centimeters and micron-level spatial resolution. Bacteria can be imaged with ultrasound by expressing acoustic reporter genes (ARGs) which result in the production of air-filled protein nanostructures called gas vesicles that scatter sound waves. We demonstrate the first ultrasound images of in situ ARG expression in engineered bacteria colonizing the GI tract of mice. We developed a method to acquire 3D ultrasound images of the entire mouse GI tract in ~15 min to reveal the spatial distribution of ARG expression by the probiotic bacterium *E. coli* Nissle (EcN) colonizing the GI tract. We engineered EcN to produce high levels of ARG-based acoustic contrast in response to the inflammation biomarkers thiosulfate and tetrathionate, and demonstrated that the thiosulfate sensor strain noninvasively reported on antibiotic-induced inflammation in mice via ultrasound. By enabling ultrasound monitoring of engineered bacteria in the GI tract, this technology could greatly improve the noninvasive study and monitoring of bacteria designed to treat or diagnose IBD or other GI diseases.

3.2 Introduction

Inflammatory bowel diseases (IBD) affect millions of people worldwide[84,85], result in severe life-altering symptoms[86,87], and are caused by a complex combination of genetic and environmental factors leading to chronic intestinal inflammation[88,89]. Current methods to diagnose and monitor IBD such as colonoscopies and biopsies can be invasive, unpleasant, and costly[90]. Other less invasive methods such as blood and stool tests often lack specificity due to inflammation elsewhere in the body and the short-lived nature of many intestinal

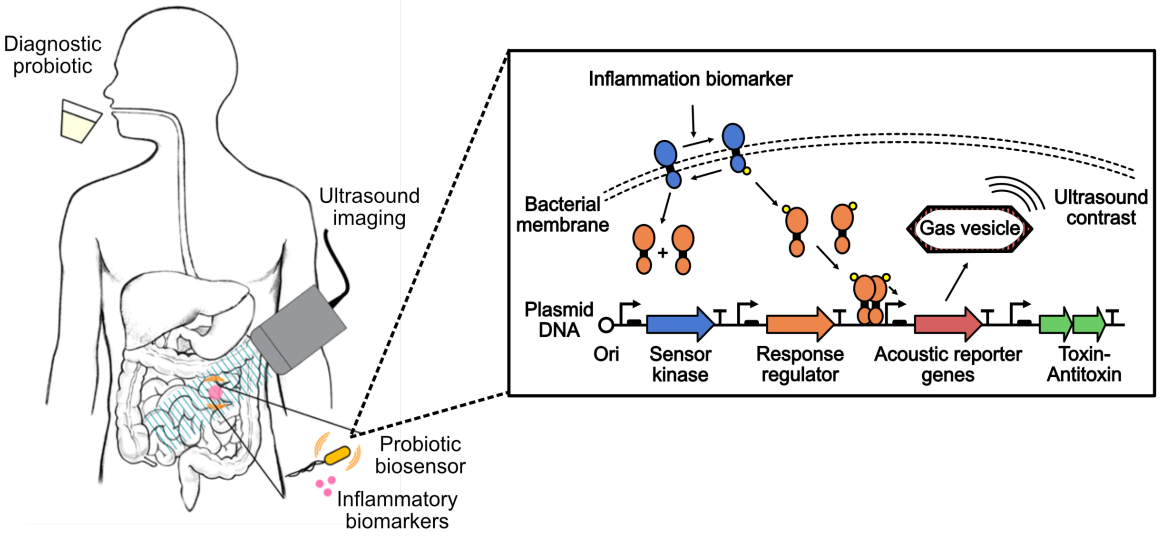

Figure 3.1: **Concept of acoustic biosensors of gastrointestinal (GI) inflammation**. Probiotic bacteria are engineered to express acoustic reporter genes (ARGs) that encode for gas vesicles (GVs) in response to sensing inflammatory biomarkers such as thiosulfate and tetrathionate using two-component systems (TCSs). Binding of the biomarker to the membrane sensor kinase protein triggers transcription of ARGs from a specific promoter via phosphorylation of a cytoplasmic response regulator protein. ARG expression can be detected via ultrasound imaging in patients after the engineered probiotic bacteria are orally administered, enabling ultrasound imaging of gastrointestinal (GI) inflammation.

species, and they do not provide spatial information[91,92]. A method to noninvasively measure inflammatory biomarkers in situ in the gastrointestinal (GI) tract could greatly facilitate the monitoring, understanding, and diagnosis of IBD and other GI diseases[93,94].

Engineered probiotic bacteria provide a solution due to their ability to persist in the GI tract and to sense and respond to specific signals in their environment[95–97]. For this reason, many strains of engineered bacteria have been developed to sense and report on a range of intestinal biomarkers, including thiosulfate[98], tetrathionate[98,99], nitric oxide[100,101], calprotectin[102], and bleeding[103]. However, most of these strains rely on the detection of a fluorescent or colorimetric reporter in the feces, which lacks spatiotemporal information. Bioluminescent reporter strains[102,104] can be imaged in situ in mice but have limited resolution and do not scale to larger animals or humans due to the poor penetration depth of light in tissue[19]. Bioluminescent reporter strains have been coupled with an electronic device in a pill whose signal can be wirelessly detected in large animals[103], but due to the transient passage of the pill through the GI tract, this approach provides limited spatiotemporal information. On the other hand, sound waves readily propagate through tissue, allowing for images with micron-level spatial resolution at depths of up to several centimeters[19] to be acquired, making ultrasound imaging of engineered diagnostic bacteria a better alternative. Furthermore, ultrasound imaging is inexpensive and ubiquitously available, increasing the potential value of diagnostics that use ultrasound as a readout.

Bacteria can be imaged with ultrasound by expressing acoustic reporter genes (ARGs), which result in the production of air-filled protein nanostructures called gas vesicles (GVs) that scatter sound waves[42]. Recently, a second-generation ARG construct called bARG$_{Ser}$ (bacterial acoustic reporter genes derived from *Serratia* sp. ATCC 39006) was

developed which enabled the probiotic bacterium *Escheriscia coli* Nissle 1917 (EcN) to robustly produce high levels of GVs and acoustic contrast; arabinose-inducible bARG$_{Ser}$ expression was imaged with ultrasound in EcN as they colonized tumors in mice[105].

We hypothesized that we could use ARG-expressing probiotic cells as the basis for a "diagnostic yogurt" that could be ingested by a patient, transiently populate the GI tract, sense an inflammatory biomarker, and produce contrast that can be detected with a simple, noninvasive ultrasound scan (**Fig. 3.1**). To develop and test this concept, we engineered EcN to express ARGs in response to small molecule biomarkers of GI inflammation and demonstrated their performance in mice. We optimized transcriptional biosensors of thiosulfate and tetrathionate[98] connected to the expression of ARGs and characterized their performance in vitro. We then developed ultrasound imaging protocols to robustly detect ARG expression in vivo in gut-colonizing EcN. Finally, we validated a mouse model of antibiotic-induced inflammation and demonstrated ultrasound imaging of their condition using a living probiotic sensor of thiosulfate.

3.3 Results

Linking inflammation biomarker sensing with bARG$_{Ser}$ expression. Thiosulfate ($S_2O_3^{2-}$) and tetrathionate ($S_4O_6^{2-}$) are biomarkers for intestinal inflammation due to altered gut sulfur metabolism during colitis. Thiosulfate is generated when host cells detoxify hydrogen sulfide (H_2S)[106], whose production is thought to be upregulated during intestinal inflammation[107–110]. Reactive oxygen species produced by host cells during inflammation further convert thiosulfate into the transient product tetrathionate[111]. The levels of thiosulfate and tetrathionate have been shown to be elevated in DSS-induced[98] and *Salmonella*-induced[99] mouse models of colitis, respectively.

Daeffler *et al.*[98] developed thiosulfate and tetrathionate sensors using two-component systems (TCS) from *Shewanella* species that function in *E. coli* and used the fluorescent protein GFP as the sensor output. We aimed to replace GFP with bARG$_{Ser}$ to enable ultrasound imaging of the sensor bacteria in situ rather than detection of GFP fluorescence in the feces via flow cytometry. We placed the TCS genes thsS/ttrS and thsR/ttrR under control of constitutive promoters and placed bARG$_{Ser}$ downstream of the thsR/ttrR-activated promoter, all together on a medium-copy number plasmid with the Axe-Txe stability cassette[68], to form plasmids thsSR-bARG$_{Ser}$ and ttrSR-bARG$_{Ser}$ (**Fig. 3.2a**). Using these constructs, we observed bARG$_{Ser}$ expression in *E. coli* in response to thiosulfate and tetrathionate, but initial expression levels were lower than with an arabinose-inducible construct pBAD-bARG$_{Ser}$ (**Fig. S3.1**).

To improve the performance of thsSR-bARG$_{Ser}$ and ttrSR-bARG$_{Ser}$, we developed a mutagenesis and screening strategy that relies on the light-scattering property of GVs that makes colonies more opaque or white in color, which can be seen visually and quickly quantified on a gel imaging system (**Fig. 3.2b-c**). After mutant libraries were transformed into a cloning strain of *E. coli* and the transformants were replica-plated onto plates with and without 1 mM thiosulfate or tetrathionate, colonies that were visually opaquer with thiosulfate/tetrathionate than without were picked and characterized in patch format at both 30ºC and 37ºC. To tune the expression levels of the response regulators thsR/ttrR, we mutagenized their constitutive promoters using semi-random primers (**Fig. S3.2a**). This

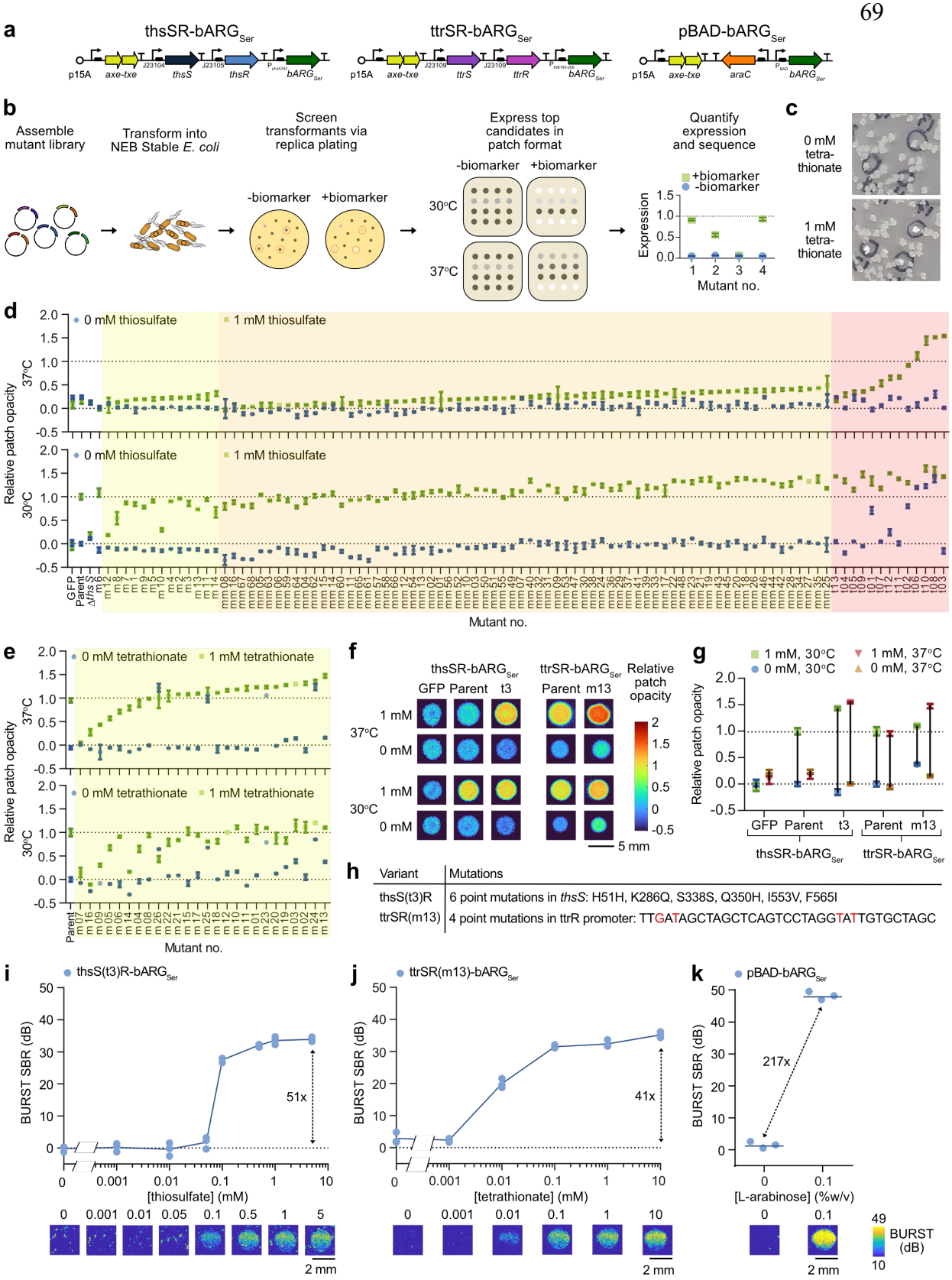
a
thsSR-bARG$_{Ser}$
ttrSR-bARG$_{Ser}$
pBAD-bARG$_{Ser}$
p15A
axe-txe
thsS
thsR
ttrS
ttrR
araC
bARG$_{Ser}$
b
Assemble mutant library
Transform into NEB Stable E. coli
Screen transformants via replica plating
Express top candidates in patch format
Quantify expression and sequence
-biomarker
+biomarker
30°C
37°C
Expression
Mutant no.
c
0 mM tetra-thionate
1 mM tetra-thionate
d
0 mM thiosulfate
1 mM thiosulfate
Relative patch opacity
Mutant no.
e
0 mM tetrathionate
1 mM tetrathionate
f
Relative patch opacity
5 mm
g
1 mM, 30°C
0 mM, 30°C
1 mM, 37°C
0 mM, 37°C
h
Variant
Mutations
thsS(t3)R
6 point mutations in thsS: H51H, K286Q, S338S, Q350H, I553V, F565I
ttrSR(m13)
4 point mutations in ttrR promoter: TTGATAGCTAGCTCAGTCCTAGGTATTGTGCTAGC
i
thsS(t3)R-bARG$_{Ser}$
BURST SBR (dB)
51x
[thiosulfate] (mM)
2 mm
j
ttrSR(m13)-bARG$_{Ser}$
41x
[tetrathionate] (mM)
k
pBAD-bARG$_{Ser}$
217x
[L-arabinose] (%w/v)
BURST (dB)

Figure 3.2: Optimization of thiosulfate and tetrathionate sensors with ARGs as the output. (**a**) Plasmid diagrams of thiosulfate (thsSR-bARG$_{Ser}$), tetrathionate (ttrSR-bARG$_{Ser}$), and L-arabinose (pBAD-bARG$_{Ser}$) sensors with ARGs from *Serratia* sp. ATCC 39006 (bARG$_{Ser}$) as the output. (**b**) Protocol for screening for optimized variants of these sensors. A mutant library is assembled via error-prone PCR or PCR with semi-random primers followed by Gibson assembly and is then transformed into NEB Stable *E. coli*. Transformants are screened by replica plating onto plates with 0 or 1 mM thiosulfate or tetrathionate. Colonies that are more opaque, corresponding to higher ARG expression, at 1 mM than at 0 mM are further characterized in patch format at 0 and 1 mM thiosulfate/tetrathionate at 30ºC and 37ºC. Patch opacity is quantified and plotted to compare variants. (**c**) Representative photographs of replica plates containing colonies at 0 and 1 mM tetrathionate, where circled colonies were more opaque at 1 mM than at 0 mM. (**d**) Relative patch opacities from screening thsSR-bARG$_{Ser}$ variants mutated in the response regulator promoter (m01-m14, yellow shading), in both the response regulator and the sensor kinase promoters (mm01-mm68, orange shading), and in the sensor kinase gene *thsS* (t01-t13, red shading). (**e**) Relative patch opacities from screening ttrSR-bARG$_{Ser}$ variants mutated in the response regulator promoter (m01-m26, yellow shading). (**f-g**) Representative images (f) and quantification in terms of relative opacity (g) of patches of the best-performing variants compared to the parent construct and a GFP control. In (d-g), a relative patch opacity of 0 corresponds to the parent construct at 0 mM thiosulfate/tetrathionate and a relative patch opacity of 1 corresponds to the parent construct at 1 mM thiosulfate/tetrathionate at 30ºC. Variants were ordered from lowest to highest relative patch opacity at 37ºC within each screening group. (**h**) Summary of mutations in the best-performing variants; see **Table S3.1** for full sequences and **Fig. S3.3** for structural predictions. (**i-k**) Representative BURST ultrasound images (bottom) and quantification of the signal-to-background ratio (SBR) (top) of the best variants for thsSR-bARG$_{Ser}$ (i) and ttrSR-bARG$_{Ser}$ (j) at varying thiosulfate/tetrathionate concentrations and of pBAD-bARG$_{Ser}$ at 0 and 0.1% L-arabinose (k) in *E. coli* Nissle (EcN) at 37ºC in liquid culture. See **Fig. S3.4** for corresponding xAM data. Cells were cast in agarose phantoms at 10^9 cells/mL for ultrasound imaging. In (d, e, g), points represent the average of 2-4 biological replicates and error bars represent the standard deviation. In (i-k), lines represent the mean of 3 biological replicates which are each averaged over 2 technical replicates.

approach yielded several variants of thsSR-bARG$_{Ser}$ with slight improvements in opacity fold-change at 1 mM versus 0 mM thiosulfate at 37ºC, but all variants still performed poorly at 37ºC compared to 30ºC (**Fig. 3.2d**). For ttrSR-bARG$_{Ser}$, this approach yielded several variants with higher opacity at 1 mM tetrathionate and 37ºC – in particular the m13 variant which had the highest opacity at 1 mM tetrathionate and 37ºC with low basal opacity at 0 mM tetrathionate and 37ºC (**Fig. 3.2e**). Similar trends were observed when mutating the response regulator promoter of the GFP versions of the sensors thsSR-GFP and ttrSR-GFP (**Fig. S3.2b-f**).

To troubleshoot the poor performance of the thiosulfate sensor at 37ºC, we mutated both the thsR and thsS constitutive promoters simultaneously, which yielded several variants with further improved opacity at 1 mM at both 30ºC and 37ºC, but opacity remained low at 37ºC. We hypothesized that the membrane sensor kinase *thsS* might not express well at 37ºC, so we mutated *thsS* using error-prone PCR and found several variants with high opacity at 37ºC and 1 mM thiosulfate. In particular, the *thsS(t3)* variant exhibited low opacity at 0 mM and very high opacity at 1 mM thiosulfate at both 37ºC and 30ºC (**Fig. 3.2d**). Overall, the thsS(t3)R-bARG$_{Ser}$ variant which contained 4 missense mutations (K286Q, Q350H, I553V, and F565I) and 2 silent mutations in *thsS* exhibited 10.5 times higher opacity at 37ºC and 1 mM thiosulfate than its parent construct (**Fig. 3.2f-h, Fig. S3.3, Table S3.1**). The ttrSR(m13)-bARG$_{Ser}$ variant which contained 4 point mutations in the *ttrR* constitutive promoter exhibited 1.5 times higher opacity at 37ºC and 1 mM tetrathionate than its parent construct (**Fig. 3.2f-h, Table S3.1**).

We next characterized thsS(t3)R-bARG$_{Ser}$ and ttrSR(m13)-bARG$_{Ser}$ at a range of thiosulfate and tetrathionate concentrations at 37ºC in liquid culture in *E. coli* Nissle (EcN). We observed increasing ultrasound signal in response to increasing concentrations of thiosulfate and tetrathionate (**Fig. 3.2i-k, Fig. S3.4**). Under BURST imaging, which is an ultrasound imaging method based on collapse of GVs providing highly sensitive and specific signals[55], thsS(t3)R-bARG$_{Ser}$ and ttrSR(m13)-bARG$_{Ser}$ exhibited maximal fold-changes of 51 and 41 in ultrasound signal, respectively. This switching performance was high compared to many inducible biosensors in the literature[98,101,102,112], though not as high as the arabinose-inducible pBAD-bARG$_{Ser}$ construct (**Fig. 3.2k**). Similar trends were observed under xAM imaging, which is a less sensitive but nondestructive imaging method that uses cross-propagating plane waves to enhance GV-specific nonlinear contrast while canceling linear background[49] (**Fig. S3.4**).

Increasing sensor activation using a recombinase-based switch. To further increase thiosulfate and tetrathionate sensor activation, we implemented a recombinase-based switch. We placed the serine integrase Bxb1 downstream of the thsR-activated promoter P$_{phsA342}$ and included a temperature-responsive terminator (TR term) upstream of Bxb1 to reduce leaky expression especially when below 37ºC outside of the body.[29] We flanked a strong constitutive promoter, P7[113], with the Bxb1 recognition sequences attB and attP, and placed bARG$_{Ser}$ downstream of attP, creating the construct thsS(t3)R-Bxb1_P7-bARG$_{Ser}$ (**Fig. 3.3a**). Before cells are exposed to thiosulfate, the P7 promoter points towards two strong terminators and bARG$_{Ser}$ is not expressed. When cells are exposed to thiosulfate, the thsS(t3)R TCS triggers Bxb1 expression which catalyzes irreversible site-specific recombination between attB and attP, flipping the direction of P7 and resulting in constitutive bARG$_{Ser}$ expression.

We compared thsS(t3)R-Bxb1_P7-bARG$_{Ser}$ and thsS(t3)R-bARG$_{Ser}$ in EcN at 37ºC, measuring the BURST and xAM ultrasound signals after inducing with a range of thiosulfate concentrations (**Fig. 3.3b-c, Fig. S3.5a, Fig. S3.6a-b**). Addition of the Bxb1 switch increased the BURST signal by 2.5-fold and the xAM signal by 2.6-fold at 100 μM thiosulfate. Addition of Bxb1 also increased the sensitivity: the data were fit to the Hill equation and addition of the Bxb1 switch decreased the constant K (corresponding to the ligand concentration that elicits a half-maximal response) from 76.4 to 48.2 μM for the BURST curves and from 72.5 to 54.9 μM for the xAM curves (**Table S3.3**).

The Bxb1 switch was also implemented in the fluorescent protein version of the thiosulfate sensor, forming plasmid thsS(t3)R-Bxb1_P7-GFP_mCherry (**Fig. 3.3d**). Flow cytometry of thsS(t3)R-Bxb1_P7-GFP_mCherry versus thsS(t3)R-GFP_mCherry EcN after inducing with a range of thiosulfate concentrations at 37ºC demonstrated increased GFP fluorescence in response to thiosulfate (19.2-fold higher at 100 μM thiosulfate), increased sensitivity (K decreased from 105 to 57.2 μM), and distinct negative and positive ("unflipped" and "flipped") GFP populations with addition of the Bxb1 switch (**Fig. 3.3e-f**, **Fig. S3.5b, Table S3.3**). Similar results were obtained by implementing the Bxb1 switch in the bARG$_{Ser}$ and fluorescent protein versions of the optimized tetrathionate sensor, forming plasmids ttrSR(m13)-Bxb1_P7-bARG$_{Ser}$ and ttrSR(m13)-Bxb1_P7-GFP_mCherry that resulted in higher maximal ultrasound signal and GFP fluorescence in response to

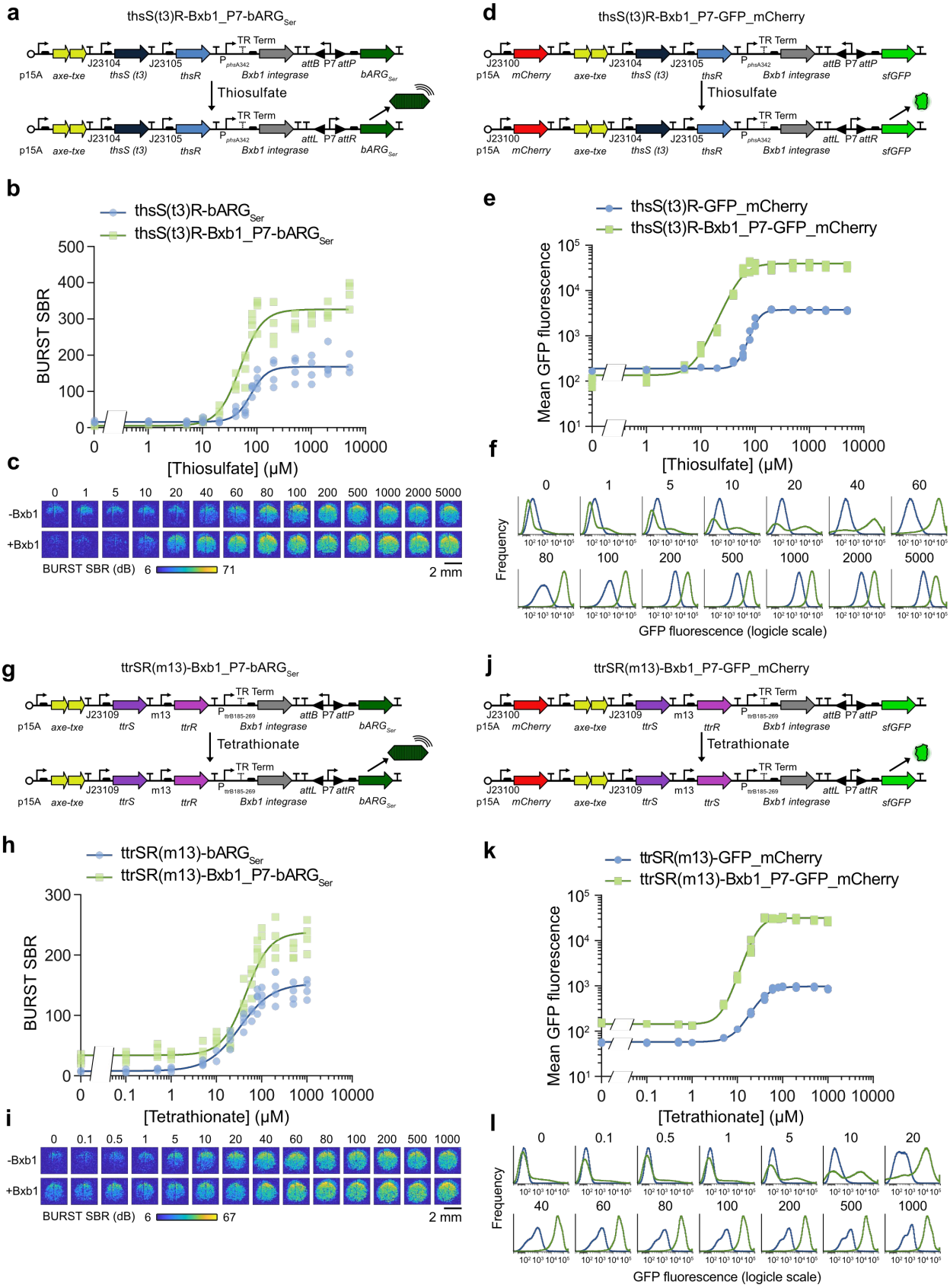
a
thsS(t3)R-Bxb1_P7-bARG$_{Ser}$
TR Term
p15A axe-txe J23104 thsS (t3) J23105 thsR $P_{phsA342}$ Bxb1 integrase attB P7 attP bARG$_{Ser}$
Thiosulfate
p15A axe-txe J23104 thsS (t3) J23105 thsR $P_{phsA342}$ Bxb1 integrase attL P7 attR bARG$_{Ser}$
d
thsS(t3)R-Bxb1_P7-GFP_mCherry
J23100 mCherry
b
thsS(t3)R-bARG$_{Ser}$
thsS(t3)R-Bxb1_P7-bARG$_{Ser}$
BURST SBR
[Thiosulfate] (µM)
e
thsS(t3)R-GFP_mCherry
thsS(t3)R-Bxb1_P7-GFP_mCherry
Mean GFP fluorescence
[Thiosulfate] (µM)
c
-Bxb1
+Bxb1
BURST SBR (dB) 6 71
2 mm
f
Frequency
GFP fluorescence (logicle scale)
g
ttrSR(m13)-Bxb1_P7-bARG$_{Ser}$
J23109 m13 ttrS ttrR $P_{ttrB185-269}$
Tetrathionate
j
ttrSR(m13)-Bxb1_P7-GFP_mCherry
h
ttrSR(m13)-bARG$_{Ser}$
ttrSR(m13)-Bxb1_P7-bARG$_{Ser}$
[Tetrathionate] (µM)
k
ttrSR(m13)-GFP_mCherry
ttrSR(m13)-Bxb1_P7-GFP_mCherry
i
BURST SBR (dB) 6 67
2 mm
l
GFP fluorescence (logicle scale)

Figure 3.3: Increasing sensor activation with addition of an integrase-based switch. (**a**) Plasmid diagram of the optimized thiosulfate sensor thsS(t3)R-bARG$_{Ser}$ with an integrase-based switch to create thsS(t3)R-Bxb1_P7-bARG$_{Ser}$. Addition of thiosulfate induces expression of the Bxb1 integrase which causes irreversible site-specific recombination between the attP and attB sites that reverses the orientation of the strong constitutive P7 promoter to activate bARG$_{Ser}$ expression. (**b-c**) BURST signal-to-background ratio (SBR) (b) and representative images (c) of the optimized thiosulfate sensor with and without the Bxb1 integrase-based switch at varying thiosulfate concentrations. See **Fig. S3.6** for the corresponding xAM data. (**d**) Plasmid diagram of the optimized thiosulfate sensor thsS(t3)R-GFP_mCherry with an integrase-based switch to create thsS(t3)R-Bxb1_P7-GFP_mCherry. (**e-f**) Mean GFP fluorescence measured via flow cytometry (e) and representative histograms (f) of the optimized thiosulfate sensor with and without the Bxb1 integrase-based switch at varying thiosulfate concentrations. (**g**) Plasmid diagram of the optimized tetrathionate sensor ttrSR(m13)-bARG$_{Ser}$ with an integrase-based switch to create ttrSR(m13)-Bxb1_P7-bARG$_{Ser}$. (**h-i**) BURST signal-to-background ratio (SBR) (h) and representative images (i) of the optimized tetrathionate sensor with and without the Bxb1 integrase-based switch at varying tetrathionate concentrations. See **Fig. S3.6** for the corresponding xAM data. (**j**) Plasmid diagram of the optimized tetrathionate sensor ttrSR(m13)-GFP_mCherry with an integrase-based switch to create ttrSR(m13)-Bxb1_P7-GFP_mCherry. (**k-l**) Mean GFP fluorescence measured via flow cytometry (k) and representative histograms (l) of the optimized tetrathionate sensor with and without the Bxb1 integrase-based switch at varying tetrathionate concentrations. In (b), (e), (h), and (k), points represent biological replicates (N=4) and curves represent fits to the Hill equation (see **Table S3.3** for fitted parameters). All strains were grown on plates with varying concentrations of thiosulfate and tetrathionate at 37ºC (see **Fig. S3.5** for images of the plates) and suspended in PBS for ultrasound imaging and flow cytometry; for ultrasound imaging, cells were cast in agarose phantoms at a concentration of 5 x 10^8 cells/mL.

tetrathionate, greater sensitivity to tetrathionate, and distinct unflipped and flipped populations compared to versions without the Bxb1 switch (**Fig. 3.3g-l, Fig. S3.5c-d, Fig. S3.6c-d, Table S3.3**). These results demonstrate that addition of a Bxb1 switch with the strong constitutive promoter P7 improves the performance of the TCS thiosulfate and tetrathionate sensors with both bARG$_{Ser}$ and GFP as outputs in EcN.

Ultrasound imaging of bARG$_{Ser}$ expression in the GI tract. As a precursor to biosensing, we aimed to demonstrate the ability to acoustically image pBAD-bARG$_{Ser}$ EcN while it colonized the GI tract of mice fed with L-arabinose. To facilitate successful colonization by the EcN, we generated a spontaneous streptomycin resistant EcN strain with a mutation in the *rpsL* gene (**Table S3.2**) and treated mice with the antibiotic streptomycin, which is commonly used to assist *E. coli* colonization in mice by lowering colonization resistance[114–117]. After 2 days of streptomycin and L-arabinose treatment, pBAD-bARG$_{Ser}$ EcN were orally administered (**Fig. 3.4a**), and their colonization levels remained high for at least 3 days after gavage (**Fig. 3.4b**), which we predicted would be sufficient for diagnostic sensing. One day after oral administration of the EcN, mice were imaged using a home-built ultrasound scanning system that enables the fast acquisition of images of the entire abdominal area (**Fig. 3.4c**), and two days later, mice were sacrificed and their intestines were imaged ex vivo using a similar setup (**Fig. 3.4d**). Scans of mice one day after gavage with BURST* ultrasound – a version of the BURST pulse sequence[55] optimized for GI probiotic imaging (as described in Methods) – revealed high levels of signal in the cecum of all mice colonized by pBAD-bARG$_{Ser}$ EcN (**Fig. 3.4e-h**), which was not present in control mice colonized by pBAD-RFP EcN (**Fig. 3.4g-h**, **Fig. S3.7a, Supplementary Videos 1-2**). Ex vivo imaging three days after gavage confirmed that the BURST* signal was primarily in the cecum and also in the colon

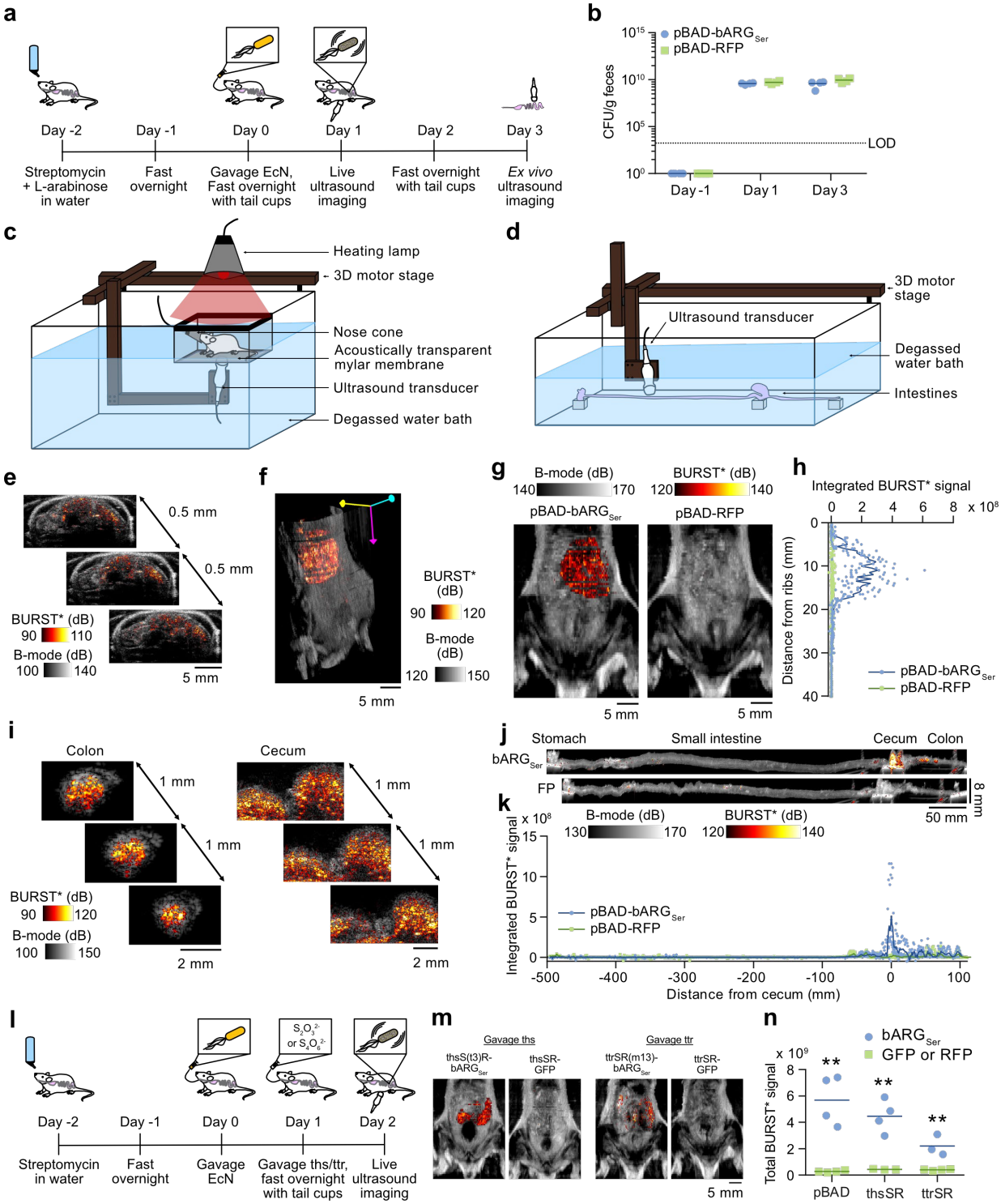

Figure 3.4: Imaging ARG expression by EcN in the GI tract in response to L-arabinose, thiosulfate, and tetrathionate. (**a**) Experimental design for testing L-arabinose-inducible $bARG_{Ser}$ expression in EcN in vivo. Mice were given water containing L-arabinose and streptomycin for 2 days, and the streptomycin-resistant EcN containing pBAD-$bARG_{Ser}$ or the control plasmid pBAD-RFP were orally administered. After fasting with tail cups overnight, mice were scanned with ultrasound. After allowing another day for

(**Fig. 3.4 caption continued**) re-expression, mice were sacrificed and their intestines were scanned with ultrasound ex vivo. (**b**) Colony forming units (CFU) per gram of feces before, 1 day after, and 3 days after administration of the L-arabinose-sensing EcN. Limit of detection (LOD) was 1.7 x 10^3 CFU/g feces. (**c-d**) Diagrams of the ultrasound imaging setups for fast and easy scanning of the entire abdominal area of live mice (c) and of the entire mouse GI tract ex vivo (d). (**e**) Representative 2-D images from scanning a mouse colonized by pBAD-bARG$_{Ser}$ EcN where the BURST* image (hot scale) was thresholded and overlaid onto the B-mode image (greyscale). Images were acquired as transverse planes spaced by 0.5 mm from the rib cage to the tail. (**f**) 3-D projection of the BURST* (hot scale) and B-mode (greyscale) images acquired from scanning a representative mouse colonized by pBAD-bARG$_{Ser}$ EcN. See **Supplementary Videos 1-2** for more views of the 3-D images. (**g**) Representative ultrasound images overlaying the integrated BURST* signal over the depth onto the integrated B-mode signal over the depth one day after administration of the L-arabinose-sensing EcN using the setup depicted in (c). See **Fig. S3.7a** for images of all mice. (**h**) Quantification of the integrated BURST* signal versus the distance from the ribs one day after administration of the L-arabinose-sensing EcN. (**i**) Representative 2-D ex vivo images from scanning the GI tract of a mouse colonized by pBAD-bARG$_{Ser}$ EcN where the BURST* images (hot scale) were thresholded and overlaid onto the B-mode images (greyscale) for the colon (left) and cecum (right). Images were acquired as transverse planes spaced by 1 mm from the stomach to the rectum. (**j**) Representative ex vivo ultrasound images of intestines 3 days after administration of the L-arabinose-sensing EcN using the setup depicted in (d). The integrated BURST* signal over the width was overlaid onto the integrated B-mode signal over the width. Note that the pixels are not isotropic due to the large length to diameter ratio of the intestines (see scale bars). See **Fig. S3.7b** for images of all intestines. (**k**) Quantification of the integrated BURST* signal versus the length of the intestines relative to the cecum. (**l**) Experimental design for testing the optimized thiosulfate- and tetrathionate-sensing EcN strains in vivo. Mice were treated with streptomycin for 2 days, EcN strains were orally administered, and the next day 1 M thiosulfate or 0.5 M tetrathionate were orally administered. After allowing a day for bARG$_{Ser}$ expression, mice were imaged with ultrasound using the setup depicted in (c). (**m**) Representative ultrasound images overlaying the integrated BURST* signal onto the integrated B-mode signal over the depth for thiosulfate-sensing EcN and tetrathionate-sensing EcN one day after oral gavage of thiosulfate or tetrathionate. Color bars are the same as in (h). See **Fig. S3.9** for images of all mice. (**n**) Total BURST* ultrasound signal imaged in mice colonized by L-arabinose-sensing (pBAD), thiosulfate-sensing (thsSR), or tetrathionate-sensing (ttrSR) EcN strains with either bARG$_{Ser}$ or GFP as the output. Asterisks represent statistical significance by two-tailed, unpaired Student's t-tests (** = $p < 0.01$). p-values from left to right: 0.00120628, 0.0026301, 0.00531767. For (b), (h), (k), and (n), each point represents a biological replicate (N=4 for all except N=3 for thsSR-GFP and ttSR-bARG$_{Ser}$ in (n)) and lines represent the mean.

(**Fig. 3.4i-k** and **Fig. S3.7b**), which is where streptomycin-resistant EcN are known to colonize in streptomycin-treated mice[104]. Negligible mutational silencing was observed in EcN plated from the feces during the course of this experiment (**Fig. S3.7c**). BURST* signal was also detected via ultrasound imaging of feces of the mice administered with pBAD-bARG$_{Ser}$ EcN (**Fig. S3.8**).

We next aimed to test whether the optimized thiosulfate- and tetrathionate-sensing EcN strains could be detected via ultrasound in mice fed with thiosulfate and tetrathionate. After 2 days of streptomycin treatment, thsS(t3)R-bARG$_{Ser}$ and ttrSR(m13)-bARG$_{Ser}$ EcN strains were orally administered and colonized mice well for at least 2 days (**Fig. 3.4l, S3.9a-b**). One day after gavage of the EcN, 1 M thiosulfate or 0.5 M tetrathionate were orally administered, and the next day all mice were imaged with ultrasound. Mice colonized with the thsS(t3)R-bARG$_{Ser}$ and ttrSR(m13)-bARG$_{Ser}$ EcN strains exhibited significantly higher BURST* signal in the cecum compared to mice colonized by control thsSR-GFP and ttrSR-GFP EcN strains (**Fig. 3.4m-n**). The amount of BURST* signal observed was also higher when greater volumes of thiosulfate or tetrathionate were administered (**Fig. S3.9c-g**). These

results demonstrate that the thsS(t3)R-bARG$_{Ser}$ and ttrSR(m13)-bARG$_{Ser}$ EcN strains function in vivo as acoustic thiosulfate and tetrathionate sensors when these compounds are present in the GI tract at sufficient levels.

To test the thiosulfate sensor in a mouse model of inflammation, we administered the thsS(t3)R-bARG$_{Ser}$ EcN strain to DSS-treated mice that were also treated with streptomycin for colonization of the bacteria. BURST* signal was not observed in either the DSS- and streptomycin-treated mice nor the control mice treated with only streptomycin (**Fig. S3.9c,h**). To determine whether the thiosulfate levels of the DSS-treated mice were insufficient to activate thsS(t3)R-bARG$_{Ser}$ to produce detectible ultrasound signal, we developed an ion chromatography-mass spectrometry (IC-MS) method to quantify intestinal thiosulfate levels (**Fig. S3.10**). We also used flow cytometry to quantify activation of a fluorescent protein version of the optimized thiosulfate sensor, thsS(t3)R-GFP_mCherry, in the feces. Mice treated with streptomycin alone for 2-3 days exhibited elevated thiosulfate levels compared to untreated controls (97.0 versus 11.6 nmol thiosulfate/g feces on average), while mice treated with DSS alone for 5-7 days or DSS for 5-7 days plus streptomycin for the last 2-3 days exhibited lower and more variable thiosulfate levels across mice (**Fig. S3.11a-b**). Mice treated with chloramphenicol or DSS and chloramphenicol also did not exhibit elevated thiosulfate levels. Accordingly, elevated GFP fluorescence of thsS(t3)R-GFP_mCherry EcN was only consistently observed in streptomycin-treated mice (**Fig. S3.11c-d**), and activation was low at only 11.8% of the maximal GFP fluorescence observed in vitro (**Fig. S3.11e**). These results indicate that streptomycin-induced inflammation[118] rather than DSS-induced colitis is a better mouse model for testing the thiosulfate sensor, and that the in vivo thiosulfate concentrations are low enough to necessitate the use of the optimized thiosulfate sensor with a Bxb1 switch to ensure high activation even at low concentrations.

Ultrasound imaging of inflammation in antibiotic-treated mice. To test whether the optimized thiosulfate sensor with a Bxb1 switch can report on streptomycin-induced inflammation[118], we treated mice with streptomycin or the control antibiotic chloramphenicol for 5 days (**Fig. 3.5a**). Streptomycin-treated mice exhibited looser stools and greater weight loss compared to chloramphenicol-treated mice, although the changes in weight were also affected by fasting with tail cups between days 2 and 3 (**Fig. 3.5b**). Two days after the start of antibiotic treatment, thsS(t3)R-Bxb1_P7-bARG$_{Ser}$ or thsS(t3)R-Bxb1_P7-GFP_mCherry EcN strains were orally-administered. Ultrasound imaging on day 3 revealed strong BURST* signal in the cecum of streptomycin-treated mice that received the thsS(t3)R-Bxb1_P7-bARG$_{Ser}$ EcN strain; this signal was not present in chloramphenicol-treated mice that received the thsS(t3)R-Bxb1_P7-bARG$_{Ser}$ EcN strain, nor in streptomycin-treated mice that received the thsS(t3)R-Bxb1_P7-GFP_mCherry EcN strain (**Fig. 3.5c-e, Fig. S3.12, Supplementary Videos 3-5**). Plating of feces on day 4 confirmed that both sensor EcN strains colonized streptomycin- and chloramphenicol-treated mice well (**Fig. 3.5f**). Flow cytometry of feces on day 4 from mice administered with thsS(t3)R-Bxb1_P7-GFP_mCherry EcN showed increased GFP fluorescence and a larger GFP positive population in streptomycin-treated versus chloramphenicol-treated mice (**Fig. 3.5g-i**). IC-MS of feces on day 4 confirmed that fecal thiosulfate levels were elevated in streptomycin-treated mice compared to chloramphenicol-treated mice (**Fig. 3.5j**, **Fig. S3.10**). Histological

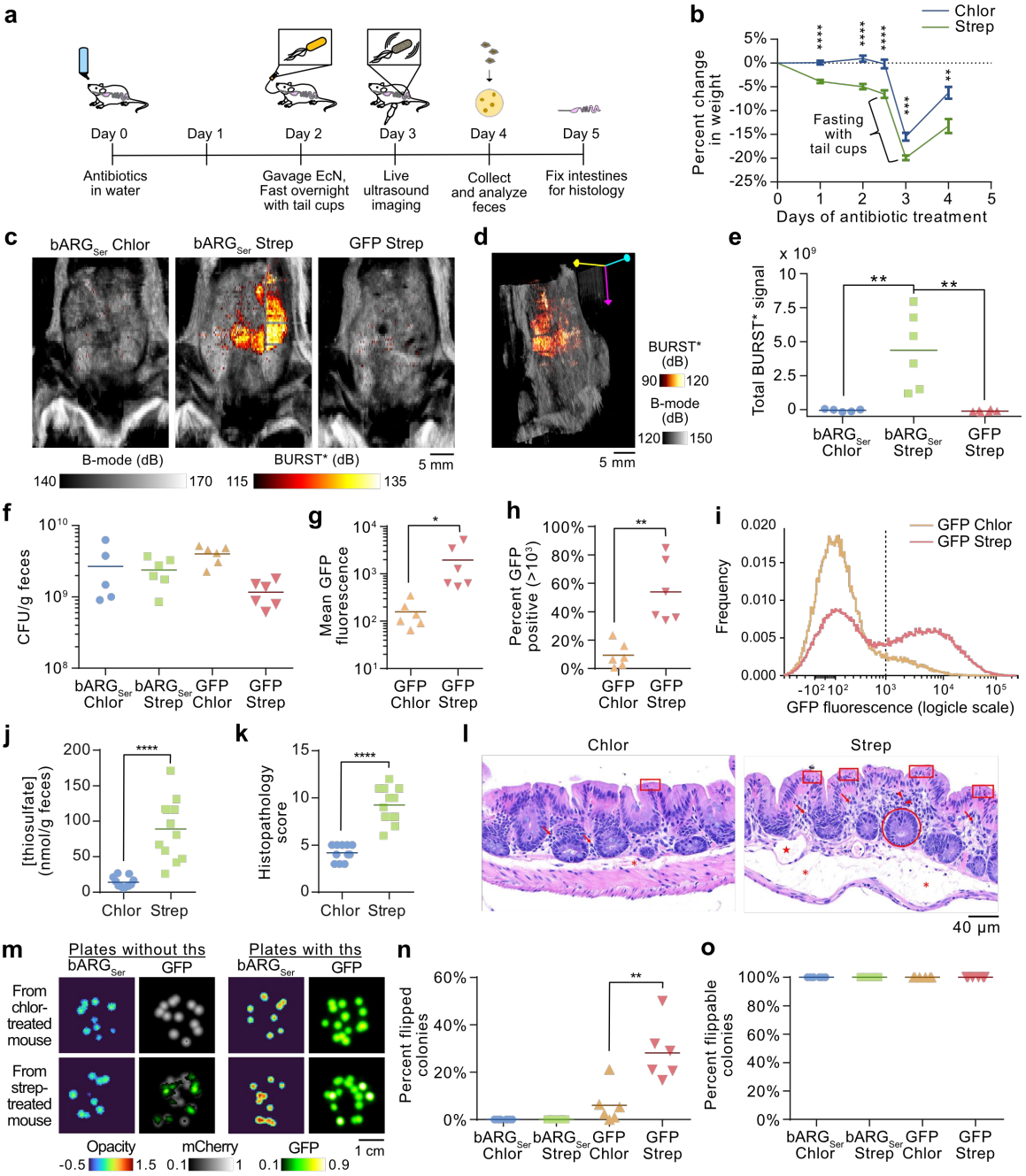

Figure 3.5: Ultrasound imaging of thiosulfate sensor activation during antibiotic-induced inflammation. (**a**) Experimental design for testing EcN strains containing plasmids for the optimized integrase-based switch thiosulfate sensors, thsS(t3)R-Bxb1_P7-bARG$_{Ser}$ or thsS(t3)R-Bxb1_P7-GFP_mCherry. (**b**) Percent change in weight after addition of chloramphenicol or streptomycin to the water of the mice. P-values from left to right: 1.309050e-07, 7.544644e-07, 3.185578e-05, 0.000135693, 0.00171773. N = 11 for chloramphenicol-treated mice and N = 12 for streptomycin-treated mice. (**c**) Representative ultrasound images overlaying the integrated BURST* signal onto the integrated B-mode signal for mice treated with chloramphenicol and colonized with thsS(t3)R-Bxb1_P7-bARG$_{Ser}$ EcN (bARG$_{Ser}$ Chlor), for mice treated with streptomycin and colonized with thsS(t3)R-Bxb1_P7-bARG$_{Ser}$ EcN (bARG$_{Ser}$ Strep), and for mice treated with streptomycin and

(**Fig. 3.5 caption continued**) colonized with thsS(t3)R-Bxb1_P7-GFP_mCherry EcN (GFP Strep) on day 3. See **Fig. S3.12** for images of all mice on day 3. (**d**) Representative 3-D projection of BURST* and B-mode images of a mouse treated with streptomycin and colonized with thsS(t3)R-Bxb1_P7-bARG$_{Ser}$ EcN. See **Supplementary Videos 3-5** for more views of 3-D projections from this experiment. (**e**) Total BURST* signal in all mice in the groups from (c) on day 3. P-values from left to right: 0.0068, 0.0029. (**f**) Colony forming units (CFU) per gram of feces on day 4 for all mice in the groups from (c), plus mice treated with chloramphenicol and colonized with thsS(t3)R-Bxb1_P7-GFP_mCherry EcN (GFP Chlor). (**g-i**) Mean GFP fluorescence, percent GFP positive events ($> 10^3$), and aggregate histograms of GFP fluorescence from flow cytometry analysis of feces from mice colonized with thsS(t3)R-Bxb1_P7-GFP_mCherry EcN and treated with chloramphenicol (GFP Chlor) or streptomycin (GFP Strep) on day 4. P-values: 0.0466 (g), 0.0010 (h). (**j**) Thiosulfate concentration in nmol per gram feces measured via IC-MS 4 days after antibiotic administration. See **Fig. S3.10** for IC-MS chromatograms and standard curves. P-value: 1.17999e-05. (**k-l**) Histopathology scores (k) and representative images (l) of H&E-stained sections of cecal tissue from mice sacrificed on day 5 after antibiotic administration. Abnormalities are indicated in red: mucosal epithelial cell death and degeneration (box), mucosal crypt hyperplasia (circle), mucosal/submucosal edema (asterisk), mononuclear infiltrates (arrow), granulocytic infiltrates (arrowhead), dilated lymphatic (star). See **Fig. S3.13** for the scoring by category and additional images. P-value: 5.38198E-08 (k). (**m**) Representative images of colonies from day 4 feces on plates with and without thiosulfate for both bARG$_{Ser}$ (thsS(t3)R-Bxb1_P7-bARG$_{Ser}$) and GFP (thsS(t3)R-Bxb1_P7-GFP_mCherry) EcN strains. (**n-o**) Percentage of colonies expressing bARG$_{Ser}$ or GFP on plates without thiosulfate (n) and with thiosulfate (o), representing the percentage of colonies that have flipped (n) and that can still be flipped if not already (o), from feces of mice on day 4. P-value: 0.0037 (n). Asterisks represent statistical significance by two-tailed, unpaired Student's t-tests (* = $p < 0.05$, ** = $p < 0.01$, *** = $p < 0.001$, **** = $p < 0.0001$). Points represent biological replicates (N=5 for bARG$_{Ser}$ Chlor, N=6 for bARG$_{Ser}$ Strep, N=6 for GFP Chlor, and N=6 for GFP Strep), lines represent means, and error bars represent the standard error of the mean.

analysis of the cecal tissue from mice sacrificed on day 5 revealed that streptomycin-treated mice had significantly higher levels of histopathological changes associated with inflammation, including mononuclear infiltrates, granulocytic infiltrates, and mucosal crypt hyperplasia (**Fig. 3.5j-k, Fig. S3.13**). The observed BURST* signal and GFP fluorescence of the sensors were positively correlated with the measured weight loss and thiosulfate levels, and the weight loss and thiosulfate levels were positively correlated with the histopathology score (**Fig. S3.14**). Overall, these results show significant activation of the thiosulfate sensor strains only in mice with streptomycin-induced inflammation, and that this activation can be imaged noninvasively with ultrasound using bARG$_{Ser}$ as the sensor output.

Because Bxb1 catalyzes an irreversible change in the direction of the P7 promoter, the fraction of cells that have been "flipped" and have constitutive bARG$_{Ser}$ or GFP expression can be measured by plating onto plates without thiosulfate (**Fig. 3.5m**). The fraction of flipped thsS(t3)R-Bxb1_P7-GFP_mCherry EcN colonies was higher in streptomycin-treated mice than in chloramphenicol-treated mice (**Fig. 3.5n**), which agrees with the flow cytometry analysis (**Fig. 3.5h**). However, no flipped thsS(t3)R-Bxb1_P7-bARG$_{Ser}$ EcN colonies were detected from fecal samples despite high BURST* signal in streptomycin-treated mice, and despite the fact that all of the colonies were "flippable" and showed bARG$_{Ser}$ expression when plated onto plates with thiosulfate (**Fig. 3.5o**). Measuring the fractions of flipped and flippable colonies from strains induced with thiosulfate in vitro gave similar results, with 1.4% of flipped GFP and 0% of flipped bARG$_{Ser}$ colonies observed after induction with 0.1 mM thiosulfate despite almost all the other colonies remaining flippable after induction with 0.1 mM thiosulfate (**Fig. S3.15**). It is likely that strong

constitutive bARG$_{Ser}$ expression is a greater burden to cells than strong constitutive GFP expression, making flipped bARG$_{Ser}$ cells less likely to remain viable. However, because strong ultrasound signals were observed, this characteristic did not hamper the performance of the bARG$_{Ser}$ thiosulfate sensor in vivo, and it could render the sensor at least partially reversible on a population level as flipped cells die off while unflipped but flippable cells remain colonized, although further experiments are required to confirm this hypothesis.

To verify that the sulfate present in the streptomycin sulfate added to the mice's water did not affect fecal thiosulfate levels, we added sodium sulfate to water and measured the fecal thiosulfate levels over the course of 4 days with IC-MS. Addition of sodium sulfate at 1x or 3x the concentrations of sulfate present in the 5 g/L streptomycin sulfate in the water of the mice from the experiment depicted in **Fig. 3.5a** did not affect fecal thiosulfate levels (**Fig. S3.16**). This result agrees with a previous study showing that supplementing drinking water with sulfate did not affect intestinal sulfide concentrations in mice[119], suggesting that intestinal sulfide and thereby thiosulfate are mostly generated through sulfur-containing amino acid catabolism rather than reduction of inorganic sulfate. Together with the histological analysis of the cecal tissue of streptomycin-treated mice, these results suggest that streptomycin treatment elevated fecal thiosulfate levels by inducing changes in the microbiome which also led to intestinal inflammation.

Additionally, we aimed to test whether antibiotics other than streptomycin could cause inflammation and elevated thiosulfate levels. We selected piperacillin because many sulfate-reducing bacteria are resistant to it[120,121], so it is unlikely to inhibit SRB-based sulfide generation in the GI tract which has been linked to colitis[110,122] and could contribute to intestinal thiosulfate generation[106]. To make EcN piperacillin-resistant, we integrated the beta lactamase gene *bla$_{TEM-1B}$* known to confer piperacillin resistance in *E. coli*[123,124] under control of a strong constitutive promoter into the genome at the phage HK022 attachment site[125] and verified growth of the resulting att$_{HK}$:bla$_{TEM1-B}$ EcN strain at up to 500 µg/mL piperacillin (**Fig. S3.17a-b, Table S3.2**). After treating mice with piperacillin for 1 day, thsS(t3)R-Bxb1_P7-bARG$_{Ser}$ and thsS(t3)R-Bxb1_P7-GFP_mCherry att$_{HK}$:bla$_{TEM1-B}$ EcN strains were orally-administered and colonized well (**Fig. S3.17c-d**). One day after bacterial administration, ultrasound scans showed strong BURST* signal in the cecum of mice treated with 200 ug/mL piperacillin and moderate BURST* signal in the cecum of mice treated with 100 ug/mL piperacillin, where both these piperacillin groups were colonized by thsS(t3)R-Bxb1_P7-bARGser att$_{HK}$:bla$_{TEM1-B}$ EcN; this signal was not present in piperacillin-treated mice colonized by thsS(t3)R-Bxb1_P7-GFP_mCherry att$_{HK}$:bla$_{TEM1-B}$ EcN (**Fig. S3.17e-f**). Histological analysis of the cecal tissue from mice sacrificed three days after the start of piperacillin treatment showed similar levels of severity of histopathological changes associated with inflammation as streptomycin-treated mice (**Fig. S3.17g-h**). Thus, in addition to streptomycin, piperacillin appears to cause dysbiosis- and inflammation-associated increases in thiosulfate that can be noninvasively imaged using our acoustic thiosulfate sensor bacteria.

3.4 Discussion

Here we demonstrate the first ultrasound images of engineered diagnostic bacteria in the gastrointestinal tract using ARGs. Our imaging and animal protocols enabled 3D ultrasound

images to be acquired of the entire mouse GI tract in ~15 min as soon as one day and up to three days after oral administration of the engineered bacteria. Both dietary (arabinose) and endogenous (thiosulfate) compounds in the GI tract triggered our engineered EcN strains to produce bARG$_{Ser}$ at levels which gave strong acoustic contrast that could be clearly distinguished from the high background levels of acoustic contrast from intestinal contents and tissue. In particular, the optimized thiosulfate sensor strain, which was the results of multiple rounds of mutagenesis, screening, and different circuit designs, noninvasively reported on inflammation in antibiotic-treated mice.

We anticipate that this technology will be useful for the noninvasive study and monitoring of commensal microbes, pathogens, and engineered bacteria in the GI tract[126]. ARGs could be expressed in different species of bacteria to visualize their locations and gene expression over time in response to different perturbations to the GI tract. In particular, to better understand the role of gut microbes in gastrointestinal cancers[127], colonization of different bacteria in tumors along the GI tract could be monitored using ARGs. Using our technology, bacteria could also be engineered to sense and noninvasively report on a range of other important species in the GI tract, including bile acids[128,129], formate[130,131], lactate[132], and short-chain fatty acids[133], to better understand their role in health and disease.

Our results emphasize the role of antibiotics in causing dysbiosis and intestinal inflammation through host-microbial interactions[134–139]. Streptomycin has been commonly used to assist *E. coli* colonization in rodent studies because it has been thought to selectively deplete facultative anaerobic bacteria while leaving the obligate anaerobe populations largely intact, opening up a niche for facultative anaerobes such as *E. coli* and *Salmonella* to colonize[115,116]. However, streptomycin has also been found to induce mild inflammation that assists *E. coli* colonization by increasing the levels of nitrate which *E. coli* can use as a terminal electron acceptor[118]. Streptomycin also depletes butyrate-producing *Clostridia*, leading to increased oxygenation of colonocytes which drives expansion of facultative anaerobic bacteria[140–143]. This mechanism could explain the increased thiosulfate levels in streptomycin-treated mice, as the resulting bloom of *Enterobacteriaceae* and other facultative anaerobes causes an increase in catabolism of sulfomucins and sulfur-containing amino acids, producing sulfide as a byproduct that is detoxified by the host to thiosulfate[107–109,144–147]. Chloramphenicol-treated mice might represent mice with a healthier GI tract by suppressing the growth of SRB[120,121] and other bacteria that contribute to sulfide generation. Overall, our results suggest that streptomycin treatment is a mouse model for dysbiosis-associated intestinal inflammation with thiosulfate as a biomarker for disease severity.

We envision several improvements to our technology. First, given the role of antibiotics in causing dysbiosis and inflammation, the colonization of sensor bacteria should not be dependent on antibiotic treatment. To instead obtain high levels of stable colonization of sensor bacteria, the bacteria could be engineered to metabolize an external carbon source that cannot be used by members of the native microbiome; this strategy has been successfully used in *Bacteroides* by engineering it to consume the polysaccharide porphyran[148]. Second, the detection of bARG$_{Ser}$ expression in the GI tract relies on collapse of GVs through BURST imaging due to the high background and non-uniformity from intestinal contents and tissue, limiting imaging sessions to at most once per day to allow time for bARG$_{Ser}$ re-expression. To overcome this limitation, bARG$_{Ser}$ could be engineered to produce more nonlinear

contrast that can be detected above background in the GI tract so that it can be imaged nondestructively with amplitude-modulation pulse sequences[49,149]. Additionally, given that thiosulfate and tetrathionate have not been validated as biomarkers for intestinal inflammation in humans, the sensors could be engineered to sense human-relevant biomarkers such as calprotectin[102] and could be tested in models of inflammation that display more localized patterns of disease, such as TNBS-induced colitis which exhibit lesions similar to those in human Crohn's disease[150].

3.5 Methods

Molecular biology

All plasmids were assembled using reagents from New England Biolabs (NEB) for Gibson Assembly and from fragments generated via PCR with Q5 High Fidelity DNA polymerase (NEB). Assemblies were transformed into NEB Stable *E. coli* via electroporation for plasmid preparation and maintenance, and all plasmids were verified with commercial Sanger sequencing (Laragen) or whole-plasmid sequencing (Primordium Labs). Plasmids containing the thiosulfate and tetrathionate TCS components, pKD236-4b (encoding *thsS*), pKD237-3a-2 (encoding *thsR*), pKD238-1a (encoding *ttrS*), and pKD239-1g-2 (encoding *ttrR*), were gifts from Jeffrey Tabor (Rice University). Components for the recombinase-based switch, including Bxb1, P7, attB, and attP, were amplified from plasmids from Abedi et al[29]. The plasmid backbone containing a chloramphenicol resistance gene and the p15A origin of replication, as well as arabinose-inducible components (araC and pBAD promoter), bARG$_{Ser}$, and Axe-Txe were amplified from plasmids from Hurt et al[105]. The pOSIP plasmid kit used for clonetegration was a gift from Drew Endy and Keith Shearwin (Addgene kit # 1000000035). Genomic modifications to *E. coli* Nissle (EcN) were verified by colony PCR with OneTaq DNA polymerase (NEB), gel purification of bands, and sequencing (Laragen or Primordium Labs). Integrated DNA Technologies synthesized other genes and all PCR primers.

Materials and Media

LB media was prepared using 10 g/L Bacto tryptone (BD Biosciences), 5 g/L Bacto yeast extract (BD Biosciences), and 5 g/L NaCl; LB-agar plates were prepared with the addition of 15 g/L Bacto agar (BD Biosciences). M9 media was prepared using 1x M9 salts (Sigma-Aldrich), 0.4% v/v glycerol, 0.2% w/v Bacto casamino acids (BD Biosciences), 2 mM $MgSO_4$, and 0.1 mM $CaCl_2$; M9-agar plates were prepared with the addition of 15 g/L Bacto agar (BD Biosciences). Sodium thiosulfate pentahydrate (Sigma-Aldrich) and potassium tetrathionate (Sigma-Aldrich) solutions were freshly prepared in water and used within a day. DSS (36,000 - 50,000 MW, colitis grade, MP Biomedicals) solutions were prepared fresh every 2 days. Chloramphenicol (Sigma-Aldrich), streptomycin sulfate (Sigma-Aldrich), and piperacillin sodium salt (Cayman Chemical Company) were prepared as 1000X stock solutions and stored at -20ºC for in vitro experiments or were prepared fresh for animal experiments. All other chemicals were of analytical grade and commercially available.

Mutant library generation and screening

For site-directed mutagenesis of constitutive Anderson promoters, semi-random primers (**Fig. S3.2a**) were used for PCR with Q5 High Fidelity DNA polymerase (NEB). For error-prone PCR of *thsS*, Taq DNA polymerase (NEB) with the standard reaction buffer (NEB), 0.2 mM dATP/dGTP, 1 mM dCTP/dTTP, 0.5 μM primers, 5.5 mM $MgCl_2$, and 0.2 mM or 0.5 mM $MnCl_2$ was used. After assembly via Gibson Assembly, mutant libraries were transformed via electroporation into NEB Stable *E. coli*. Various 10-fold dilutions of the outgrowth were plated onto LB-agar plates with antibiotics (30 μg/mL chloramphenicol + 100 μg/mL streptomycin) to ensure evenly spaced colonies for replica plating. Transformant colonies were transferred to M9-agar plates with antibiotics with and without the appropriate inducer (1 mM thiosulfate or tetrathionate) via replica plating, and replica plates were grown at 30ºC or 37ºC for 20-24 hours. Colonies that were more opaque or that had higher GFP expression at 1 mM than at 0 mM inducer were picked from the plate with 0 mM inducer into LB media with antibiotics and grown at 37ºC overnight. One μL of the overnight culture was then dropped onto M9-agar plates with varying thiosulfate or tetrathionate concentrations to make patches, and patch plates were grown at 30ºC or 37ºC for 20-24 hours. ARG-expressing patches were quantified in terms of opacity by acquiring white trans images with the standard filter using a Bio-Rad ChemiDoc MP gel imager. GFP-expressing patches or colonies were quantified by acquiring an image using blue epi illumination and a 530/28 filter. For quantifying patch opacity, ROIs were drawn around patches and the background directly adjacent to the patch using ImageJ. The mean pixel intensity of the background ROI next to the patch was subtracted from the mean pixel intensity of the patch ROI to correct for nonuniformity in the background of the white trans image. The background-subtracted mean pixel intensities were then normalized so that a value of 0 represented the opacity of the parent strain at 0 mM inducer and 30ºC, and a value of 1 represented the opacity of the parent strain at 1 mM inducer and 30ºC. These values were termed "relative patch opacity."

Because *E. coli* Nissle (EcN) appeared to mutate plasmids during transformation, all EcN transformants had to be screened. Sequence-verified plasmids purified from NEB Stable *E. coli* cultures were transformed into *E. coli* Nissle (EcN) via electroporation. The resulting transformant colonies were screened by streaking onto plates with antibiotics and with and without the appropriate inducer (thiosulfate and tetrathionate). Only colonies which expressed GFP/$bARG_{Ser}$ on the inducer plate were picked from the plate without inducer into LB media with antibiotics. LB cultures were grown at 37ºC or 30ºC overnight, and cryostocks was prepared by gently mixing 500 μL of the overnight culture with 500 μL of 30% glycerol and placing at -80ºC.

In vitro characterizations

To characterize strains in vitro, the appropriate cryostock was used to inoculate LB + 0.4% glucose + antibiotics which was grown overnight at 37ºC and 250 rpm. For characterizations in liquid culture, the overnight culture was used to inoculate 25-50 mL of M9 media + antibiotics in 250 mL baffled flasks at an initial OD_{600} of 0.05. Once the OD600 of the M9 culture reached 0.1-0.3, 1 mL aliquots were distributed in 15 mL tubes and induced with thiosulfate, tetrathionate, or L-arabinose or left uninduced. The 1 mL cultures were grown at

37ºC and 250 rpm for 20-24 hours before being placed at 4ºC or on ice until analyzed by ultrasound imaging or flow cytometry. For characterizations on solid media, the 1 μL from the overnight culture was dropped onto M9 plates + antibiotics and the desired inducer concentrations. Plates were grown at 37ºC for 20-24 hours and the resulting patches were scraped off using inoculating loops into PBS and kept on ice or at 4ºC until ultrasound imaging or flow cytometry.

Ultrasound imaging of in vitro bacterial samples and feces

To prepare phantoms of bacterial cells for ultrasound imaging, wells were cast with a custom 3D-printed mold using 1% (w/v) agarose in PBS, which was degassed by incubating at 65-75ºC for at least 16 hours. The culture or cell suspension to be imaged was diluted to 2x the final desired cell concentration in a volume of 100 μL in PBS on ice. The 100 μL of cells in PBS was placed on a heating block at 42ºC for approximately one minute, 100 μL of molten 1% agarose in PBS at 42ºC was gently mixed in, and the mixture was pipetted into the wells of the phantom in duplicate, taking care to avoid bubbles. To prepare phantoms of feces for ultrasound imaging, 10 μL of molten 1% agarose in PBS at 55ºC was pipetted into a well and a fecal pellet was quickly pushed into the well into the molten agarose. More molten agarose was pipetted on top of the fecal pellet to completely fill the well and any air pockets.

Once solidified, the phantoms were submerged in PBS, and ultrasound images were acquired using a Verasonics Vantage programmable ultrasound scanning system and an L22-14v (**Fig. 3.2, S3.1, S3.4, S3.8**) or an L22-14vX (**Fig. 3.3, S3.6**) 128-element linear array transducer. The L22-14v transducer had a center frequency of 18.5 MHz with 67%-6-dB bandwidth and an elevation focus of 6 mm. The L22-14vX transducer had a center frequency of 18.0 MHz with >60%-6-dB bandwidth and an elevation focus of 8 mm. Both transducers had an element pitch of 100 μm and an elevation aperture of 1.5 mm. The transducer was attached to a custom-made manual translation stage to move between samples.

B-mode and xAM images were acquired using the same parameters as described previously[105]: the frequency and transmit focus were set to 15.625 MHz and 5 mm, respectively, and each image was an average of 50 accumulations. B-mode imaging was performed with a conventional 128-ray-lines protocol, where each ray line was a single pulse transmitted with an aperture of 40 elements. xAM imaging was performed using a custom sequence detailed previously[49] with an angle of 19.5º and an aperture of 65 elements. With the L22-14v transducer, BURST images were acquired as a series of pAM[149] images where the focus was set to 6 mm and the frequency was set to 18.0 MHz with 2 waveform cycles, and the voltage was set to 1.6V for the first 10 frames and 25V for the last 46 frames. With the L22-14vX transducer, BURST images were acquired as a series of B-mode images, where three 32-aperature focused beams were acquired at a time to improve the frame rate by a factor of 3, and where the first image was acquired at 1.6 V and the last 7 images were acquired at 20V. The focus was set to 6 mm and the frequency was set to 18.0 MHz with 2 waveform cycles (3 half-cycles plus a half-cycle equalization).

For image processing and analysis, custom beamforming scripts were applied on-line to reconstruct images from the acquired RF data. BURST images were calculated as the first collapsing frame minus the last collapsing frame (**Fig. S3.18**). Circular ROIs were drawn around the sample wells and around the background regions in the phantom without wells in

MATLAB. The signal-to-background ratio was calculated as the mean pixel intensity of the sample ROI divided by the mean pixel intensity of the background ROI. Conversion to decibels (dB) was calculated as 20*log10(SBR). For display, images were normalized by dividing by the average background signal of all images being compared and setting the lower and upper limits of the colormaps to be the same, where the lower limit was equal to a constant A and the upper limit was equal to a constant B times the maximum pixel intensity divided by the average background out of all images being compared; images were then converted to dB. For BURST images, A=3 and B=1 with the L22-14v transducer, and A=2 and B=0.5 with the L22-14vX transducer. For xAM images, A=2 and B=0.5 with the L22-14v transducer, and A=2 and B=0.4 with the L22-14vX transducer.

Animal procedures

All animal experiments were approved by the California Institute of Technology Institutional Animal Care and Use Committee (IACUC). Animals were housed in a facility maintained at 71-75ºF and 30-70% humidity, with a lighting cycle of 13 hours on & 11 hours off (light cycle 6:00 AM - 7:00 PM). All mice were 6-10 week-old female Balb/c (**Fig. 3.4, S3.7, S3.8, S3.9**) or male C57BL/6 (**Fig. 3.5, S3.11, S3.12, S3.13, S3.16, S3.17**) mice obtained from Jackson Labs. For antibiotic, DSS, and inducer treatments administered in the drinking water *ad libitum*, the appropriate compounds were dissolved in water and filtered with a 0.2 μm membrane; the water was freshly prepared at least every 2 days. Standard rodent diet (5053 - PicoLab Rodent Diet 20) was provided *ad libitum* unless mice were being fasted. Oral gavage was performed using a 20 gauge 1.5" length animal feeding needle and with a volume of 200 uL. Prior to gavage, mice were fasted in individual housing for 2-3 hours. EcN strains were prepared for gavage by growing an overnight culture in LB + 0.4% glucose + antibiotics at 37ºC from a cryostock, diluting the overnight culture 1:100 into 50 mL of fresh M9 or LB + 0.4% glucose + antibiotics in 250 mL baffled flasks, incubating at 37ºC and 250 rpm until the OD_{600} reached 0.4-0.6, pelleting the culture at 3500g at room temperature for 10 min, and suspending in an appropriate volume of sterile PBS for an OD_{600} of 20. Feces were collected by placing mice individually in empty cages without food or bedding for approximately 20-30 minutes.

In vivo ultrasound imaging

Prior to imaging, mice were fasted overnight with tail cups in individual housing with access to water only to reduce the amount of material and background ultrasound signal in the GI tract[151,152]. Shortly before imaging, mice were anesthetized with 2% isoflurane, the tail cups were removed, and the abdominal fur was removed with shaving and Nair. Approximately 5 minutes before imaging, 1.2 μg atropine in a volume of 60 μL saline was injected subcutaneously on either side of the abdomen to slow movement of intestines due to peristalsis[153,154]. Mice were placed prone and partially submerged in water onto a thin film of mylar (2.5 μm thickness, Chemplex, catalogue number 100) which was acoustically transparent. A nose cone provided isoflurane and kept the head out of the water, white a heating lamp was used to regulate the body temperature. The ultrasound transducer (L22-14v or L22-14vX) was submerged using a probe cover (Protek, part number 1-519-2450) and attached to a BiSlide computer-controlled 3-D translatable stage (Velmex). The

transducer was positioned 6 mm below the mylar at an angle of 15° from the vertical to minimize specular reflection, and at a distance from the mylar to center the 6 mm focus on the intestines. See **Fig. 3.4c** for a diagram.

A custom MATLAB script was used to control the ultrasound system and the 3-D translatable stage at the same time so that the entire abdominal area of the mouse was automatically scanned. Starting at the rib cage, the transducer was moved in three 9.6-mm steps across the body and in eighty 0.5-mm steps lengthwise down the body to the tail. At each spot, BURST imaging was performed, giving a total of 240 BURST acquisitions per mouse which took around 15 min to acquire. BURST acquisitions were a series of B-mode images, where three 32-aperature focused beams were acquired at a time to improve the frame rate by a factor of 3[Ref. 55], with the first image taken at 1.6 V and the last seven images taken at the collapsing voltage. The focus was set to 6 mm and the frequency was set to 18.0 MHz. With the L22-14v transducer (used for in vivo data in **Fig. 3.4, S3.7, and S3.9**), 3 transmit waveform cycles were used and the collapsing voltage was 25V. With the L22-14vX transducer (used for in vivo data in **Fig. 3.5, S3.12, and S3.17**), 2 transmit waveform cycles were used and the collapsing voltage was 20V due to its higher pressure-to-voltage curve.

BURST* images were calculated by subtracting the first collapsing frame from the second because most of the ARG-specific signal occurred during the second collapsing frame and using more frames was confounded by tissue motion (**Fig. S3.18**). Acquisitions during which breathing occurred were manually excluded. The first collapsing frame was used for the B-mode images. At each transverse plane, the three acquisitions across the body were stitched together to form one B-mode image and ROIs were drawn around the GI tract in each transverse plane B-mode image. 3-D BURST* and 3-D B-mode images were formed by stitching all 240 acquisitions together. For 3-D BURST* images, pixels were set to zero anywhere breathing occurred or outside of the ROIs. For display in 3-D, 3-D BURST* and 3-D B-mode arrays were converted to dB and loaded into napari[155] where the BURST* image rendering and blending was set to "additive." For display in 2-D, the B-mode signal was summed over the depth of the mouse from 4 to 8 mm, and the BURST* signal was summed over the depth of the entire ROI. The 2-D integrated BURST* image was thresholded, converted to dB, and overlaid onto the dB-converted 2-D integrated B-mode image. To calculate the total BURST* signal, all pixel intensities in the 3-D BURST* array (where pixels were set to zero outside the ROI or where breathing occurred) were summed.

Ex vivo ultrasound imaging

Prior to imaging, mice were fasted overnight with tail cups in individual housing with access to water only to reduce the amount of material and background ultrasound signal in the GI tract. Mice were euthanized by sedating with isoflurane and performing cervical dislocation, and the entire GI tract (stomach to rectum) was quickly removed and linearized by removing mesenteric tissue, taking care not to rip the intestines. The intestines were submerged in a degassed water bath where the stomach, cecum, and rectum were pinned down on platforms so that the entire GI tract was in approximately a straight line at constant depth. The platforms consisted of acoustic absorbers (Precision acoustics) on top and magnets embedded into the platforms on the bottom so that the platforms would stay submerged and could be moved to

stretch out the intestines (whose length varied between mice) using another external magnet on the bottom of the water bath. The L22-14v ultrasound transducer was attached to a BiSlide computer-controlled 3-D translatable stage (Velmex) and was positioned 8 mm above the intestines at an angle of 15° from the vertical to minimize specular reflection. See **Fig. 3.4d** for a diagram.

A custom MATLAB script was used to control the ultrasound system and the 3-D translatable stage at the same time so that the entire GI tract was automatically scanned. Starting at the stomach, the transducer was moved in approximately six hundred 1-mm steps lengthwise down to the rectum, which took around 30 min. At each spot, BURST acquisitions were obtained as a series of B-mode images, where three 32-aperature focused beams were acquired at a time to improve the frame rate by a factor of 3, with the first image taken at 1.6 V and the last seven images taken at 25V. The focus was set to 8 mm and the frequency was set to 18.0 MHz with 3 transmit waveform cycles.

As with the in vivo images, ex vivo BURST* images were calculated by subtracting the first collapsing frame from the second, and the first collapsing frame was used for the B-mode images. For display in 2-D, both BURST* and B-mode images were summed over the width of the transducer (9.6 mm). The 2-D integrated BURST* image was thresholded, converted to dB, and overlaid onto the dB-converted 2-D integrated B-mode image. To calculate the total BURST* signal, all BURST* pixel intensities were summed between a depth of 4 and 12 mm.

Processing fecal samples for downstream analysis

Approximately 50-150 mg of feces were collected per mouse and were stored on ice immediately after collection. Feces were homogenized at 100 mg feces per mL in sterile ice-cold PBS using vortexing and an MP Biomedical FastPrep 24 Tissue Homogenizer set to 5 m/s for 20-40 seconds. One-hundred µL of the homogenized feces were saved for plating, 100-200 µL were saved for flow cytometry, and the rest were centrifuged at 10,000g and 4ºC for 20 min. The supernatant was filtered through a 0.2 µm cellulose acetate membrane and was frozen at -80ºC until analysis via IC-MS. The 100-200 µL that were saved for flow cytometry were mixed 1:1 with PBS containing 2 mg/mL chloramphenicol, filtered through a 40 µm membrane (Falcon Cell Strainers), and incubated at 37ºC and 250 rpm for one hour to allow fluorophore maturation while protein synthesis was inhibited by the 1 mg/mL chloramphenicol[98]. The mixture was then stored at 4ºC until analysis via flow cytometry within 24 hours. The 100 µL that was saved for plating was diluted in 900 µL sterile PBS, and five more 10-fold serial dilutions were made and plated on agar plates with antibiotics (30 ug/mL chloramphenicol and 100 µg/mL streptomycin or piperacillin) and with and without inducers (1 mM thiosulfate, 1 mM tetrathionate, or 0.1% L-arabinose) using the drop plate method[156]. Total colony counts were used to calculate colony forming units (CFUs) per gram of feces, and the number of colonies that expressed reporter genes was used to calculate the fraction mutant colonies, percent flipped colonies, and percent flippable colonies, depending on if the plate contained inducer.

Flow cytometry

A MACSQuant VYB flow cytometer (Miltenyi Biotec) was used for all flow cytometry analysis with the following settings: low flow rate, medium mixing, 25-50 uL uptake volume, standard mode, chilled 96 rack, and a trigger by SSC with a threshold of 2.0. The Y2 channel was used for mCherry and the B1 channel was used for GFP. For analyzing in vitro samples, appropriate dilutions in PBS + 0.5% (w/v) BSA + 1 mg/mL chloramphenicol were prepared to target 10^6 cells/mL. For analyzing fecal samples, the 50 mg/mL feces + 1 mg/mL chloramphenicol in PBS samples that were stored at 4ºC were diluted to 2.5 mg/mL feces in PBS + 0.5% (w/v) BSA + 1 mg/mL chloramphenicol (1/20 dilution). Cytoflow[157] was used with custom Python scripts for flow cytometry data analysis. Events were gated on FSC-A and SSC-A characteristic of *E. coli* and on positive mCherry fluorescence. The geometric mean was used to calculate mean GFP fluorescence, and the fraction of GFP positive cells was calculated as the number of events above 1000 in the B1 channel. For histograms, the number of bins was calculated according to the Freedman-Diaconis rule (with a minimum of 100 bins) and a logicle scale with parameters from Cytoflow was used for the x-axis.

Ion chromatography mass spectrometry (IC-MS)

Thiosulfate was quantified via IC-MS using a Dionex Integrion HPIC system coupled to an ISQ EC Single Quadrupole Mass Spectrometer (Thermo Scientific). A Dionex AS-AP autosampler was used to inject 5 µL of sample into a 25 µL sample loop in push-partial mode. Ion chromatography was performed using a Dionex IonPac AS18 analytical column (2 x 250 mm) with a guard column (2 x 50 mm) at a flow rate of 0.25 mL/min. An eluent generator (with Dionex Cartridge EGC 500 KOH) was used to create the following KOH gradient: 12 to 44 mM from 0-5 min, 44 mM from 5-8 min, 44-52 mM from 8-10 min, 52 mM from 10-15min, 52 to 12 mM from 15-15.05 min, and 12 mM from 15.05-22 min. A Dionex 2 mm AERS suppressor operated at 33 mA was used to remove the KOH before conductivity detection and negative ion mode mass spectrometry. The mass spectrometer was operated in component mode to scan for thiosulfate at m/z=113 using a source CID voltage of 10.

Thiosulfate standards were freshly prepared at concentrations ranging from 100 to 3000 nM in water with 1/10x PBS. The 100 mg/mL fecal filtrates in PBS to be analyzed with IC-MS were removed from -80ºC, rapidly thawed in a room temperature water bath, and diluted 1/10 in water. Peaks were automatically integrated using Chromeleon 7.2.10 software with the Chromeleon 6 detection algorithm and custom parameters. Because all samples contained the same PBS concentration (1/10x), phosphate which was detected via conductivity was used as an internal standard; the thiosulfate peak area was normalized by the phosphate peak area to correct for variations in sampler injection volume.

Histology of cecal tissue

Mice were euthanized by sedating with isoflurane and performing cervical dislocation. The GI tract was quickly removed and a portion of the cecum was excised, flushed with ice-cold PBS to remove the contents, and fixed in 10% neutral buffered formalin for 24 hours at 4ºC. Fixed cecal tissues were transferred to 70% ethanol and stored at 4ºC until being shipped to IDEXX Laboratories for paraffin-embedding, sectioning, and H&E staining. A pathologist performed blinded grading of microscopic changes twice independently as to severity using

the International Harmonization of Nomenclature and Diagnostic (INHAND) Criteria grading system whereby 0 = no significant change, 1= minimal, 2 = mild, 3 = moderate, and 4 = severe[158].

Structural predictions
3D models for *thsS* and *thsS(t3)* were generated from their amino acid sequences using AlphaFold 3[Ref. 159] using a seed value of 100. Structures were displayed and aligned using ChimeraX[160].

Data availability
Plasmids will be made available through Addgene upon publication. All other materials and data are available from the corresponding author upon reasonable request.

Code availability
Ultrasound data acquisition and analysis code will be made available on the Shapiro Lab GitHub at https://github.com/shapiro-lab upon publication.

3.6 Acknowledgements

The authors would like to thank the Caltech Flow Cytometry & Cell Sorting Facility for assistance with flow cytometry, Dr. Nathan Dalleska & the Water and Environment Lab (WEL) at Caltech for assistance with IC-MS, and Dr. Genevieve Remmers & IDEXX Laboratories for assistance with histopathology sample preparation and interpretation. The authors would also like to thank Dr. Jeffrey Tabor and Dr. Moshe Baruch for sending their thiosulfate and tetrathionate sensor plasmids. MTB was supported by an NSF GRFP fellowship. This research was supported by the National Institutes of Health (R01-EB018975 to MGS) and Pew Charitable Trust. Related research in the Shapiro Laboratory is supported by the David and Lucille Packard Foundation, the Burroughs Wellcome Fund, the Heritage Medical Research Institute and the Chen Zuckerberg Initiative. MGS is an investigator of the Howard Hughes Medical Institute.

3.7 Supplementary information

Table S3.1: Sequences of optimized thiosulfate and tetrathionate sensor components.

Description	Sequence (5' -> 3')
Variant *thsS*(t3) with improved performance at 37ºC (point mutations highlighted)	ATGTCCCGCCTGCTGCTGTGTATCTGTGTTCTGCTGTTCTCTTCTGTGGCGTGGTC TAAACCGCAGCAGTTTTATGTGGGCGTACTGGCTAACTGGGGTCATCAGCAAGC CGTTGAACGTTGGACCCCGATGATGGAGTATCTGAACGAACACGTGCCGGACGC GGAATTTCACGTCTACCCGGGCAACTTCAAAGCACTGAACCTGGCAATGGAACT GGGCCAGATTCAGTTCATTATCACTAACCCGGGCCAATATCTGTACCTGAGCAAT CAGTACCCGCTGTCTTGGCTGGCGACCATGCGTTCTAAGCGTCACGATGGTACC ACTTCTGCGATCGGTTCCGCCATTATTGTCCGCGCGGACAGCGACTACCGCACCC TGTACGACCTGAAAGGTAAAGTGGTGGCTGCGTCCGACCCGCATGCTCTGGGTG GCTACCAAGCGACCGTCGGTCTGATGCATTCCCTGGGCATGGATCCGGACACCT TCTTCGGTGAAACCAAGTTTCTGGGCTTTCCACTGGATCCGCTGCTGTACCAAG TTCGTGATGGCAACGTTGACGCGGCCATTACCCCACTGTGCACTCTGGAGGACA TGGTTGCACGCGGCGTACTGAAATCTTCCGATTTTCGTGTGCTGAACCCTAGCCG CCCGGATGGTGTAGAATGCCAGTGCTCTACCACCCTGTACCCGAACTGGTCTTTC GCTGCGACTGAGTCTGTATCCACCGAACTGTCTAAAGAAATCACGCAGGCACTG CTGGAACTGCCATCCGACAGCCCGGCAGCTATCAAAGCGCAACTGACCGGCTG GACCAGCCCGATCTCCCAACTGGCGGTAATCAAACTGTTCCAAGAGCTGCACGT AAAAACCCCGGACTCTAGCCGTTGGGAAGCCGTTAAGAAGTGGCTGGAAGAAA ACCGTCACTGGGGTATCCTGTCTGTTCTGGTGTTCATCATTGCAACGCTGTATCA CCTGTGGATTGAATACCGCTTCCACCAAAAAAGCTCCTCTCTGATCGAATCTGAA CGTCAGCTGAAACAGCATGCTGTTGCCCTGGAACGTCTGCAATCTGCTAGCATC GTTGGTGAAATTGGTGCGGGTCTGGCCCACGAGATTAATCAGCCGATCGCTGCA ATTACCTCTTATTCTGAAGGTGGCATCATGCGCCTGCAAGGTAAAGAACAGGCG GATACGGATAGCTGCATCGAACTGCTGGAAAAAATCCACAAACAGAGCACTCGC GCAGGCGAAGTGGTGCACCGCATCCGTGGTCTGCTGAAACGTCGTGAAGCGGT GATGGTAGATGTTAACATCCTGACCCTGGTGGAAGAATCCATCAGCCTGCTGCGT CTGGAGCTGGCACGTCGCGAAATCCAGATCAACACTCAGATCAAAGGTGAACC GTTCTTCATTACTGCCGACCGCGTTGGCCTGCTGCAAGTTCTGATTAACCTGATC AAAAACTCCCTGGACGCGATCGCTGAATCTGATAATGCCCGTTCTGGTAAAATCA ACATCGAACTGGACTTTAAAGAGTACCAGGTAAACGTCTCCATCATCGATAACG GTCCGGGCCTGGCGATGGATTCTGACACTCTGATGGCTACGTTTTACACTACCAA AATGGATGGCCTGGGCCTGGGTCTGGCAGTCTGCCGCGAAGTTATCAGCAACCA CGACGGCCACATCCTGCTGTCCAACCGTGACGACGGCGTTCTGGGCTGTGTGGC AACCCTGAATCTGAAAAAACGCGGTTCTGAAGTGCCGATCGAAGTCTAA
Constitutive promoter for *ttrR* in variant m13 (point mutations highlighted)	TTGATAGCTAGCTCAGTCCTAGGTATTGTGCTAGC

Table S3.2: Sequence verification of genomic modifications to EcN.

Description	**Sequence (5' -> 3')**
Fwd primer1	ccagccagatggcctgg
Rev primer1	gacgcgacgacgtggc
Colony PCR spontaneous streptomycin-resistant EcN with Fwd primer1 and Rev primer1 *rpsL* underlined Point mutation in *rpsL* highlighted	GGAGCTATTTAATGGCAACAGTTAACCAGCTGGTACGCAAACCACGTGCTC GCAAAGTTGCGAAAAGCAACGTGCCTGCGCTGGAAGCATGCCCGCAAAAA CGTGGCGTATGTACTCGTGTATATACTACCACTCCTACAAAACCGAACTCCG CGCTGCGTAAAGTATGCCGTGTTCGTCTGACTAACGGTTTCGAAGTGACTTC CTACATCGGTGGTGAAGGTCACAACCTGCAGGAGCACTCCGTGATCCTGAT CCGTGGTGGTCGTGTTAAAGACCTCCCGGGTGTTCGTTACCACACCGTACGT GGTGCGCTTGACTGCTCCGGCGTTAAAGACCGTAAGCAGGCTCGTTCCAAG TATGGCGTGAAGCGTCCTAAGGCTTAATGGTTCTCCGTTAAGTAAGGCCAAA CGTTTTAACTTAAATGTCAAACTAAACTCGTAGAGTTTTGGACAATCCTGAA TTAACAACGGAGTATTTCCATGCCACGTCGTCGCGTCA
Fwd primer2	GGAATCAATGCCTGAGTG
Rev primer2	GGCATCAACAGCACGTTC
Colony PCR EcN att_{HK}::bla_{TEM1-B} with Fwd primer 2 and Rev primer 2 **J23119 promoter bolded** bla_{TEM1-B} underlined	gtttaccgtggctccattgcaccagatatcgtcctggttgatagcccatctgaaaccagggcacaccaacgcggcttttcacgt ggggagcatcaatagcattcaccagttcgatcaccggcagacttgctacctgcttttgcagatcgggaaatgacgtcgtgctac taccgagcaaaatggcctctgcgccccactgtttacactggtcgatttgtgcttgctgcgtagccaactggctgtagccgcctg cctccagcacttttaaatccacaccgtagcggcgagcagcctcctgcataccatagttcaacgataaccagtatgaatctttcag gctgggataaagcgcgcacagtttccatgcgcgtttggctttaagcggcgtagaggcttgcaccgtgtaatgctgcgcatcat gccagcgcaacaggttatcagccgaaaatgccgataacatgaaaagggaaagaagtaaaaatagcagtacgcgcatgata gcctcatcaataataaggctttatgctagatgcattctgctttgcgactcaacctttttcacctaaaggatgacaaaataacattaat cacttaaaaatcatcgcattacactaatctgtggttaaatgatagactacataatgcgacaaaacgcaacatatccagtcactatg aatcaactacttagatagtattagtgacctgagacagagcattagctagcttcttcgtctgtttctactggtattggcacaaacctg attccaatttgagcaaggctatgtgccatctcgatactcgttcttaactcaacagaagatgctttgtgcatacagcccctcgtttatt atttatctcctcagccagccgctgtgctttcagtggatttcggataacagaaaggccgggaaatacccagcctcgctttgtaacg gagtagagacgaaagtgattgcgcctacccggatattatcgtgaggatgcgtcatcgccattaattcactgatcagtgataagc tgtcaaacatgagaattgatccggctgcctcgcgcgtttcggtgatgacggtgaaaacctctgacacatgcagctcccggaga cggtcacagcttgtctgtaagcggatgccgggagcagacaagcccgtcagggcgcgtcagcgggtgttggcgggtgtcgg ggcgcagccatgacccagtcacgtagcgatagcggagtgtatgctgcacatgacattaacctataaaaataggcgtatcacg aggccctttcgtcttcaagaattaattcccaattccccaggcatcaaataaaacgaaaggctcagtcgaaagactgggcctttc gttttatctgttgtttgtcggtgaacgctctcctgagtaggacaaatccgccgggagcggatttgaacgttgcgaagcaacggc ccggagggtggcgggcaggacgcccgccataaactgccaggaattaattccccaggcatcaaataaaacgaaaggctcag tcgaaagactgggcctttcgttttatctgttgtttgtcggtgaacgctctcctgagtaggacaaatccgccgggagcggatttgaa cgttgcgaagcaacggcccggagggtggcgggcaggacgcccgccataaactgccaggaattaattccccaggcatcaa ataaaacgaaaggctcagtcgaaagactgggcctttcgttttatctgttgtttgtcggtgaacgctctcctgagtaggacaaatcc gccgggagcggatttgaacgttgcgaagcaacggcccggagggtggcgggcaggacgcccgccataaactgccaggaa ttggggatcggcgtttctacaaactct**ttgacagctagctcagtcctaggtataatgctagc**aaagaggagaaatactagat gagtattcaacattttcgtgtcgcccttattccctttttgcggcattttgccttcctgtttttgctcacccagaaacgctggtgaaagt aaaagatgctgaagatcagttgggtgcacgagtgggttacatcgaactggatctcaacagcggtaagatccttgagagttttcg ccccgaagaacgttttccaatgatgagcacttttaaagttctgctatgtggtgcggtattatcccgtgttgacgccgggcaagag caactcggtcgccgcatacactattctcagaatgacttggttgagtactcaccagtcacagaaaagcatcttacggatggcatg acagtaagagaattatgcagtgctgccataaccatgagtgataacactgctgccaacttacttctgacaacgatcggaggacc gaaggagctaaccgcttttttgcacaacatgggggatcatgtaactcgccttgatcgttgggaaccggagctgaatgaagcca taccaaacgacgagcgtgacaccacgatgcctgcagcaatggcaacaacgttgcgcaaactattaactggcgaactacttac tctagcttcccggcaacaattaatagactggatggaggcggataaagttgcaggaccacttctgcgctcggcccttccggctg gctggtttattgctgataaatctggagccggtgagcgtgggtctcgcggtatcattgcagcactggggccagatggtaagccct cccgtatcgtagttatctacacgacggggagtcaggcaactatggatgaacgaaatagacagatcgctgagataggtgcctc

	actgattaagcattggtaacaaaaaaaaaccccgcccctgacagggcggggttttttttcaggcatttgagaagcacacgcatg cctcgagatgcatggcgcctaacctaaactgacaggcatcaaattaagcagaaggccatcctgacggatggccttttgcgttt cgaacaattgaaaaaacctcgcgccttacctgttgagtaatagtcaaaagcctccggtcggaggcttttgactttctgcttactga atttcggtggtgccgttaattaaccggtgggccctcatgataataatggtttcttagacgtccgaagttcctattctctagaaagtat aggaacttccatatgccatgggacaaaattgaaatcgacaaatgattttattttgactaataatgacctacttacattaatttactgat aattaaagagattttaaatatacaacttattcacctaaagtgcaccgaccgtgaatttaaccctgacccgaagactctggatggg ctttgccctgatggcgctgttaaccctgaccagtaccctggtgggatggtacaacctgcgctttatcagccaggtggaaaaa

Table S3.3: Parameters for fitting sensor characterization data from **Fig. 3.4** and **Fig. S3.6** to the Hill equation:

$$Y = A + \frac{B}{1 + \left(\frac{K}{x}\right)^{n}} .$$

Here, Y is the sensor output (ultrasound signal or fluorescence) at the ligand (thiosulfate or tetrathionate) concentration x in μM. A, B, K, and n are constants where A is the minimum output with no ligand, B is the maximum output with saturating ligand concentration, K is ligand concentration that elicits a half-maximal response, and n is the Hill coefficient. Parameters are reported as the fitted value ± the standard error.

Output	BURST SBR		xAM SBR	
Strain	thsS(t3)R-bARG$_{Ser}$	thsS(t3)R-Bxb1_P7-bARG$_{Ser}$	thsS(t3)R-bARG$_{Ser}$	thsS(t3)R-Bxb1_P7-bARG$_{Ser}$
A	14.96 ± 0.9762	4.043 ± 0.3336	1.017 ± 0.01991	1.081 ± 0.03498
B	152.1 ± 10.20	321.4 ± 16.83	5.416 ± 0.1221	12.88 ± 0.3666
K	76.42 ± 6.386	48.23 ± 4.128	72.53 ± 2.080	54.93 ± 2.247
n	2.912 ± 0.4397	2.126 ± 0.1304	3.002 ± 0.1860	2.654 ± 0.1585
R^2	0.8769	0.9336	0.9834	0.9760

Output	Mean GFP Fluorescence	
Strain	thsS(t3)R-GFP	thsS(t3)R-Bxb1_P7-GFP_mCherry
A	188.8 ± 5.021	135.3 ± 11.75
B	3580 ± 104.9	39473 ± 2254
K	105.0 ± 2.756	57.20 ± 3.942
n	4.634 ± 0.2870	2.790 ± 0.1454
R^2	0.9701	0.9180

Output	BURST SBR		xAM SBR	
Strain	ttrSR(m13)-bARG$_{Ser}$	ttrSR(m13)-Bxb1_P7-bARG$_{Ser}$	ttrSR(m13)-bARG$_{Ser}$	ttrSR(m13)-Bxb1_P7-bARG$_{Ser}$
A	8.280 ± 0.5146	34.57 ± 1.830	1.034 ± 0.01942	2.124 ± 0.04621
B	145.2 ± 10.37	203.7 ± 17.02	4.782 ± 0.1206	12.28 ± 0.4240
K	32.77 ± 5.688	44.56 ± 7.114	25.58 ± 1.361	41.98 ± 2.996
n	1.205 ± 0.1125	1.646 ± 0.2303	1.945 ± 0.1185	1.490 ± 0.08407
R^2	0.9367	0.8859	0.9842	0.9801

Output	Mean GFP Fluorescence	
Strain	ttrSR(m13)-GFP	ttrSR(m13)-Bxb1_P7-GFP_mCherry
A	57.80 ± 1.068	143.6 ± 5.553
B	916.1 ± 18.95	31452 ± 1046
K	34.53 ± 1.200	27.84 ± 1.271
n	2.328 ± 0.08339	2.981 ± 0.1149
R^2	0.9896	0.9668

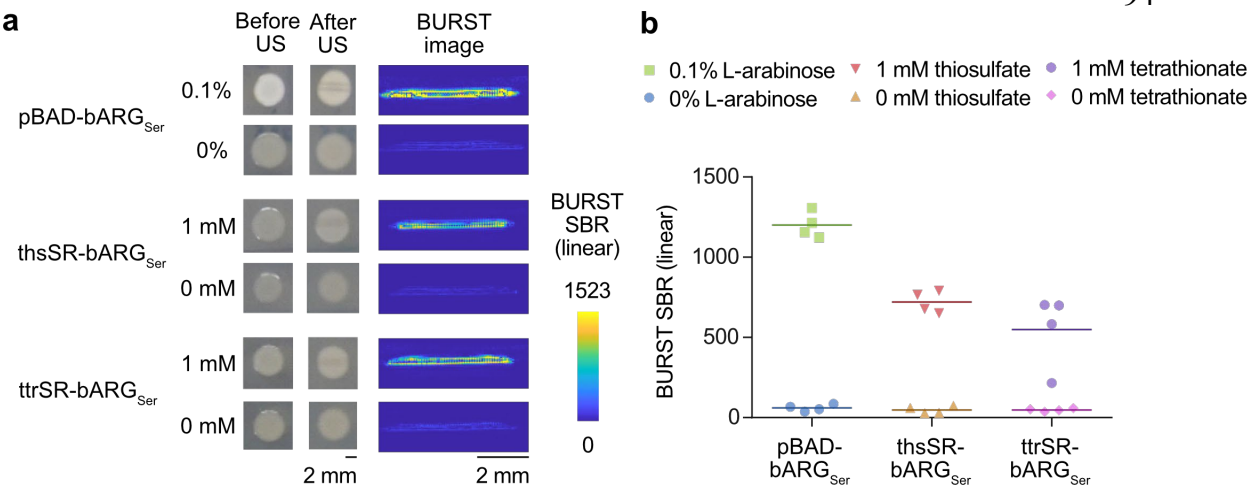

Figure S3.1: Arabinose-inducible versus initial thiosulfate and tetrathionate sensor constructs. (**a**) Images of patches of EcN strains containing the arabinose-inducible construct pBAD-bARG$_{Ser}$, the initial thiosulfate sensor construct thsSR-bARG$_{Ser}$, or the initial tetrathionate sensor construct ttrSR-bARG$_{Ser}$ on M9 plates without inducer or with 0.1% L-arabinose, 1 mM thiosulfate, or 1 mM tetrathionate, respectively. Photographs show the opacity of representative patches before ultrasound (US) imaging (left) or after being covered with agar and imaged using BURST ultrasound which reduces opacity along the imaging plane due to GV collapse (middle). Representative BURST images (right) show the ARG-specific ultrasound signal in cross-sections of the EcN patches. (**b**) Quantification of BURST images in terms of signal-to-background ratio (SBR).

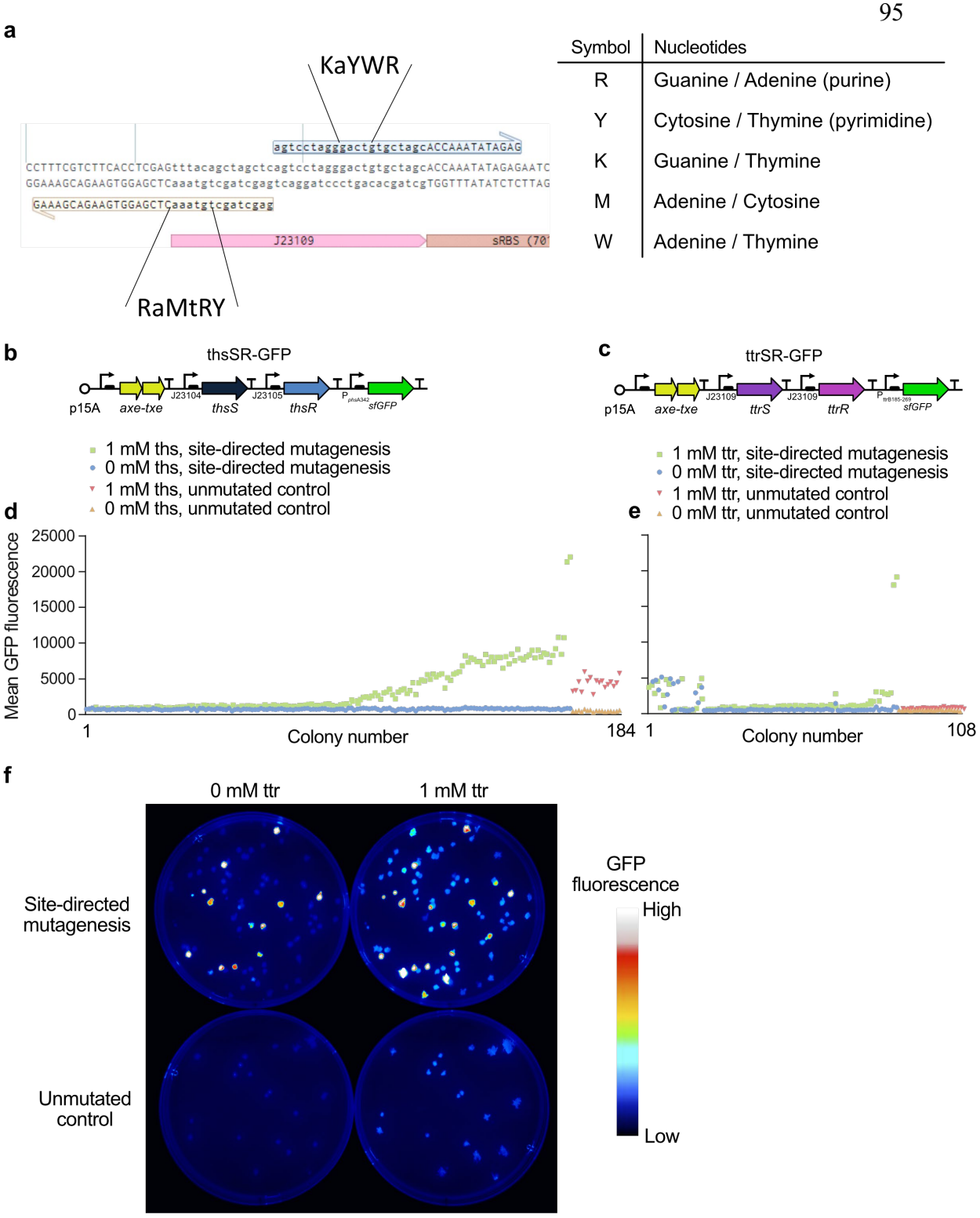

Figure S3.2: Site-directed mutagenesis and screening of GFP versions of thiosulfate and tetrathionate sensors. (**a**) Diagram of semi-random primers used for PCR for site-directed mutagenesis of the response regulator promoter, here J23109. The semi-random bases were

chosen to broadly sample the Anderson promoter library[161]. (**b-c**) Plasmid diagrams of thiosulfate (thsSR-GFP) and tetrathionate (ttrSR-GFP) sensors with GFP as the output. (**d-e**) Mean GFP fluorescence of NEB Stable *E. coli* colonies from replica plating transformants on plates with 0 or 1 mM thiosulfate (ths) or tetrathionate (ttr) at 30°C after performing site-directed mutagenesis on the response regular promoter (site-directed mutagenesis) or leaving the plasmid unmutated (unmutated control). (d-e) Share the same y-axis values. (**f**) Representative GFP fluorescence images of replica plates of mutant library (top) or unmutated control (bottom) of ttrSR-GFP with 0 or 1 mM ttr.

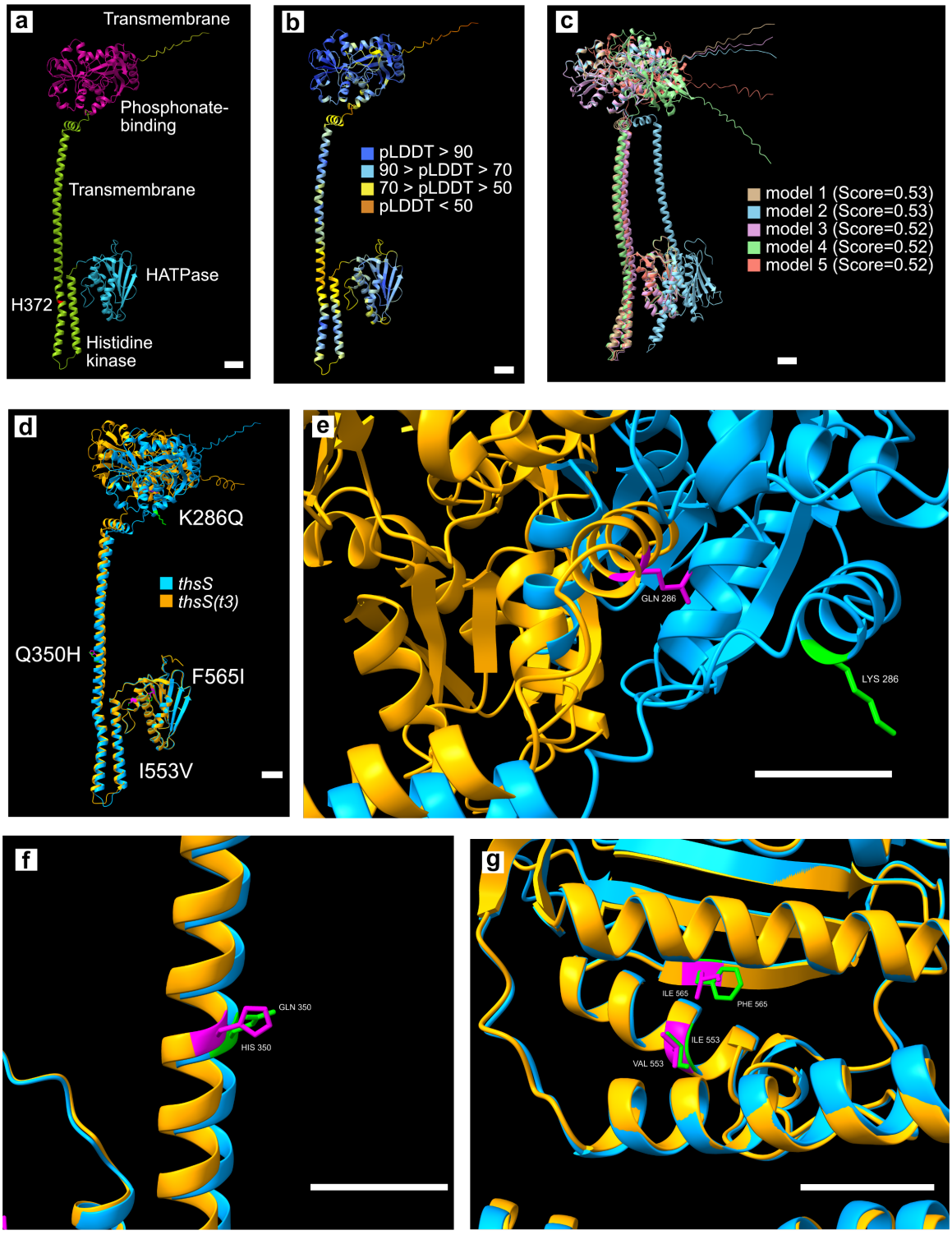

Figure S3.3: Structural predictions of the thiosulfate membrane sensor kinase protein *thsS* from *Shewanella halifaxensis* using AlphaFold 3[Ref. 159]. (**a**) Highest-ranked model of *thsS* colored by the predicted domains[98]. The histidine predicted to be involved in phospho-transfer is indicated in red (H372). (**b**) Highest-ranked model of *thsS* colored by the

confidence score in terms of the pLDDT (predicted local distance difference test). (**c**) Alignment of the top-five highest ranked models of *thsS* and their corresponding overall ranking score. (**d**) Alignment of the highest-ranked models for *thsS* and the *thsS(t3)* variant which was identified in the screen depicted in **Fig. 3.2d**. The four amino acids that are different between the *thsS* and *thsS(t3)* are indicated in green and magenta, respectively. (**e-g**) Close-up views of the K286Q (e), Q350H (f), and I553V & F565I (g) point mutations from the structures depicted in (d). These four point mutations in *thsS(t3)* do not appear to significantly affect the structure. All scale bars are 10 Å.

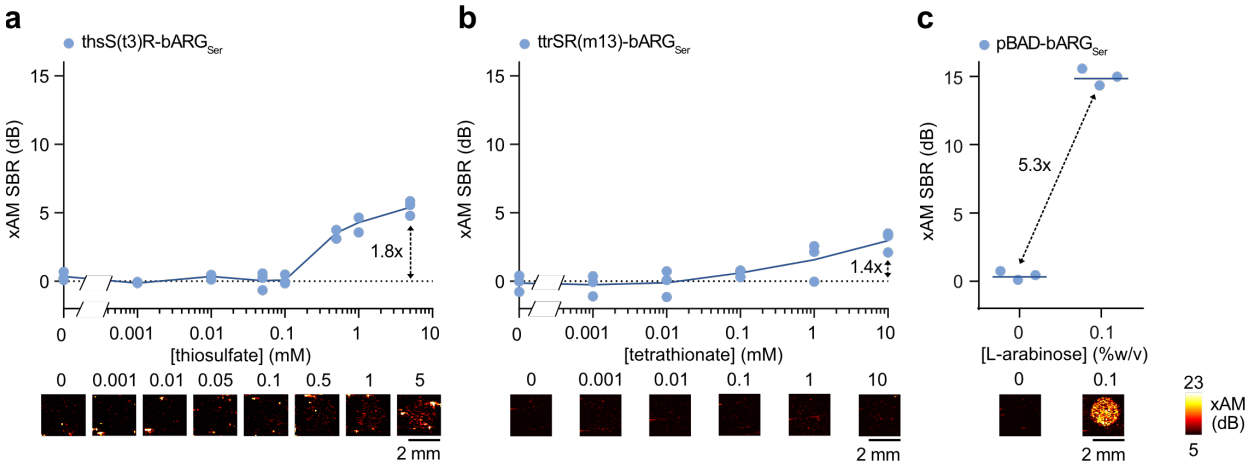

Figure S3.4: xAM ultrasound imaging of optimized thiosulfate and tetrathionate sensors and arabinose-inducible construct. (**a-c**) Representative xAM ultrasound images (bottom) and quantification of the signal-to-background ratio (SBR) (top) of the best variants for thsSR-bARG$_{Ser}$ (a) and ttrSR-bARG$_{Ser}$ (b) at varying thiosulfate/tetrathionate concentrations and of pBAD-bARG$_{Ser}$ at 0 and 0.1% L-arabinose (c) in EcN at 37°C in liquid culture. Cells were cast in agarose phantoms at 10^9 cells/mL for ultrasound imaging. Lines represent the mean of 3 biological replicates which are each averaged over 2 technical replicates.

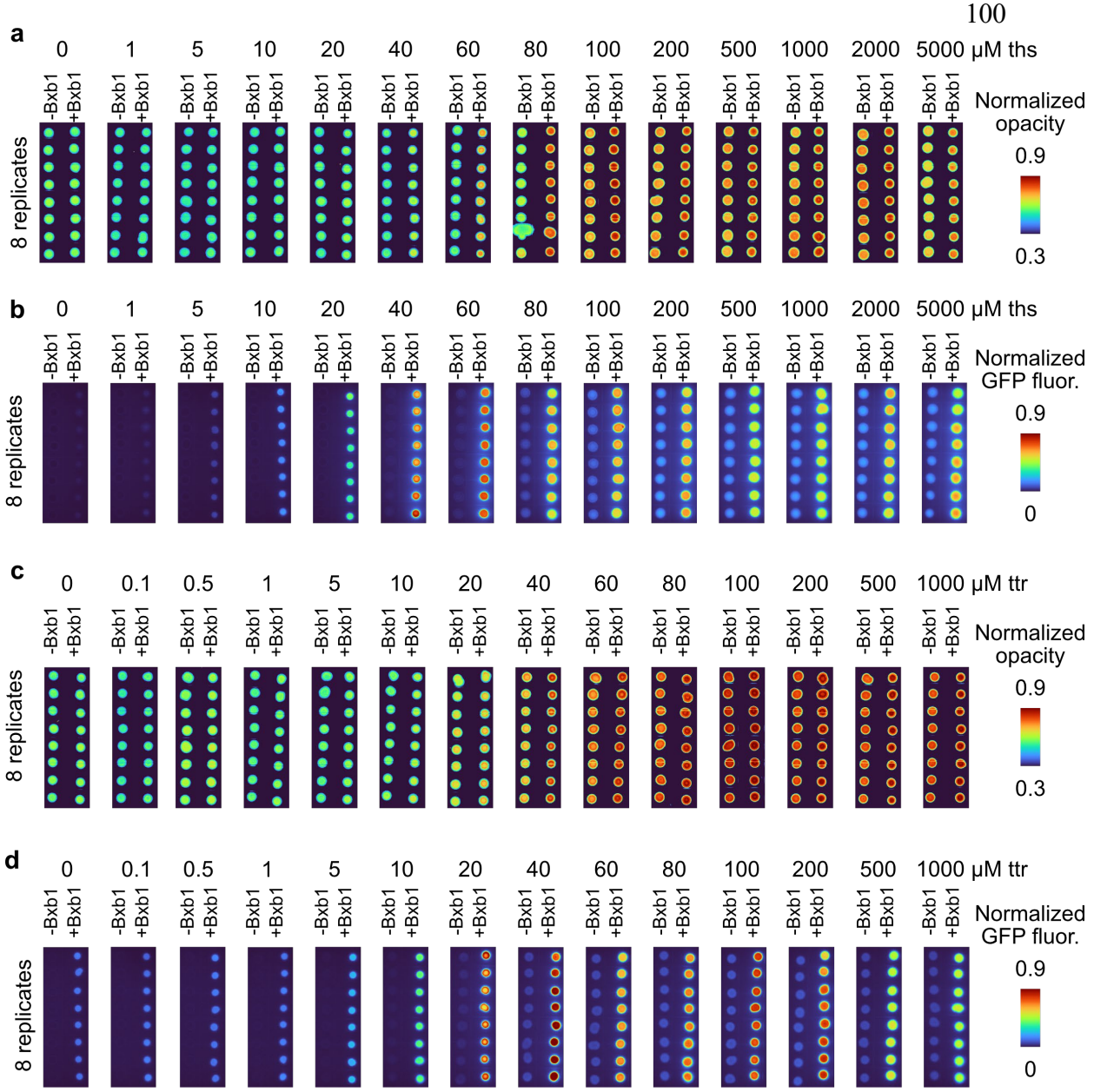

Figure S3.5: Images of patches of EcN sensor strains with and without the Bxb1 switch on plates with varying thiosulfate and tetrathionate concentrations. (**a**) Normalized transmitted white light images showing the opacity of thsS(t3)R-bARG$_{Ser}$ (-Bxb1) and thsS(t3)R-Bxb1_P7-bARG$_{Ser}$ (+Bxb1) EcN patches grown on plates at varying thiosulfate concentrations. (**b**) Normalized green fluorescence images of thsS(t3)R-GFP_mCherry (-Bxb1) and thsS(t3)R-Bxb1_P7-GFP_mCherry (+Bxb1) EcN patches grown on plates at varying thiosulfate concentrations. (**c**) Normalized transmitted white light images showing the opacity of ttrSR(m13)-bARG$_{Ser}$ (-Bxb1) and ttrSR(m13)-Bxb1_P7-bARG$_{Ser}$ (+Bxb1) EcN patches grown on plates at varying tetrathionate concentrations. (**d**) Normalized green fluorescence images of ttrSR(m13)-GFP_mCherry (-Bxb1) and ttrSR(m13)-Bxb1_P7-GFP_mCherry (+Bxb1) EcN patches grown on plates at varying tetrathionate concentrations.

All patches were grown on M9 plates at 37ºC. Patches were suspended in PBS for the ultrasound imaging and flow cytometry depicted in **Fig. 3.3**.

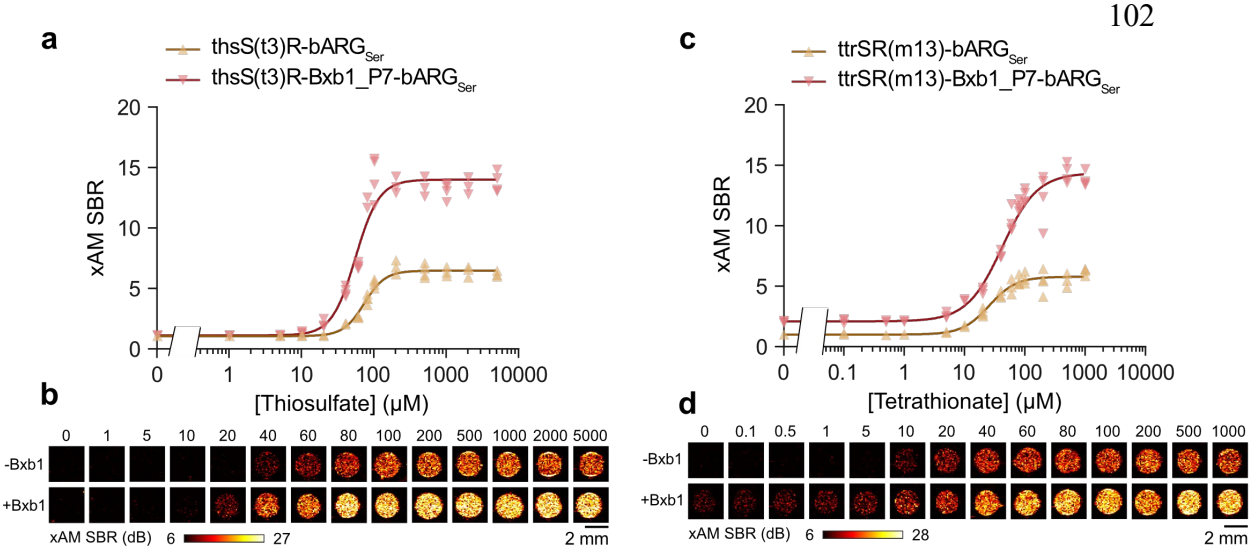

Figure S3.6: xAM images of integrase-based switch sensors. (**a-b**) xAM signal-to-background ratio (SBR) (a) and representative images (b) of the optimized thiosulfate sensor with and without the Bxb1 integrase-based switch at varying thiosulfate concentrations. (**c-d**) xAM signal-to-background ratio (SBR) (c) and representative images (d) of the optimized tetrathionate sensor with and without the Bxb1 integrase-based switch at varying tetrathionate concentrations. See **Fig. 3.3b-c, 3.3h-i** for the corresponding BURST data. In (a) and (c), points represent biological replicates (N=4) and curves represent fits to the Hill equation (see **Table S3.3** for fitted parameters). All strains were grown on plates with varying concentrations of thiosulfate and tetrathionate at 37°C (see **Fig. S3.5** for images of the plates) and suspended in PBS for ultrasound imaging and flow cytometry; for ultrasound imaging, cells were cast in agarose phantoms at a concentration of 5 x 10^8 cells/mL.

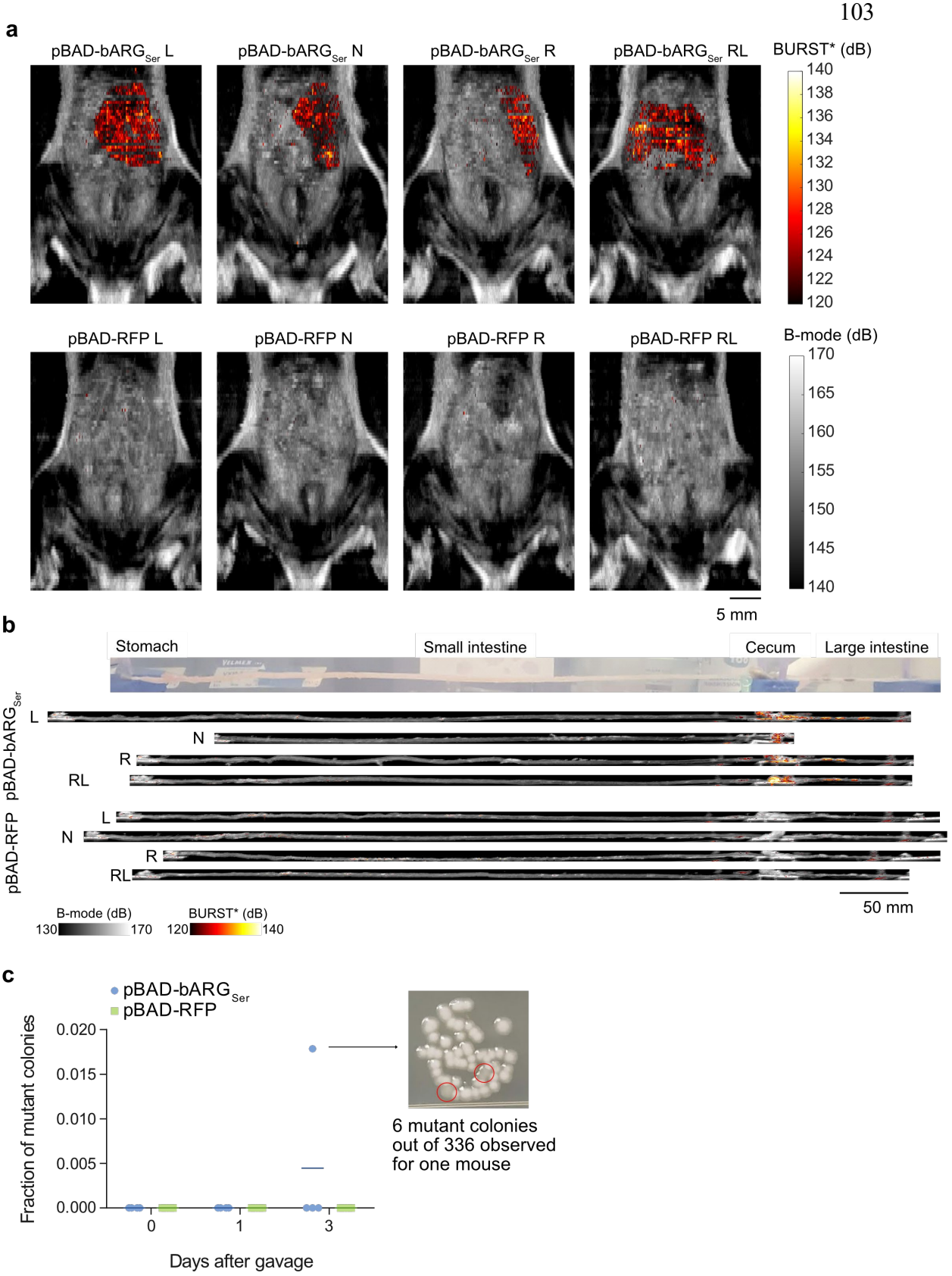
a
pBAD-bARG$_{Ser}$ L
pBAD-bARG$_{Ser}$ N
pBAD-bARG$_{Ser}$ R
pBAD-bARG$_{Ser}$ RL
BURST* (dB)
140
138
136
134
132
130
128
126
124
122
120
pBAD-RFP L
pBAD-RFP N
pBAD-RFP R
pBAD-RFP RL
B-mode (dB)
170
165
160
155
150
145
140
5 mm
b
Stomach
Small intestine
Cecum
Large intestine
pBAD-bARG$_{Ser}$
L
N
R
RL
pBAD-RFP
L
N
R
RL
50 mm
B-mode (dB)
130
170
BURST* (dB)
120
140
c
pBAD-bARG$_{Ser}$
pBAD-RFP
Fraction of mutant colonies
0.020
0.015
0.010
0.005
0.000
0
1
3
Days after gavage
6 mutant colonies
out of 336 observed
for one mouse

Figure S3.7: All replicates and additional data for imaging arabinose-inducible bARG$_{Ser}$ expression in EcN colonizing the GI tract. (**a**) Ultrasound images overlaying the integrated BURST* signal over the depth onto the integrated B-mode signal over the depth for all mice one day after administration of the L-arabinose-sensing EcN using the setup depicted in **Fig. 3.4c**. (**b**) Ex vivo ultrasound images of intestines from all mice 3 days after administration of the L-arabinose-sensing EcN using the setup depicted in **Fig. 3.4d**. The integrated BURST* signal over the width was overlaid onto the integrated B-mode signal over the width. (**c**) Fraction of non-opaque or non-RFP-fluorescent mutant colonies detected by plating the gavage mixtures (day 0) or the feces on days 1 and 3 after gavage of the L-arabinose-sensing EcN onto plates with L-arabinose. Six non-opaque colonies (out of 336 total colonies) were observed in one mouse colonized by pBAD-bARG$_{Ser}$ EcN on day 3. Three of these colonies (red circles) are depicted in the image on the right.

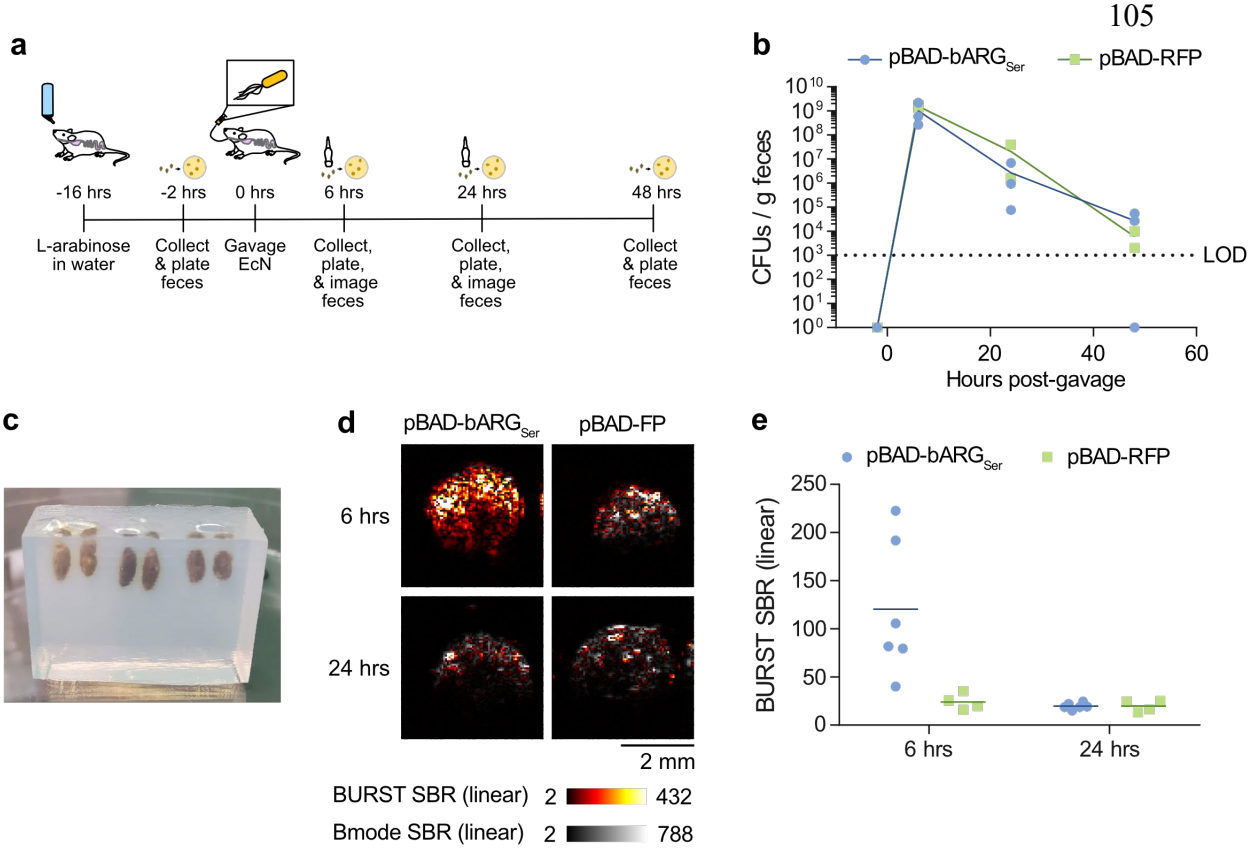

Figure S3.8: Ultrasound imaging of bARG$_{Ser}$-expressing EcN in feces without antibiotic treatment. (**a**) Experimental design for testing L-arabinose-inducible bARG$_{Ser}$ expression in EcN in vivo without antibiotics. Mice were given water containing L-arabinose for 16 hours, and EcN containing pBAD-bARG$_{Ser}$ or the control plasmid pBAD-RFP were orally administered. Feces were collected at various time points and imaged with ultrasound and/or plated on selective media to measure colonization. (**b**) Colony forming units (CFUs) per gram of feces collected 2 hours before, and 6, 24, and 48 hours after oral gavage of the EcN strains. Limit of detection (LOD) was 1.7 x 10^3 CFU/g feces. N = 3 mice per strain. (**c-e**) Representative phantom containing feces for ultrasound imaging (c), representative ultrasound images of feces overlaying the thresholded BURST image (hot scale) over the B-mode image (grayscale) (d), and quantification of the BURST signal-to-background ratio (SBR) of feces (e). Two fecal pellets were imaged per mouse, giving N = 6 per strain. In (b) and (e), points represent biological replicates and lines represent the mean.

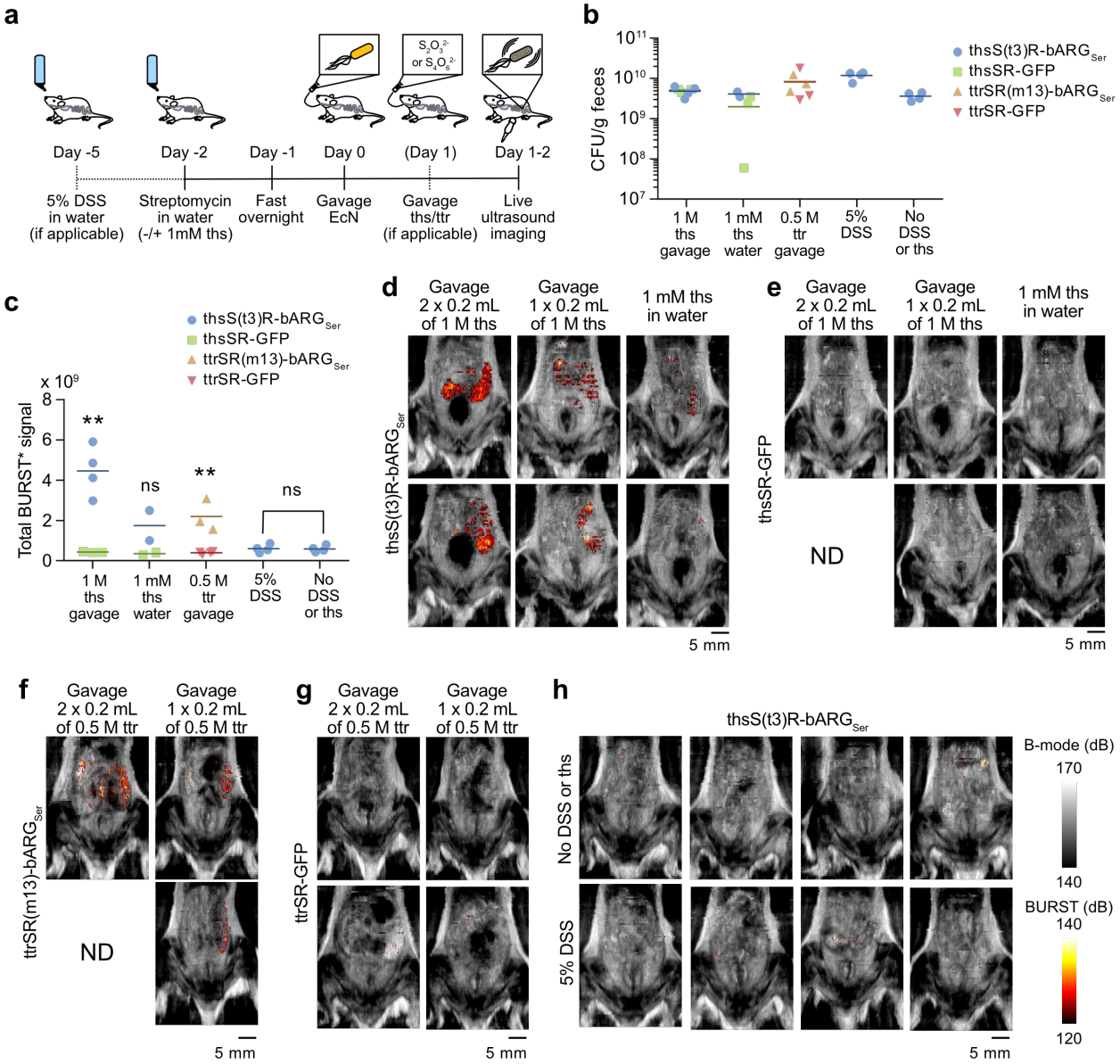

Figure S3.9: All replicates and additional data for testing thS(t3)R-bARG$_{Ser}$ and ttrSR(m13)-bARGSer sensor EcN strains in vivo. (**a**) Diagram summarizing the experimental design involving DSS treatment, thiosulfate in the drinking water, or thiosulfate/tetrathionate administered via oral gavage. All mice received streptomycin in the drinking water for 2 days before oral gavage of sensor EcN strains, and all mice were imaged using the setup depicted in **Fig. 3.4c** one to two days after EcN gavage. (**b**) Colony forming units (CFU) per gram of feces one day after oral gavage of the sensor EcN strains. (**c**) Total BURST* ultrasound signal imaged in mice one day (1 mM ths water, 5% DSS, and no DSS or ths) or two days (1 M ths gavage and 0.5 M ttr gavage) after EcN gavage. (**d-e**) Overlay of the integrated BURST* images onto the integrated B-mode images over the depth for all mice colonized by thsS(t3)R-bARGSer (d) or thsSR-GFP (e) EcN and treated with thiosulfate via oral gavage or in the drinking water. (**f-g**) Overlay of the integrated BURST* images

onto the integrated B-mode images over the depth for all mice colonized by ttrSR(m13)-bARG$_{Ser}$ (f) or ttrSR-GFP (g) EcN and treated with tetrathionate via oral gavage. (**h**) Overlay of the integrated BURST* images onto the integrated B-mode images over the depth for all mice colonized by thS(t3)R-bARG$_{Ser}$ EcN and treated with DSS or left untreated (no DSS or thiosulfate).

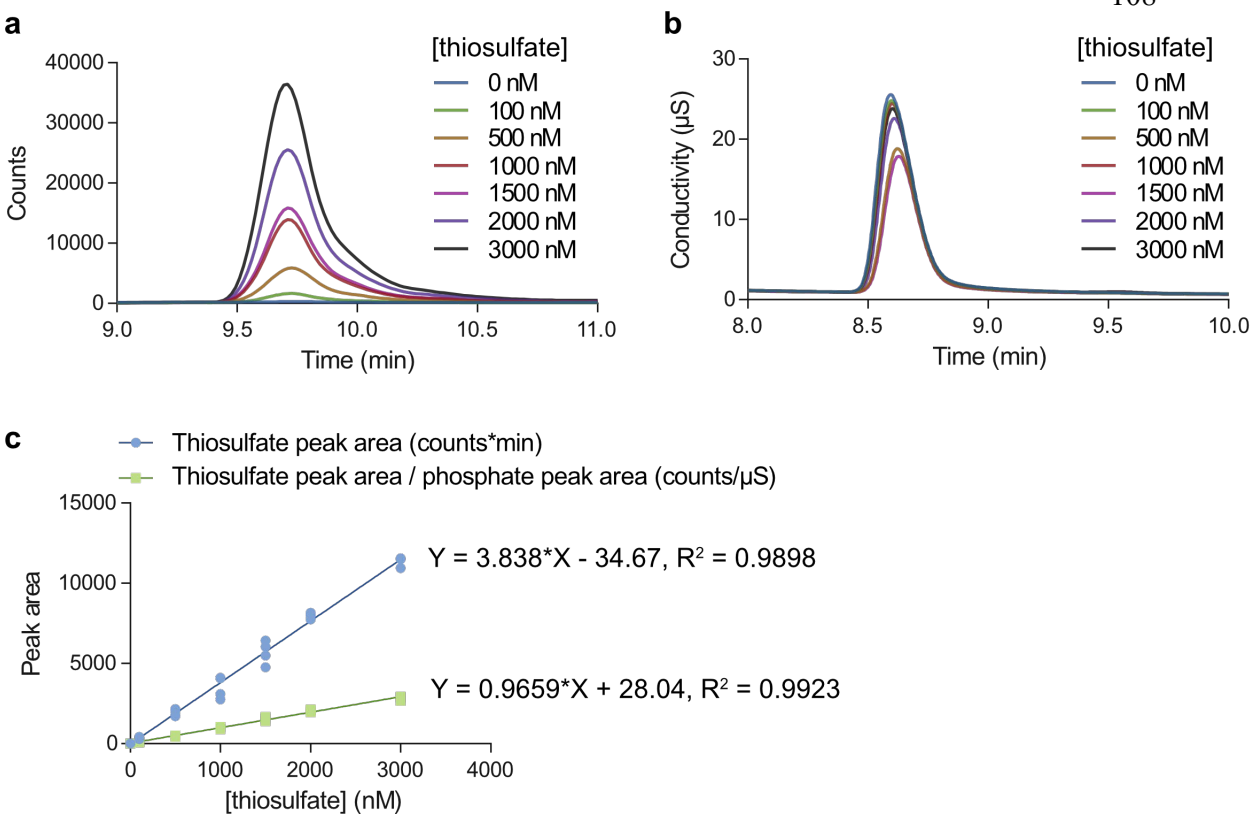

Figure S3.10: Ion chromatography-mass spectrometry (IC-MS) chromatograms and standard curves for quantifying thiosulfate. (**a**) Representative extracted ion chromatograms showing the thiosulfate peaks (m/z = 112.5-113.5 filter) in thiosulfate samples at concentrations ranging from 0 to 3000 nM in a PBS background. (**b**) Representative conductivity chromatograms showing the phosphate peaks in thiosulfate samples at concentrations ranging from 0 to 3000 nM in a PBS background. The concentration of PBS was the same in all samples, so the phosphate served as an internal standard. (**c**) Standard curve for the raw thiosulfate peak area and for the thiosulfate peak area normalized by the corresponding phosphate peak area. The normalized peak areas were used for quantification of thiosulfate in fecal and intestinal samples because normalization resulted in less variation between technical replicates. Points represent technical replicates (N=4) and lines represent a linear regression.

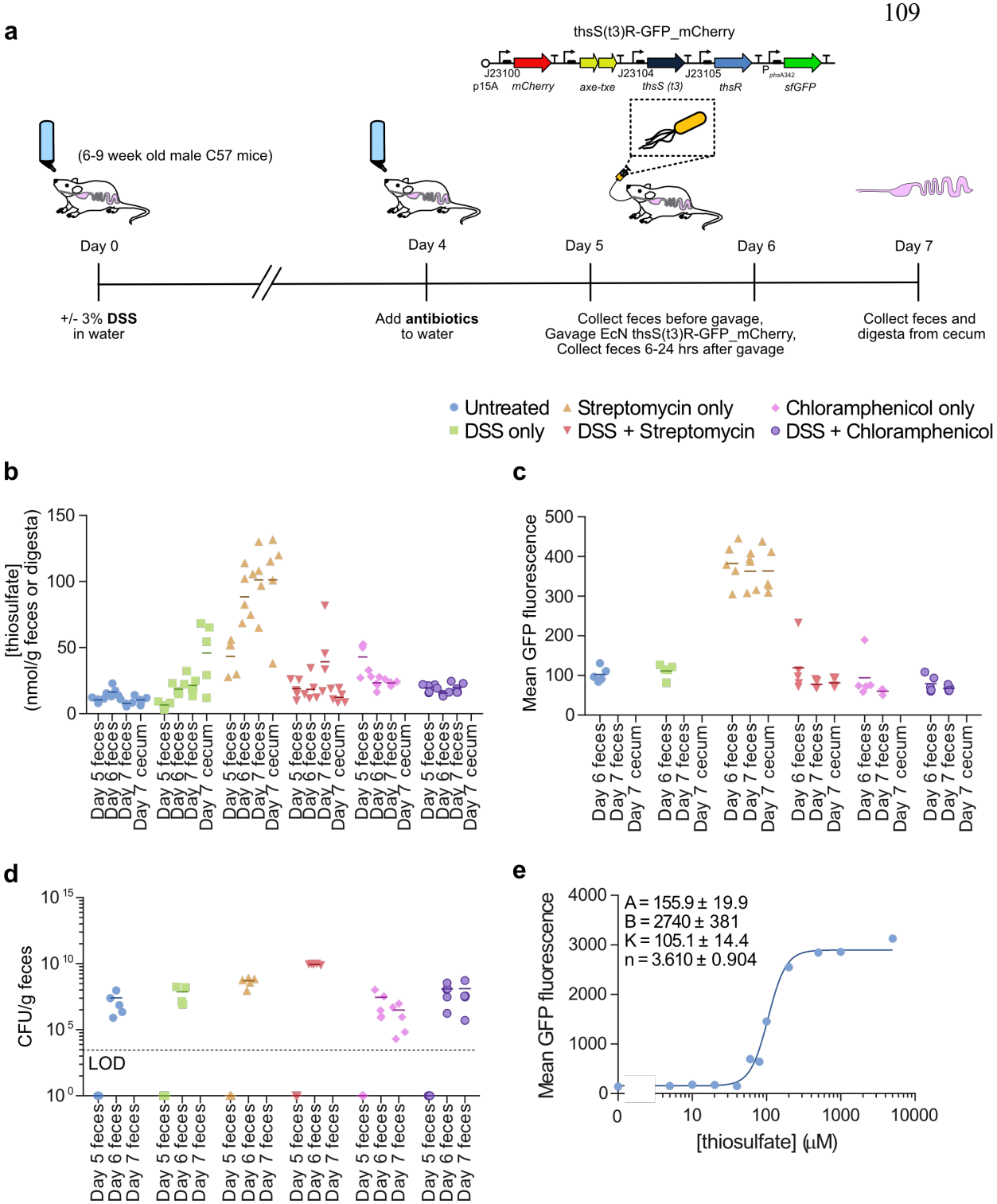

Figure S3.11: Measuring thiosulfate levels and thsS(t3)R-GFP_mCherry sensor activation in response to DSS and antibiotics in vivo. (**a**) Experimental design for testing the effect of DSS and antibiotics on intestinal thiosulfate levels and thiosulfate sensor activation. Mice were given water with 3% DSS or without DSS on day 0, and on day 4

antibiotics were added to the water. The thiosulfate-sensing EcN strain with plasmid thsS(t3)R-GFP_mCherry was administered via oral gavage on day 5 for antibiotic-treated mice and on day 6 for mice not given antibiotics. Feces were collected on days 5-7, cecal contents were collected on day 7, and they were analyzed via IC-MS, flow cytometry, and plating. (**b**) Concentrations of thiosulfate measured via IC-MS in the feces or digesta of the cecum. (**c**) Mean GFP fluorescence of positive mCherry events of the sensor strain measured via flow cytometry. There is no flow cytometry data for mice not treated with antibiotic on day 7 because the strain did not colonize without antibiotics. (**d**) Colony forming units (CFU) per gram of feces measured by plating on selective media to assess colonization of the sensor bacteria. (**e**) In vitro characterization of the thsS(t3)R-GFP_mCherry EcN sensor strain in terms of mean GFP fluorescence measured via flow cytometry after inducing with varying thiosulfate concentrations in liquid culture at 37ºC. Maximal sensor activation observed in vivo in streptomycin-treated mice was only 11.8% that of maximal sensor activation observed in vitro.

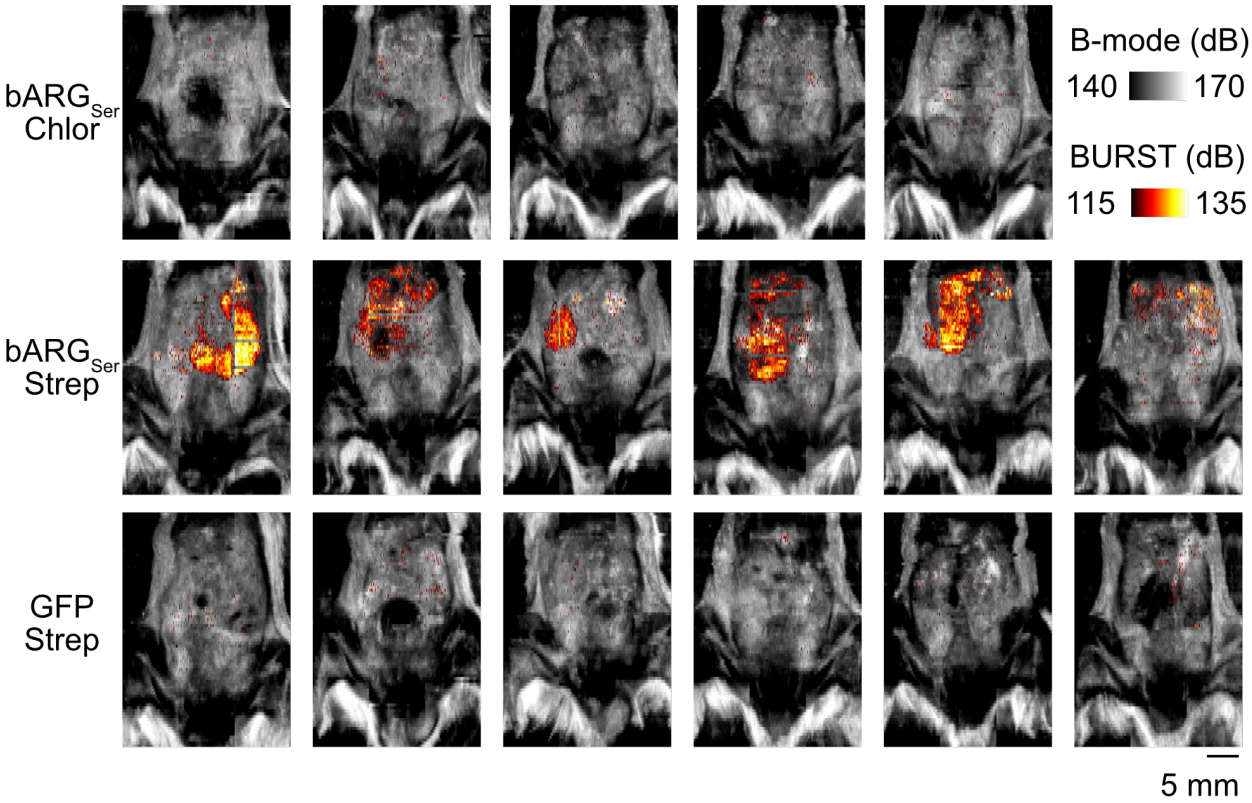

Figure S3.12: All ultrasound images of mice from the experiment depicted in Fig. 3.5. The integrated BURST* signal was overlaid onto the integrated B-mode signal for all mice treated with chloramphenicol and colonized with thsS(t3)R-Bxb1_P7-bARG$_{Ser}$ EcN (bARG$_{Ser}$ Chlor), for all mice treated with streptomycin and colonized with thsS(t3)R-Bxb1_P7-bARG$_{Ser}$ EcN (bARG$_{Ser}$ Strep), and for all mice treated with streptomycin and colonized with thsS(t3)R-Bxb1_P7-GFP_mCherry EcN (GFP Strep) on day 3.

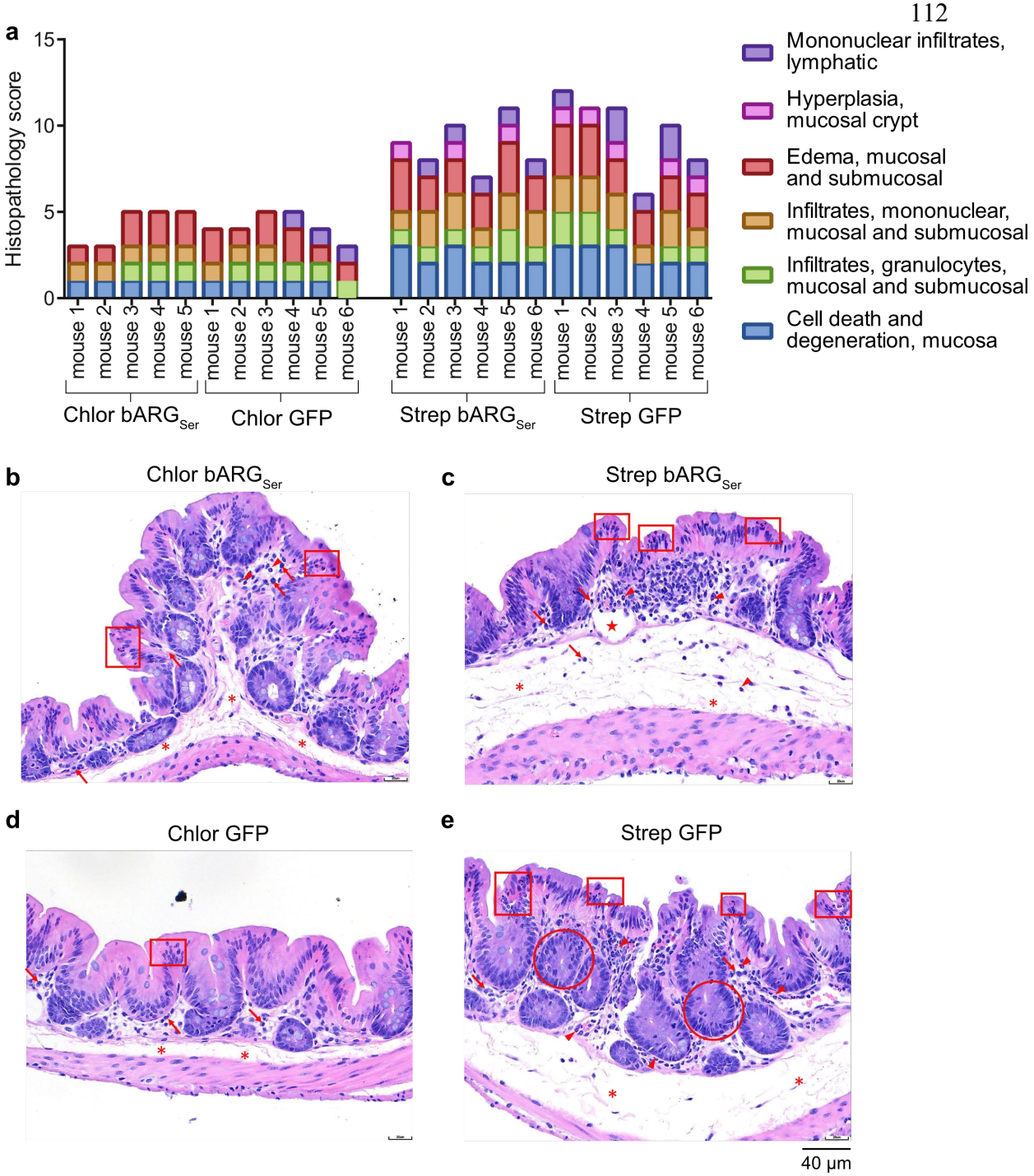

Figure S3.13: Full scoring data and additional histopathology images of cecal tissues from chloramphenicol- and streptomycin-treated mice. (**a**) Histopathology scoring of cecal tissues from chloramphenicol- and streptomycin-treated mice on day 5 of treatment broken down by category of abnormality. This data was aggregated for display in **Fig. 3.5k**. (**b-e**) Representative images of H&E-stained sections of cecal tissue on day 5 of antibiotic treatment for mice treated with chloramphenicol and colonized with thsS(t3)R-Bxb1_P7-bARG$_{Ser}$ EcN (b), treated with streptomycin and colonized with thsS(t3)R-Bxb1_P7-

bARG$_{Ser}$ EcN (c), treated with chloramphenicol and colonized with thsS(t3)R-Bxb1_P7-GFP_mCherry EcN (d), and treated with streptomycin and colonized with thsS(t3)R-Bxb1_P7-GFP_mCherry EcN (e). Abnormalities are indicated in red: mucosal epithelial cell death and degeneration (box), mucosal crypt hyperplasia (circle), mucosal/submucosal edema (asterisk), mononuclear infiltrates (arrow), granulocytic infiltrates (arrowhead), dilated lymphatic (star).

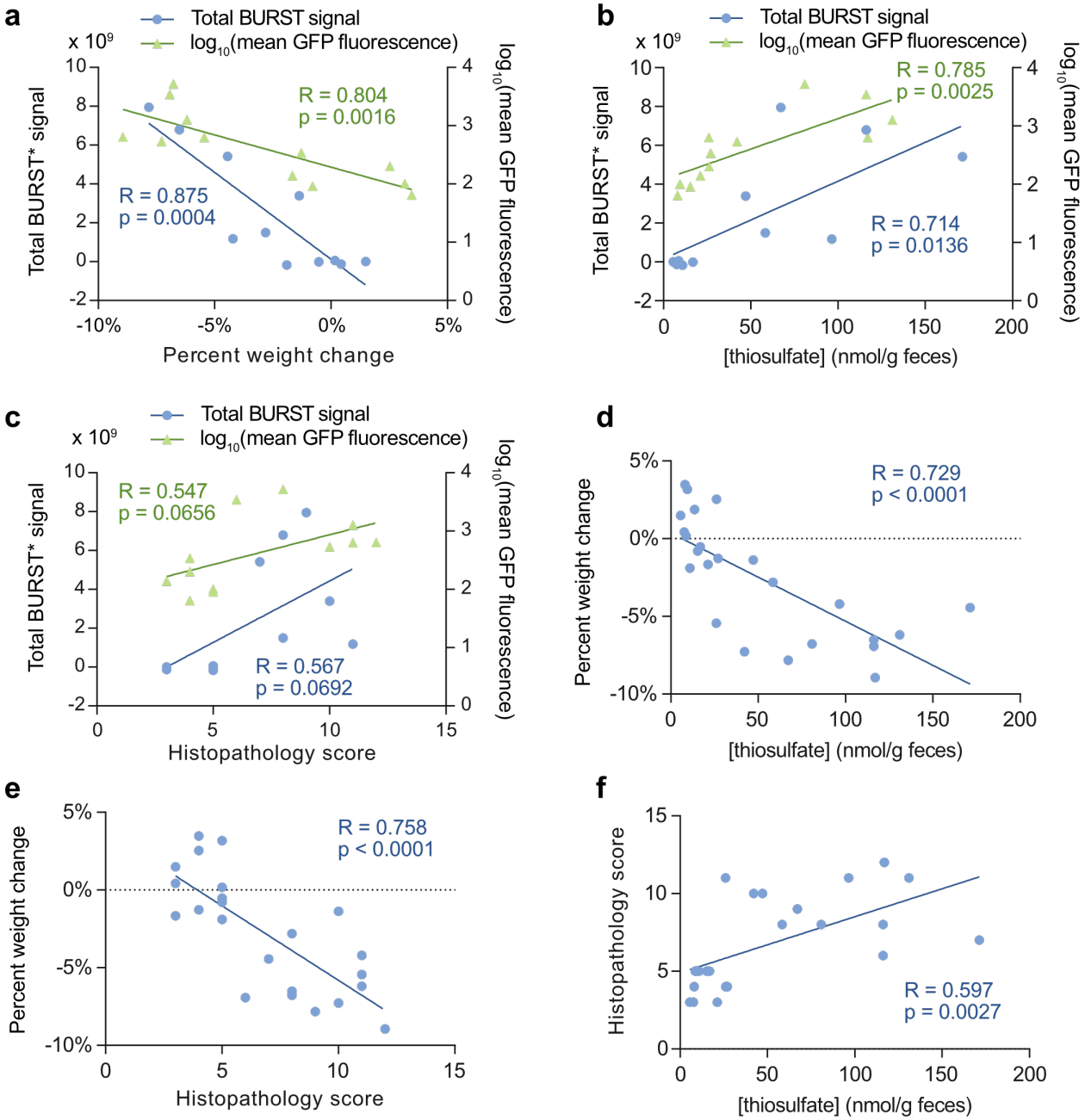

Figure S3.14: Correlations between thiosulfate sensor activation and disease severity in chloramphenicol- and streptomycin-treated mice. (**a-c**) Total BURST* signal imaged on day 3 or mean GFP fluorescence measured on day 4 versus the percent weight change on day 2 before mice were fasted with tail cups (a), versus the fecal thiosulfate levels measured via IC-MS on day 4 (b), and versus the histopathology score of cecal tissue on day 5 (c). (**d-e**) percent weight change on day 2 before mice were fasted with tail cups versus the fecal thiosulfate levels measured via IC-MS on day 4 (d), and versus the histopathology score of cecal tissue on day 5 (e). (**f**) Histopathology score of cecal tissue on day 5 versus the fecal thiosulfate levels measured via IC-MS on day 4. Lines represent linear regressions where R

represents the goodness of fit and the p value indicates whether the slope is significantly non-zero.

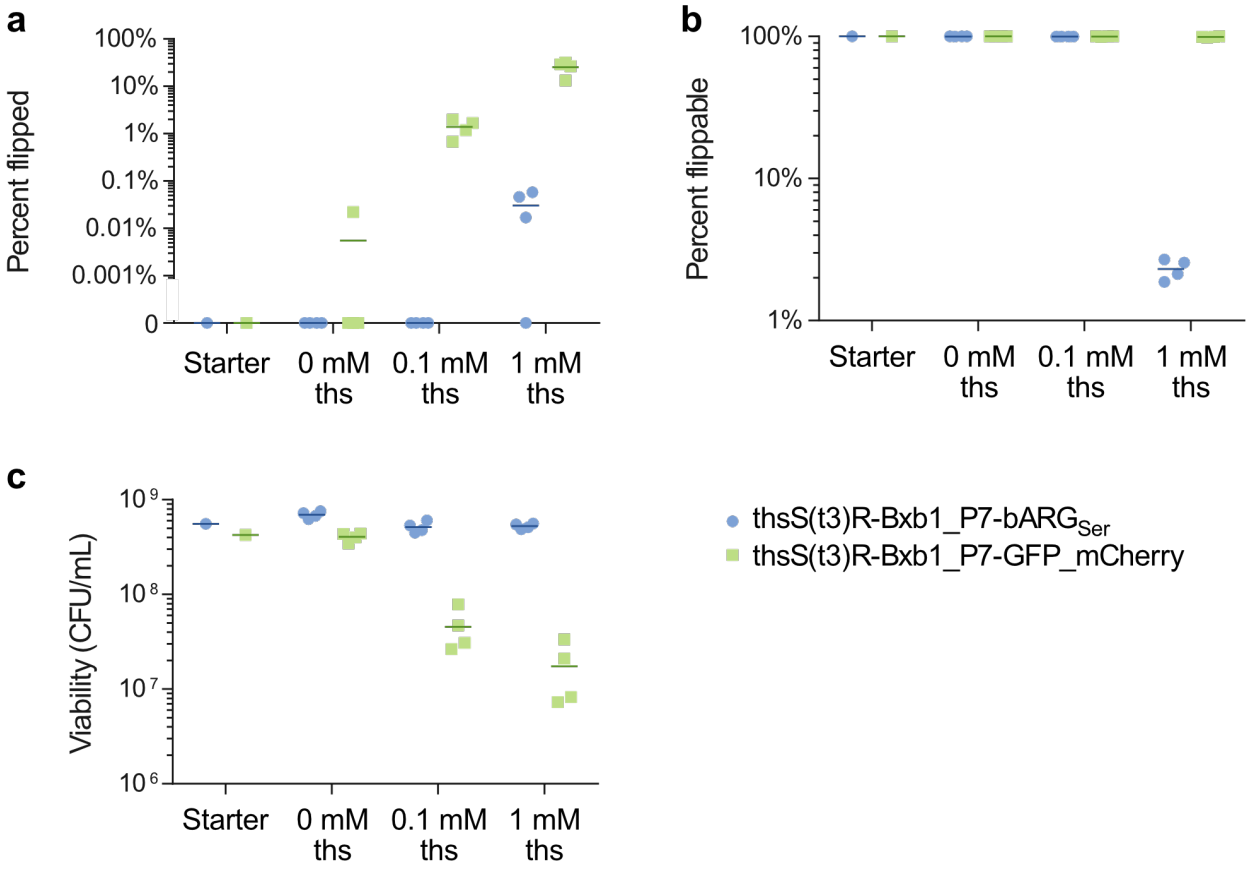

Figure S3.15: Percentage of flipped and flippable colonies and viability of Bxb1 switch strains after inducing with thiosulfate in vitro. (**a-c**) Percentage of colonies that were opaque or green fluorescent on plates without thiosulfate indicating the percent flipped (a), percentage of colonies that were opaque or green fluorescent on plates with thiosulfate indicating the percent flippable (b), and number of total colonies (CFU) per mL of culture plated (c) after inducing thsS(t3)R-Bxb1_P7-bARG and thsS(t3)R-Bxb1_P7-GFP_mCherry EcN strains with 0, 0.1, and 1 mM thiosulfate (N=4 biological replicates) or plating the uninduced starter culture (N=1 biological replicate). Points represent replicates and lines represent means.

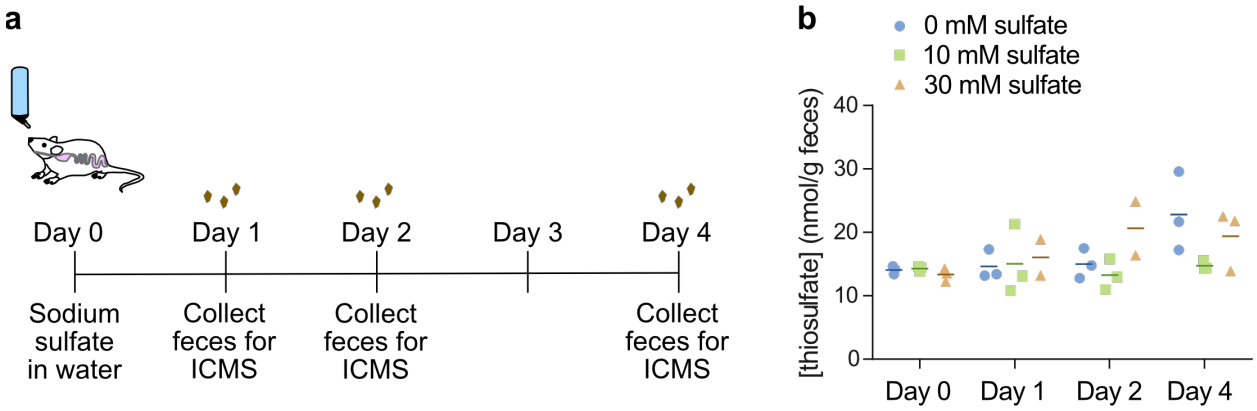

Figure S3.16: Effect of sodium sulfate in drinking water on fecal thiosulfate levels. (**a**) Experimental design, where mice were given drinking water containing 0, 10, or 30 mM sodium thiosulfate on day 0, and feces were collected and analyzed via IC-MS on days 0, 1, 2, and 4. 10 mM sodium thiosulfate corresponds to the concentration of sulfate in 5 g/L streptomycin sulfate. (**b**) Concentration of fecal thiosulfate measured by IC-MS. Supplementing the drinking water with sulfate did not significantly affect the fecal thiosulfate levels at any time point. Points represent biological replicates (N = 3 mice) and lines represent the mean.

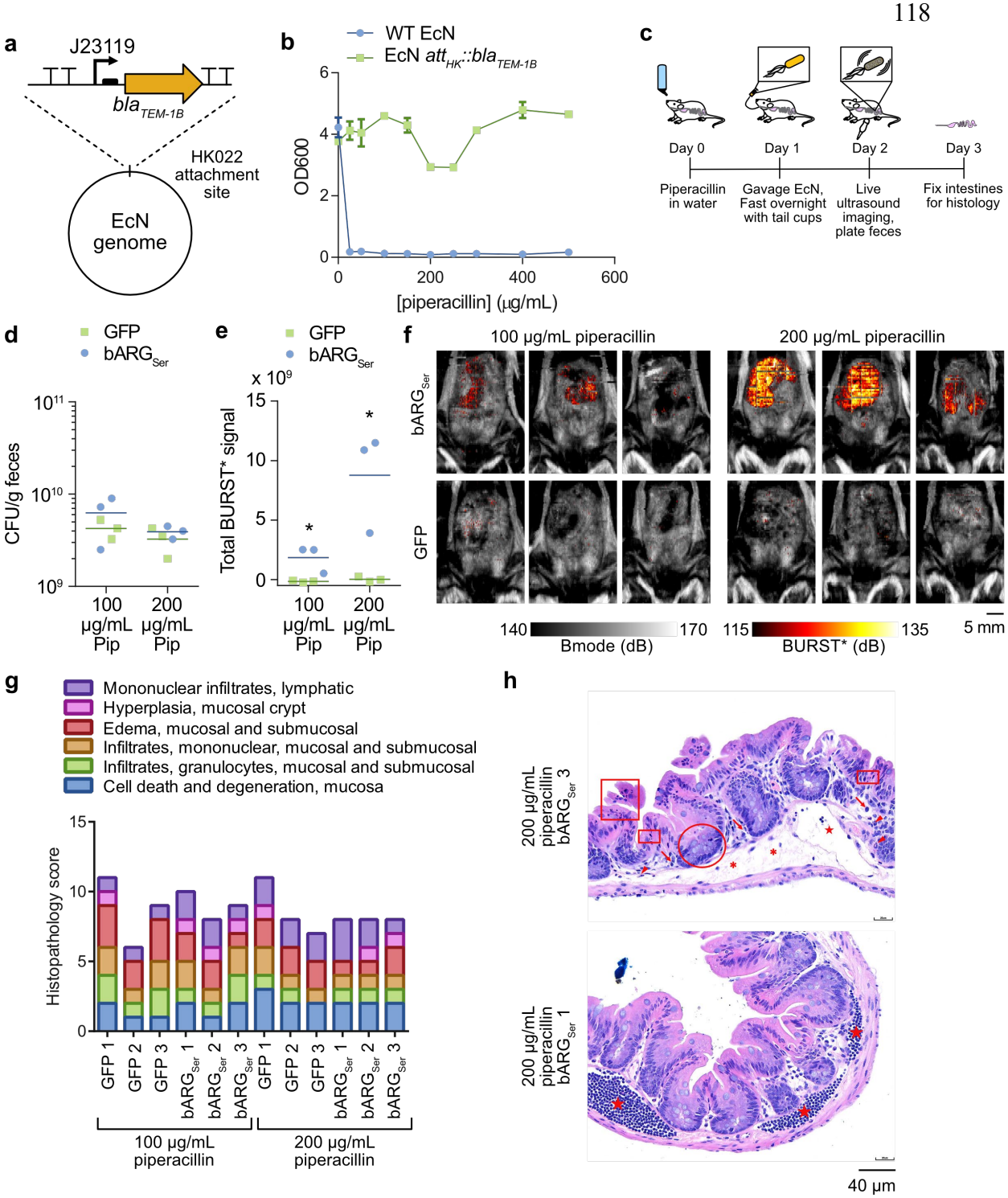

Figure S3.17: Ultrasound imaging of thiosulfate sensor activation in piperacillin-treated mice. (**a**) Diagram of genomic modification of EcN to confer piperacillin resistance. The beta lactamase gene *bla*$_{TEM\text{-}1B}$ known to confer piperacillin resistance in *E. coli*[123,124] was placed under control of the strong constitutive promoter J23119. This cassette was integrated into the genome at the phage HK022 attachment site in EcN using the clontegration

system[125]. See Table S2 for sequencing confirmation. (**b**) Optical density at 600 nm (OD600) after incubating wild-type (WT) EcN and the att_{HK}:bla_{TEM-1B} EcN in media at varying piperacillin concentrations to confirm piperacillin resistance of the att_{HK}:bla_{TEM-1B} strain. Points represent the mean of two biological replicates, error bars represent the standard deviation, and lines connect the points. (**c**) Experimental design for testing EcN strains containing plasmids for the optimized integrase-based switch thiosulfate sensors, thsS(t3)R-Bxb1_P7-$bARG_{Ser}$ or thsS(t3)R-Bxb1_P7-GFP_mCherry, in piperacillin-treated mice. One day after piperacillin was administered via drinking water, the EcN strains were administered via oral gavage and the next day mice were scanned with ultrasound using the setup depicted in **Fig 3.4c**. One day later on day 3, mice were sacrificed and their intestines were fixed for histology. (**d-e**) Colony forming units (CFU) per gram of feces (d) and total BURST* ultrasound signal imaged (e) on day 2 of piperacillin treatment (100 or 200 μg/mL) for mice colonized by thsS(t3)R-Bxb1_P7-$bARG_{Ser}$ ($bARG_{Ser}$) or thsS(t3)R-Bxb1_P7-GFP_mCherry (GFP) EcN. (**f**) Ultrasound images overlaying the integrated BURST* signal onto the integrated B-mode images for all mice on day 2 of piperacillin treatment. (**g**) Histopathology scoring of cecal tissues from piperacillin-treated mice on day 3 of treatment broken down by category of abnormality. Mice which received 200 ug/mL piperacillin did not exhibit significantly more signs of disease than mice which received 100 ug/mL piperacillin, but both piperacillin-treated groups exhibited more signs of disease than chloramphenicol-treated mice (see **Fig. S3.13a**). (**h**) Representative images of H&E-stained sections of cecal tissue on day 3 of piperacillin treatment. Abnormalities are indicated in red: mucosal epithelial cell death and degeneration (box), mucosal crypt hyperplasia (circle), mucosal/submucosal edema (asterisk), mononuclear infiltrates (arrow), granulocytic infiltrates (arrowhead), dilated lymphatic (star).

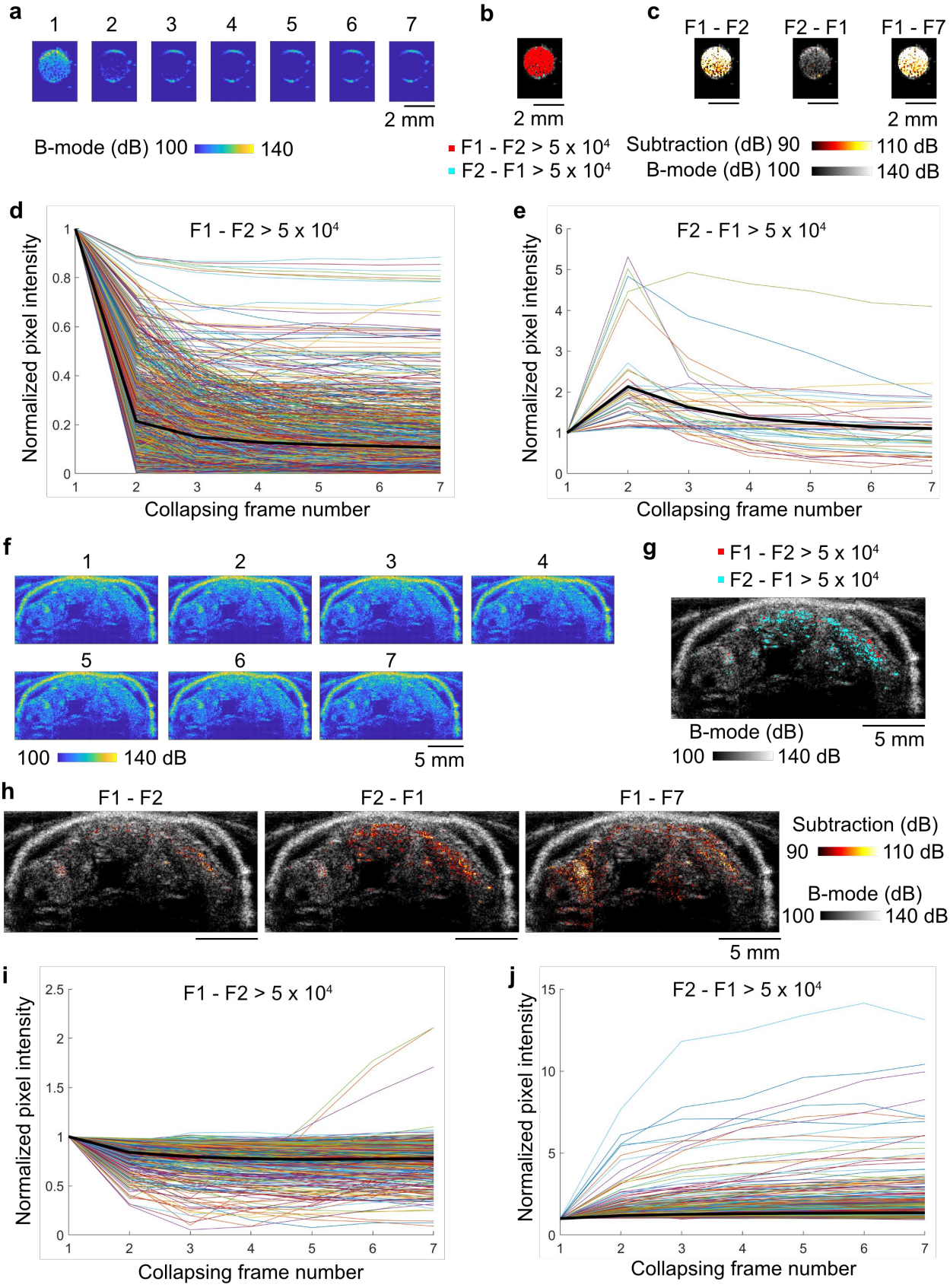
a
1
2
3
4
5
6
7
2 mm
B-mode (dB) 100
140
b
2 mm
F1 - F2 > 5 x 10⁴
F2 - F1 > 5 x 10⁴
c
F1 - F2
F2 - F1
F1 - F7
2 mm
Subtraction (dB) 90
110 dB
B-mode (dB) 100
140 dB
d
F1 - F2 > 5 x 10⁴
Normalized pixel intensity
Collapsing frame number
e
F2 - F1 > 5 x 10⁴
Normalized pixel intensity
Collapsing frame number
f
1
2
3
4
5
6
7
100
140 dB
5 mm
g
F1 - F2 > 5 x 10⁴
F2 - F1 > 5 x 10⁴
B-mode (dB)
100
140 dB
5 mm
h
F1 - F2
F2 - F1
F1 - F7
Subtraction (dB)
90
110 dB
B-mode (dB)
100
140 dB
5 mm
i
F1 - F2 > 5 x 10⁴
Normalized pixel intensity
Collapsing frame number
j
F2 - F1 > 5 x 10⁴
Normalized pixel intensity
Collapsing frame number

Figure S3.18: Processing BURST images in vitro versus in vivo. (**a**) B-mode images of the 7 collapsing frames acquired using a rapid BURST script (that uses 3 focused beams at a time) of an in vitro sample of EcN expressing $bARG_{Ser}$ at 5 x 10^8 cells/mL. The majority of the BURST signal is visible in the first collapsing frame. (**b**) For the in vitro sample, overlay of the pixels where the signal in the first collapsing frame (F1) is greater than the second (F2) by more than 5 x 10^4 (red), and the pixels where the signal from the second collapsing frame (F2) is greater than the first (F1) by more than 5 x 10^4 (cyan). (**c**) For the in vitro sample, overlay of different subtraction BURST images (hot scale) onto the B-mode image (greyscale): the first collapsing frame minus the second (F1-F2), the second collapsing frame minus the first (F2-F1), and the first collapsing frame minus the last (F1-F7). (**d-e**) For the in vitro sample, traces of normalized pixel intensities where the signal in the first collapsing frame (F1) is greater than the second (F2) by more than 5 x 10^4 (d) and where the signal from the second collapsing frame (F2) is greater than the first by more than 5 x 10^4 (e). The majority of pixels fall into the former category (d). (**f**) In vivo B-mode images of the 7 collapsing frames acquired using a rapid BURST script (that uses 3 focused beams at a time) of EcN expressing $bARG_{Ser}$ in the GI tract of a mouse. The background signal remains high throughout all 7 collapsing frames due to tissue. (**g**) For the in vivo acquisition, overlay of the pixels where the signal in the first collapsing frame (F1) is greater than the second (F2) by more than 5 x 10^4 (red), and the pixels where the signal from the second collapsing frame (F2) is greater than the first (F1) by more than 5 x 10^4 (cyan). The majority of pixels are in the latter category. (**h**) For the in vivo acquisition, overlay of different subtraction BURST images (hot scale) onto the B-mode image (greyscale): the first collapsing frame minus the second (F1-F2), the second collapsing frame minus the first (F2-F1), and the first collapsing frame minus the last (F1-F7). F1-F7 gives high background signal due to tissue movement over the 7 frames. (**i-j**) For the in vivo acquisition, traces of normalized pixel intensities where the signal in the first collapsing frame (F1) is greater than the second (F2) by more than 5 x 10^4 (d) and where the signal from the second collapsing frame (F2) is greater than the first by more than 5 x 10^4 (e). The majority of pixels fall into the latter category (j). For (d-e) and (i-j), pixel traces were normalized by dividing by their intensity at frame 1. Colored lined represent individual pixel traces while thick black lines represent the mean. The F2-F1 method was used to calculate BURST images for in vivo experiments, termed BURST*, because the majority of the ARG-specific signal occurs in F2, the signal does not uniformly collapse/decrease by F3, and using subsequent frames leads to high background due to tissue movement. We speculate that the majority of ARG-specific signal occurs in F2 rather than F1 due to shadowing from tissue. In contrast, since there is no movement of in vitro samples and the first collapsing frame displays the highest BURST signal while the last displays the least, the F1-F7 method was used to calculate the BURST image for all in vitro samples.

Chapter 4

SPATIAL CONTROL OF PROBIOTIC BACTERIA IN THE GASTROINTESTINAL TRACT ASSISTED BY MAGNETIC PARTICLES

Sections of this chapter have been adapted from:
Buss, M. T.#, Ramesh, P.#, English, M. A., Lee-Gosselin, A. & Shapiro, M. G. Spatial control of probiotic bacteria in the gastrointestinal tract assisted by magnetic particles. *Adv. Mater.* **33**, 2007473 (2021). https://doi.org/10.1002/adma.202007473. # Equal contribution.

4.1 Abstract

Engineered probiotics have the potential to diagnose and treat a variety of gastrointestinal (GI) diseases. However, these exogenous bacterial agents have limited ability to effectively colonize specific regions of the GI tract due to a lack of external control over their localization and persistence. Magnetic fields are well suited to provide such control, since they freely penetrate biological tissues. However, they are difficult to apply with sufficient strength to directly manipulate magnetically labeled cells in deep tissue such as the GI tract. Here, we demonstrate that a composite biomagnetic material consisting of micron-sized magnetic particles and probiotic bacteria, when orally-administered and combined with an externally applied magnetic field, enables the trapping and retention of probiotic bacteria within the mouse GI tract. This technology improves the ability of these probiotic agents to accumulate at specific locations and stably colonize without antibiotic treatment. By enhancing the ability of GI-targeted probiotics to be at the right place at the right time, cellular localization assisted by magnetic particles (CLAMP) adds external physical control to an important emerging class of microbial theranostics.

4.2 Introduction

The central role of the gastrointestinal (GI) microbiome in human health and disease[162] makes the GI tract a major target for the development of microbe-based diagnostic and therapeutic agents.[4] Probiotic bacteria have been engineered to sense and respond to markers of disease and release various therapeutic molecules in the GI tract.[27,163] However, the efficacy of such agents is often limited by the difficulty of achieving precise spatial distribution and persistence within the GI tract. In many cases, the limited ability of engineered probiotic bacteria to compete against native gut microbes necessitates the use of antibiotics to clear the native flora,[163,164] risking dysbiosis,[163,165] while the inability to spatially target colonization to certain segments of the tract after oral administration can reduce efficacy.[163] A method to non-invasively localize and retain bacteria at specified locations could greatly facilitate the development and application of GI probiotics.[27,163]

Here we introduce cellular localization assisted by magnetic particles (CLAMP) – an approach that uses locally amplified magnetic fields to provide non-invasive spatial control of cells within the GI tract. This approach takes advantage of the ability of magnetic fields

to penetrate biological tissue and exert force on magnetic objects, as has been shown in numerous studies. In previous work, magnetic fields have been used to localize therapeutic mammalian cells and magnetotactic bacteria to tumors,[36,166,167] enhance site-specific cellular uptake of viral vectors or drug-containing liposomes,[168,169] pattern tissues,[170–173] and remotely control microrobots in vivo.[174] However, while these approaches were effective for heavily iron-loaded cells or nanoparticles, they are challenging to apply to common probiotic bacterial species in the GI tract. This challenge arises fundamentally from the difficulty of creating a sufficiently strong magnetic force to overcome viscous drag forces at the desired location of magnetic manipulation within the GI tract. The force on a magnetized (*e.g.*, superparamagnetic) particle or cell is a product of the local magnetic field (**B**) and magnetic field gradient ($\nabla\mathbf{B}$) (Equation 4.1),[175] which decay rapidly in space as $1/r^3$ and $1/r^4$, respectively.

$$\mathbf{F_{mag}} = \frac{V\Delta\chi}{\mu_0}(\mathbf{B}\cdot\nabla)\mathbf{B}\,. \tag{4.1}$$

Here, $\Delta\chi$ represents the difference in magnetic susceptibility between the magnetized cell and its surrounding medium, V represents the volume of the magnetized cell, and μ_0 represents the permeability of free space. Since the magnetic force decays as $1/r^7$, previous efforts to maximize the localization and capture of magnetized cells in vivo have largely focused on increasing $\Delta\chi$ and $\nabla\mathbf{B}$ through the use of strong magnetic labels, and minimizing the distance between the external magnet and the desired target.[36,167,168,176] While these methods are successful in enhancing targeting to tissues that are near the magnet surface (d < 1 mm), they are insufficient for controlling the localization of engineered cells in the gastrointestinal (GI) tract, which spans approximately 3 – 13 mm from the abdominal surface in mice.[177] Additionally, viscous drag forces that act on cells in the GI tract counteract any externally supplied magnetic force. The viscosities of mucus, digesta, and feces in intestines are orders of magnitude higher than that of water,[178,179] making magnetic capture of cells in this environment extremely difficult.[180]

The CLAMP approach overcomes these challenges by combining an externally applied field with microscale amplification by co-administered magnetic microparticles (**Fig. 4.1a**). This approach is inspired by the design of magnetic in vitro separation columns,[181] in which a ferromagnetic matrix comprising a tightly packed slurry of ferromagnetic beads creates microscale field gradients of up to 10^4 T/m within the matrix mesh in response to a relatively weak externally applied "bulk" field (~0.45 T).[181] By locally amplifying the field gradients by a factor of $>10^4$, magnetic separation columns effectively capture sparsely labeled and even paramagnetic cells.[34,35,182,183] Given the success of this 'local amplifier' strategy in vitro, we hypothesized that a composite magnetic slurry approach could be extended towards the capture of magnetically labeled cells in the GI tract, where the field and field gradients are too weak on their own due to the distance between an external magnet and the intestines, in addition to the high viscosities encountered in the GI tract. In this study, we tested this basic hypothesis through computational modeling, in vitro experiments, and in vivo experiments in mice using BL21 *Escherichia coli* and the probiotic agent *E. coli* Nissle 1917.[184] Our results demonstrate the ability of CLAMP to enhance the spatial localization, retention, and colonization of orally administered therapeutic bacteria using an external magnetic field.

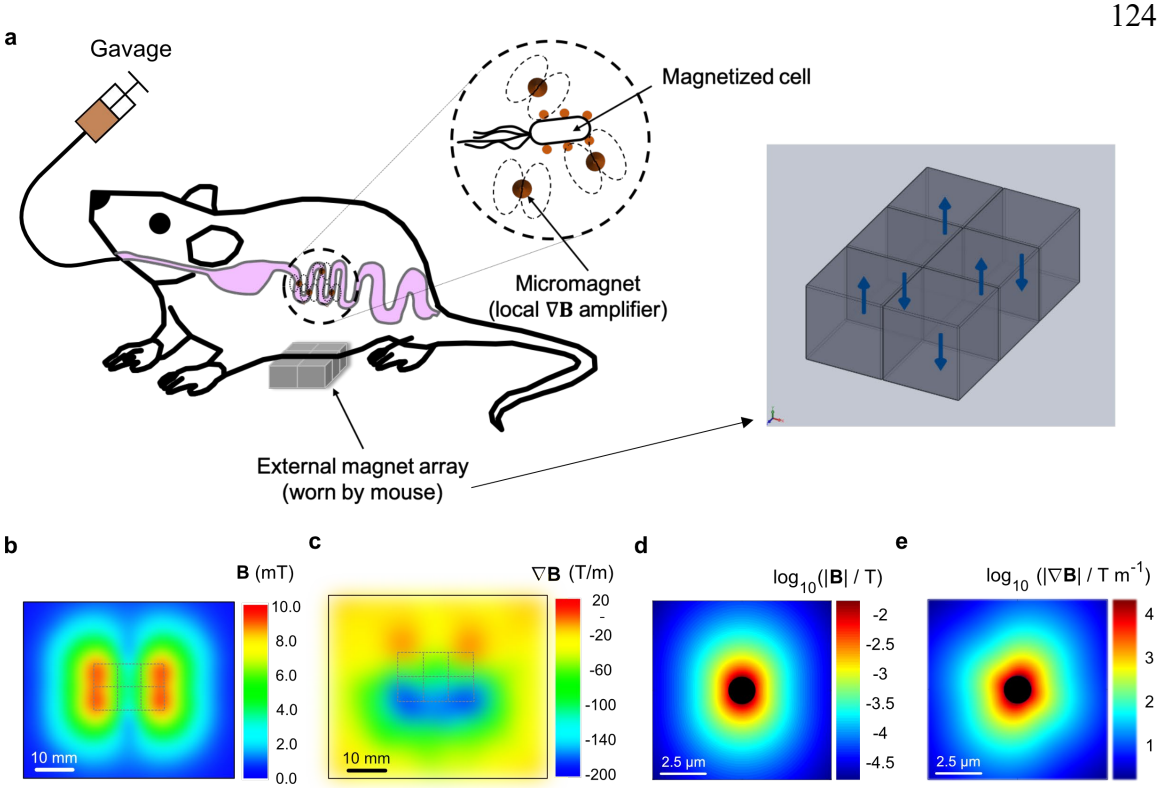

Figure 4.1. **Concept of cellular localization assisted by magnetic particles (CLAMP)**. **a**) A slurry consisting of synthetically magnetized cells and micromagnets is administered by oral gavage. An external magnet array placed on the abdomen captures the micromagnets in the small intestine, and causes the micromagnets to produce strong local field gradients that capture the magnetized cells. The magnet array used in this study consists of six B444-N52 magnets arranged in a 2 x 3 array with alternating magnetizations (grey box). Simulation of the **b**) magnetic flux density and **c**) magnetic field gradient at 10 mm from the surface of the magnet array. Simulation of the resulting **d**) magnetic flux density and **e**) magnetic field gradient produced by the micromagnets at 10 mm (plotted in log scale for clarity). The black circle indicates the micromagnet.

4.3 Results

To assess the feasibility of in vivo magnetic amplification, we simulated the magnetic field and field gradients generated by N52 NdFeB magnets and micron-sized amplifier particles, which we refer to as "micromagnets." As our micromagnets, we selected commercially available 1.5 μm diameter carboxyl-functionalized superparamagnetic iron oxide particles. Both the magnet configuration and the micromagnets were selected based on preliminary experiments with multiple configuration and particle types. At a distance of 10 mm from the surface of the permanent magnets, corresponding to the deepest location of most of the mouse GI tract[177] (**Fig. S4.1a**), the maximum field strength magnitude is 11.8 mT and the maximum magnitude of the field gradient is 271 T/m (**Fig. 4.1b-c**). Upon experiencing this field, the micromagnets amplify the field gradient to over 10^4 T/m (**Fig. 4.1e**). This amplification would be expected to increase the force acting on a magnetized bacterial cell in the vicinity of the micromagnet by approximately two orders of magnitude.

This force would act to attract the bacterium to the micromagnet, and the micromagnet, in turn, experiences a force due to the bulk field gradient, such that both the amplifier and the bacterial agent can be manipulated.

To study the conditions required for CLAMP to capture magnetically labeled *E. coli*, we started with a simplified in vitro model of the mouse GI tract (**Fig. 4.2a**). The average diameter of the mouse GI tract is 3.2 ± 0.76 mm,[185] with an average flow rate of approximately 30 µl/min.[169,186] To simulate these conditions, we used non-stick tubing with an inner diameter of 3.175 mm, and created a flow of 100 µl/min using a syringe pump (in excess of the upper range of peristaltic flow in vivo). We placed a R822-N52 magnet 10 mm away from the surface of the tubing using a 3D-printed holder. Into our flow tube, we administered several different 1 mL mixtures of micromagnets and magnetized mScarlet-expressing BL21 *E. coli*, followed by a 5 mL wash with clean buffer. The *E. coli* were rendered magnetic by biotinylation followed by incubation with streptavidin-coated 150 nm superparamagnetic iron oxide nanoparticles (SPIONs). The retention of bacteria in the flow chamber was quantified after each flow experiment using flow cytometry. We hypothesized that the presence of micromagnet amplifiers would greatly enhance the capture of magnetized cells. Furthermore, we hypothesized that if the micromagnets could be made to cluster in the flow medium, this would enhance their own capture by the bulk field (given the linear and cubic scaling of hydrodynamic drag and magnetic force, respectively), and therefore create a composite biomagnetic material that enhances the trapping of cells.

The capture of micromagnets was visually obvious 1 cm away from the N52 magnet (**Fig. 4.2b-d**), and was enhanced by including 100 mM Mg^{2+} to promote the clustering of the negatively-charged micromagnets via counter-ion interactions (**Fig. S4.2a-b**). As expected, flow cytometry revealed that the micromagnets significantly enhanced the capture of magnetized *E. coli* (**Fig. 4.2e**) by around 3-fold relative to a solution without micromagnets ($p<0.001$ by Welch's t-test). Clustering using 100 mM $MgCl_2$ further boosted capture of the magnetized *E. coli* ($p<0.001$), resulting in the retention of 51 ± 2.5% of the input cells (**Fig. 4.2e**). Notably, clustering also increased the concomitant capture of non-magnetized *E. coli* from 4.7 ± 0.2% to 22 ± 0.6% ($p<0.001$). This phenomenon likely arises from cationic crosslinking of the micromagnets and *E. coli*, since both have a negative surface charge (**Fig. S4.2**), as well as the enmeshment of the cells in the micromagnet clusters. This capture of non-magnetic cells may be beneficial in scenarios where the magnetic labeling of cells is not convenient or deleterious to cellular viability or function.

After establishing the conditions for effective use of CLAMP in vitro, we tested the ability of this technique to localize bacterial cells in vivo in the mouse small intestine. We selected this anatomical site because it is a target of many potential therapeutic interventions, but is challenging to colonize with common probiotic chasses like *E. coli*. In addition, transit through the small intestine is more rapid than through the large intestine,[187–190] providing a stringent test for our technology. In these experiments, we administered a mixture of clustered micromagnets and magnetized *E. coli* via oral gavage shortly before attaching permanent N52 magnets to the abdominal area above the small intestine (**Fig. 4.3a**). X-ray CT imaging confirmed that the composite biomagnetic material rapidly exited the stomach

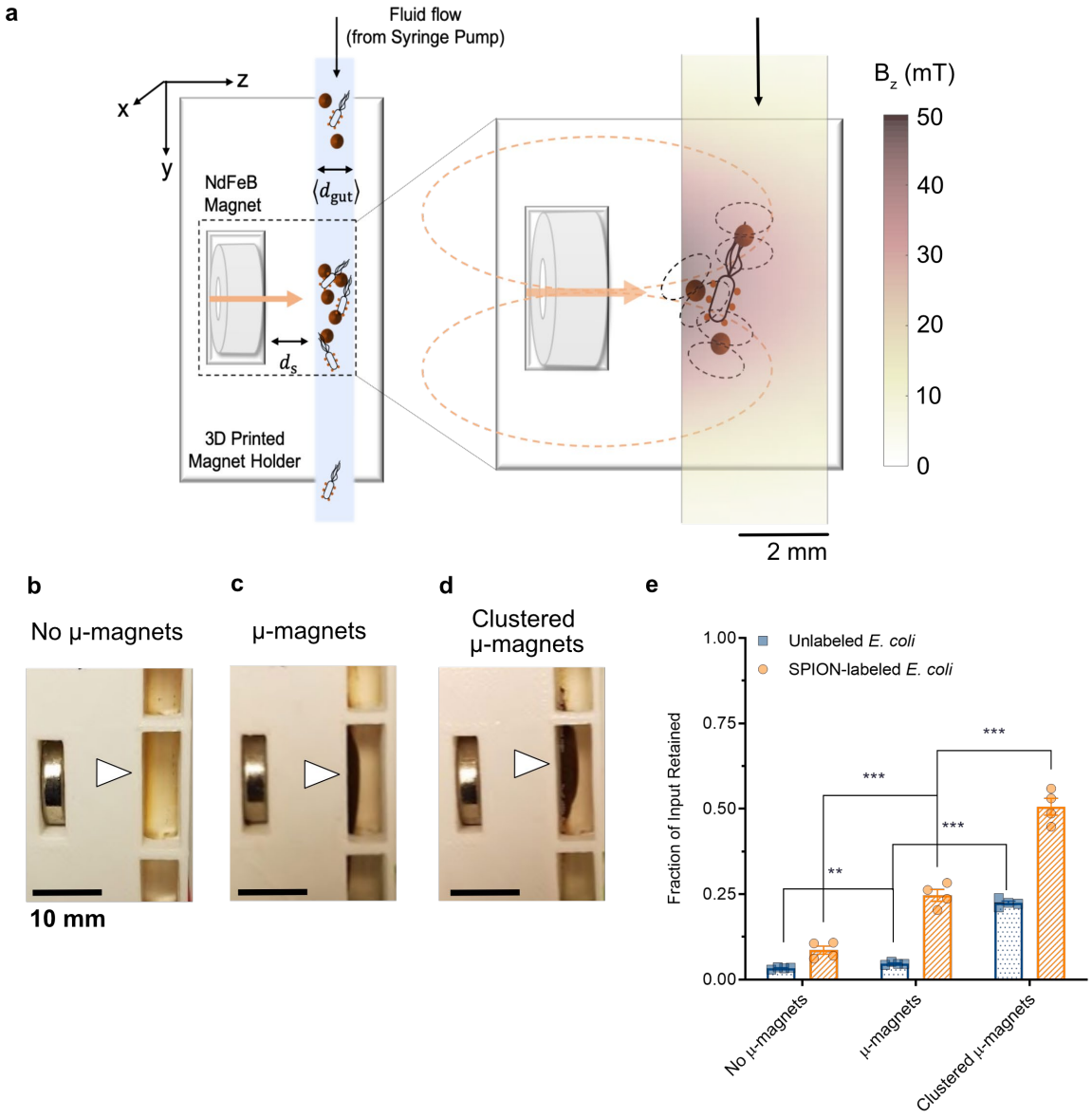

Figure 4.2. In vitro efficacy of CLAMP. **a**) In vitro model of the mouse GI tract. Synthetically magnetized BL21(DE3) *E. coli* cells express mScarlet to facilitate downstream quantification using flow cytometry. The color variation within the tube in the right inset represents the simulated magnetic field strength at a distance of z = 10-13 mm from the N52 magnet surface. The orange arrow indicates the direction of magnetization for the permanent magnet, while the dotted orange ellipses denote the magnetic field lines produced by the external magnet, as well as by the micromagnets within the tube. The coordinate frame is oriented such that gravity acts in the $+y$ direction and the center of the magnet is at (y = 40, z = 0). In vitro capture of micromagnets seen as dark clusters near the permanent magnet, indicated by white arrows: **b**) without micromagnets, **c**) with micromagnets, and **d**) with ionically clustered micromagnets. The slight brownish color in (b) is from the magnetic label used in magnetizing cells. **e**) In vitro capture of non-magnetic and synthetically magnetized BL21(DE3) *E. coli* without micromagnets, with micromagnets, and with clustered micromagnets. Error bars represent the standard error of mean (N = 4). Asterisks represent statistical significance by Welch's t-test (** = $p < 0.01$ and *** = $p < 0.001$).

and transited through the small intestine by 45-min post-gavage (**Fig. S4.1c**). To prevent the degradation of this composite biomagnetic material in the stomach, we added 10% (w/v) sodium bicarbonate to the gavage mixture and fasted mice overnight prior to gavage.[191,192] We also kept the mice on a diet of 5% (w/v) sucrose water after gavage to avoid the confounding effects of solids in the intestines and to facilitate detection of the composite biomagnetic material. X-ray CT confirmed that adding bicarbonate, fasting before gavage, and replacing solid food with 5% (w/v) sucrose after gavage water eliminated the signal from iron in the bladder and reduced background signal from food particles (**Fig. S4.1d-e**). Furthermore, to prevent the confounding effects of coprophagy,[193] tail cups were attached to all mice throughout the experiment (**Fig. 4.3b**). The abdominal magnets were kept on for 9 hours after gavage, as material largely exits the small intestine by this time,[190] and then mice were euthanized and dissected. This protocol (**Fig. 4.3a**) was reasonably well-tolerated by mice, which were monitored at least every two hours for signs of significant distress.

To maximize retention of the composite biomagnetic material in vivo, we assembled an array of permanent magnets with alternating magnetizations (**Fig. 4.1a** and **Fig. 4.3b**), which results in multiple magnetic field-gradient hotspots in vivo, both at the surface (**Fig. S4.3b-c**) and at depth. These hotspots produce a stronger force on magnetic particles, localizing accumulation at distinct spatial regions. Our abdominal magnet array spread the magnetic attractor points across the abdomen of the mouse (**Fig. 4.3b**), covering most of the small intestine, which spans the largest area in the GI tract. Attaching this magnet array to mice gavaged with clustered micromagnets resulted in capture of the micromagnets (seen as dark clusters) near the edges of the block magnets at 9 hours post-gavage (**Fig. 4.3c**), as expected. Furthermore, capture was consistent across all mice with this magnet array: all exhibited dark clusters in the small intestine (**Fig. 4.3e**) at 9 hours post-gavage. These clusters were strongly magnetic and attracted to a permanent magnet (**Fig. 4.3f**), and could be visualized with magnetic resonance imaging (MRI) (**Fig. S4.4**). In contrast, mice wearing non-magnetic washers of equivalent weight and size as the magnet array did not have these clusters in their small intestines. Instead, the micromagnets accumulated in the cecum, as seen by its darkened color and magnetic behavior, as well as in the large intestine at 9 hours-post gavage (**Fig. 4.3c-d**). These data collectively demonstrate that we were able to retain micromagnets in the small intestine for 9 hours using our optimized in vivo protocol and magnet configuration.

This retention of micromagnets at magnetic field and field gradient hotspots allowed us to concomitantly retain the co-gavaged magnetized *E. coli* cells at these loci. To quantify capture of the *E. coli*, the small intestine was divided into 4 segments of roughly equal length (8 cm each) (**Fig. 4.3d-e**) and the contents were analyzed with flow cytometry. For ease of detection and to prevent confounding effects of proliferation in the GI tract during initial experiments, we used BL21(DE3) *E. coli* that exhibits bright fluorescence when expressing mScarlet and does not normally persist or proliferate in the mouse GI tract because it is not adapted to this environment.[194,195] In mice wearing magnet arrays, the gavaged *E. coli* were retained throughout the small intestine (**Fig. 4.3g**), as expected based on the distribution of micromagnet clusters. In contrast, in mice wearing non-magnetic washers, significantly fewer *E. coli* were detected in the small intestine ($p<0.05$ for all segments); only a small fraction of the gavaged *E. coli* were detected in the last segment of the small intestine near

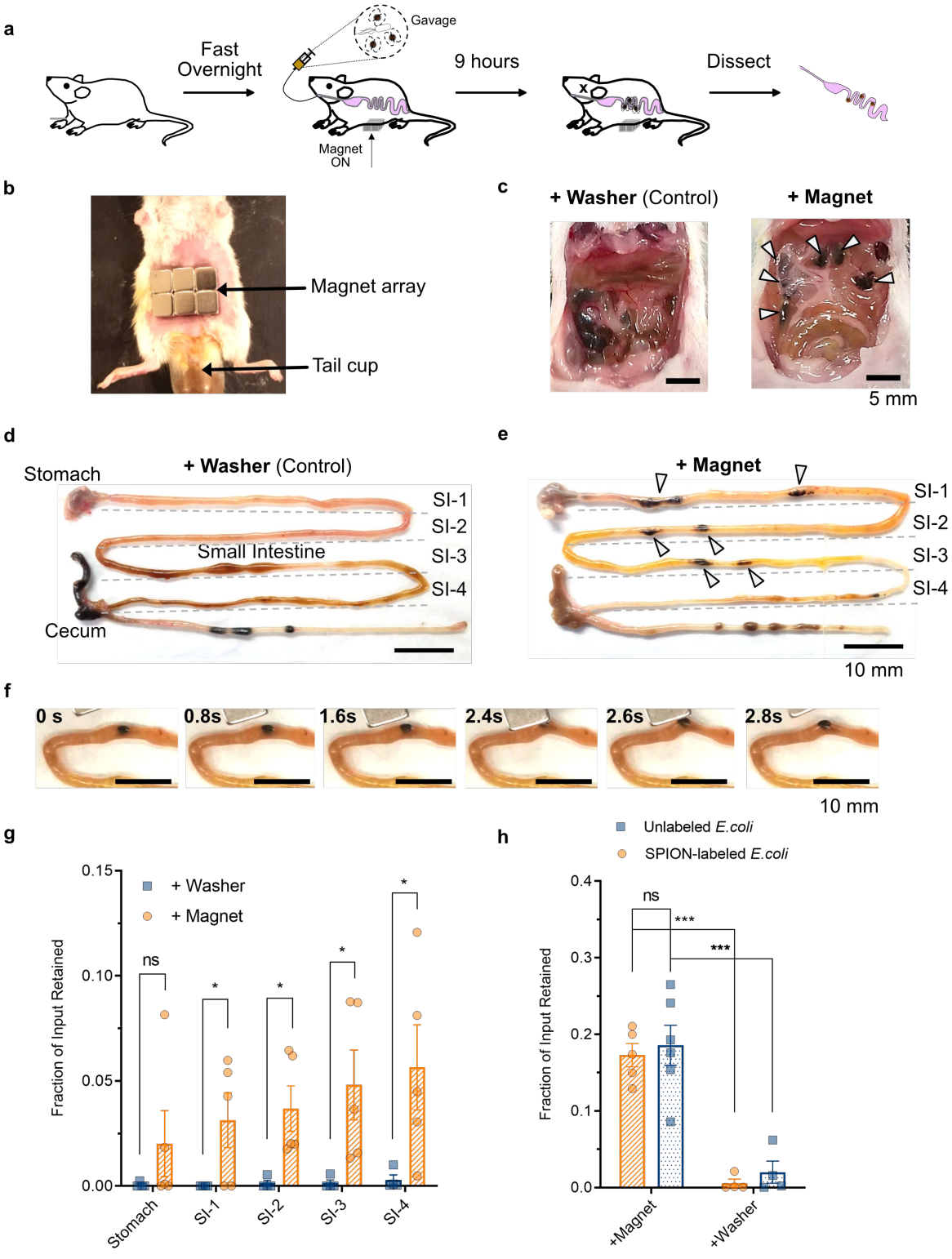
a
Fast
Overnight
Gavage
Magnet
ON
9 hours
Dissect
b
Magnet array
Tail cup
c
+ Washer (Control)
+ Magnet
5 mm
d
Stomach
+ Washer (Control)
SI-1
SI-2
Small Intestine
SI-3
SI-4
Cecum
e
+ Magnet
SI-1
SI-2
SI-3
SI-4
10 mm
f
0 s
0.8s
1.6s
2.4s
2.6s
2.8s
10 mm
g
+ Washer
+ Magnet
Fraction of Input Retained
0.15
0.10
0.05
0.00
ns
*
Stomach
SI-1
SI-2
SI-3
SI-4
h
Unlabeled E.coli
SPION-labeled E.coli
Fraction of Input Retained
0.4
0.3
0.2
0.1
0.0
ns
***
+Magnet
+Washer

Figure 4.3. CLAMP enables the localization of non-colonizing BL21(DE3) *E. coli* in the small intestine. **a**) Protocol for testing CLAMP in vivo with BL21(DE3) *E. coli*, which does not normally colonize or persist in the mouse GI tract, avoiding confounding effects of proliferation on measurements of fractional retention. After fasting overnight with tail cups, a mixture of micromagnets and *E. coli* is administered via oral gavage and the magnet array is attached to the abdomen. Nine hours after gavage, mice are euthanized and dissected. **b**) Placement of the magnet array and tail cup on a representative mouse. **c**) Representative images of mice dissected 9 h post-gavage that were wearing the magnet array or a non-magnetic washer of equivalent weight. Arrows indicate the dark puncta of micromagnets that appeared to cluster near the edges in the magnet array. Representative images of intestines from mice dissected 9 h post-gavage that were wearing the **e**) magnet array or a **d**) non-magnetic washer of equivalent weight. **f**) The clusters of micromagnets, indicated by the arrows in (e), were attracted to a permanent magnet (still video images here are from a mouse gavaged with fluorescent particles instead of *E. coli*, see Fig. 4.5, but are representative of all mice wearing magnet arrays). No magnetic clusters were observed in the small intestine of mice wearing the washer; instead the micromagnets appeared to be accumulated in the cecum (d). For quantification, the small intestines were divided into 4 segments (SI-1 through SI-4) of roughly equal length as indicated in (d) and (e). **g**) Distribution of magnetized BL21(DE3) *E. coli* detected in the contents of the small intestinal segments and the stomach at 9 h post-gavage. **h**) Overall fractional retention of magnetized and non-magnetic BL21(DE3) *E. coli* in the small intestine of mice wearing magnet arrays or non-magnetic washers at 9 h post-gavage. Error bars represent the standard error of mean ($N = 5$ for +Magnet group with SPION-labeled *E. coli*, $N = 6$ for +Magnet group with unlabeled *E. coli*, $N = 4$ for +Washer groups). Asterisks represent statistical significance by the Mann–Whitney test in (g) and by Welch's *t*-test in (h) (*** = $p < 0.001$, * = $p < 0.05$, and ns = no significance).

the cecum, again consistent with micromagnet localization (**Fig. 4.3g**). The levels of *E. coli* detected were significantly higher in small intestinal segments in each mouse where micromagnet clusters were observed (**Fig. S4.5**), indicating the bacteria were trapped in the micromagnet clusters, consistent with our in vitro observations. Collectively, 17 ± 1.5% of the gavaged magnetized *E. coli* were retained in the small intestines of mice wearing magnet arrays at 9 hours post-gavage, compared with 0.60 ± 0.50% in the small intestines of mice wearing non-magnetic washers (**Fig. 4.3h**; $p<0.001$ by Welch's t-test). To our surprise, when we repeated the same experiment with non-magnetized *E. coli*, the non-magnetized *E. coli* were equivalently retained as the magnetized *E. coli* (no statistically significant difference between the two groups), with 19 ± 2.6% of the input bacteria captured (**Fig. 4.3h**). This result suggests that the electrostatic binding of *E. coli* with the micromagnets mediated by Mg^{2+} is sufficient for capture in vivo, consistent with our observations in vitro. Serendipitously, this voids the need for magnetically labeling cells, greatly simplifying our CLAMP strategy, and overcoming possible challenges of magnetic label dilution during cell growth in vivo or certain cells' intolerance of the labeling protocol.

We next aimed to use CLAMP to enhance the GI persistence of a therapeutically-relevant bacterium, *E. coli* Nissle 1917 which, in contrast to the strain used in **Fig. 4.3** above, is adapted to the gut environment.[184] It is normally difficult for exogenously introduced bacteria to colonize the GI tact because of colonization resistance due to endogenous flora[196]. Consequently predominant strategies used to obtain colonization involve treatment with antibiotics (e.g. streptomycin for *E. coli* colonization in mice[197]), repeated gavage of large numbers of bacteria, or the use of germ-free/gnotobiotic animals.[198] Instead of these highly perturbative and time-consuming methods for colonization, we hypothesized that CLAMP could offer a more straightforward colonization strategy. Accordingly, we co-gavaged

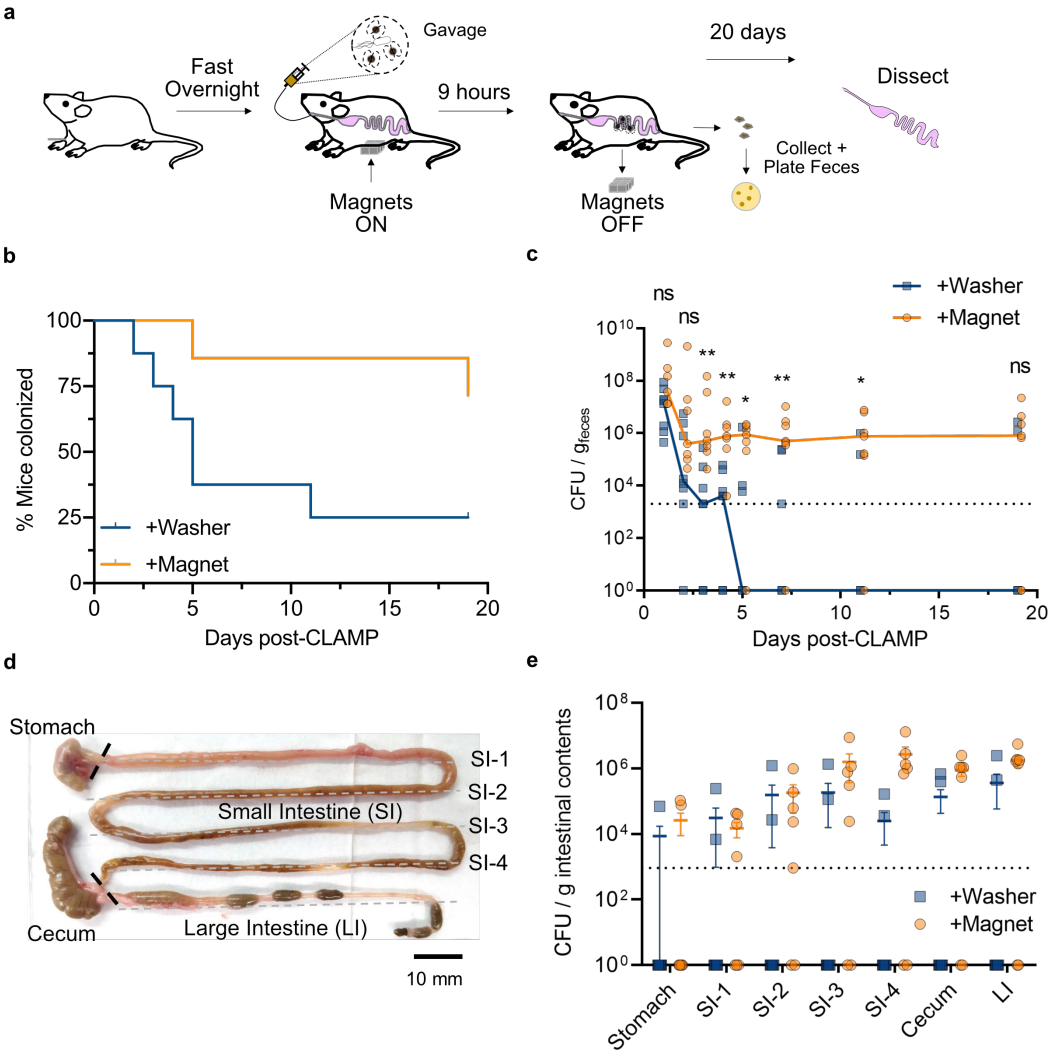

Figure 4.4. CLAMP enhances GI persistence of probiotic *E. coli* Nissle. **a**) Protocol for testing the effect of CLAMP on persistence of *E. coli* Nissle. After CLAMPing non-magnetic *E. coli* Nissle using clustered micromagnets for 9 h, magnets are removed and mice are returned to normal food and bedding. Feces are collected and plated on days 1-5, 7, 11, and 19 after CLAMP. On day 20 post-CLAMP, mice are euthanized and their intestinal contents are plated. **b**) Percent of mice with any detectable *E. coli* Nissle ($\geq$ 2000 CFU g^{-1} feces) in the feces after gavage as determined by plating on selective media. The magnet group (orange line) was $N = 7$ and the washer group (blue line) was $N = 8$. No *E. coli* Nissle were detected before gavage. The two curves are significantly different by both the log-rank (p = 0.0436) and Gehan–Breslow–Wilcoxon (p = 0.036) tests. **c**) Colony forming units (CFUs) per gram of feces at 1, 2, 3, 4, 5, 7, 11, and 19 days after CLAMP. The limit of detection (LOD) was 2000 CFU g^{-1} feces, which is indicated using dashed lines. For clarity, the median of the data are also plotted. Asterisks represent statistical significance by the Mann–Whitney test without correction for multiple comparisons (** = $p < 0.01$, * = $p < 0.05$, and ns = no significance). **d**) Representative image of intestines from a mouse wearing a magnet array on day 20 post-gavage. No micromagnets can be seen and the intestines appear healthy. **e**) Distribution of *E. coli* Nissle in intestinal segments as indicated in (d) at day 20 post-gavage. There appears to be no significant difference between the distributions of mice from the two groups that were still colonized at day 20 ($N = 5$ for +Magnet mice, $N = 2$ for +Washer mice). Horizontal lines represent the mean and error bars represent the SEM.

~5 x 10^7 CFU of non-magnetized *E. coli* Nissle and clustered micromagnets into mice wearing magnet arrays or non-magnetic washers. Our dose of probiotic *E. coli* was below that which is typically administered in pre-clinical mouse models.[199] The cells were engineered to contain a plasmid with a stability cassette and antibiotic resistance marker. After 9 hours, the magnets or washers, as well as tail cups, were removed and mice were returned to normal bedding and diet. Fresh fecal pellets were collected daily for 5 days, and at 7, 11, and 19 days post-gavage, and analyzed for engineered *E. coli* Nissle CFUs by plating on selective media (**Fig. 4.4a**).

We found that in mice that were CLAMPed with magnets, *E. coli* Nissle persisted for much longer than in mice which wore non-magnetic washers. *E. coli* Nissle was detectable (≥ 2,000 CFU/g feces) for up to 19 days in 5 of 7 mice that wore the magnet arrays, versus in only 2 of 8 mice that wore non-magnetic washers (**Fig. 4.4b**). Starting at 3 days post-CLAMP, the levels of *E. coli* Nissle in the feces of mice that wore the magnet arrays were significantly higher than in mice that wore non-magnetic washers ($p<0.05$); the levels stabilized at around 10^6 CFU/g feces in mice from both magnet and washer groups that were still colonized by 11 days post-CLAMP (**Fig. 4.4c**). At day 20, all mice were sacrificed and their intestines were dissected. No micromagnets were observed in the intestines of either the magnet or washer groups (**Fig. 4.4d**), indicating that all administered micromagnets had exited the GI tract. The intestines also appeared healthy, indicating that CLAMP did not cause visible tissue damage in the long term. The intestinal contents from different sections were also analyzed for CFUs (**Fig. 4.4e**). In all mice where no *E. coli* Nissle was detected in the feces at day 19, no *E. coli* Nissle was detected in the intestinal contents at day 20. In mice with detectable *E. coli* Nissle in the intestinal contents at day 20, there appeared to be no significant difference in the distribution between the magnet (5 colonized mice) and washer (2 colonized mice) groups. These results suggest that CLAMP does not affect the spatial distribution of exogenously introduced bacteria after stable colonization, but significantly enhances the likelihood of successful colonization.

Finally, as a complement to microbial colonization, we tested whether CLAMP can be used to enterically retain orally administered synthetic nanoparticles, which would be useful to deliver drugs affecting the microbiome or GI diseases. In this experiment, we gavaged magnetically-labeled 500 nm fluorescent polystyrene particles, which are approximately the same size and surface charge as *E. coli*[200] (**Fig. S4.2a-b**), with clustered micromagnets into mice shortly before attaching magnet arrays or washers, as depicted in **Fig. 4.3a**. After 9 hours, the mice were euthanized and dissected, and the intestines were analyzed visually for the presence micromagnets and with flow cytometry for the presence of fluorescent particles. Micromagnet localization was similar to that observed after co-administration with bacteria (**Fig. 4.5a-d**). Magnetized nanoparticles were also localized in the upper GI tract (**Fig. 4.5e**). Overall, 42 ± 4.0% of the administered magnetized particles were retained in the small intestine of mice wearing magnet arrays at 9 hours post-gavage, compared with 3.8 ± 2.8% in mice wearing washers (**Fig. 4.5f**; $p<0.0001$). When the same experiment was repeated with non-magnetized particles, we observed some (10 ± 3.6%) non-specific capture of non-magnetized particles in mice wearing the magnet array, consistent with our in vitro experiments with particles (**Fig. S4.6**). We hypothesize that the significant difference ($p<0.0001$) in in vivo capture between magnetically-labeled and unlabeled

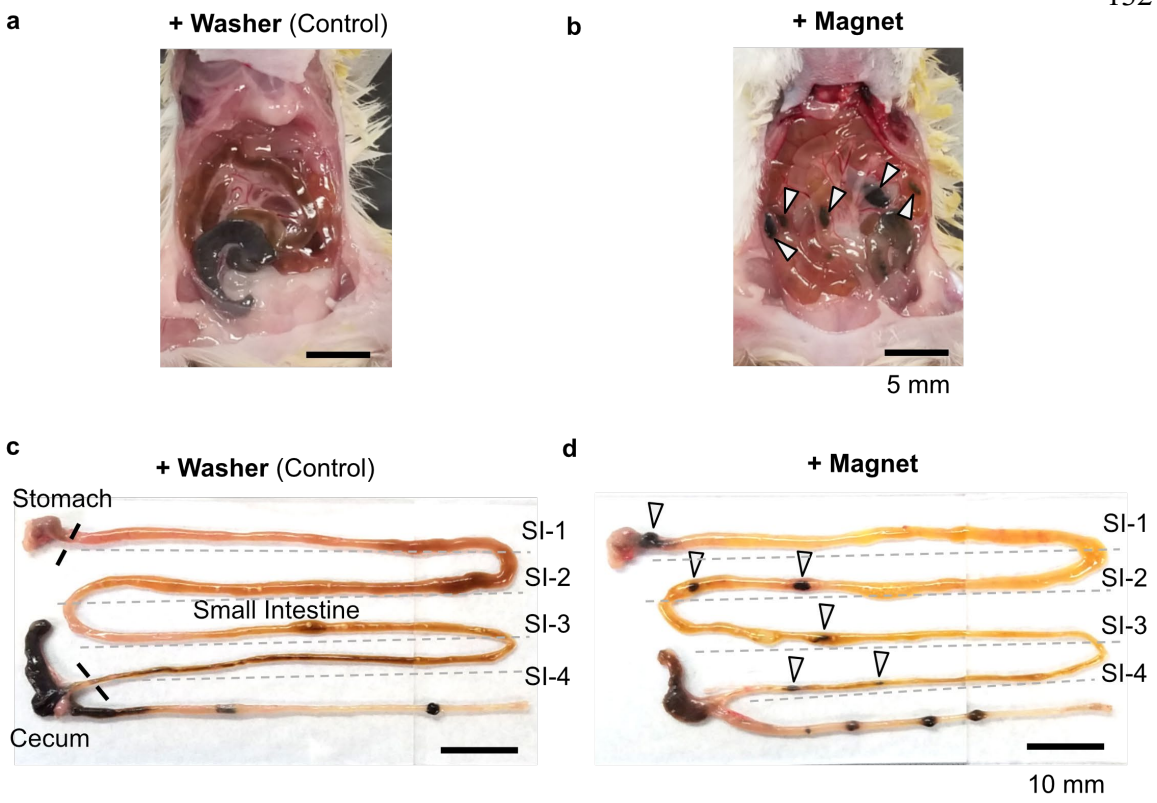
a
+ Washer (Control)
b
+ Magnet
5 mm
c
+ Washer (Control)
Stomach
SI-1
SI-2
Small Intestine
SI-3
SI-4
Cecum
d
+ Magnet
SI-1
SI-2
SI-3
SI-4
10 mm
e
+ Washer
+ Magnet
Fraction of Input Retained
0.4
0.3
0.2
0.1
0.0
ns
**
**
*
ns
Stomach
SI-1
SI-2
SI-3
SI-4
f
Unlabeled Particle
SPION-labeled Particle
Fraction of Input Retained
0.75
0.50
0.25
0.00
****
****
+Magnet
+Washer

Figure 4.5. CLAMP enables upper GI localization of synthetic particles. Representative images of mice dissected 9 h post-gavage that were wearing **b**) the magnet array or **a**) a non-magnetic washer of equivalent weight. Arrows indicate the dark puncta of micromagnets that appeared to cluster near the edges in the magnet array. Representative images of intestines from mice dissected 9 h post-gavage that were **d**) wearing the magnet array or **c**) a non-magnetic washer of equivalent weight. For quantification, the small intestines were divided into 4 segments (SI-1 through SI-4) of roughly equal length as indicated in (c) and (d). **e**) Distribution of magnetized particles detected in the contents of the small intestinal segments and the stomach at 9 h post-gavage. **f**) Overall fractional retention of magnetized and non-magnetic particles in the small intestine of mice wearing magnet arrays or non-magnetic washers at 9 h post-gavage. Error bars represent the standard error of mean (N = 6 for +Magnet groups, N = 4 for +Washer groups). Asterisks represent statistical significance by the Mann–Whitney test for (e) and by Welch's t-test for (f) (**** = $p < 0.0001$, ** = $p < 0.01$, * = $p < 0.05$, ns = no significance).

nanoparticles exists, in contrast to magnetically-labeled and unlabeled bacteria, because the nanoparticles have a higher extent of SPION-labeling, making them more strongly magnetic. Additionally, bacteria may be more effective in clustering non-magnetically with micromagnets in the more complex in vivo conditions due to their more complex surface chemistry and geometry.

4.4 Discussion

In sum, remote control of cellular localization is a long sought-after goal within the synthetic biology community, which if successful would enable new applications in biological research and therapy. Current methods to localize microbes in the GI tract rely on species' natural niche preference; however, even microbial species that can stably colonize a specific GI niche find it difficult to gain a foothold in the presence of resident flora. Deeply penetrant forms of energy such as magnetic fields provide a potential solution for enabling remote control of cells in the GI tract. However, to-date most applications involving magnetic control or actuation require that the cells be immediately adjacent (< 1mm) to the magnetic source.

Inspired by decades-old magnetic separation columns which enable the capture of weakly magnetized cells, CLAMP extends magnetic control to depths > 1 cm. In mice, this approach provides an approximately 50-fold enhancement of *E. coli* retention in the small intestine. While the wearable magnet configuration used in our study targeted the bacteria to locations throughout the entire small intestine, in principle magnets can be similarly assembled to target a specific region of the small intestine or other GI segment through local hotspots of magnetic field and field gradients. It should be noted that the timing of when the magnet is worn is also important because once the composite biomagnetic material passes through a particular GI segment it would be difficult to pull it back against the natural flow of peristalsis. Additionally, magnetic field and field gradient hotspots reach maxima at shallower depth, making it important to time the magnet placement to avoid off-target capture. It should also be noted that, serendipitously, we found that ionically mediated clustering of micromagnets and negatively charged cells, which results in the local assembly of a composite biomagnetic material, enables robust retention or colonization even when cells are not magnetically labeled. Since most bacteria have a net negative surface charge under physiologically relevant conditions[201], we anticipate that CLAMP can be generalized to microbes other than *E. coli*, to be confirmed in follow-up studies.

In addition to enabling targeted retention in the small intestine for up to 9 hours after gavage, CLAMP also enhanced the persistence of probiotic *E. coli* Nissle for up to 20 days without antibiotic treatment – in fact, the administered bacteria persisted long after the external magnets had been removed and the micromagnets had passed out of the GI tract. This suggests that magnetically retaining the *E. coli* Nissle cells near the small intestinal walls for 9 hours allows the bacteria to establish a local foothold and subsequently colonize throughout the GI tract. We believe that this magnetically enhanced colonization can be useful for studies of the gut microbiome by obviating the need for antibiotic treatment, which causes large-scale disruption of the endogenous microbiome, or germ-free animals, which are difficult to work with. Importantly, our optimized CLAMP protocol was well-tolerated by the animals in our experiments, as it did not require restraint of the mice and did not result in any intestinal blockages or other adverse effects. Furthermore, our CT experiments confirmed that the addition of bicarbonate in the gavage formulation was successful in mitigating micromagnet degradation and subsequent iron adsorption by the GI tract - which is undesirable despite the fact that iron-oxide particles are approved for human use by the FDA.[202]

Finally, this technique can potentially be scaled for use in larger animals, as has similarly been demonstrated in studies that use either permanent magnets or electromagnets to localize magnetic capsules in the GI tracts of human subjects.[203] We estimate that if the external magnet is scaled to several centimeters and the micromagnets are scaled to several microns in size, then sufficient magnetic forces should be exerted on micromagnets in the human small intestine, which is on average 6 cm from the abdominal skin (**Fig. S4.7**; see "Scaling estimations" section in the supporting methods for more details). Rather than attaching the magnet to the patient during use, the patient could lie down during the procedure, consistent with the current approach to magnetically guided capsule endoscopy.[204] As with any other novel treatment, such administration of engineered probiotic agents would need to be justified by significant therapeutic benefits, such as treatment of metabolic diseases or cancer.[205] Future studies would need to determine the optimal design parameters for micromagnets, permanent magnets, dosing and timing to apply CLAMP to larger animals and ensure safety.

4.5 Methods

Materials: NEB Turbo *E. coli* were used for all cloning and plasmid maintenance purposes. BL21(DE3) *E. coli* and *E. coli Nissle* 1917 were used for in vitro and in vivo experiments. LB Broth and LB-agar (Lennox) plates were prepared according to the manufacturer's instructions (Millipore-Sigma). Magnets were obtained from K&J Magnetics and non-stick plastic tubing was obtained from McMaster-Carr. The following nano- and micro-particles were used (manufacturer indicated in parentheses): Hi-Sur Mag 150 nm Streptavidin Beads (Ocean Nanotech), 1.5 μm BioMag Carboxyl particles (Bangs Laboratories), and 0.5 μm Biotin Coated Fluorescent Nile Red Particles (Spherotech). All particles were washed 3 times and re-suspended at the appropriate concentration in the appropriate buffer before use. All chemicals were of analytical grade and commercially available.

In vitro model of the mouse GI tract: To test capture of *E. coli* and 0.5 μm particles in vitro, a syringe pump was used to flow a suspension of mScarlet-expressing magnetized BL21(DE3) *E. coli* or magnetized 0.5 μm Nile-red particles and micromagnets (1.5 μm BioMag Carboxyl) at 100 μL min^{-1} through non-stick tubing (1/8" ID x 3/16" OD). The tubing was held vertically and flow was in the direction of gravity to avoid issues with beads settling and bubbles being introduced while changing the syringe. A 1/2" OD x 1/8" ID x 1/8" thick ring magnet (D822-N52) with the axial direction pointing toward the tube was held at 10 mm away from the surface of the tubing using a 3D-printed holder. For each run, first 1 mL of 4 mg micromagnets and ~10^8 magnetized *E. coli* or ~10^8 magnetized Nile red particles in the appropriate buffer + 0.5% (w/v) BSA was flowed at 100 μL min^{-1}; non-magnetized *E. coli* or non-magnetized particles were used as controls where indicated. Next, 5 mL of buffer + 0.5% (w/v) BSA at 100 μL min^{-1} was used to wash away beads that were not trapped and the flow through + wash was collected (~5.2 mL); during changing the syringe before the wash, care was taken not to introduce bubbles and a stopcock valve was used to prevent the fluid from flowing out the bottom due to gravity. Then the magnets were removed from the holder and the remaining liquid in the tubing was collected as the eluate (~0.8 mL). The mass of each fraction (flow through + wash and eluate) was measured to get an estimate of the volume assuming the density is approximately that of water. Capture of the magnetized *E. coli* or magnetized particles was quantified by counting the number of cells or particles in each fraction with flow cytometry (described below). Percent capture was calculated by dividing the number of cells or particles in the eluate by the total number of cells or particle or in the two fractions.

Animal procedures: All animal experiments were approved by the California Institute of Technology Institutional Animal Care and Use Committee (IACUC). All mice were 5-7 week-old female Balb/c mice obtained from Jackson Labs and were gavaged using a 20 gauge 1.5" length animal feeding needle. Gavage volume was 200 μl and consisted of a mixture of micromagnets (4 mg), magnetized *E. coli* or magnetized 0.5 μm Nile red particles (~10^8), 10% (w/v) $NaHCO_3$, and 0.5% (w/v) BSA in 100 mM $MgCl_2$. If the *E. coli* were induced to express mScarlet, the gavage mixture was also supplemented with 0.2% L-arabinose. Prior to gavage, mice were fasted overnight with tail cups and individual housing with access to water only. The abdominal fur was also removed with Nair prior to gavage. Within 5 minutes after oral gavage, mice were sedated with isoflurane (2%) and the appropriate magnet array or a non-magnetic washer of similar size and weight was glued onto the abdominal area with GLUture Topical Tissue Adhesive (Abbott Laboratories). Adhesive tape was wrapped around the abdomen to further secure the magnet or washer and prevent it from hanging off the skin. The tail cups were changed while the mice were on their backs under isoflurane anesthesia. The entire process of attaching the magnet or washer and changing the tail cup took no longer than 10 minute per mouse. Water with 5% (w/v) sucrose (and 0.2% (w/v) L-arabinose if the *E. coli* were induced to express mScarlet) was provided and mice were housed individually while the magnet/washer was attached.

For dissection experiments, mice were euthanized at 9 hours after gavage by sedating with isoflurane and performing cervical dislocation. Intestines were removed, connective tissue and mesenteric fat were carefully removed from the intestines with forceps, and a wet

Kimwipe was used to remove any blood. Intestines were then photographed and analyzed with MRI or flow cytometry.

For colonization experiments, *E. coli* Nissle transformed with a plasmid containing a chloramphenicol resistance cassette and the Axe-Txe toxin-antitoxin stability cassette[206] was grown in LB + 25 μg mL^{-1} chloramphenicol to an OD of 0.4-0.6 and washed three times in PBS shortly before gavage. Gavage volume was 200 μl and consisted of a mixture of micromagnets (4 mg), *E. coli* Nissle (~5 x 10^7 CFU), 10% (w/v) $NaHCO_3$, and 0.5% (w/v) BSA in 100 mM $MgCl_2$. At 9-hours post gavage the magnets or washers and tail cups were removed while mice were under isoflurane anesthesia. Mice were then placed in fresh cages with standard bedding, food, and water in pairs of the same experimental group. Fresh fecal samples were collected at various time points (1, 2, 3, 4, 5, 7, 11, and 19 days post-gavage) by placing mice in fresh cages with wire bottoms for around 5 min each. To quantify Colony Forming Units (CFUs) in the feces, samples were homogenized at 100 mg mL^{-1} in PBS using a MP Biomedical FastPrep 24 Tissue Homogenizer set to 6 m s^{-1} for 20 sec. Eight 10-fold serial dilutions were prepared in PBS and plated on LB plates with 25 μg mL^{-1} chloramphenicol using the drop plate method as described previously.[156] At 20 days post gavage all mice were euthanized and dissected. Their intestines were segmented into stomach, 4 small intestinal segments (SI-1 through SI-4), cecum, and large intestine. The contents of these segments were homogenized in 1 mL PBS and plated in the same way the fecal samples were plated.

Flow-cytometry: A MACSQuant VYB flow cytometer (Miltenyi Biotec) was used for all flow cytometry analysis with the following settings: low flow rate, medium mixing, 25 uL uptake volume, standard mode, chilled 96 rack, and a trigger by SSC with a threshold of 4.00. For analyzing in vitro samples, appropriate dilutions in PBS + 0.5% (w/v) BSA were prepared to target 10^5 – 10^6 particles mL^{-1}. For analyzing in vivo samples, the small intestines were divided into four ~8 cm segments and the contents were carefully squeezed out using forceps. The stomach contents were also carefully squeezed out. The contents were suspended in PBS at a concentration of 100 mg mL^{-1} and homogenized by vortexing and sonicating. The resulting homogenates were filtered through 40 μm Cell Strainers (VWR) and diluted in PBS + 0.5% (w/v) BSA to concentrations of 10 mg mL^{-1} and 1 mg mL^{-1} before being run. The Y1 channel (561 nm laser, 586/15 nm filter) was used to quantify Nile red particles as well as mScarlet-expressing *E. coli*. Gains and thresholds were set based on control samples.

Particle labeling: To label 0.5 μm biotin-coated fluorescent Nile red particles with Hi-Sur Mag 150 nm streptavidin beads, 10^8 biotin-coated Nile red particles were first suspended in 850 μL PBS with vortexing. A mixture of 0.05 mg Neutravidin DyLight633 (ThermoFisher) and 0.5 mg Hi-Sur Mag 150 nm streptavidin beads in PBS (150 μL) was then added to the suspension. The suspension was immediately vortexed and incubated at room temperature with rotation for 90 minutes. The excess dye and unlabeled biotin-coated particles were removed by magnetic separation and washed twice with PBS + 0.5% (w/v) BSA. To prepare the corresponding non-magnetized particles, the above procedure was followed except no Hi-Sur Mag 150 nm streptavidin beads were added and the excess dye was removed by centrifugation and washing with PBS + 0.5% (w/v) BSA at 6500g.

SPION labeling of E. coli: The appropriate strain of BL21(DE3) *E. coli* or *E. coli* Nissle 1917 was used to inoculate 2 mL of LB medium + 25 μg mL^{-1} chloramphenicol. This starter culture was grown overnight at 37ºC and 250 rpm and sub-cultured into 25 mL or 50 mL of LB medium + 25 μg mL^{-1} chloramphenicol in 250 mL baffled shake flasks at a 1:100 dilution ratio. The subculture was grown at 37ºC and 250 rpm until the OD_{600} reached 0.4 to 0.6. If the cultures were to be induced, at this point 0.2% (w/v) arabinose was added and the cultures were grown at 37ºC and 250 rpm for an additional 6 hours to allow for expression. Subsequently, 20 mL of culture was spun down at 3500 x g and 4ºC, washed four times with PBS (pH 8.1), and re-suspended in PBS (pH 8.1) at an OD_{600} of ~2. One mg of EZ-Link Sulfo-NHS-LC-LC-Biotin (Thermo Fisher Scientific) was added to 1 mL of the suspension, which was then incubated with rotation at 4ºC for 60 to 90 min. The biotinylation reaction was quenched by adding 1 mL of PBS + 100 mM glycine and mixing. The suspension was then pelleted at 3500 x g and 4ºC and re-suspended in 400 μL routine PBS with 0.2% L-arabinose if the cells were induced. Next, 100 μL of 5x (5 mg mL^{-1}) Hi-Sur Mag 150 nm Streptavidin Beads (SPIONs) were added and the cells + beads mixture was incubated overnight at 4ºC with rotation. The next day, directly before use in subsequent experiments, the cells + beads mixture was magnetically separated by holding a magnet to the side of the tube, allowing the beads and labeled cells to migrate towards the magnet, and pipetting off the supernatant. The pellet containing SPION-labeled *E. coli* was washed twice in and re-suspended in the appropriate amount buffer for use in subsequent experiments. Unlabeled *E. coli* was prepared the same as labeled *E. coli* except that no EZ-Link Sulfo-NHS-LC-LC-Biotin or Hi-Sur Mag 150 nm Streptavidin Beads were added and centrifugation was used for washing steps.

Simulations: The magnetic flux density and magnetic field gradient for the array of permanent magnets were calculated using EMWorks with a global element size of 3.52 mm, a tolerance of 3.6×10^{-6}, and 4,520,208 elements. The magnetic flux density and magnetic field gradient for the micromagnets were calculated in MATLAB using a mesh size of 100 nm X 100 nm, respectively. The manufacturer supplied mass magnetization curves and initial volume susceptibility were fitted to a classical Langevin magnetization function, in order to estimate the magnetization of a bead under an applied magnetic field. EMWorks magnetic field simulations were used to deduce the strength and direction of the magnetic field at 10 mm from the surface of the magnet array. The axial (Bz) magnetic field was chosen as the magnetizing field, and the bead's resulting magnetic moment was calculated from the fitted Langevin function. Thereafter, the bead's dipole field and field gradients were numerically calculated using the classical field-dipole equations in a 2D plane, corresponding to a distance of 10 mm.

X-ray CT imaging: CT images of the abdominal area (45 x 45 mm field-of-view) were acquired using 3D micro-CT (Rigaku) with a resolution of 90 μm, tube potential peaks of 90 kV, tube current of 88 μA, and imaging duration of approximately 5 min. Mice were sedated during imaging using isoflurane (1%) at various time points after gavage. The magnets/non-magnetic washers were removed prior to imaging and immediately re-attached afterwards. Thresholding and 3D image reconstruction was performed using ImageJ.

MRI: Shortly after dissection, mouse intestines were fixed using 10% formalin at room temperature for 20 minutes. Fixed intestines were washed using cold PBS + 0.1 mM

L-ascorbic acid and stored at 4ºC until imaging. Before imaging, intestines were cast in a 1% (w/v) agarose gel phantom to minimize susceptibility artifacts. A Bruker 7 T small-animal scanner was used for all MR imaging, with a Rat volume coil (70 mm inner diameter) supplying the RF for ^{1}H spin-excitation and subsequent readout. Given the high relaxivity of the micromagnets gavaged, a 3D UTE sequence (T_E = 20 μs, T_R = 8 ms, N_{avg} = 2) was used to localize micromagnets within the intestines, using an isotropic voxel size of 234 μm. A 3D FLASH sequence, with an isotropic voxel size of 325 μm, was used to obtain anatomical images of the *ex vivo* GI tract specimens.

Scaling estimations: To estimate the approximate sizes of the external wearable magnet and internal micromagnets needed to use CLAMP in larger animals such as humans, we first approximate the wearable magnets as a sphere. This approximation yields an order-of-magnitude scaling insight into the relevant sizes of the magnets used for CLAMP, as well as the expected field and field-gradient strengths. Furthermore, we neglect any azimuthal components, focusing to model just the axial magnetic field for simplicity (Equation 2)[207]:

$$B(z) = \frac{2\mu_0 M R_{\text{magnet}}^3}{3z^3} \quad . \tag{2}$$

Here, z is the axial distance from the center of the spherical magnet, M is the volume magnetization, R_{magnet} is the magnet's radius, and μ_0 is the permeability of free space constant. The magnitude of the magnetic field gradient is then given by equation 3:

$$\left|\frac{dB}{dz}\right| = \frac{2\mu_0 M R_{\text{magnet}}^3}{z^4} \quad . \tag{3}$$

Substituting these expressions into equation 1 (see main text), the magnitude of the force on the micromagnets is approximated by equation 4:

$$\left|F_{\text{mag}}\right| = \frac{16\pi}{9} \frac{\mu_0 M^2 \Delta\chi R_{\text{bead}}^3 R_{\text{magnet}}^6}{z^7} \, . \tag{4}$$

Here R_{bead} is the radius of the micromagnets and $\Delta\chi$ is the difference in magnetic susceptibility between the micromagnets and the surrounding medium. In mice, the small intestine is at an average distance of 10 mm from the abdominal surface; in humans the small intestine is at an typical distance of 60 mm[208,209]. From our in vivo results, we can conclude that the magnetic forces achieved by CLAMP are sufficient to arrest downstream peristaltic transport of the composite biomagnetic material once formed at a desired GI locus. Similar magnetic forces need to be achieved in larger animals to obtain similar retention of magnetized cells and particles. If we assume that the same magnetic materials are used in larger animals, then M and $\Delta\chi$ are the same, and the following relation must hold:

$$\frac{R_{\text{bead, mouse}}^3 R_{\text{magnet, mouse}}^6}{(R_{\text{magnet, mouse}} + 10)^7} = \frac{R_{\text{bead, human}}^3 R_{\text{magnet, human}}^6}{(R_{\text{magnet, human}} + 60)^7} \, . \tag{5}$$

Here we specifically provide the scaling relationship for use of CLAMP in humans, but the approach is generalizable to any other animal. In our in vivo experiments with mice, the micromagnets had an average diameter of 1.5 μm, so $R_{\text{bead, mouse}} = 7.5 \times 10^{-4}$ mm; and the volume of the wearable magnet array was 1.54 cm^3 , so the equivalent radius is $R_{\text{magnet, mouse}} = 7.16$ mm. To estimate the radius of micromagnets and the permanent magnet needed for use in humans, these values were plugged into equation 5 and $R_{\text{bead, human}}$ was solved for using varying values of $R_{\text{magnet, human}}$ in MATLAB (**Fig. S4.7**).

4.6 Acknowledgements

MTB and PR contributed equally to this work. This work was supported by the Pew Charitable Trust, the Packard Foundation, and the Heritage Medical Research Institute. MTB was supported by an NSF GRFP fellowship. PR was supported by a Rosen center for Bioengineering predoctoral fellowship. The authors would like to thank Dr. Said Bogatyrev and Dr. Asher Preska Steinberg for their helpful advice, the Caltech Flow Cytometry Facility for assistance with flow cytometry, and Ivetta Vorobyova for her help with X-ray CT studies.

4.7 Supplementary information

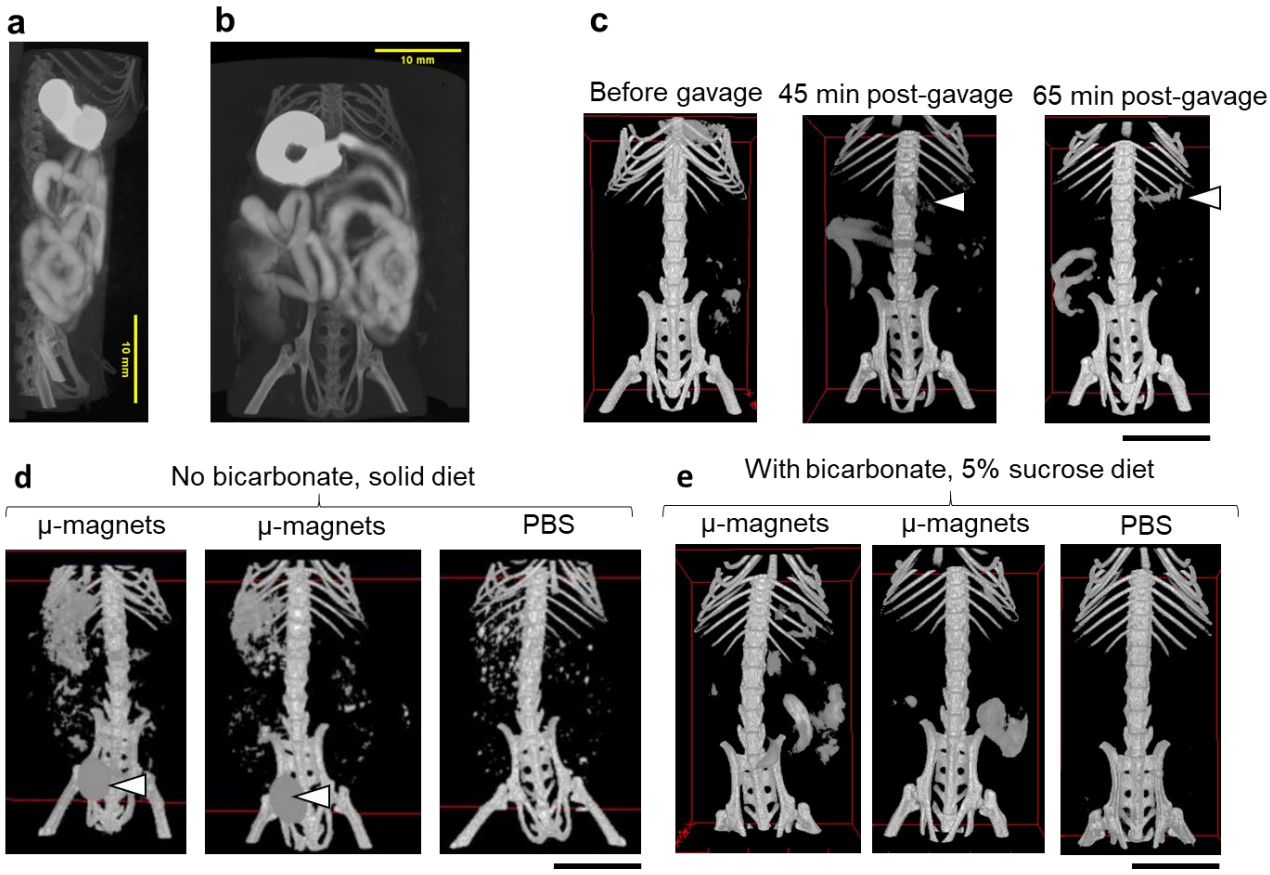

Figure S4.1. X-ray CT data. a,**b**, Representative sagittal (**a**) and coronal (**b**) X-ray CT images of the mouse GI tract after oral gavage of a CT contrast agent (Isovue-370). **c**, Representative images before gavage, 45-min post-gavage, and 65 min post-gavage of a mixture of micromagnets. The mouse was fasted prior to gavage and given only sucrose water after gavage. The white arrows point to the micromagnets remaining in the stomach. **d**,**e**, Representative images of mice at 6 hours after gavage of micromagnets without bicarbonate (**d**) and with bicarbonate (**e**). Mice in (**d**) were given normal solid food after gavage while mice in (**e**) were given sucrose water after gavage; both were fasted prior to gavage. Arrows in (**d**) point to the signal from iron accumulation in the bladder; no signal from the bladder was observed in (**e**). All scale bars are 10 mm.

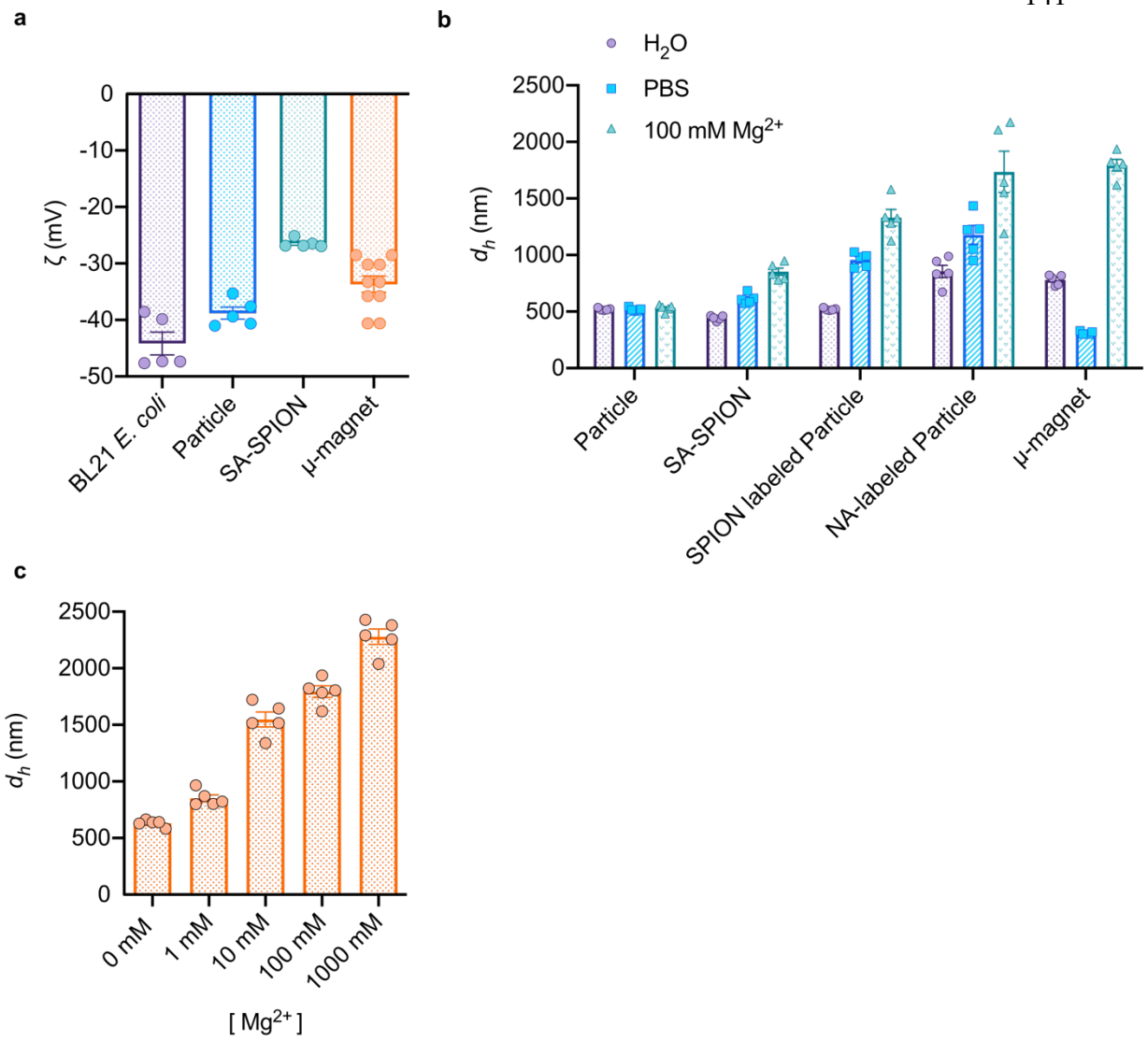

Figure S4.2. Characterization of particles and cells. **a**, Zeta potential measurements of BL21(DE3) *E. coli*, 0.5 μm fluorescent polystyrene particles, magnetic label (150 nm streptavidin-coated superparamagnetic iron oxide nanoparticles, SA-SPION), and micromagnets (BioMag Carboxyl) used in this study. **b**, Hydrodynamic radius measured by DLS of 0.5 μm fluorescent polystyrene particles, magnetic label (SA-SPION), SPION-labeled particles, Neutravidin (NA)-labeled particles, and micromagnets (BioMag Carboxyl) used in this study in water and 100 mM $MgCl_2$. **c**, Hydrodynamic radius measured by DLS of micromagnets (BioMag Carboxyl) as a function of $MgCl_2$ concentration.

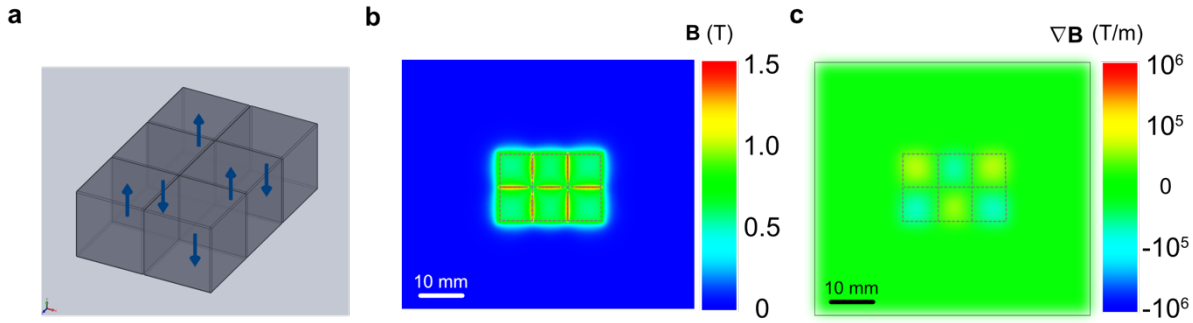

Figure S4.3. Additional simulation results for the magnet array. a, Schematic of magnet array of 3 x 2 B444-N52 magnets used in in vivo experiments. The magnets were arranged in a checkerboard pattern of alternating magnetization to maximize areas of high field and field gradient strength. **b**,**c**, Simulation of the magnetic flux density (**b**) and magnetic field gradient (**c**) at the surface of the magnet array.

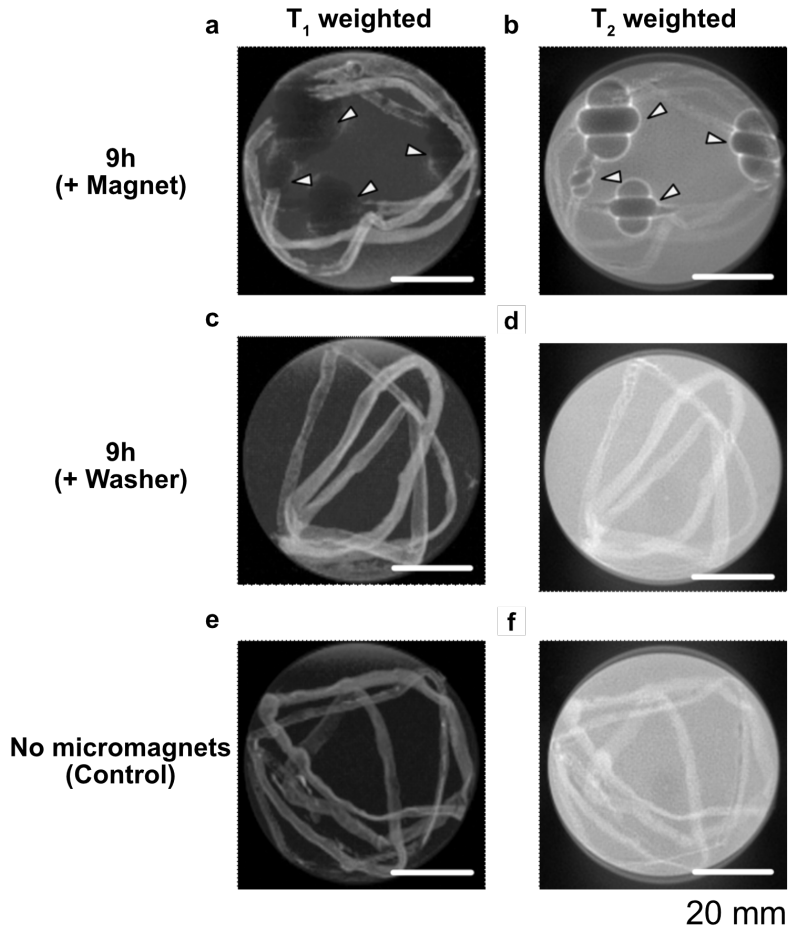

Figure S4.4. **Representative *ex vivo* MRI on mouse small intestines**. **a**, T1 weighted anatomical image alongside **b**, T2 weighted image of a mouse small intestine (SI), with arrows indicating regions of susceptibility artefacts which are caused by the presence of micromagnets. The SI was isolated from a mouse 9h post-gavage. A magnet was placed on the mouse abdomen 75 mins after gavage with the micromagnet and synthetic-cell mixture. **c**, T1 weighted anatomical image alongside **d**, T2 weighted image of a mouse SI 9h post gavage. A non-magnetic washer of equivalent weight was placed on the mouse abdomen 75 mins after gavage with the same experimental mixture as in (**a**). No susceptibility artefacts were observed in the SI as evidenced by the lack of T2* blooming in the T2 weighted image. **e**, T1 and **f**, T2 weighted images of a control mouse SI, respectively. The mouse was not gavaged with any beads but was maintained under the same experimental conditions as in (**a**) and (**c**). The SI was dissected from the GI tract and placed within an agarose matrix to minimize susceptibility artefacts during imaging. All scale bars are 20 mm.

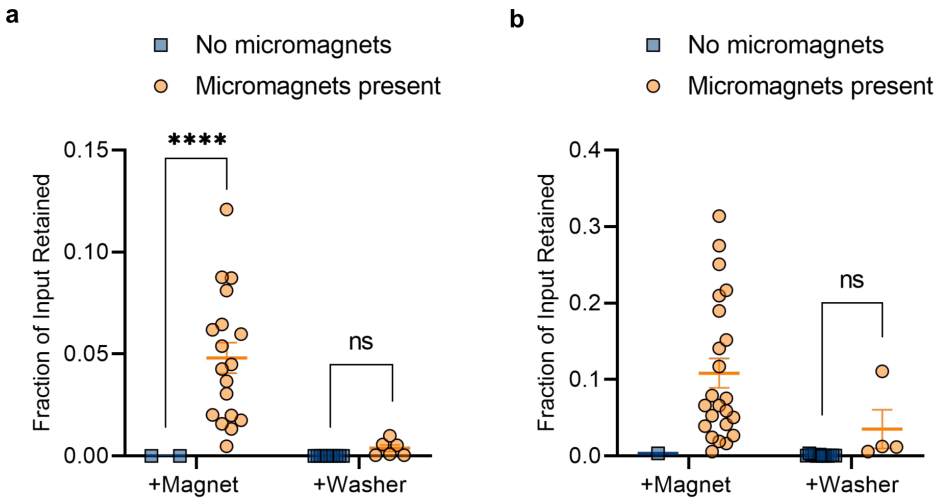

Figure S4.5. Co-localization of magnetically-labeled *E. coli* and particles with micromagnets in vivo. **a-b**, Fraction of SPION-labeled *E. coli* (**a**) and SPION-labeled particles (**b**) retained in small intestinal segments where micromagnets were observed or absent in a given mouse. Small intestinal segments SI-1 through SI-4 (see **Fig. 4.3d-e**) were examined by eye for the presence of micromagnets before quantification of the *E. coli* or particles retained. Lines represent the mean and error bars represent the SEM. Asterisks represent statistical significance by the Welch's t-test (**** = $p<0.0001$, ns=no significance).

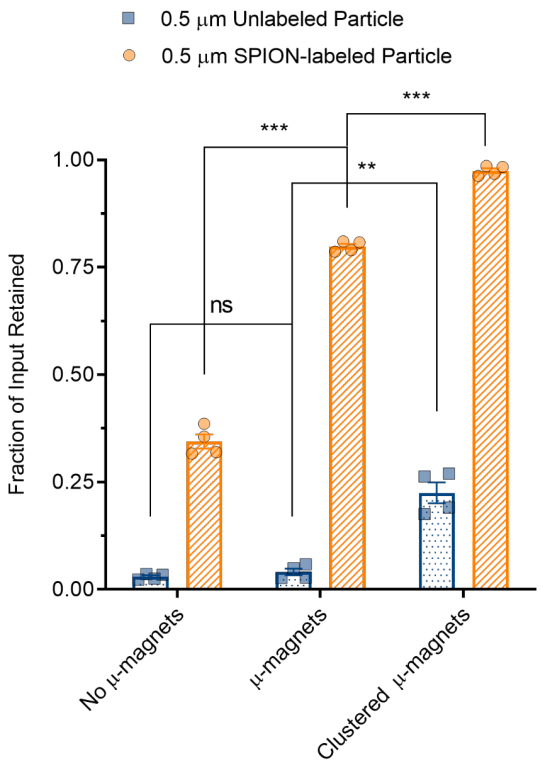

Figure S4.6. **In vitro efficacy of CLAMP with particles**. In vitro capture of non-magnetic and magnetized 0.5 μm fluorescent particles without micromagnets, with micromagnets, and with clustered micromagnets. The experimental setup is as illustrated in **Fig. 4.2** except with particles instead of *E. coli*. Asterisks represent statistical significance by Welch's t-test (*** = $p<0.001$, ** = $p<0.01$, ns = no significance).

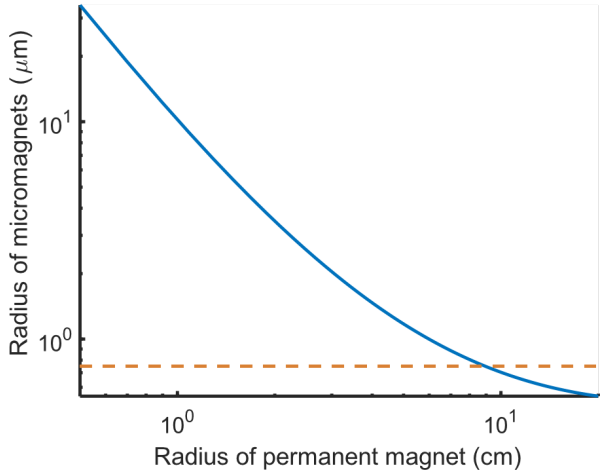

Figure S4.7. **Estimates for scaling CLAMP to humans**. Radius of internal micromagnets versus equivalent radius of wearable magnet needed to achieve sufficient force to CLAMP cells in the small intestine of humans. The orange dotted line indicates the radius of micromagnets used in our in vivo experiments with mice. Here, we assumed that the wearable magnet is spherical, the small intestine is at a distance of 6 cm from the abdominal skin, and the micromagnets and wearable magnet are made of the same materials as those used in our studies with mice. See supporting methods section for more details.

REFERENCES

1. Yamashiro, Y. Gut Microbiota in Health and Disease. *Ann. Nutr. Metab.* **71**, 242–246 (2018).
2. Gao, Y., Li, D. & Liu, Y.-X. Microbiome research outlook: past, present, and future. *Protein Cell* **14**, 709–712 (2023).
3. Cullen, C. M. *et al.* Emerging Priorities for Microbiome Research. *Front. Microbiol.* **11**, (2020).
4. Dou, J. & Bennett, M. R. Synthetic Biology and the Gut Microbiome. *Biotechnol. J.* (2018) doi:10.1002/biot.201700159.
5. Hongyu Zhang, D. J. Manipulation of Microbiome, a Promising Therapy for Inflammatory Bowel Diseases. *J. Clin. Cell. Immunol.* (2014) doi:10.4172/2155-9899.1000234.
6. Mao, N., Cubillos-Ruiz, A., Cameron, D. E. & Collins, J. J. Probiotic strains detect and suppress cholera in mice. *Sci. Transl. Med.* (2018) doi:10.1126/scitranslmed.aao2586.
7. Archer, E. J., Robinson, A. B. & Süel, G. M. Engineered E. coli that detect and respond to gut inflammation through nitric oxide sensing. *ACS Synth. Biol.* (2012) doi:10.1021/sb3000595.
8. Riglar, D. T. *et al.* Engineered bacteria can function in the mammalian gut long-term as live diagnostics of inflammation. *Nat. Biotechnol.* **35**, 653–658 (2017).
9. Sepich-Poore, G. D. *et al.* The microbiome and human cancer. *Science* **371**, eabc4552 (2021).

10. Chen, Y., Wu, F.-H., Wu, P.-Q., Xing, H.-Y. & Ma, T. The Role of The Tumor Microbiome in Tumor Development and Its Treatment. *Front. Immunol.* **13**, (2022).

11. Ciernikova, S., Sevcikova, A., Stevurkova, V. & Mego, M. Tumor microbiome – an integral part of the tumor microenvironment. *Front. Oncol.* **12**, 1063100 (2022).

12. Chien, T., Doshi, A. & Danino, T. Advances in bacterial cancer therapies using synthetic biology. *Curr. Opin. Syst. Biol.* **5**, 1–8 (2017).

13. Kramer, M. G., Masner, M., Ferreira, F. A. & Hoffman, R. M. Bacterial therapy of cancer: Promises, limitations, and insights for future directions. *Front. Microbiol.* (2018) doi:10.3389/fmicb.2018.00016.

14. Panteli, J. T., Forkus, B. A., Van Dessel, N. & Forbes, N. S. Genetically modified bacteria as a tool to detect microscopic solid tumor masses with triggered release of a recombinant biomarker. *Integr. Biol. Quant. Biosci. Nano Macro* **7**, 423–434 (2015).

15. Berlec, A., Završnik, J., Butinar, M., Turk, B. & Štrukelj, B. In vivo imaging of Lactococcus lactis, Lactobacillus plantarum and Escherichia coli expressing infrared fluorescent protein in mice. *Microb. Cell Factories* **14**, 181 (2015).

16. Multamäki, E. *et al.* Optogenetic Control of Bacterial Expression by Red Light. *ACS Synth. Biol.* **11**, 3354–3367 (2022).

17. Hartsough, L. A. *et al.* Optogenetic control of gut bacterial metabolism to promote longevity. *eLife* **9**, e56849 (2020).

18. Campisciano, G. & Biffi, S. Microbiota *in vivo* imaging approaches to study host-microbe interactions in preclinical and clinical setting. *Heliyon* **8**, e12511 (2022).

19. Piraner, D. I. *et al.* Going Deeper: Biomolecular Tools for Acoustic and Magnetic Imaging and Control of Cellular Function. *Biochemistry* **56**, 5202–5209 (2017).

20. Bettegowda, C. *et al.* Imaging bacterial infections with radiolabeled 1-(2'-deoxy-2'-fluoro- -D-arabinofuranosyl)-5-iodouracil. *Proc. Natl. Acad. Sci.* **102**, 1145–1150 (2005).

21. Soghomonyan, S. A. *et al.* Positron emission tomography (PET) imaging of tumor-localized Salmonella expressing HSV1-TK. *Cancer Gene Ther.* (2005) doi:10.1038/sj.cgt.7700779.

22. James, M. L. & Gambhir, S. S. A Molecular Imaging Primer: Modalities, Imaging Agents, and Applications. *Physiol. Rev.* **92**, 897–965 (2012).

23. Shapiro, M. G. *et al.* Biogenic gas nanostructures as ultrasonic molecular reporters. *Nat. Nanotechnol.* (2014) doi:10.1038/nnano.2014.32.

24. Maresca, D. *et al.* Nonlinear ultrasound imaging of nanoscale acoustic biomolecules. *Appl. Phys. Lett.* (2017) doi:10.1063/1.4976105.

25. Maresca, D., Sawyer, D. P., Renaud, G., Lee-Gosselin, A. & Shapiro, M. G. Nonlinear X-Wave Ultrasound Imaging of Acoustic Biomolecules. *Phys. Rev. X* (2018) doi:10.1103/PhysRevX.8.041002.

26. Bourdeau, R. W. *et al.* Acoustic reporter genes for noninvasive imaging of microorganisms in mammalian hosts. *Nature* (2018) doi:10.1038/nature25021.

27. Riglar, D. T. & Silver, P. A. Engineering bacteria for diagnostic and therapeutic applications. *Nat. Rev. Microbiol.* **16**, 214–225 (2018).

28. Bar-Zion, A. *et al.* Acoustically triggered mechanotherapy using genetically encoded gas vesicles. *Nat. Nanotechnol.* **16**, 1403–1412 (2021).

29. Abedi, M. H. *et al.* Ultrasound-controllable engineered bacteria for cancer immunotherapy. *Nat. Commun.* **13**, 1585 (2022).

30. Liu, G. *et al.* Noninvasive imaging of infection after treatment with tumor-homing bacteria using Chemical Exchange Saturation Transfer (CEST) MRI. *Magn. Reson. Med.* (2013) doi:10.1002/mrm.24955.

31. Zheng, L. *et al.* MRI-monitored intra-tumoral injection of iron-oxide labeled Clostridium novyi-NT anaerobes in pancreatic carcinoma mouse model. *PLoS ONE* (2014) doi:10.1371/journal.pone.0116204.

32. Hoerr, V. *et al.* Bacteria tracking by in vivomagnetic resonance imaging. *BMC Biol.* **11**, 63 (2013).

33. Zhang, L. *et al.* Gadolinium-Labeled Aminoglycoside and Its Potential Application as a Bacteria-Targeting Magnetic Resonance Imaging Contrast Agent. *Anal. Chem.* **90**, 1934–1940 (2018).

34. Ramesh, P. *et al.* Ultraparamagnetic Cells Formed through Intracellular Oxidation and Chelation of Paramagnetic Iron. *Angewandte Chemie - International Edition* (2018) doi:10.1002/anie.201805042.

35. Liu, X. *et al.* Engineering Genetically-Encoded Mineralization and Magnetism via Directed Evolution. *Sci. Rep.* (2016) doi:10.1038/srep38019.

36. Felfoul, O. *et al.* Magneto-aerotactic bacteria deliver drug-containing nanoliposomes to tumour hypoxic regions. *Nat. Nanotechnol.* **11**, 941–947 (2016).

37. Piraner, D. I. *et al.* Going Deeper: Biomolecular Tools for Acoustic and Magnetic Imaging and Control of Cellular Function. *Biochemistry* **56**, 5202–5209 (2017).

38. Maresca, D. *et al.* Biomolecular Ultrasound and Sonogenetics. *Annu. Rev. Chem. Biomol. Eng.* **9**, 229–252 (2018).

39. Shapiro, M. G. *et al.* Biogenic Gas Nanostructures as Ultrasonic Molecular Reporters. *Nat. Nanotechnol.* **9**, 311–316 (2014).

40. Walsby, A. E. Gas vesicles. *Microbiol. Rev.* **58**, 94–144 (1994).

41. Pfeifer, F. Distribution, formation and regulation of gas vesicles. *Nat. Rev. Microbiol.* **10**, 705–715 (2012).

42. Bourdeau, R. W. *et al.* Acoustic reporter genes for noninvasive imaging of microbes in mammalian hosts. *Nature* **553**, 86–90 (2018).

43. Farhadi, A., Ho, G. H., Sawyer, D. P., Bourdeau, R. W. & Shapiro, M. G. Ultrasound imaging of gene expression in mammalian cells. *Science* **365**, 1469–1475 (2019).

44. Chow, B. Y. *et al.* High-performance genetically targetable optical neural silencing by light-driven proton pumps. *Nature* **463**, 98–102 (2010).

45. Matz, M. V. *et al.* Fluorescent proteins from nonbioluminescent Anthozoa species. *Nat. Biotechnol.* **17**, 969–973 (1999).

46. Stanton, B. C. *et al.* Genomic mining of prokaryotic repressors for orthogonal logic gates. *Nat. Chem. Biol.* **10**, 99–105 (2014).

47. Mak, W. S. *et al.* Integrative genomic mining for enzyme function to enable engineering of a non-natural biosynthetic pathway. *Nat. Commun.* **6**, 10005 (2015).

48. Burstein, D. *et al.* New CRISPR–Cas systems from uncultivated microbes. *Nature* **542**, 237–241 (2017).

49. Maresca, D., Sawyer, D. P., Renaud, G., Lee-Gosselin, A. & Shapiro, M. G. Nonlinear X-Wave Ultrasound Imaging of Acoustic Biomolecules. *Phys. Rev. X* **8**, 041002 (2018).

50. Tashiro, Y., Monson, R. E., Ramsay, J. P. & Salmond, G. P. C. Molecular genetic and physical analysis of gas vesicles in buoyant enterobacteria. *Environ. Microbiol.* **18**, 1264–1276 (2016).

51. Oren, A., Pri-El, N., Shapiro, O. & Siboni, N. Gas vesicles isolated from Halobacterium cells by lysis in hypotonic solution are structurally weakened. *FEMS Microbiol. Lett.* **252**, 337–341 (2005).

52. Ramsay, J. P., Williamson, N. R., Spring, D. R. & Salmond, G. P. C. A quorum-sensing molecule acts as a morphogen controlling gas vesicle organelle biogenesis and adaptive flotation in an enterobacterium. *Proc. Natl. Acad. Sci.* **108**, 14932–14937 (2011).

53. Lee, C. M., Monson, R. E., Adams, R. M. & Salmond, G. P. C. The LacI–Family Transcription Factor, RbsR, Is a Pleiotropic Regulator of Motility, Virulence, Siderophore and Antibiotic Production, Gas Vesicle Morphogenesis and Flotation in Serratia. *Front. Microbiol.* **8**, (2017).

54. Li, N. & Cannon, M. C. Gas Vesicle Genes Identified in Bacillus megaterium and Functional Expression in Escherichia coli. *J. Bacteriol.* **180**, 2450–2458 (1998).

55. Sawyer, D. P. *et al.* Ultrasensitive ultrasound imaging of gene expression with signal unmixing. *Nat. Methods* **18**, 945–952 (2021).

56. Farhadi, A. *et al.* Genetically Encoded Phase Contrast Agents for Digital Holographic Microscopy. *Nano Lett.* **20**, 8127–8134 (2020).

57. Lu, G. J. *et al.* Genetically Encodable Contrast Agents for Optical Coherence Tomography. *ACS Nano* **14**, 7823–7831 (2020).

58. Li, Z. & Rinas, U. Recombinant protein production associated growth inhibition results mainly from transcription and not from translation. *Microb. Cell Factories* **19**, (2020).

59. Borkowski, O., Ceroni, F., Stan, G.-B. & Ellis, T. Overloaded and stressed: whole-cell considerations for bacterial synthetic biology. *Curr. Opin. Microbiol.* **33**, 123–130 (2016).

60. Sleight, S. C. & Sauro, H. M. Visualization of Evolutionary Stability Dynamics and Competitive Fitness of Escherichia coli Engineered with Randomized Multigene Circuits. *ACS Synth. Biol.* **2**, 519–528 (2013).

61. Schultz, M. Clinical use of E. coli Nissle 1917 in inflammatory bowel disease. *Inflamm. Bowel Dis.* **14**, 1012–1018 (2008).

62. Stritzker, J. *et al.* Tumor-specific colonization, tissue distribution, and gene induction by probiotic Escherichia coli Nissle 1917 in live mice. *Int. J. Med. Microbiol.* **297**, 151–162 (2007).

63. Sonnenborn, U. & Schulze, J. The non-pathogenic Escherichia coli strain Nissle 1917–features of a versatile probiotic. *Microb. Ecol. Health Dis.* **21**, 122–158 (2009).

64. Gurbatri, C. R. *et al.* Engineered Probiotics for Local Tumor Delivery of Checkpoint Blockade Nanobodies. *Sci. Transl. Med.* **12**, (2020).

65. Duong, M. T.-Q., Qin, Y., You, S.-H. & Min, J.-J. Bacteria-cancer interactions: bacteria-based cancer therapy. *Exp. Mol. Med.* **51**, 1–15 (2019).

66. Leventhal, D. S. *et al.* Immunotherapy with engineered bacteria by targeting the STING pathway for anti-tumor immunity. *Nat. Commun.* **11**, 2739 (2020).

67. Zhang, Y. *et al.* E. coli Nissle 1917-Derived Minicells for Targeted Delivery of Chemotherapeutic Drug to Hypoxic Regions for Cancer Therapy. *Theranostics* **8**, 1690–1705 (2018).

68. Grady, R. & Hayes, F. Axe–Txe, a broad-spectrum proteic toxin–antitoxin system specified by a multidrug-resistant, clinical isolate of Enterococcus faecium. *Mol. Microbiol.* **47**, 1419–1432 (2003).

69. Ceroni, F. *et al.* Burden-driven feedback control of gene expression. *Nat. Methods* **15**, 387 (2018).

70. Charbonneau, M. R., Isabella, V. M., Li, N. & Kurtz, C. B. Developing a new class of engineered live bacterial therapeutics to treat human diseases. *Nat. Commun.* **11**, 1738 (2020).

71. Jimenez, M., Langer, R. & Traverso, G. Microbial therapeutics: New opportunities for drug delivery. *J. Exp. Med.* **216**, 1005–1009 (2019).

72. Lakshmanan, A. *et al.* Acoustic Biosensors for Ultrasound Imaging of Enzyme Activity. *Nat. Chem. Biol.* **16**, 988–996 (2020).

73. Hui, C.-Y., Guo, Y., Zhang, W. & Huang, X.-Q. Rapid monitoring of the target protein expression with a fluorescent signal based on a dicistronic construct in Escherichia coli. *AMB Express* **8**, 81 (2018).

74. Alnahhas, R. N. *et al.* Majority sensing in synthetic microbial consortia. *Nat. Commun.* **11**, 3659 (2020).

75. Hays, S. G., Patrick, W. G., Ziesack, M., Oxman, N. & Silver, P. A. Better together: engineering and application of microbial symbioses. *Curr. Opin. Biotechnol.* **36**, 40–49 (2015).

76. Ziesack, M. *et al.* Engineered Interspecies Amino Acid Cross-Feeding Increases Population Evenness in a Synthetic Bacterial Consortium. *mSystems* **4**, (2019).

77. Wacklin, P., Hoffmann, L. & Komárek, J. Nomenclatural validation of the genetically revised cyanobacterial genus Dolichospermum (RALFS ex BORNET et FLAHAULT) comb. nova. *Fottea* **9**, 59–64 (2009).

78. Komárek, J. *et al.* Polyphasic evaluation of Limnoraphis robusta, a water-bloom forming cyanobacterium from Lake Atitlán, Guatemala, with a description of Limnoraphis gen. nov. *Fottea* **13**, 39–52 (2013).

79. Komárek, J. Planktic oscillatorialean cyanoprokaryotes (short review according to combined phenotype and molecular aspects). in *Phytoplankton and Equilibrium Concept: The Ecology of Steady-State Assemblages* (eds. Naselli-Flores, L., Padisák, J. & Dokulil, M. T.) 367–382 (Springer Netherlands, Dordrecht, 2003). doi:10.1007/978-94-017-2666-5_30.

80. Sievers, F. *et al.* Fast, scalable generation of high-quality protein multiple sequence alignments using Clustal Omega. *Mol. Syst. Biol.* **7**, 539 (2011).

81. Larkin, M. A. *et al.* Clustal W and Clustal X version 2.0. *Bioinformatics* **23**, 2947–2948 (2007).

82. Subramanian, B., Gao, S., Lercher, M. J., Hu, S. & Chen, W.-H. Evolview v3: a webserver for visualization, annotation, and management of phylogenetic trees. *Nucleic Acids Res.* **47**, W270–W275 (2019).

83. Maresca, D. *et al.* Nonlinear ultrasound imaging of nanoscale acoustic biomolecules. *Appl. Phys. Lett.* **110**, (2017).

84. Talley, N. J. *et al.* An Evidence-Based Systematic Review on Medical Therapies for Inflammatory Bowel Disease: *Am. J. Gastroenterol.* **106**, S2–S25 (2011).

85. Wang, R., Li, Z., Liu, S. & Zhang, D. Global, regional and national burden of inflammatory bowel disease in 204 countries and territories from 1990 to 2019: a systematic analysis based on the Global Burden of Disease Study 2019. *BMJ Open* **13**, e065186 (2023).

86. Kahn-Boesel, O., Cautha, S., Ufere, N. N., Ananthakrishnan, A. N. & Kochar, B. A Narrative Review of Financial Burden, Distress, and Toxicity of Inflammatory Bowel Diseases in the United States. *Off. J. Am. Coll. Gastroenterol. ACG* **118**, 1545 (2023).

87. Le Berre, C. *et al.* Impact of inflammatory bowel diseases on working life: A French nationwide survey. *Dig. Liver Dis.* **51**, 961–966 (2019).

88. Dalal, S. R. & Chang, E. B. The microbial basis of inflammatory bowel diseases. *J. Clin. Invest.* **124**, 4190–4196 (2014).

89. Baumgart, D. C. & Carding, S. R. Inflammatory bowel disease: cause and immunobiology. *The Lancet* **369**, 1627–1640 (2007).

90. Buisson, A. *et al.* Comparative Acceptability and Perceived Clinical Utility of Monitoring Tools: A Nationwide Survey of Patients with Inflammatory Bowel Disease. *Inflamm. Bowel Dis.* **23**, 1425–1433 (2017).

91. Derkacz, A., Olczyk, P. & Komosinska-Vassev, K. Diagnostic Markers for Nonspecific Inflammatory Bowel Diseases. *Dis. Markers* **2018**, 7451946 (2018).

92. Nikolaus, S. & Schreiber, S. Diagnostics of Inflammatory Bowel Disease. *Gastroenterology* **133**, 1670–1689 (2007).

93. Shi, J.-T. *et al.* Diagnostic Utility of Non-invasive Tests for Inflammatory Bowel Disease: An Umbrella Review. *Front. Med.* **9**, (2022).

94. Dolinger, M. T. & Kayal, M. Intestinal ultrasound as a non-invasive tool to monitor inflammatory bowel disease activity and guide clinical decision making. *World J. Gastroenterol.* **29**, 2272–2282 (2023).

95. Riglar, D. T. & Silver, P. A. Engineering bacteria for diagnostic and therapeutic applications. *Nat. Rev. Microbiol.* **16**, 214–225 (2018).

96. Landry, B. P. & Tabor, J. J. Engineering Diagnostic and Therapeutic Gut Bacteria. *Microbiol. Spectr.* **5**, (2017).

97. Barra, M., Danino, T. & Garrido, D. Engineered Probiotics for Detection and Treatment of Inflammatory Intestinal Diseases. *Front. Bioeng. Biotechnol.* **8**, (2020).

98. Daeffler, K. N. *et al.* Engineering bacterial thiosulfate and tetrathionate sensors for detecting gut inflammation. *Mol. Syst. Biol.* **13**, (2017).

99. Riglar, D. T. *et al.* Engineered bacteria function in the mammalian gut as long term live diagnostics of inflammation. *Nat. Biotechnol.* **35**, 653–658 (2017).

100. Archer, E. J., Robinson, A. B. & Süel, G. M. Engineered E. coli That Detect and Respond to Gut Inflammation through Nitric Oxide Sensing. *ACS Synth. Biol.* **1**, 451–457 (2012).

101. Chen, X. J., Wang, B., Thompson, I. P. & Huang, W. E. Rational Design and Characterization of Nitric Oxide Biosensors in *E. coli* Nissle 1917 and Mini SimCells. *ACS Synth. Biol.* **10**, 2566–2578 (2021).

102. Xia, J. Y. *et al.* Engineered calprotectin-sensing probiotics for IBD surveillance in humans. *Proc. Natl. Acad. Sci.* **120**, e2221121120 (2023).

103. Mimee, M. *et al.* An ingestible bacterial-electronic system to monitor gastrointestinal health. *Science* **360**, 915–918 (2018).

104. Foucault, M.-L., Thomas, L., Goussard, S., Branchini, B. R. & Grillot-Courvalin, C. In Vivo Bioluminescence Imaging for the Study of Intestinal Colonization by Escherichia coli in Mice. *Appl. Environ. Microbiol.* **76**, 264–274 (2010).

105. Hurt, R. C. *et al.* Genomically mined acoustic reporter genes for real-time in vivo monitoring of tumors and tumor-homing bacteria. *Nat. Biotechnol.* **41**, 919–931 (2023).

106. Levitt, M. D., Furne, J., Springfield, J., Suarez, F. & DeMaster, E. Detoxification of hydrogen sulfide and methanethiol in the cecal mucosa. *J. Clin. Invest.* **104**, 1107–1114 (1999).

107. Blachier, F. *et al.* Production of hydrogen sulfide by the intestinal microbiota and epithelial cells and consequences for the colonic and rectal mucosa. *Am. J. Physiol.-Gastrointest. Liver Physiol.* **320**, G125–G135 (2021).

108. Mottawea, W. *et al.* Altered intestinal microbiota–host mitochondria crosstalk in new onset Crohn's disease. *Nat. Commun.* **7**, 13419 (2016).

109. Carbonero, F., Benefiel, A. C., Alizadeh-Ghamsari, A. H. & Gaskins, H. R. Microbial pathways in colonic sulfur metabolism and links with health and disease. *Front. Physiol.* **3**, 448 (2012).

110. Rowan, F. E., Docherty, N. G., Coffey, J. C. & O'Connell, P. R. Sulphate-reducing bacteria and hydrogen sulphide in the aetiology of ulcerative colitis. *Br. J. Surg.* **96**, 151–158 (2009).

111. Winter, S. E. *et al.* Gut inflammation provides a respiratory electron acceptor for Salmonella. *Nature* **467**, 426–429 (2010).

112. Landry, B. P., Palanki, R., Dyulgyarov, N., Hartsough, L. A. & Tabor, J. J. Phosphatase activity tunes two-component system sensor detection threshold. *Nat. Commun.* **9**, 1433 (2018).

113. Mutalik, V. K. *et al.* Precise and reliable gene expression via standard transcription and translation initiation elements. *Nat. Methods* **10**, 354–360 (2013).

114. Hentges, D. J., Pongpech, P. & Que, J. U. Hypothesis: How Streptomycin Treatment Compromises Colonisation Resistance Against Enteric Pathogens in Mice. *Microb. Ecol. Health Dis.* **3**, 105–111 (1990).

115. Leatham, M. P. *et al.* Precolonized Human Commensal Escherichia coli Strains Serve as a Barrier to E. coli O157:H7 Growth in the Streptomycin-Treated Mouse Intestine. *Infect. Immun.* **77**, 2876–2886 (2009).

116. Maltby, R., Leatham-Jensen, M. P., Gibson, T., Cohen, P. S. & Conway, T. Nutritional Basis for Colonization Resistance by Human Commensal Escherichia coli Strains HS and Nissle 1917 against E. coli O157:H7 in the Mouse Intestine. *PLoS ONE* **8**, (2013).

117. Myhal, M. L., Laux, D. C. & Cohen, P. S. Relative colonizing abilities of human fecal and K 12 strains of Escherichia coli in the large intestines of streptomycin-treated mice. *Eur. J. Clin. Microbiol.* **1**, 186–192 (1982).

118. Spees, A. M. *et al.* Streptomycin-Induced Inflammation Enhances Escherichia coli Gut Colonization Through Nitrate Respiration. *mBio* **4**, e00430-13 (2013).

119. Deplancke, B. *et al.* Gastrointestinal and Microbial Responses to Sulfate-Supplemented Drinking Water in Mice. *Exp. Biol. Med.* **228**, 424–433 (2003).

120. Nakao, K. *et al.* Susceptibilities of 23 Desulfovibrio Isolates from Humans. *Antimicrob. Agents Chemother.* **53**, 5308–5311 (2009).

121. Lozniewski, A., Labia, R., Haristoy, X. & Mory, F. Antimicrobial Susceptibilities of Clinical Desulfovibrio Isolates. *Antimicrob. Agents Chemother.* **45**, 2933–2935 (2001).

122. Gibson, G. R., Cummings, J. H. & Macfarlane, G. T. Growth and activities of sulphate-reducing bacteria in gut contents of healthy subjects and patients with ulcerative colitis. *FEMS Microbiol. Lett.* **86**, 103–111 (1991).

123. Hubbard, A. T. M. *et al.* Piperacillin/tazobactam resistance in a clinical isolate of Escherichia coli due to IS26-mediated amplification of blaTEM-1B. *Nat. Commun.* **11**, 4915 (2020).

124. Hansen, K. H. *et al.* Resistance to piperacillin/tazobactam in Escherichia coli resulting from extensive IS26-associated gene amplification of blaTEM-1. *J. Antimicrob. Chemother.* **74**, 3179–3183 (2019).

125. St-Pierre, F. *et al.* One-Step Cloning and Chromosomal Integration of DNA. *ACS Synth. Biol.* **2**, 537–541 (2013).

126. Lin, L., Du, Y., Song, J., Wang, W. & Yang, C. Imaging Commensal Microbiota and Pathogenic Bacteria in the Gut. *Acc. Chem. Res.* **54**, 2076–2087 (2021).

127. Ağagündüz, D. *et al.* Understanding the role of the gut microbiome in gastrointestinal cancer: A review. *Front. Pharmacol.* **14**, (2023).

128. Keely, S. J. *et al.* Contributions of bile acids to gastrointestinal physiology as receptor agonists and modifiers of ion channels. *Am. J. Physiol. - Gastrointest. Liver Physiol.* **322**, G201–G222 (2022).

129. Khodakivskyi, P. V. *et al.* Noninvasive imaging and quantification of bile salt hydrolase activity: From bacteria to humans. *Sci. Adv.* **7**, eaaz9857 (2021).

130. Hughes, E. R. *et al.* Microbial respiration and formate oxidation as metabolic signatures of inflammation-associated dysbiosis. *Cell Host Microbe* **21**, 208–219 (2017).

131. Dacquay, L. C. *et al.* E.coli Nissle increases transcription of flagella assembly and formate hydrogenlyase genes in response to colitis. *Gut Microbes* **13**, 1994832 (2021).

132. Remund, B., Yilmaz, B. & Sokollik, C. D-Lactate: Implications for Gastrointestinal Diseases. *Children* **10**, 945 (2023).

133. van der Hee, B. & Wells, J. M. Microbial Regulation of Host Physiology by Short-chain Fatty Acids. *Trends Microbiol.* **29**, 700–712 (2021).

134. Tong, G. *et al.* Establishment and evaluation of a specific antibiotic-induced inflammatory bowel disease model in rats. *PLOS ONE* **17**, e0264194 (2022).

135. Zeng, M. Y., Inohara, N. & Nuñez, G. Mechanisms of inflammation-driven bacterial dysbiosis in the gut. *Mucosal Immunol.* **10**, 18–26 (2017).

136. Strati, F. *et al.* Antibiotic-associated dysbiosis affects the ability of the gut microbiota to control intestinal inflammation upon fecal microbiota transplantation in experimental colitis models. *Microbiome* **9**, 39 (2021).

137. Ramirez, J. *et al.* Antibiotics as Major Disruptors of Gut Microbiota. *Front. Cell. Infect. Microbiol.* **10**, (2020).

138. Hviid, A., Svanström, H. & Frisch, M. Antibiotic use and inflammatory bowel diseases in childhood. *Gut* **60**, 49–54 (2011).

139. Faye, A. S. *et al.* Antibiotic use as a risk factor for inflammatory bowel disease across the ages: a population-based cohort study. *Gut* **72**, 663–670 (2023).

140. Sekirov, I. *et al.* Antibiotic-Induced Perturbations of the Intestinal Microbiota Alter Host Susceptibility to Enteric Infection. *Infect. Immun.* **76**, 4726–4736 (2008).

141. Rivera-Chávez, F. *et al.* Depletion of butyrate-producing Clostridia from the gut microbiota drives an aerobic luminal expansion of Salmonella. *Cell Host Microbe* **19**, 443–454 (2016).

142. Kelly, C. J. *et al.* Crosstalk between Microbiota-Derived Short-Chain Fatty Acids and Intestinal Epithelial HIF Augments Tissue Barrier Function. *Cell Host Microbe* **17**, 662–671 (2015).

143. Rivera-Chávez, F., Lopez, C. A. & Bäumler, A. J. Oxygen as a driver of gut dysbiosis. *Free Radic. Biol. Med.* **105**, 93–101 (2017).

144. Baldelli, V., Scaldaferri, F., Putignani, L. & Del Chierico, F. The Role of Enterobacteriaceae in Gut Microbiota Dysbiosis in Inflammatory Bowel Diseases. *Microorganisms* **9**, 697 (2021).

145. Antunes, L. C. M. *et al.* Effect of Antibiotic Treatment on the Intestinal Metabolome. *Antimicrob. Agents Chemother.* **55**, 1494–1503 (2011).

146. Richie, T. G. *et al.* Limitation of amino acid availability by bacterial populations during enhanced colitis in IBD mouse model. *mSystems* **8**, e00703-23 (2023).

147. Barton, L. L., Ritz, N. L., Fauque, G. D. & Lin, H. C. Sulfur Cycling and the Intestinal Microbiome. *Dig. Dis. Sci.* **62**, 2241–2257 (2017).

148. Shepherd, E. S., DeLoache, W. C., Pruss, K. M., Whitaker, W. R. & Sonnenburg, J. L. An exclusive metabolic niche enables strain engraftment in the gut microbiota. *Nature* **557**, 434–438 (2018).

149. Maresca, D. *et al.* Nonlinear ultrasound imaging of nanoscale acoustic biomolecules. *Appl. Phys. Lett.* **110**, (2017).

150. Antoniou, E. *et al.* The TNBS-induced colitis animal model: An overview. *Ann. Med. Surg.* **11**, 9–15 (2016).

151. Bogatyrev, S. R., Rolando, J. C. & Ismagilov, R. F. Self-reinoculation with fecal flora changes microbiota density and composition leading to an altered bile-acid profile in the mouse small intestine. *Microbiome* **8**, 19 (2020).

152. Buss, M. T., Ramesh, P., English, M. A., Lee-Gosselin, A. & Shapiro, M. G. Spatial Control of Probiotic Bacteria in the Gastrointestinal Tract Assisted by Magnetic Particles. *Adv. Mater.* **n/a**, 2007473.

153. Freeling, J. L. & Rezvani, K. Assessment of murine colorectal cancer by micro-ultrasound using three dimensional reconstruction and non-linear contrast imaging. *Mol. Ther. Methods Clin. Dev.* **5**, 16070 (2016).

154. El Kaffas, A. *et al.* Molecular Contrast-Enhanced Ultrasound Imaging of Radiation-Induced P-Selectin Expression in Healthy Mice Colon. *Int. J. Radiat. Oncol.* **97**, 581–585 (2017).

155. Sofroniew, N. *et al.* napari: a multi-dimensional image viewer for Python. Zenodo https://doi.org/10.5281/zenodo.7276432 (2022).

156. Herigstad, B., Hamilton, M. & Heersink, J. How to optimize the drop plate method for enumerating bacteria. *J. Microbiol. Methods* (2001) doi:10.1016/S0167-7012(00)00241-4.

157. Teague, B. Cytoflow: A Python Toolbox for Flow Cytometry. 2022.07.22.501078 Preprint at https://doi.org/10.1101/2022.07.22.501078 (2022).

158. Nolte, T. *et al.* Nonproliferative and Proliferative Lesions of the Gastrointestinal Tract, Pancreas and Salivary Glands of the Rat and Mouse. *J. Toxicol. Pathol.* **29**, 1S-125S (2016).

159. Abramson, J. *et al.* Accurate structure prediction of biomolecular interactions with AlphaFold 3. *Nature* 1–3 (2024) doi:10.1038/s41586-024-07487-w.

160. Pettersen, E. F. *et al.* UCSF ChimeraX: Structure visualization for researchers, educators, and developers. *Protein Sci. Publ. Protein Soc.* **30**, 70–82 (2021).

161. Promoters/Catalog/Anderson - parts.igem.org. https://parts.igem.org/Promoters/Catalog/Anderson.

162. Shreiner, A. B., Kao, J. Y. & Young, V. B. The gut microbiome in health and in disease. *Curr. Opin. Gastroenterol.* (2015) doi:10.1097/MOG.0000000000000139.

163. Landry, B. P. & Tabor, J. J. Engineering Diagnostic and Therapeutic Gut Bacteria. *Microbiol. Spectr.* **5**, 1–22 (2017).

164. Maltby, R., Leatham-Jensen, M. P., Gibson, T., Cohen, P. S. & Conway, T. Nutritional Basis for Colonization Resistance by Human Commensal Escherichia coli Strains HS and Nissle 1917 against E. coli O157:H7 in the Mouse Intestine. *PLoS ONE* **8**, 1–10 (2013).

165. Francino, M. P. Antibiotics and the human gut microbiome: Dysbioses and accumulation of resistances. *Front. Microbiol.* **6**, 1–11 (2016).

166. Muthana, M. *et al.* Directing cell therapy to anatomic target sites in vivo with magnetic resonance targeting. *Nat. Commun.* (2015) doi:10.1038/ncomms9009.

167. Chiang, C. *et al.* Combination of fucoidan-based magnetic nanoparticles and immunomodulators enhances tumour-localized immunotherapy. *Nat. Nanotechnol.* **13**, 746–754 (2018).

168. Zhu, H. *et al.* Spatial control of in vivo CRISPR–Cas9 genome editing via nanomagnets. *Nat. Biomed. Eng.* **3**, 126–136 (2019).

169. Chen, H. & Langer, R. Magnetically-Responsive Polymerized Liposomes as Potential Oral Delivery Vehicles. *Pharm. Res.* **14**, 537–540 (1997).

170. Zwi-Dantsis, L. *et al.* Remote Magnetic Nanoparticle Manipulation Enables the Dynamic Patterning of Cardiac Tissues. *Adv. Mater.* (2020) doi:10.1002/adma.201904598.

171. Zhang, W. *et al.* Magnetically Controlled Growth-Factor-Immobilized Multilayer Cell Sheets for Complex Tissue Regeneration. *Adv. Mater.* (2017) doi:10.1002/adma.201703795.

172. Kim, J., Staunton, J. R. & Tanner, K. Independent Control of Topography for 3D Patterning of the ECM Microenvironment. *Adv. Mater.* (2016) doi:10.1002/adma.201503950.

173. Fayol, D. *et al.* Use of magnetic forces to promote stem cell aggregation during differentiation, and cartilage tissue modeling. *Adv. Mater.* (2013) doi:10.1002/adma.201300342.

174. Servant, A., Qiu, F., Mazza, M., Kostarelos, K. & Nelson, B. J. Controlled in vivo swimming of a swarm of bacteria-like microrobotic flagella. *Adv. Mater.* (2015) doi:10.1002/adma.201404444.

175. Shevkoplyas, S. S., Siegel, A. C., Westervelt, R. M., Prentiss, M. G. & Whitesides, G. M. The force acting on a superparamagnetic bead due to an applied magnetic field. *Lab. Chip* **7**, 1294–1302 (2007).

176. Kang, J. H. *et al.* An extracorporeal blood-cleansing device for sepsis therapy. *Nat. Med.* **20**, 1211–1216 (2014).

177. Zhang, Y. *et al.* Non-invasive multimodal functional imaging of the intestine with frozen micellar naphthalocyanines. *Nat. Nanotechnol.* **9**, 631–638 (2014).

178. Yang, P. J., Lamarca, M., Kaminski, C., Chu, D. I. & Hu, D. L. Hydrodynamics of defecation. *Soft Matter* **13**, 4960–4970 (2017).

179. TAKAHASHI, T. Flow Behavior of Digesta and the Absorption of Nutrients in the Gastrointestine. *J. Nutr. Sci. Vitaminol. Nutr. Sci. Vitaminol.* **57**, 265–273 (2011).

180. Garraud, A. *et al.* Investigation of the capture of magnetic particles from high-viscosity fluids using permanent magnets. *IEEE Trans. Biomed. Eng.* (2016) doi:10.1109/TBME.2015.2458783.

181. Miltenyi, S., Müller, W., Weichel, W. & Radbruch, A. High gradient magnetic cell separation with MACS. *Cytometry* (1990) doi:10.1002/cyto.990110203.

182. Matsumoto, Y., Chen, R., Anikeeva, P. & Jasanoff, A. Engineering intracellular biomineralization and biosensing by a magnetic protein. *Nat. Commun.* (2015) doi:10.1038/ncomms9721.

183. Kim, T., Moore, D. & Fussenegger, M. Genetically programmed superparamagnetic behavior of mammalian cells. *J. Biotechnol.* (1970) doi:10.1016/j.jbiotec.2012.09.019.

184. Sonnenborn, U. & Schulze, J. The non-pathogenic Escherichia coli strain Nissle 1917-features of a versatile probiotic. *Microb. Ecol. Health Dis.* (2009) doi:10.3109/08910600903444267.

185. Casteleyn, C., Rekecki, A., Van Der Aa, A., Simoens, P. & Van Den Broeck, W. Surface area assessment of the murine intestinal tract as a prerequisite for oral dose translation from mouse to man. *Lab. Anim.* (2010) doi:10.1258/la.2009.009112.

186. Teply, B. A. *et al.* The use of charge-coupled polymeric microparticles and micromagnets for modulating the bioavailability of orally delivered macromolecules. *Biomaterials* **29**, 1216–1223 (2008).

187. Masaoka, Y., Tanaka, Y., Kataoka, M., Sakuma, S. & Yamashita, S. Site of drug absorption after oral administration: Assessment of membrane permeability and luminal concentration of drugs in each segment of gastrointestinal tract. *Eur. J. Pharm. Sci.* (2006) doi:10.1016/j.ejps.2006.06.004.

188. Kimura, T. & Higaki, K. Gastrointestinal transit and drug absorption. *Biol. Pharm. Bull.* (2002) doi:10.1248/bpb.25.149.

189. Ibrahim, M., Naguib, Y., Sarhan, H. & Abdelkader, H. Gastro-retentive oral drug delivery systems: a promising approach for narrow absorption window drugs. *J. Adv. Biomed. Pharm. Sci.* (2019) doi:10.21608/jabps.2019.11357.1042.

190. Padmanabhan, P., Grosse, J., Asad, A. B. M. A., Radda, G. K. & Golay, X. Gastrointestinal transit measurements in mice with 99mTc-DTPA-labeled activated charcoal using NanoSPECT-CT. *EJNMMI Res.* (2013) doi:10.1186/2191-219X-3-60.

191. Rodriguez-Palacios, A., Khoretonenko, M. V. & Ilic, S. Institutional protocols for the oral administration (gavage) of chemicals and microscopic microbial communities to mice: Analytical consensus. *Exp. Biol. Med.* (2019) doi:10.1177/1535370219838203.

192. Jensen, T. L., Kiersgaard, M. K., Sørensen, D. B. & Mikkelsen, L. F. Fasting of mice: A review. *Lab. Anim.* (2013) doi:10.1177/0023677213501659.

193. Bogatyrev, S. R., Rolando, J. C. & Ismagilov, R. F. Self-reinoculation with fecal flora changes microbiota density and composition leading to an altered bile-acid profile in the mouse small intestine. *Microbiome* (2020) doi:10.1186/s40168-020-0785-4.

194. Chart, H., Smith, H. R., La Ragione, R. M. & Woodward, M. J. An investigation into the pathogenic properties of Escherichia coli strains BLR, BL21, DH5α and EQ1. *J. Appl. Microbiol.* (2000) doi:10.1046/j.1365-2672.2000.01211.x.

195. Li, P., Lin, J. E., Snook, A. E. & Waldman, S. A. ST-producing E. Coli oppose carcinogen-induced colorectal tumorigenesis in mice. *Toxins* (2017) doi:10.3390/toxins9090279.

196. Lawley, T. D. & Walker, A. W. Intestinal colonization resistance. *Immunology* (2013) doi:10.1111/j.1365-2567.2012.03616.x.

197. Lasaro, M. *et al.* Escherichia coli isolate for studying colonization of the mouse intestine and its application to two-component signaling knockouts. *J. Bacteriol.* (2014) doi:10.1128/JB.01296-13.

198. Lundberg, R., Toft, M. F., August, B., Hansen, A. K. & Hansen, C. H. F. Antibiotic-treated versus germ-free rodents for microbiota transplantation studies. *Gut Microbes* (2016) doi:10.1080/19490976.2015.1127463.

199. Jimenez, M., Langer, R. & Traverso, G. Microbial therapeutics: New opportunities for drug delivery. *J. Exp. Med.* (2019) doi:10.1084/jem.20190609.

200. Volkmer, B. & Heinemann, M. Condition-Dependent cell volume and concentration of Escherichia coli to facilitate data conversion for systems biology modeling. *PLoS ONE* (2011) doi:10.1371/journal.pone.0023126.

201. Wilson, W. W., Wade, M. M., Holman, S. C. & Champlin, F. R. Status of methods for assessing bacterial cell surface charge properties based on zeta potential measurements. *J. Microbiol. Methods* (2001) doi:10.1016/S0167-7012(00)00224-4.

202. Thakor, A. S. *et al.* Clinically Approved Nanoparticle Imaging Agents. *J. Nucl. Med.* (2016) doi:10.2967/jnumed.116.181362.

203. Magnets in the GI tract. *Gastrointest. Endosc.* (2013) doi:10.1016/j.gie.2013.07.020.

204. Shamsudhin, N. *et al.* Magnetically guided capsule endoscopy: *Med. Phys.* (2017) doi:10.1002/mp.12299.

205. Charbonneau, M. R., Isabella, V. M., Li, N. & Kurtz, C. B. Developing a new class of engineered live bacterial therapeutics to treat human diseases. *Nat. Commun.* (2020) doi:10.1038/s41467-020-15508-1.

206. Grady, R. & Hayes, F. Axe-Txe, a broad-spectrum proteic toxin-antitoxin system specified by a multidrug-resistant, clinical isolate of Enterococcus faecium. *Mol. Microbiol.* **47**, 1419–1432 (2003).

207. Camacho, J. M. & Sosa, V. Alternative method to calculate the magnetic field of permanent magnets with azimuthal symmetry. *Rev. Mex. Fis. E* (2013).

208. Small bowel mri (enterography) planning and preparation | mri enteroclysis protocols and indications. https://mrimaster.com/PLAN%20SMALL%20BOWEL.html.

209. abdomen anatomy | MRI abdomen axial anatomy | free cross sectional anatomy |. https://mrimaster.com/anatomy%20abdomen%20axial.html.